The contribution of traumatic brain injury to Alzheimer's disease progression

Jaezah Adlina binti Zainal Azman

University of Oxford

Department of Pharmacology

St Peter's College

A thesis submitted in partial fulfilment of the requirements for the degree of Doctor of Philosophy at the University of Oxford

Michaelmas Term 2023

Abstract

The collective data from human and rodent studies indicate that a single traumatic brain injury (TBI) in healthy individuals can lead to an increased plaque burden, potentially accelerating the onset of Alzheimer's Disease (AD). However, there is limited research on the effects of TBI in patients already diagnosed with AD. Gilbert et al. (2014) found that AD patients with a history of TBI (AD-TBI) experienced a more rapid progression of the disease, with a faster decline in cognitive abilities compared to AD patients without TBI. This suggests an interaction between AD pathology and TBI, accelerating disease progression. Yet, it remains unclear whether amyloid plaques, tau tangles, or both, are responsible for this outcome. Understanding the mechanisms behind this accelerated AD progression post-TBI is crucial, as it can guide interventions for AD-TBI patients. Notably, elderly AD patients are particularly susceptible to TBI, often due to falls, as shown in TBI epidemiology reports.

This study hypothesizes that dysregulated systemic acute phase response (APR) following TBI in AD subjects is a key factor in hastening AD progression. In AD brains, existing conditions like plaques and/or tangles can keep microglia in a chronically active or "primed" state. Subsequent TBI can over-activate these primed microglia, leading to excessive cytokine secretion and abnormally high systemic APR. This could increase the mobilization of peripheral inflammatory cells and exacerbate brain injury, worsening AD. I tested this hypothesis using two transgenic AD mouse models, J20 and P301S, representing amyloid plaques and tau tangles, respectively, subjected to acute and chronic TBI. The J20-TBI model, compared to a wild-type TBI (WT-TBI) group, confirmed the two-hit hypothesis after acute contusion. 6-month-old (prodromal stage) and 12-month-old (AD dementia stage) J20 mice were used to study the impact of varying plaque burdens on APR. Mice in the prodromal stage showed a heightened APR compared to the AD dementia group. However, the P301S-TBI group did not display significant differences post-acute brain trauma compared to the WT-TBI control, suggesting a synergistic interaction between amyloid plaques and acute TBI, absent in tau tangles. Additionally, chronic TBI exposure in both J20-TBI and P301S-TBI groups resulted in negligible brain and systemic inflammatory profiles compared to the WT-TBI group.

1H NMR coupled with OPLS-DA untargeted approach was performed in J20 vs WT groups to ascertain the top discriminatory metabolites as well as to generate a comprehensive J20 mutant metabolite profile covering pre-frontal cortex, hippocampus, liver, spleen, and serum. Citrate, glucose, and glutamine were discovered as the overlapping metabolites that are present in both central nervous system and periphery tissues which may hold the potential as peripheral biomarkers for AD. In conclusion, this study sheds light on a critical aspect of AD research, namely, the interplay between TBI and AD pathology. The findings suggest that in AD individuals, the dysregulated systemic APR triggered by TBI can exacerbate the progression of the disease, particularly in the presence of

amyloid plaques. This insight not only provides a deeper understanding of the mechanisms underlying AD acceleration following TBI but also underscores the potential significance of targeting the APR pathway as an intervention strategy for AD patients with a history of TBI. These findings may pave the way for the development of novel therapies and the identification of peripheral biomarkers for AD, ultimately offering hope for improved clinical outcomes and better management of this devastating neurodegenerative condition, especially among the elderly population at higher risk of TBI.

Acknowledgement

I would like to express sincere gratitude to my supervisors, Prof Daniel Anthony and Dr Alexander Jeans, for their continuous support and guidance throughout my DPhil years. Daniel, I appreciate the opportunity to acquire valuable skills and techniques under your mentorship. Special thanks to Dr Fay Probert for her invaluable advice and assistance in 1H NMR experiments and analysis. I extend my thanks to Victor, Ron, Gabriela, Marcus, Halwan, Karolina, Pippa, Daan, Megan, Jay, Marta, Yifan, Dan, Izzy, Sofija, Kary Chan, and all other friends from Oxford who have been great company.

Additionally, my profound gratitude goes to Kak Hani, Kak Wan Mai, Kak Sofia, Hasif, Adli, Omar, Rabeah, Aijud, Fareez, Zikri, James Tan, Megat, Maryam – thank you for your generosity in cooking and sharing Malaysian food. Your kindness has made Oxford feel like a home, far away from home. To my ice cream and dessert buddies, Rasyiqah and Kak Jamaliah – my social life would be less *sweet* if not for both of you. I have thoroughly enjoyed exploring new dessert spots and having fun outings together. A special shoutout to Ibu, Nurin, Damia, and Hannah – the frequent video and audio calls from Malaysia have meant the world to me, your constant support is deeply appreciated. To my besties since undergraduate years, Aina and Aisyah – thank you for the humour and endless texts on our chat groups. They have been my mood boosters in times of need! Finally, to Ayah, Aqil, Kakak, Abang Long, Hafizh Siraj, Izzah Farhana, Najiha Norizan, extended family members, friends near and far, thank you for making my DPhil journey a memorable one. Your unwavering support and encouragement have been my pillars of strength.

Special thanks to the departmental staff, especially Paula, Hicham, James, and Graeme, for their kindness and assistance. My sincere gratitude extends to the Government of Malaysia, specifically the Merdeka scholarship under Yayasan Khazanah - OxCIS, for the invaluable financial support throughout my study. Your contribution has made this academic pursuit possible, and I am eternally grateful. My heartfelt thanks to the King's Scholarship of Malaysia (Biasiswa Yang di-Pertuan Agong 2017) for sponsoring my master's degree under the same department, which has become the stepping stone for my DPhil journey.

As I embark on the next chapter of my journey, I carry with me the lessons, memories, and the immense support I have received. To myself, well done for your perseverance in finishing this highest academic pursuit, despite the global pandemic and related difficulties – congratulations! To everyone who has been part of my academic adventure, your role in shaping my experience is immeasurable, thank you.

Table of contents

Abstract. ……i
Acknowledgement……iii
List of figures……ix
List of tables……xii
Abbreviations…… xiii

CHAPTER 1 : INTRODUCTION 1

1.1 General introduction..... 1
1.1.1 General aim and hypothesis 3

1.2 Alzheimer's disease 7
1.2.1 Historical perspective 7
1.2.2 Dementia and the classification of AD 10
1.2.2.1 Early onset AD 11
1.2.2.2 Late-onset AD 12
1.2.3 The amyloid cascade hypothesis 17
1.2.3.1 Amyloid precursor protein 18
1.2.3.2 Non-amyloidogenic pathway 20
1.2.3.3 Amyloidogenic pathway 23
1.2.3.4 Neurofibrillary tangles aggregation 29
1.2.4 Clinical stages of AD 33
1.2.4.1 NINDCS-ADRDA criteria 34
1.2.4.2 NIA-AA criteria 34
1.2.5 Neuropathological staging of AD 37
1.2.6 AD pharmacotherapies 43
1.2.7 Animal models of AD 55
1.2.7.1 Transgenic J20 mutant (PDGF-APPSw,Ind) 55
1.2.7.2 Transgenic P301S mutant (hTau.P301S) 58

1.3 Two-hit hypothesis 61
1.3.1 History 61

1.4 Traumatic brain injury 63
1.4.1 Pathophysiology of traumatic brain injury 66
1.4.2 Neuroinflammation 66
1.4.2.1 Microglia and astrocytes 69
1.4.2.2 Systemic acute phase response 77
1.4.2.3 Neutrophils, monocytes, and macrophages 80
1.4.2.4 Extracellular vesicles 84
1.4.3 Animal models of TBI 87
1.4.3.1 Limitations and advantages of rodent TBI model 89

1.5 Metabolomics 91
1.5.1 Advantages of NMR spectroscopy 93
1.5.2 1H NMR spectroscopy 95

CHAPTER 2 : METHODOLOGY 99

2.1 Animals 99
2.1.1 Mutant genotyping 99

2.2 Brain contusion 100

2.3 Behavioural test 102
2.3.1 Adhesive tape removal test 102
2.3.2 Two-trial Y-maze 103
2.3.3 Light-dark box 106

2.4 Tissue sample collection 109

2.5 Histology 109
2.5.1 Tissue sectioning 110
2.5.2 Immunohistochemistry 110
2.5.3 Cell quantification and histology analysis 114
2.5.3.1 Brain infarct size, brain atrophy and neuronal cell count 114
2.5.3.2 Brain plaque and tau tangles 114
2.5.3.3 MBS+ and Iba-1+ cells 116

2.6 Molecular biology 117
2.6.1 mRNA extraction and cDNA conversion 117
2.6.2 RT-qPCR 118

2.7 Extracellular vesicles 121
2.7.1 Pellet isolation 121
2.7.2 ZetaView nanoparticle tracking analysis 121

2.8 Statistical analysis and data presentation 122

2.9 Metabolomics 124
2.9.1 Sample collection 124
2.9.2 Sample extraction for fresh tissues 124
2.9.2.1 Brain 124
2.9.2.2 Liver and spleen 125
2.9.3 Sample preparation and spectral acquisition 126
2.9.3.1 Serum 126
2.9.3.2 Brain, liver, and spleen 126
2.9.4 Spectra processing and multivariate analysis 127
2.9.4.1 Orthogonal partial-least square discriminant analysis 127
2.9.4.2 Statistical analysis and metabolite assignment 128

CHAPTER 3 : THE EFFECT OF ACUTE TBI ON J20 AND P301S MUTANTS 130

3.1 Introduction 130
3.1.1 Chapter aims 133
3.1.2 Experimental design 133

3.2 Results 135
3.2.1 J20 mice exhibit sensorimotor deficit following TBI 135
3.2.2 Increased CASP3+ apoptotic neurons in J20 mice at 24 hours post-TBI 139
3.2.3 No difference in brain neutrophils and microglia 143
3.2.4 Plaque deposition increases systemic APR through increased liver *CCL-9*, *SAA-2*, and *CXCL-10* molecules post-TBI 146
3.2.5 Liver MBS and Iba-1 counts of J20 mutants are indifferent to WT controls 150
3.2.6 Brain RT-qPCR profile of J20 is indifferent to WT control 152
3.2.7 EV profile and exosomes quantification of J20 mutants are indifferent to WT controls 154
3.2.8 Brain injury profile of 6 months old J20/ WT mice 156
3.2.9 *SAA-2* and *CXCL-1* upregulation in 6 months old J20 mice following acute TBI 160
3.2.10 Liver MBS+ counts increased in 6 months old J20 mice at 6-hour post-TBI 163
3.2.11 *IL-1β* level in J20 brain is higher in contrast to WT control at 6-hour timepoint 165
3.2.12 EV profile and exosomes quantification of J20 mutants were indifferent to WT controls 167
3.2.13 Brain histological outcomes at 6-hour post-TBI in P301S mutant 169
3.2.14 No heightened APR response was seen in P301S group as compared to WT control 173
3.2.15 Increased EV concentration in P301S mice at 6-hour timepoint 177

3.3 Discussion 179
3.3.1 Principal findings 179
3.3.2 Heightened hepatic APR and brain injury observed in the 6 months old J20 cohort 182

CHAPTER 4 : THE EFFECT OF CHRONIC TBI EXPOSURE ONTO J20 AND P301S MUTANTS 194

4.1 Introduction 194
4.1.1 Chapter aims 196
4.1.2 Experimental design 197

4.2 Results 199
4.2.1 Chronic TBI increases AT8 tau burden in the brain 199
4.2.2 Increased impulsivity in both P301S and WT mice after chronic TBI202
4.2.3 Brain microglia basal number is unchanged post-TBI in both J20 and P301S mutants 207
4.2.4 Chronic TBI resulted in increased hepatic *IL-6* expression in P301S group 209

4.2.5 No changes in liver neutrophils and Kupffer cell number after chronic TBI 212
4.2.6 Decreased total EV and exosome concentration after chronic TBI in P301S group 214

4.3 Discussion 216
4.3.1 Principal findings 216
4.3.2 Higher AT8 burden in the brain after chronic TBI is correlated with higher *IL-6* expression in the liver 217

CHAPTER 5 : THE METABOLITE PROFILE OF J20 MUTANT USING UNTARGETED APPROACH 225

5.1 Introduction 225
5.1.1 Chapter aims 227
5.1.2 Experimental design 228

5.2 Results 230
5.2.1 J20 metabolomics profile is different to WT 230
5.2.2 Prefrontal cortex 233
5.2.2.1 Identifying the top discriminatory metabolites between early AD and late AD 235
5.2.2.2 Concentration of top PFC metabolites during early and late AD phase 237
5.2.3 Hippocampus 240
5.2.3.1 Identifying HC top discriminatory metabolites 242
5.2.3.2 Concentration of top metabolites during early and late AD phase…….244
5.2.4 Liver 245
5.2.4.1 Identifying liver discriminatory metabolites 246
5.2.4.2 Concentration of top liver metabolites during early and late AD phase…. 248
5.2.5 Spleen 250
5.2.5.1 Identifying spleen discriminatory metabolites 252
5.2.5.2 Concentration of top spleen metabolites during early and late AD phase…. 253
5.2.6 Serum 257
5.2.6.1 Identifying serum top discriminatory metabolites 258
5.2.6.2 Concentration of top serum metabolites during early and late AD phase…. 260
5.2.7 Overlapping brain-periphery metabolites 264

5.3 Discussion 266
5.3.1 Principal findings 266
5.3.2 Potential peripheral biomarkers of AD 268
5.3.2.1 Glucose 268
5.3.2.2 Citrate 270
5.3.2.3 Glutamine 271

CHAPTER 6 : FINAL DISCUSSION AND CONCLUSION 274

6.1 Key contributions 274

6.2 General discussion, future research, and conclusion 275

BIBLIOGRAPHY 280

List of figures

Figure 1.1 Schematic diagram of the general hypothesis. 6
Figure 1.2 Dr Alois Alzheimer (left) and Auguste Deter (right) 9
Figure 1.3 Amyloid cascade hypothesis. 17
Figure 1.4 Amyloid precursor protein 19
Figure 1.5 APP processing pathways 24
Figure 1.6 Amyloid plaque formation over time 26
Figure 1.7 The components of gamma-secretase 28
Figure 1.8 Neurofibrillary tau tangles 29
Figure 1.9 Microtubules held by tau proteins in a healthy neuronal axon 30
Figure 1.10 Alzheimer's disease is a progressive disease continuum that spans a period of years 33
Figure 1.11 Spatio-temporal evolution of amyloid and NFT pathologies according to Thal and Braak stages 40
Figure 1.12 Neuritic plaque density and its CERAD scoring 41
Figure 1.13 Acetylcholinesterase inhibitor mechanism of action 46
Figure 1.14 NMDA blocker mechanism of action 49
Figure 1.15 Monoclonal antibodies against amyloid 54
Figure 1.16 Hippocampal sections immunoperoxidase-stained for Aβ with 3D6 antibody. 56
Figure 1.17 Aβ immunoreactivity in cortex and hippocampus region of J20 mice. 57
Figure 1.18 Progressive neuronal loss of transgenic P301S was observed in the cerebral cortex starting at 3 months old 58
Figure 1.19 Tau proteins stained using AT8 antibody 59
Figure 1.20 Brain pathology and phenotypic characterisation of transgenic P301S mice (developed by Michel Goedert) 60
Figure 1.21 Pathophysiological cascades (secondary injury) following TBI 68
Figure 1.22 Resting and activated microglia 71
Figure 1.23 Two types of CNS astrocytes 73
Figure 1.24 Astrocytes line the blood vessels with their end feet 74
Figure 1.25 CNS - liver interplay during neuroinflammation 83
Figure 1.26 Biogenesis of exosomes and microvesicles 86
Figure 1.27 Controlled cortical impactor instruments 89
Figure 1.28 Overview of the omics family 92
Figure 1.29 The orientation of nuclei with and without an external magnetic field. 97
Figure 2.1 Brain sections immunostained against AB42 for amyloid detection 100
Figure 2.2 Experimental timeline for adhesive tape removal behavioural test 103

Figure 2.3 Experimental timeline for two-trial Y-maze, light dark box, and spontaneous alternations. 105
Figure 2.4 Two-trial Y-maze. 105
Figure 2.5 Good reference memory vs poor reference memory.. 106
Figure 2.6 Light-dark box. 107
Figure 2.7 Representative figure illustrating an alternation. 108
Figure 2.8 Quantification site for brain plaque and tau tangles. 115
Figure 2.9 Site of brain MBS+ and Iba-1+ cells quantification. 116
Figure 3.1 Experimental design for acute TBI study. 134
Figure 3.2 Adhesive tape removal behavioural assessment in 12 months old J20/ WT mice cohort. 138
Figure 3.3 Brain histopathological assessment following acute TBI in 12 months old J20/ WT mice cohort 142
Figure 3.4 Brain neutrophils and microglia counts after acute TBI in 12 months old J20/ WT mice cohort. 145
Figure 3.5 Liver molecular expression as measured through RT-qPCR in 12 months old J20/ WT mice cohort. 149
Figure 3.6 Peripheral inflammatory response post-acute TBI in 12 months old J20/ WT mice cohort 151
Figure 3.7 Brain mRNA expression of pro-inflammatory molecules at 24-hr timepoint in 12 months old J20/ WT mice cohort 153
Figure 3.8 EV profile and total exosome quantification in 12 months old J20/WT cohort following acute TBI 155
Figure 3.9 Brain infarct size and inflammatory profile following acute TBI in 6 months old J20/ WT mice cohort 158
Figure 3.10 Liver molecular expression as measured through RT-qPCR following acute TBI in 6 months old J20/ WT mice cohort. 162
Figure 3.11 Liver neutrophils and Kupffer cells count following acute TBI in 6 months old J20/ WT mice cohort 164
Figure 3.12 Brain mRNA expression of pro-inflammatory molecules at 6-hour timepoint in 6 months old J20/ WT mice cohort 166
Figure 3.13 EV profile and exosome quantification following acute TBI in 6 months old J20/ WT mice cohort. 168
Figure 3.14 Brain histopathological assessment following acute TBI in WT and P301S mutants following 6-hour TBI. 171
Figure 3.15 Hepatic RT-qPCR and histology profile of WT and P301S mutants at 6-hour post-injury 175
Figure 3.16 EV profile and exosome quantification of WT and P301S mutants at 6-hr post-injury. 178
Figure 3.17 Principal findings for the 6-month-old J20 cohort when compared against age-matched WT control. 180
Figure 3.18 Principal findings of the 12-month-old J20 cohort when compared against age-matched WT control 181

Figure 4.1 Experimental design for chronic TBI using transgenic J20 and P301S mutants 198
Figure 4.2 Abnormal hyperphosphorylated tau burden.. 201
Figure 4.3 Behavioural assessments after chronic TBI in P301S mice 205
Figure 4.4 Brain histological outcome after chronic TBI 208
Figure 4.5 Relative expression of pro-inflammatory molecules in the liver as examined by RT-qPCR..... 211
Figure 4.6 Relative expression of hepatic chemokines and histological outcomes 213
Figure 4.7 EV profile and exosome quantification following chronic TBI 215
Figure 5.1 J20 mutant phenotypic timeline 229
Figure 5.2 Box plots of predictive accuracies from the OPLS-DA models of J20 vs WT (all age) against random chance. 232
Figure 5.3 Box plots of predictive accuracies from the PFC OPLS-DA models of J20 vs WT against random chance 234
Figure 5.4 VIP ranking plot for PFC samples 235
Figure 5.5 PFC VIP metabolites 239
Figure 5.6 Box plots of predictive accuracies from the HC OPLS-DA models of J20 vs WT against random chance 241
Figure 5.7 VIP ranking plot for HC samples 242
Figure 5.8 HC VIP metabolites 244
Figure 5.9 Box plots of predictive accuracies from the liver OPLS-DA models of J20 vs WT against random chance 246
Figure 5.10 VIP ranking plot for liver samples. 247
Figure 5.11 Liver VIP metabolites 249
Figure 5.12 Box plots of predictive accuracies from the spleen OPLS-DA models of J20 vs WT against random chance..... 251
Figure 5.13 VIP ranking plot for spleen samples 252
Figure 5.14 Spleen VIP metabolites. 256
Figure 5.15 Box plots of predictive accuracies from the serum OPLS-DA models of J20 vs WT against random chance..... 258
Figure 5.16 VIP ranking plot for serum samples. 259
Figure 5.17 Serum VIP metabolites. 263
Figure 5.18 Heatmap on principal VIP metabolites that are present in both brain and periphery tissues 265

List of tables

Table 1.1 Summary of human APP secretases and their products when processed through the non-amyloidogenic and amyloidogenic pathway. 24
Table 1.2 Thal phases of Aβ accumulation 38
Table 1.3 Braak staging of NFT deposition based on the anatomical distribution of tau NFT 39
Table 1.4 The CERAD scoring for neuritic plaque deposition 41
Table 1.5 The combination of ABC scores is translated into "Not", "Low", "Intermediate" or "High" AD neuropathologic change level 42
Table 1.6 Summary of AChEI and NMDA blocker pharmacotherapies available for the treatment of AD 50
Table 1.7 Classification system for traumatic brain injury 65
Table 2.1 Antibodies used for immunohistochemistry 112
Table 2.2 Steps for cresyl violet or Harris haematoxylin counterstaining…. .. 113
Table 2.3 RT-qPCR primers. 119
Table 2.4 Components for RT-qPCR reaction for Sigma primers. 120
Table 2.5 Components for RT-qPCR reaction for Primerdesign and Bio-rad primers. 120
Table 5.1 OPLS-DA plots of J20 vs WT (all age) 231
Table 5.2 Prefrontal cortex OPLS-DA plots illustrated a distinct separation for J20 vs WT samples in early and late AD stage 233
Table 5.3 List of top discriminatory metabolites in PFC samples 236
Table 5.4 Hippocampus OPLS-DA plots illustrated a great separation for J20 vs WT samples in early and late AD stage. 240
Table 5.5 List of top discriminatory metabolites in HC samples. 243
Table 5.6 Liver OPLS-DA plots illustrated a great separation for J20 vs WT samples late AD stage, but not in the early AD stage 245
Table 5.7 List of top discriminatory metabolites in liver samples. 247
Table 5.8 Spleen OPLS-DA plots illustrated a great separation for J20 vs WT samples early and late AD stage. 250
Table 5.9 List of top discriminatory metabolites in spleen samples 253
Table 5.10 Serum OPLS-DA plots illustrated a great separation for J20 vs WT samples late AD stage, but not in the early AD stage 257
Table 5.11 List of top discriminatory metabolites in serum samples 259
Table 5.12 Summary of principal VIP metabolites across tissues. 264

Abbreviations

1H NMR	proton NMR
Aβ	amyloid beta
ABCA7	ATP-binding cassette transporter A7
acetyl-CoA	acetyl-Coenzyme A
ACh	acetylcholine
AChE	acetylcholinesterase
AChEI	acetylcholinesterase inhibitors
AD	Alzheimer's disease
ADAM10	A Disintegrin and Metalloproteinase 10
AICD	APP intracellular domain
ANOVA	analysis of variance
APH1	anterior pharynx defective phenotype 1
apoE	apolipoprotein E protein
APOE4	apolipoprotein epsilon 4 gene
APP	amyloid precursor protein
APP	amyloid precursor protein gene
APPa	soluble APPa derivative
APR	acute phase response
ATP	adenosine triphosphate
B0	external magnetic field
BACE1	β-site amyloid precursor protein cleaving enzyme 1
BDNF	brain derived neurotrophic factor
BBB	blood-brain barrier
CASP3	caspase-3
CCI	controlled cortical impact injury
CD33	cluster of differentiation 33
cDNA	complementary deoxyribonucleic acid
CERAD	Consortium to Establish a Registry for Alzheimer's Disease
ChAT	choline acetyltransferase
CSF	cerebrospinal fluid
CTE	chronic traumatic encephalopathy
CTFa	membrane-bound a-carboxyl-terminal fragment
CTFβ	β-carboxyl-terminal fragment
CCL	C-C motif ligand
CXCR	C-X-C motif receptor

CXCL	C-X-C motif ligand
DAMPs	danger-associated molecular patterns
EOAD	early-onset AD
ERK	extracellular-signal-regulated kinase
EV	extracellular vesicle
FAD	familial AD
fMRI	functional magnetic resonance imaging
FPI	fluid percussion injury
FWER	family-wise error rate
GABA	gamma-aminobutyric acid
GC	gas chromatography
GFAP	glial acidic fibrillary protein
GOI	gene of interest
GS	glutamine synthetase
GWAS	genome-wide association studies
hAPP	human APP
HC	hippocampus
HMDB	human metabolome database
HMGB1	high mobility group box-1
Iba-1	ionized calcium-binding adaptor molecule 1
IHC	immunohistochemistry
IL	interleukin
ILV	intraluminal vesicle
IQR	interquartile range
LC	liquid chromatography
LOAD	late-onset AD
mAb	monoclonal antibody
MAP	microtubule-associated protein
MAPK	mitogen activated protein kinase
MBR	microtubule-binding region
MCI	mild cognitive impairment
MAPT	microtubule-associated protein tau
MHC	major histocompatibility complex
MIP-1γ	macrophage inflammatory protein 1γ
MS4A6A	membrane spanning four domain subfamily A members 4A and 6A
MVBs	multivesicular bodies
NF-κB	nuclear factor kappa B
NFT	neurofibrillary tau tangles

NIA-AA	National Institute on Aging and the Alzheimer's Association
NIA-Reagan	National Institute on Aging/Reagan Institute of the Alzheimer Association Consensus Recommendations for the Postmortem Diagnosis of AD
NINCDS-ADRDA	National Institute of Neurological and Communicative Disorders and Stroke and the Alzheimer's Disease and Related Disorders Association
NMDA	N-methyl-D-aspartate
O-PLS	orthogonal projections to latent structures
OPLS-DA	orthogonal partial-least square discriminant analysis
PI3K/Akt	phosphatidylinositol 3-kinase/Akt
p-Tau	phosphorylated tau
p3	truncated Aβ peptide of 3kDa size
PCA	principal component analysis
PDGF-β	human platelet-derived growth factor β chain
PEN-2	presenilin enhancer 2
PFC	prefrontal cortex
PFP	platelet-free plasma
PRRs	pattern recognition receptors
PSEN	presenilin gene
PSEN1/2	presenilin protein 1 and 2
RNA	ribonucleic acid
ROS	reactive oxygen species
RT	room temperature
RT-qPCR	real-time quantitative polymerase chain reaction
S100B	S100 calcium binding protein B
SAA	serum amyloid A
sAPPβ	shorter soluble APPβ
SD	standard deviation
SEM	standard error of the mean
SNPs	single-nucleotide polymorphisms
sTREM2	soluble TREM2
TBI	traumatic brain injury
TCA	tricarboxylic acid
TGF-β	tumor growth factor-β
TNF-α	tumor necrosis factor-α
TREM2	triggering receptor expressed on myeloid cells 2
VIP	variable importance in projection

CHAPTER 1

INTRODUCTION

Chapter 1 : Introduction

1.1 General introduction

Alzheimer's disease (AD) is a progressive neurodegenerative disease that results in synaptic dysfunction and brain atrophy over time. The deposition of extracellular amyloid beta (Aβ) plaques and intracellular neurofibrillary tau tangles (NFT) in AD brain are two key pathologies that characterise this disease. These pathologic lesions trigger the formation of reactive oxygen species (ROS), dysregulate mitochondrial function, neuronal death, and the downstream inflammatory processes that interfere with normal brain function (Ghidoni, Paterlini, & Benussi, 2013). Broadly, AD stages are divided into pre-clinical AD, mild cognitive impairment (MCI, also known as prodromal stage), and AD dementia.

The pre-clinical AD stage is a long asymptomatic period that can take up to 20-30 years during which the abnormal brain pathology develops, but the disease burden has yet to pass the threshold for an individual to report observable clinical signs (Bernardini & Zima, 2019; Braak & Del Tredici, 2015). The prodromal stage is the transition stage between the asymptomatic pre-clinical phase and AD dementia where the signs of cognitive impairment become manifest. However, in this stage, the cognitive anomalies experienced by the patients are not severe enough to interfere with daily activities (Chételat et al., 2020; Dubois et al., 2007). The AD dementia stage can be further classified into mild, moderate, and severe AD dementia. Patients in AD dementia stage show memory disturbance and

severe incompetency to perform work and usual activities, which, therefore, require caregiver assistance (Della Sala, Spinnler, & Venneri, 2004; Scharre, 2019). This stage has an enormous economic consequence for the family and wider society.

The hippocampus is the area that is primarily affected in AD, which largely explains the deterioration of memory and cognitive ability that generate the earliest symptoms exhibited by the patients (Annaert & De Strooper, 2002; Perluigi, Barone, Di Domenico, & Butterfield, 2016). As the disease progresses and abnormal deposition of Aβ plaques and NFTs spread throughout the brain, the chronic deficit of neuronal reserve leads to the loss of motor function. Henceforth, in AD late stage, a patient's ability to carry out simple tasks such as walking and controlling bowel movement diminishes. Subsequently, the failure in regulating the respiratory system eventually results in death (Della Sala et al., 2004).

Age is the principal risk factor for AD, which is also used as a basis to classify AD into early-onset AD (EOAD) or late-onset AD (LOAD). EOAD affects younger people of late 30s to early 60s, whereas LOAD begins at the age of 65 years old (Bekris, Yu, Bird, & Tsuang, 2010). Mutations to amyloid precursor protein gene (*APP*) and presenilin gene (*PSEN*) sequences have been reported to be causal for AD development (Bertram, Lill, & Tanzi, 2010; Soria Lopez, González, & Léger, 2019). Mutations to these genes promote overexpression of amyloid precursor protein (APP) and abnormal APP proteolysis, leading to excess Aβ protein production and subsequent Aβ aggregate formation (Mendez, 2019;

Weggen & Beher, 2012). In addition to intrinsic factors that affect progression, extrinsic factors are also implicated such as traumatic brain injury (TBI) which occurs when the brain is penetrated by an object (open head injury), or when a massive blow to the head causes the brain to ricochet rapidly within the skull resulting in tissue damage (closed head injury) (Prins et al, 2013; Adrian et al, 2016). Although the association between TBI and the development of AD in later life is widely discussed to be a contributory factor, there is lack of research on how TBI contributes to progression of AD at a mechanistic level. One key study (Gilbert et al, 2014) showed that the rate of disease progression, demonstrated through faster cognitive decline is hastened in AD patients with TBI history, as compared to patients without such exposure. Nonetheless, the mechanism underlying this observation is unknown.

1.1.1 General aim and hypothesis

In this thesis, I have sought to better understand the effect of TBI on AD progression, by exposing two transgenic AD mutants: the J20 and P301S lines, to a moderate brain contusion using a controlled cortical impactor device. The J20 mutant overexpresses human APP protein whereas the P301S mutant expresses hyperphosphorylated tau tangles in their brains respectively.

It was my hypothesis that the exposure of TBI onto AD mutants would worsen the AD-like disease, and that the process would be coordinated through an excessive hepatic acute phase response (APR) post-TBI, which is known to contribute to the outcome of TBI. The systemic APR is an innate defense

mechanism that is activated in response to injury or disease (Cray, Zaias, & Altman, 2009; Sá-Pereira et al., 2018). In a normal healthy brain, the microglia are present in a non-activated ("resting") state; they quickly respond to brain injury by becoming 'activated' which is typically associated with morphological changes such as the retraction of their processes and proliferation. They also release cytokines as injury signals that activate local astrocytes and endothelial cells. The injury signals are also carried into the circulation, in the form of astrocyte-derived extracellular vesicles, which reach the liver and spleen resulting in the upregulation and release of chemokines that mobilise leukocytes from the bone marrow to the blood, and subsequently to the site of injury – the brain. While the systemic APR is pivotal in the injury recovery process when it occurs in a timely manner, a sustained or excessive APR can lead to organ damage (Ziebell & Morganti-Kossmann, 2010).

In AD brain, the resident immune cells microglia remain in an activated ("primed") state due to the presence of Aβ and NFT foreign entities. Therefore, in the case of a AD-TBI concomitant incident (two-hit theory[1]), it is my postulate that the primed microglia would secrete an abnormally high concentration of cytokines into the circulation, which would trigger an increase in hepatic APR activity. In turn, this will result in an increased inflammatory cell migration into the brain, leading to unwanted additional brain tissue damage and further neuronal loss (Figure 1.1). Therefore, the hypothesized worsened AD condition post-TBI may arise because of the two-hit phenomena whereby the occurrence of both AD

[1] Two-hit theory: Both insults need to be present to cause the phenotypic outcome (Knudson, 1971)

pathology (first-hit) and TBI (second-hit) synergise to accelerate the disease condition via the dysregulated systemic APR.

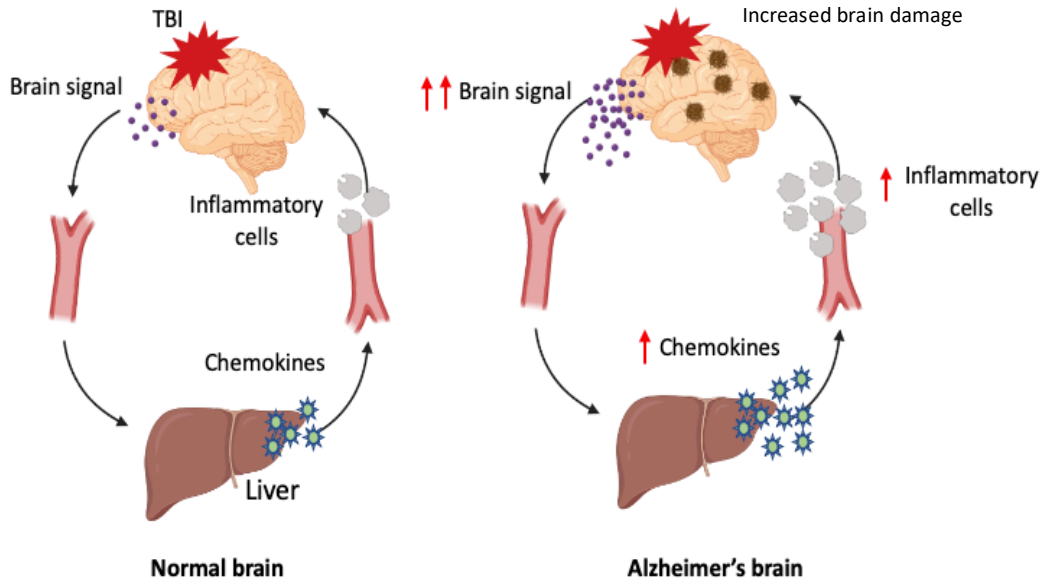


Figure 1.1 Schematic diagram of the general hypothesis. AD brain with amyloid plaque and NFT pathologies sends out a greater brain signal to the liver in response to TBI. In AD brain, the plaques and NFTs are perceived as foreign entities, causing the microglia to be in an activated ("primed") state. Primed microglia have a higher phagocytic capacity and enhanced sensitivity towards external insults such as TBI. When AD brain with primed microglia was subjected to TBI, they produce an elevated level of cytokines and ROS which are harmful to local and systemic environment. The liver responds to the brain cytokines through the activation of systemic APR, leading to the mobilisation of extensive peripheral inflammatory cells to the site of inflammation. The uncontrolled infiltration of inflammatory cells into the brain is expected to contribute to further exacerbation of the brain injury and worsen the AD condition. The illustration was created using Bio-render website and Microsoft PowerPoint.

1.2 Alzheimer's disease

1.2.1 Historical perspective

The discovery of AD was first presented by Dr Alois Alzheimer (1864-1915, Figure 1.2) at a scientific congress of German psychiatrists in Tubingen, 1906. His finding was prompted by an atypical behavioral observation of his female patient, named Auguste Deter (Sanabria-Castro, Alvarado-Echeverría, & Monge-Bonilla, 2017). The 50-year-old female patient was admitted into Frankfurt Psychiatric Hospital in 1901 when Alzheimer was working as a senior assistant. She was presented with fast-progressing psychological symptoms, such as severe confusion, aggressiveness, and sleep disorders (Hippius & Neundorfer, 2003). Alzheimer recorded an extensive documentation on Deter's clinical findings highlighting her memory disorder (Bondi, Edmonds, & Salmon, 2017); some of which are as below:

"When objects are shown to her, she does not remember after a short time which objects have been shown…"
"Asked to write Auguste D, she tried to write Mrs. and forgets the rest…"
"She seems not to understand what she reads…"

Following her death in 1906, Dr Alzheimer studied her brain and observed a diffuse brain atrophy and abnormal pathological lesions, which he described the finding as "*the peculiar disease process of the cerebral cortex*". These lesions are now known as the amyloid plaque (previously called miliary foci) and neurofibrillary tangles (previously referred as abnormal intracellular aggregates)

respectively (O'Brien & Wong, 2011; Soria Lopez et al., 2019). The observation of these lesions were made possible through the Bielchowsky silver staining technique (Ferrer, 2022).

In addition to Auguste D, the medical case of Josef F (also known as Johann F) has contributed greatly to the understanding of AD development, albeit less commonly cited. In 1911, Alzheimer reported the case of a 56-year-old male patient whom clinical and histological presentation fits the diagnosis of AD, except that no tangles were observed (Hippius & Neundorfer, 2003). In the past, the presence of both plaques and tangles was deemed necessary for an AD diagnosis. Eighty years after Alzheimer passed away, this puzzling observation was finally solved in 1998 by Möller and Graeber (Möller & Graeber, 1998). Using modern neuro-histochemical techniques, they re-investigated the materials of both cases and concluded that Auguste D and Josef F both had AD but were in different stages of the disease process. This outcome highlights histopathological changes in AD progression, which is another important contribution of Alzheimer in the field of AD, although long after his death.

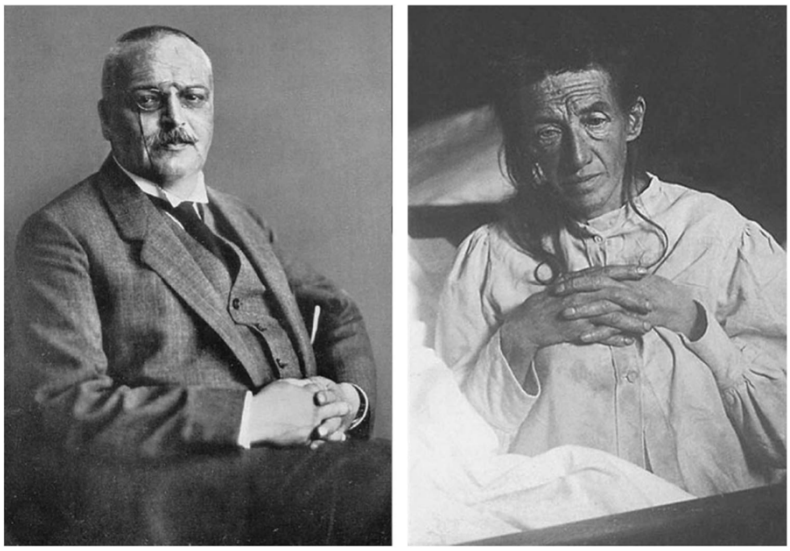


Figure 1.2 Dr Alois Alzheimer (left) and Auguste Deter (right). Dr Alzheimer (1864–1915) was working at Frankfurt Psychiatric Hospital when he came across Deter who showed abnormal cognitive disturbance. Images retrieved from Bondi et al (2017).

1.2.2 Dementia and the classification of AD

It is estimated that 47.5 million people in the world are affected by dementia, and nearly 7.7 million new cases are reported every year (Dai, Zheng, Zeng, & Zhang, 2018). In 2018, the cost of catering to dementia needs was expected to exceed trillion dollars USD (Deture & Dickson, 2019). Dementia is an umbrella term for cognitive dysfunction that includes memory loss, language impairment, and deterioration in problem-solving abilities that significantly interferes with daily life (Alzheimer's Association, 2018). The word dementia comes from Latin terminology, *demens* that is defined as 'out of one's mind' (Bishara, Justin, & Taylor, 2015). The majority of dementia patients (>80%) also display accompanying behavioral and psychological symptoms such as agitation, aggression, mood disorder, wandering and psychosis (Bishara et al., 2015). AD is the most common form of dementia, accounting to 60-80% of all cases (Fricker, Tolkovsky, Borutaite, Coleman, & Brown, 2018). Other causes of dementia include Parkinson's disease, vascular dementia, and Lewy body dementia (Deture & Dickson, 2019).

Females are more commonly diagnosed with AD, and two-thirds of AD cases are are female. This observation is often attributed to the longer life span of women as compared to men as age is the most significant known risk factor for Alzheimer's, the longer life expectancy for women naturally results in more women being diagnosed with the disease (Soria Lopez et al., 2019), but, in the post war period, is seems likely that other factors may also play a role. Some studies suggest that biological or genetic differences might make women more

susceptible to the disease. For example, the presence of the APOE-e4 gene, a known risk factor for Alzheimer's, seems to pose a greater risk for women than men. Ther role of estrogen has also been studied for its potential role in brain health. The decline in estrogen levels after menopause might have a connection to the onset of Alzheimer's disease. However, the relationship between estrogen replacement therapy and Alzheimer's prevention remains controversial and unclear. Other Health Issues, such as heart disease, diabetes, and stroke, which are known to increase the risk of Alzheimer's, have different prevalence and manifestations in women compared to men (Nichols et al., 2019). As the number of ageing population increases over time, the prevalence of AD is expected to triple by 2050 (Baumgart et al., 2015). This is a concern as demented patients require constant caregiver support, which are emotionally and economically costly.

1.2.2.1 Early onset AD

1-5% of all AD cases are considered early onset (Deture & Dickson, 2019), which is defined as the case with clinical onset earlier than 65 years old (DeFina, Moser, Glenn, Lichtenstein, & Fellus, 2013; Mendez, 2019). EOAD cases are mainly caused by the autosomal dominant mutation with 90% heritability to the next generation, while LOAD cases are due to the mixture of both genetic (58 – 79% heritability) and environmental factors (Sims, Hill, & Williams, 2020). Between these two classes of AD, there is no histopathological difference recognised, although several studies reported that EOAD patients may experience a more aggressive progression with a higher risk of mortality in comparison to LOAD

(Mendez, 2019). Nonetheless, the symptoms of cognitive impairment experienced by the patients are similar and are clinically indistinguishable (Reitz, Brayne, & Mayeux, 2011). Three known genes preferentially affected in EOAD as compared to LOAD are (1) *APP* located on chromosome 21, (2) *PSEN1* on chromosome 21, and (3) *PSEN2* on chromosome 1 (Bertram et al., 2010; Soria Lopez et al., 2019).

Mutations to these genes promote the production of toxic Aβ42 fragments and the subsequent Aβ aggregation (Tanzi, 2012). Patient carrying these pathogenic genetic modifications is almost certain to develop EOAD. Nonetheless, it is noteworthy to point out that the mutation in these genes only explain a small fraction (approximately 5-10%) of all EOAD cases, which is sub-classified under familial AD (FAD), whereas a larger proportion of EOAD cases remain genetically unexplained (Dai et al., 2018; Sirkis, Bonham, Johnson, La Joie, & Yokoyama, 2022).

1.2.2.2 Late-onset AD

The prevalence of LOAD is more frequent - 95% of all AD cases - and is defined by clinical onset after age 65 (DeFina et al., 2013). Although the etiology of LOAD is not fully understood, the complex interaction between the genetic and environmental factors that occurs through ageing has been suggested as the underpinning mechanism (Panpalli Ates, Karaman, Guntekin, & Ergun, 2016; Soria Lopez et al., 2019). Apolipoprotein epsilon 4 gene (*APOE4*) was the first confirmed susceptibility gene for LOAD (Bekris et al., 2010; Naj & Schellenberg,

2017). The *APOE* gene encodes a protein called apolipoprotein E (apoE), which plays a crucial role the transport and metabolism of cholesterol and other lipids. Specifically, apoE is found in chylomicron remnants, very low-density lipoproteins (VLDL), and high-density lipoproteins (HDL). ApoE binds to various receptors on the surface of cells, particularly liver cells, facilitating the uptake of lipoprotein particles into cells. This process is essential for the normal catabolism of triglyceride-rich lipoprotein constituents. In the brain, apoE helps distribute cholesterol to neurons for nerve repair and growth. It is produced primarily by astrocytes and microglia in the central nervous system. The *APOE* gene has several variants, but three of them—*APOE2, APOE3, and APOE4*—are the most common. Of these, *APOE4* is associated with an increased risk for late-onset AD (Cacace, Sleegers, & Broeckhoven, 2016; Obenaus et al., 2018).

Interestingly, protection against AD has been demonstrated by *APOE2* allele, which is carried in less than 2% of the general population. Although the mechanism by which *APOE4* contributes to the pathogenesis is unclear, it is presumed that it promotes Aβ aggregation and interferes with its clearance, thereby enhancing Aβ deposition (Briggs, Kennelly, & O'neill, 2016). It was shown that the *APOE4* gene acts in a dose-dependent manner, as risk for AD increases from 3-fold for heterozygous carriers to 15-fold for homozygotes carriers (Cacace et al., 2016). However, unlike FAD-related genes, no clear association can be drawn between *APOE4* gene and LOAD development, as its presence alone is not sufficient nor necessary for AD initiation (Cacace et al., 2016).

Various environmental risk factors have been associated with the development of dementia and/or AD in later life (Reitz et al., 2011). Examples include TBI, alcohol intoxication, atherosclerosis, cardiovascular diseases, diabetes mellitus, high-fat diet, hyperlipidemia, stroke, and smoking (Abeysinghe, Deshapriya, & Udawatte, 2020; Panpalli Ates et al., 2016). These factors may contribute to the disease through one or more pathogenic mechanisms such as dysregulation the rate of Aβ production and clearance, increased oxidative stress and inflammation, as well as increased cholinergic deficits (G. Chen et al., 2017; Reitz et al., 2011).

1.2.2.2.1 Microglial TREM2 genetic alteration in AD

Thirty genetic risk loci for AD were identified through genome-wide association studies (GWAS), to which majority of the genes related to microglial function was recognised, including *APOE*, triggering receptor expressed on myeloid cells 2 (*TREM2*), cluster of differentiation 33 (*CD33*), ATP-binding cassette transporter A7 (*ABCA7*) and membrane spanning four domain subfamily A members 4A and 6A (*MS4A6A*). Among these variants, *TREM2* is associated with the highest risk of developing AD, as seen by 2- to 4-fold increase in disease risk (Long et al., 2022; McQuade & Blurton-Jones, 2019), hence will be the focus for this section.

As the name suggests, TREM2 is restrictively expressed on cells within the myeloid lineage. Thus, in the brain, TREM2 expression is dominated by microglia (McQuade & Blurton-Jones, 2019). Microglia originate from primitive macrophages in the yolk sac, and plays a pivotal role in maintaining brain

homeostasis (Long et al., 2022). Further information on microglia morphology and function can be found in section 1.4.2.1. The role of microglia in AD pathophysiology is complex, whereby in the early stage of AD, microglia exert neuroprotective function by reducing Aβ accumulation through phagocytosis (Shippy, Watters, & Ulland, 2022). The phagocytosis and clearance of Aβ by microglia was evidenced through the visualization of Aβ within microglia cell body (Wisniewski, Moretz, & Lossinsky, 1981). However, in response to AD pathology, microglia in homeostatic resting state transition to activated state, which can either mitigate or exacerbate neuroinflammation during AD through the release of pro-inflammatory chemokines and cytokines (Shippy et al., 2022). The activation of microglia was hypothesized to be triggered by Aβ. This is because the microglia in close proximity to Aβ plaque were seen to be preferentially activated (McQuade & Blurton-Jones, 2019).

Genetic alteration in microglia has been proposed to influence AD progression in many aspects, such as altered phagocytosis and synaptic pruning, dysregulated cytokine secretion as well as changes in trophic support (McQuade & Blurton-Jones, 2019). *R47H, R62H*, and *H157Y* are several of AD-associated single-nucleotide polymorphisms (SNPs) that occur within the *TREM2* coding region. *R47H TREM2* mutation resulted in worse AD prognosis, as the carriers of this variant showed an increased level of AD cerebrospinal fluid (CSF) biomarkers such as tau, p-tau181, and soluble TREM2 (sTREM2). Mutation to *TREM2* leads to early onset dementia in Nasu-Hakola disease patients, which highlights the role of microglia in cognitive function (Yeh, Hansen, & Sheng, 2017). It is suggested that the increased risk of AD associated with *R47H* mutation and other

variants in the *TREM2* gene may result from a partial loss of function, potentially affecting the receptor's ability to carry out phagocytosis. It was observed that deletion of *TREM2* gene in 5×FAD model mice resulted in increased Aβ aggregates in the brain. In addition, microglial TREM2 was shown to aggravate the propagation of tau proteins during late stage of AD (Gao, Jiang, Tan, & Chen, 2023) suggesting that microglia may play a crucial role in AD progression.

1.2.3 The amyloid cascade hypothesis

In this thesis, emphasis and elaboration is given to the amyloid cascade hypothesis (Figure 1.3) due to its reputation as the leading theory in AD field. According to this theory, Aβ plaque accumulation is the most important step and is considered to be the causative event in AD pathophysiology (Hardy & Higgins, 1992). The amyloid cascade hypothesis also supports the view that the formation of NFT, neuronal cell loss, cognitive deterioration and dementia are the downstream effects of Aβ deposition (Chételat, 2018). In addition to the amyloid cascade hypothesis, a number of other hypotheses have been proposed to explain AD pathophysiology, such as the cholinergic hypothesis, calcium hypothesis, tau propagation hypothesis, metal ion hypothesis, inflammatory hypothesis and neurovascular hypothesis, which will not be discussed here, but there are plenty of reviews available on these hypotheses (P. P. Liu, Xie, Meng, & Kang, 2019; Sanabria-Castro et al., 2017; Schweber, 1986).

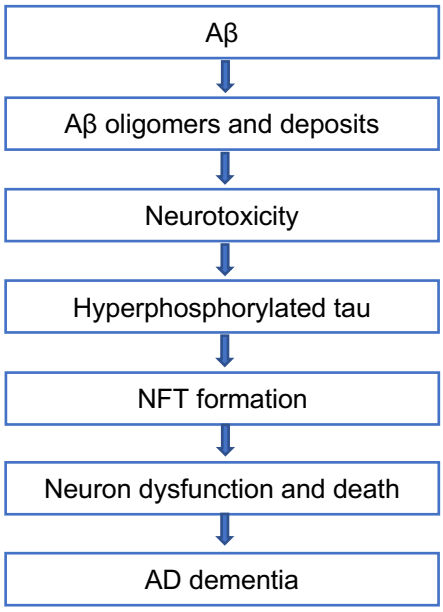


Figure 1.3 Amyloid cascade hypothesis. This hypothesis posits the notion that Aβ is the initiator of subsequent events that leads to AD dementia.

1.2.3.1 Amyloid precursor protein

APP plays an important role in the neuronal development and signaling, as well as regulating synaptic formation and repair (G. Chen et al., 2017). Encoded by the *APP* gene, this protein consists of a single transmembrane domain, a large extracellular glycosylated N-terminus, and a short cytoplasmic C-terminus fragment (G. Chen et al., 2017) (Figure 1.4). There are eight isoforms of APP (splice variants), with three most common forms are APP695 (695 amino acids), APP751 (751 amino acids) and APP770 (770 amino acids) respectively (Lopez Sanchez, van Wijngaarden, & Trounce, 2019; Y. W. Zhang, Thompson, Zhang, & Xu, 2011). The APP695 isoform is the dominant isoform (Bi, Bi, & Li, 2019), and is almost exclusively expressed in the neurons, hence they are the primary source of APP in the brain (Zheng & Koo, 2011).

By contrast, although APP751 and APP770 isoforms are also expressed within the glial cells of the central nervous system (CNS), they accounts for less than 14% of the total APP produced in the brain (Bi et al., 2019). Conversely, these APP751 and APP770 are extensively expressed in the peripheral organs such as the lungs, liver, spleen, thymus, kidney, heart (Plummer, Van Den Heuvel, Thornton, Corrigan, & Cappai, 2016), as well as in platelets (Lopez Sanchez et al., 2019). The difference between these two isoforms against APP695, is through the presence of the Kunitz-type protease inhibitor (KPI) sequence in their ectodomain (Ben Khalifa et al., 2012; Bi et al., 2019). There has been interest in understanding the relationship between the KPI-containing isoforms of APP and Alzheimer's disease. Some studies have shown increased levels of KPI-

containing APP in the brains of Alzheimer's patients and a correlation with neuritic plaques, but not with other hallmarks of the disease. Thus, the exact role and mechanism of the KPI domain in the pathogenesis of the disease are not fully understood. Regardless of the isoforms, human APPs can be processed via two pathways; the non-amyloidogenic and amyloidogenic pathways (G. Chen et al., 2017), with the former being the dominant pathway under physiological condition (Lopez Sanchez et al., 2019).

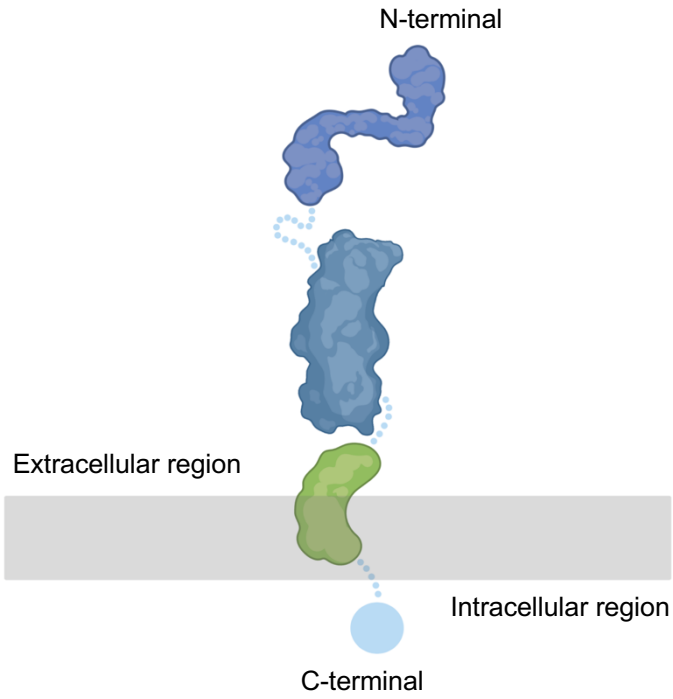


Figure 1.4 Amyloid precursor protein. APP consists of a single membrane spanning domain, one large, glycosylated N-terminus ectodomain and a cytoplasmic C-terminus domain. The transmembrane protein is represented by the grey rectangular shape, whereas the small blue dots represent the flexible portions of the protein that are not included in the structure. The illustration was created using Bio-render website.

1.2.3.2 Non-amyloidogenic pathway (physiological condition dominant pathway)

Under the non-amyloidogenic pathway (Figure 1.5), the full-length APP are sequentially processed by two enzymes; α-secretase [(principally A Disintegrin and Metalloproteinase 10 (ADAM10)] and γ-secretase (Endres & Deller, 2017; Sanabria-Castro et al., 2017). The first excision of APP through α-secretase leads to the detachment of almost the entire ectodomain into the extracellular environment. The products from this excision are a large soluble APPα derivative (sAPPα) and a membrane-bound α-carboxyl-terminal fragment (CTFα) consisting of 83 amino acid sequence. The CTFα (also known as C83) fragment is further cleaved by γ-secretase to produce a truncated Aβ peptide of 3kDa size (p3) and the APP intracellular domain (AICD) (Bi et al., 2019; Sanabria-Castro et al., 2017; Zheng & Koo, 2011). AICD has been reported to assist in transcriptional modulation through its translocation into the nucleus, which regulates the cellular gene expression, such as initiating cell apoptosis (G. Chen et al., 2017; Dohoon Kim & Tsai, 2009). However, not much is known about the function of p3 product (Plummer et al., 2016) though it has been indicated to be pathologically irrelevant (Haass, Kaether, Thinakaran, & Sisodia, 2012).

Here it is important to mention that, while the APPs are preferentially cleaved through the non-amyloidogenic pathway under physiological condition, there are always low level of APPs that are being processed through amyloidogenic pathway at the same time. However, the notable difference of the by-product of amyloidogenic pathway yielded under physiological condition as compared to

that of Alzheimer's disease, is they are predominantly in the form of soluble Aβ1-40 isoform (made up of approximately 90% of total Aβ, with the insoluble Aβ1-42 isoform only accounts for about 5-10% of total Aβ (Kent, Spires-Jones, & Durrant, 2020). While the Aβ protein exists throughout life in the healthy individuals, more studies are required to ascertain its physiological role. Nonetheless, it has been suggested that these Aβ proteins may inhibit the γ-secretase activity in a negative feedback loop manner (Sun, Chen, & Wang, 2015).

1.2.3.2.1 sAPPα

The excision of the APP through α-secretase helps to prevent pathogenic Aβ formation as this enzyme cleaves APP in the middle of coding region for Aβ, therefore providing neuroprotection (Plummer et al., 2016). In addition to that, the protein by-product sAPPα also contributes towards neuroprotection, as shown through in vivo and in vitro studies (Lopez Sanchez et al., 2019) through its ability to modulate neuronal excitability, regulate synaptic plasticity, assist axonal growth and branching, as well as moderating synaptogenesis (Kögel, Deller, & Behl, 2012). Furthermore, increased ADAM10 activity in transgenic AD models, resulting in a subsequent increase in sAPPα levels in the brain, has been shown to attenuate plaque load and reduce learning and memory deficits (Endres & Deller, 2017).

Moreover, the neuroprotective role of APP against head injury exacerbation was further highlighted through an APP knockout mouse model experiment. A greater cortical neuronal loss, accompanied by an aggravated cognitive and motor

impairments was significant in an APP knockout model after mild TBI in comparison to its WT controls (Lopez Sanchez et al., 2019). In a separate study whereby an intracranial injection of sAPPα was made post-TBI, an improvement of cognitive and motor outcomes was observed (Kögel et al., 2012). It has been suggested that the neuroprotection conferred by APP is likely through its protection against oxidative injury. Additionally, APP has also been proposed to safeguard against glucose deprivation, glutamate toxicity (Lopez Sanchez et al., 2019), and iron toxicity (Kent et al., 2020).

Similarly, in vitro studies have also reported potential beneficial roles of sAPPα in stimulating neurite outgrowth in rat hippocampal neurons (Qiu, Ferreira, Miller, Koo, & Selkoe, 1995) and rat neocortical explant culture (Ohsawa, Takamura, & Kohsaka, 1997). It was suggested that the mechanism of APP-dependent neuroprotection are through the (i) stabilization of calcium homeostasis which protects against excitotoxicity and (ii) activation of survival signaling pathways such as the phosphatidylinositol 3-kinase/Akt (PI3K/Akt), the nuclear factor kappa B (NF-κB) and the extracellular-signal-regulated kinase (ERK) pathway (Kögel et al., 2012). Nonetheless, the insights into the exact neuroprotective mechanisms exerted by sAPPα are largely unknown.

1.2.3.3 Amyloidogenic pathway (Alzheimer's disease dominant pathway)

In the amyloidogenic pathway (Figure 1.5), Aβ protein is generated through the sequential proteolysis of β-secretase [mediated by β-site amyloid precursor protein cleaving enzyme 1 (BACE1)] and γ-secretase (Chow, Mattson, Wong, & Gleichmann, 2010; Reitz et al., 2011). The excision of APP by β-secretase releases a shorter soluble APPβ (sAPPβ) into the extracellular area and a longer 99 amino acid sequence of β-carboxyl-terminal fragment (CTFβ). Subsequent cleavage of CTFβ (also known as C99) by γ-secretase generates Aβ peptide and AICD fragment (Lopez Sanchez et al., 2019). The length of Aβ peptide produced are between 39 – 43 amino acids long depending on the site of γ-secretase excision on the CTFβ protein (Chow et al., 2010; O'Brien & Wong, 2011). The insoluble Aβ1-42 isoform is more prevalent in both EOAD and LOAD patients (Kent et al., 2020; Zheng & Koo, 2011). The Aβ1-42 isoform is highly insoluble and assumes a β-pleated configuration rapidly at physiological pH, which are prone to aggregation (Finder & Glockshuber, 2007; Reitz et al., 2011; Sanabria-Castro et al., 2017). Summary of human APP secretases and their products when processed through the non-amyloidogenic and amyloidogenic pathway is presented in Table 1.1.

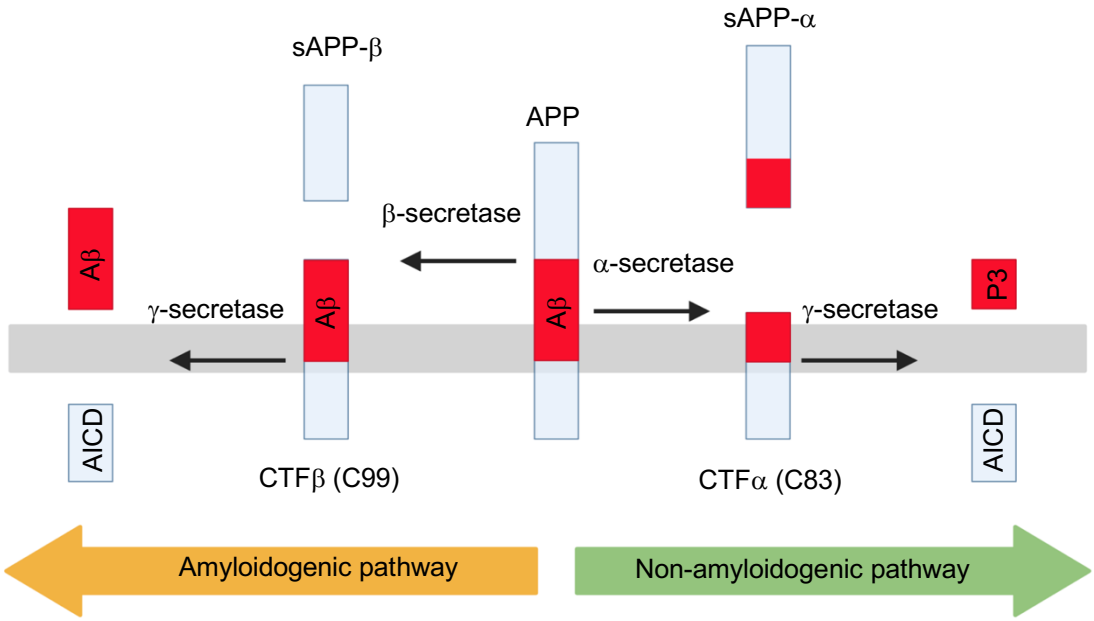


Figure 1.5 APP processing pathways. The APP can be processed through non-amyloidogenic or amyloidogenic pathways. In Alzheimer's disease, the APP undergoes amyloidogenic pathway through β-secretase and γ-secretase excisions, yielding Aβ protein and AICD. The illustration was created using Bio-render website.

Table 1.1 Summary of human APP secretases and their products when processed through the non-amyloidogenic and amyloidogenic pathway.

Pathway	Secretases	Product
Non-amyloidogenic	(i) α-secretase cleavage	• sAPPα • CTFα (C83)
	(ii) γ-secretase cleavage	• P3 • AICD
Amyloidogenic	(i) β-secretase cleavage	• sAPPβ • CTFβ (C99)
	(ii) γ-secretase cleavage	• Aβ • AICD

1.2.3.3.1 Aβ

It was believed that Aβ was generated in the subcellular region, specifically the endosomal compartment and trans-Golgi network, as these areas are enriched with both β- and γ-secretases. The produced Aβ was then transported outwards through exocytosis (Chow et al., 2010). Aβ peptides formed in the extracellular space then aggregate in spontaneous manner, producing soluble oligomers deposits (Sun et al., 2015). The predominant hypothesis claims that the soluble oligomers are the most neurotoxic species that can trigger synaptic dysfunction by inhibiting the N-methyl-D-aspartate (NMDA)-mediated synaptic transmission, causing functional loss through spine and synapse reduction (Chow et al., 2010; Delic, Beck, Pang, & Citron, 2020). This is in keeping with previous findings in human and mouse models that observed synaptic loss and symptoms of cognitive deficits correlate better with the amount of soluble Aβ oligomers as compared to the insoluble plaques deposits (Finder & Glockshuber, 2007).

Aβ exists in various forms, which includes monomers, oligomers, protofibrils and insoluble fibrils in plaques (Söderberg et al., 2022) (Figure 1.6). Among the Aβ species, the soluble oligomers are not only the most toxic intermediate, but also the most prone to aggregation (Fricker et al., 2018) They then appear to deposit themselves into fibrils and senile Aβ plaques, with the latter containing long fibrillar β-sheets, and is the pathological signature of AD (Mulaj, Foley, & Muschol, 2014). The Aβ plaque deposits are predominantly observed in the hippocampus region, neocortex and in the cerebral vasculatures (G. Chen et al., 2017). Findings from functional magnetic resonance imaging (fMRI) on

individuals with prodromal AD have shown excessive neuronal activities in these two regions with Aβ depositions (Selkoe, 2019).

In addition, the accumulation of Aβ senile plaque promotes ROS generation which leads to oxidative injury. This would results in oxidative alteration to the enzymes critical for neuronal functions such as that activities of glutamine synthetase and creatine kinase (Sun et al., 2015). Moreover, sustained aggregation of Aβ appears to elicit a chronic innate immune system response through dysregulated activation of microglial and astrocytic activity (Tahami Monfared, Byrnes, White, & Zhang, 2022) that is suggested to result in the release of complement factors, chemokines, and pro-inflammatory cytokines, and to contribute to neuronal apoptosis (Finder & Glockshuber, 2007; Sun et al., 2015).

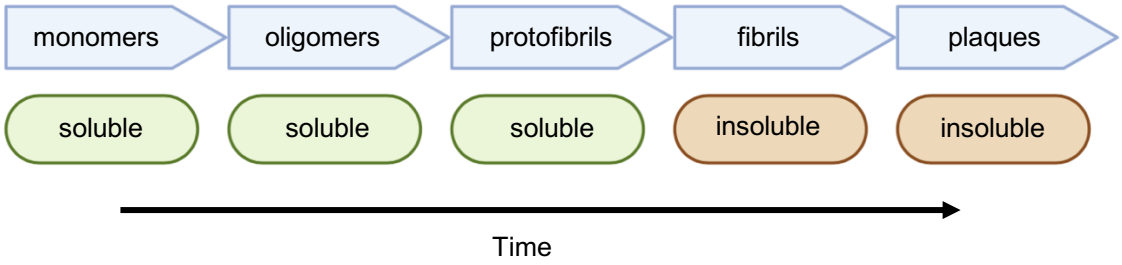


Figure 1.6 Amyloid plaque formation over time. The aggregation of non-pathogenic soluble monomers results in the development of soluble neurotoxic oligomers. Further aggregation of oligomers yields protofibril formation, and the subsequent insoluble fibrils and Aβ plaques. The illustration was created using Bio-render website.

1.2.3.3.2 APP and γ-secretase mutations

Consistent findings from EOAD studies showed an increase in the ratio of Aβ1-42/ Aβ1-40, suggesting that the elevated Aβ1-42 level is central to AD pathogenesis, presumably by providing the materials for Aβ assembly into soluble oligomers deposit, insoluble Aβ fibrils and eventually senile plaques (Y. W. Zhang et al., 2011). Mutation in the genes encoding APP and PSEN are vital in yielding the increased level of pathogenic Aβ1-42 peptides (Sun et al., 2015). There are over 50 known APP mutations, and the widely studied mutations include the Artic (E693G), Indiana (V717F), London (V717I) and Swedish (KM670/671NL) mutations (Huang, 2020). The *APP* gene modifications lead to increased APP expression and processing, and hence subsequent increase in Aβ peptides level in the brain. In addition, mutations to *PSEN1* or *PSEN2* gene of the γ-secretase enzyme alter the APP processing by favouring the generation of the pathogenic Aβ1-42 isoform, and abnormal accumulation of Aβ (Bertogliat, Morris-Blanco, & Vemuganti, 2020; Lopez Sanchez et al., 2019; McNaughton et al., 2012; Tcw & Goate, 2017). Altogether, the increased level of Aβ production led to increased Aβ1-42/ Aβ1-40 ratio resulting in increased amyloid accumulation (Huang, 2020).

The γ-secretase is a heterometric complex consisting of four different proteins, namely (i) presenilin protein 1 and 2 (PSEN1/2), (ii) nicastrin, (iii) presenilin enhancer 2 (PEN-2) and (iv) anterior pharynx defective phenotype 1 (APH1) (Sanabria-Castro et al., 2017).

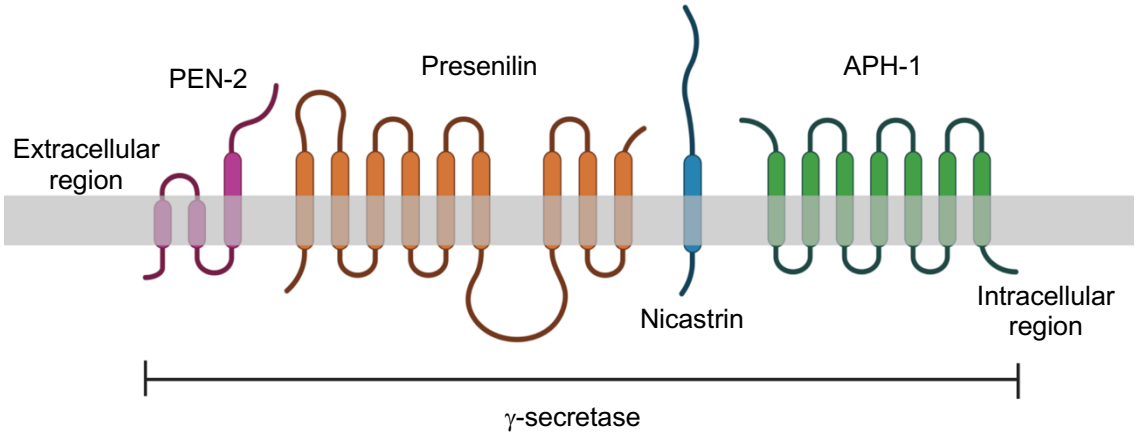


Figure 1.7 The components of gamma-secretase. Gamma-secretase consists of four protein subunits, which are PEN-2, presenilin (PSEN1/ PSEN2), nicastrin, and APH-1. Mutation to gene *PSEN1/2* influences the affinity of gamma-secretase to favour the generation of pathogenic Aβ1-42 protein, hence increasing the Aβ1-42/Aβ1-40 ratio in human, leading to AD development. The illustration was created using Bio-render website.

1.2.3.4 Neurofibrillary tangles aggregation

The products of APP processing, which are intracellular CTFs, and extracellular Aβ1-42 deposits impose stress on the neuronal organelles, resulting on abnormal activation of kinases. Impaired kinase activity is the predecessor to the hyperphosphorylation of intracellular tau (Bi et al., 2019). Tau hyperphosphorylation would promote their propensity to aggregate and forms the paired helical filaments deposit, which would evolve into NFTs (Luan, Rosales, & Lee, 2013) (Figure 1.8).

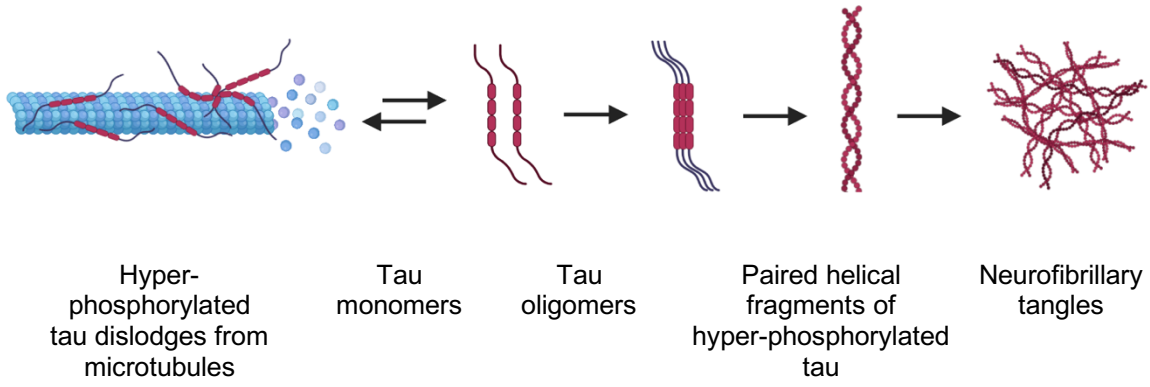


Figure 1.8 Neurofibrillary tau tangles. In Alzheimer's disease, the hyperphosphorylated tau protein dislodges from microtubules, leading to microtubule de-stabilisation and promotes binding of individual tau towards each other. This results in the formation of oligomeric tau aggregate, and the subsequent development of paired helical fragments, and finally the accumulation of neurofibrillary tangles. The illustration was created using Bio-render website.

1.2.3.4.1 Tau

Tau is a microtubule-associated protein (MAP) that can be found on neuronal and non-neuronal cells, which is encoded by the MAPT (microtubule-associated protein tau) gene on human chromosome 17. Healthy neurons are supported by cytoskeleton microtubule bundle (MT) that provides support to the internal axon structure, helps govern cell division, and maintains cell morphology (Figure 1.9). MT is considered to be the 'backbone' of a neuron owing to its track-like structure, capable of guiding nutrients and molecules from the cell body towards extremities (Bishara et al., 2015). The dynamic behavior and spatial organisation of MT are modulated by MAPs such as tau, neuronal MAP2 and non-neuronal MAP4 proteins that possess carboxyl-terminal domain containing the microtubule-binding region (MBR). In neurons, MAP2 is principally contained in the dendrites while tau is enriched in the axonal region (Brandt, Trushina, & Bakota, 2020).

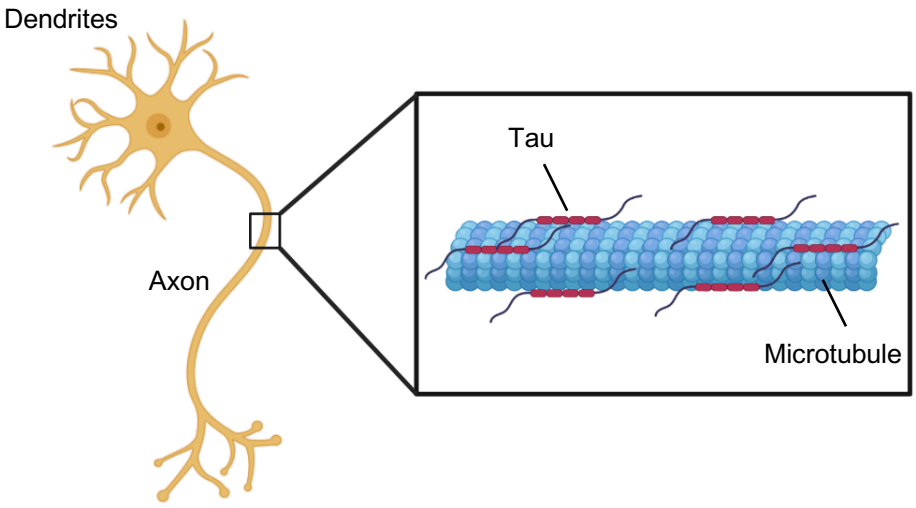


Figure 1.9 Microtubules held by tau proteins in a healthy neuronal axon. Tau is a microtubule-binding protein, that is principally located at the axonal region, where it forms internal support to the axon, maintains cell morphology and helps govern cell division. Microtubules supported by tau protein enables nutrient transfer from the cell body to the neuronal extremities. The illustration was created using Bio-render website.

Tau plays an important role in microtubule self-assembly by binding to tubulin via its MBR domains. A single tau molecule is able to crosslink multiple tubulin heterodimers at once, forming protofilaments that make up the MT (Kadavath et al., 2015; Kent et al., 2020). The importance of tau protein has been highlighted in tau knockout animals, where changes in memory formation and anxiety-related behavior are noted in the absence of tau. These observed deficits could arise for a number of reasons including microtubule-dependent processes, endo- or exocytosis, signaling mechanism and plasma related functions (Brandt et al., 2020).

Tau amino acid sequence can be characterised into four compartments; (i) N-terminal domain, (ii) proline-rich domain, (iii) microtubule binding domain, and (iv) C-terminal domain (VanItallie, 2019). The degree of tau protein phosphorylation is developmentally regulated under normal conditions (Alonso et al., 2018). However, under pathologic AD condition, the tau proteins are abnormally phosphorylated and becomes a toxic entity that aggregates to form NFT. Although the exact mechanism that causes tau hyperphosphorylation is not well established, experimental evidence are pointing towards abnormalities in kinase and phosphatase activity (Leuzy et al., 2019). Decreased phosphatase activity was demonstrated in post-mortem AD brain analysis, and has direct correlation to the elevation of phosphorylated tau (p-Tau) proteins (VanItallie, 2019). Furthermore, several tau regions have been identified to be more susceptible to pathogenic phosphorylation. For instance, mid-domain p-Tau residues commonly associated with AD are threonine 181 (p-Tau181), threonine 231 (p-Tau231), serine 235 (p-Tau235), and serine 199 (p-Tau199), while

phosphorylated C-terminal residues include serine 396 and serine 404 (Lewczuk, Łukaszewicz-Zając, Mroczko, & Kornhuber, 2020).

The presence of intracellular NFT aggregates in AD causes MT disassembly and disrupts axonal transport. In consequence, mobilisation of essential nutrients and molecules to the synapses is jeopardised, followed by a steady deterioration of synapses and neuron disintegration. MT deconstruct will release soluble tau proteins into neuronal cytoplasm (Leuzy et al., 2019; Okamura et al., 2014). This is consistent with findings in AD patients, as brain microtubule perturbation is evident through decreased MT level and multi-fold increase in CSF tau concentration as compared to healthy individuals (Alonso et al., 2018; Kadavath et al., 2015; Lewczuk et al., 2020).

The severity of dementia has been found to correlate with the density of the NFT load in a patient's brain (Bishara et al., 2015). Although extracellular Aß plaque has been suggested to initiate tau hyperphosphorylation, there are evidence showing NFT encourages Aβ formation through a feedback loop mechanism (Briggs et al., 2016). Throughout AD development, the accumulation of aggregated Aβ plaque and NFT continues progressively as these abnormal proteins are highly resistant to enzymatic degradation and removal from the brain (Braak & Del Tredici, 2015).

1.2.4 Clinical stages of AD

Alzheimer's disease is a continuum that stretches over an extended period of time, from pre-clinical AD to MCI and overt dementia (Scheltens et al., 2021) (Figure 1.10). It can be challenging to discern the cognitive symptoms of AD from the normal cognitive decline due to ageing. The normal cognitive disturbance due to ageing may include a reduction in the speed of processing information, as well as declines in capabilities related to memory, language, and decision-making (Scheltens et al., 2021).

Henceforth, a clinical disease staging has been established to assist physicians in diagnosing AD. In 1984, the diagnosis using the 'National Institute of Neurological and Communicative Disorders' and 'Stroke and the Alzheimer's Disease and Related Disorders Association' (NINCDS-ADRDA) criteria was first established and generally used. However, in recent years, this criterion has been replaced by 'National Institute on Aging' and the 'Alzheimer's Association' (NIA-AA) guidelines.

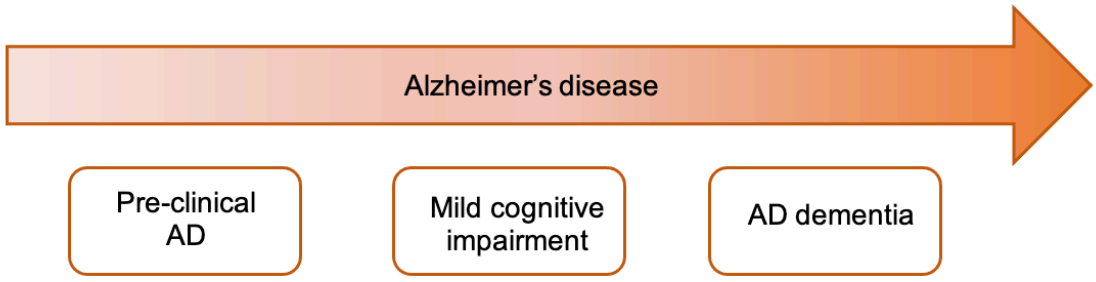


Figure 1.10 Alzheimer's disease is a progressive disease continuum that spans a period of years. Clinical stages range from cognitively normal (pre-clinical AD) to mild cognitive impairment and AD dementia. The illustration was created using Microsoft PowerPoint.

1.2.4.1 NINDCS-ADRDA criteria

The clinical diagnosis of AD was first established in 1984 by the NINCDS-ADRDA. According to these guidelines, the classification of AD was defined into three stages: (i) possible AD, (ii) probable AD, and (iii) definite AD (McKhann et al., 2012). While the diagnosis of possible and probable AD is for living individuals, the definite AD diagnosis will only be specified after histopathological signatures of AD are observed during post-mortem investigation (C. Yang & Xiao, 2015).

The diagnosis of AD using NINDCS-ADRDA criteria depends almost entirely on the combination of neurological examination and the use of neuropsychological tests (Ghidoni et al., 2013). Therefore, the diagnosis of AD is commonly made when patients are already in the late stage where clinical symptoms are apparent (Márquez & Yassa, 2019). This 1984 criteria was used widely for over 27 years and in the field of clinical research and trials (Ghidoni et al., 2013).

1.2.4.2 NIA-AA criteria

In recent years, advancements in the neuroimaging field have made it possible to monitor AD molecular alterations through modern medical imaging, such as positron emission tomography and biofluid analysis (C. Yang & Xiao, 2015). Therefore, in 2011, the NINCDS-ADRDA criteria were revised by the NIA-AA workgroup, incorporating the consideration of sensitive biomarkers of amyloid plaque deposition, tau accumulation and neuronal degeneration in the decision-making process for AD diagnosis (McKhann et al., 2012; C. Yang & Xiao, 2015).

According to the revised criteria (2011) for the diagnosis of AD, the stages of AD are classified into three categories: (i) pre-clinical AD, (ii) mild cognitive impairment (MCI), and (iii) AD dementia (Ghidoni et al., 2013).

1. Pre-clinical AD

The pre-clinical AD stage is the earliest phase in the AD continuum, encompasses a long asymptomatic period that can take up to 20-30 years. In this stage, abnormal brain pathology has started, as indicated by biomarker detection (Ferrer, 2022), but its burden has yet to pass the threshold to show observable symptoms, such as memory loss (Bernardini & Zima, 2019; Braak & Del Tredici, 2015). Henceforth, the patient's daily life is not affected by cognitive or functional decline (Porsteinsson, Isaacson, Knox, Sabbagh, & Rubino, 2021). As this pre-clinical stage diagnosis is done through biomarker detection, its importance lies in research purposes to identify at-risk individuals who might benefit from future disease-modifying therapies (Dubois et al., 2016; Pais et al., 2020; C. Yang & Xiao, 2015).

2. Mild cognitive impairment

The second AD category is the MCI stage, also known as the prodromal stage. It is the transitional stage between the asymptomatic pre-clinical phase and AD dementia, where symptoms of cognitive impairment begin to surface. However, in this stage, the cognitive anomalies experienced by the patients are not severe enough to interfere with daily activities (Chételat et al., 2020; Dubois et al., 2007). Studies have reported that around 10-20% MCI patients progress to AD dementia annually (Lewczuk et al., 2020).

3. AD dementia

The primary feature distinguishing AD dementia from MCI is the ability of patients to care for themselves independently (Scheltens et al., 2021). Patients in the AD dementia stage show apparent memory disturbance and severe incompetency to perform work and usual activities, which therefore requires caregiver assistance. The AD dementia stage can be further classified into mild, moderate, and severe AD dementia (Scharre, 2019). In mild-to-moderate AD dementia, patients have trouble recognising familiar faces and difficulties remembering typical information such as their name and finding their way home (McKhann et al., 2012; Scharre, 2019).

As the disease progresses to severe AD dementia, patients experience loss of motor functions, which causes walking difficulties, an inability to regulate bowel movement, and respiratory system failure, eventually followed by death (Della Sala et al., 2004). Generally, this phase can last from 5 to 12 years (Bernardini & Zima, 2019), although it is worth noting that the rate of disease progression may differ from one individual to another (Sluimer et al., 2008). According to the 2011 NIA-AA criteria, both MCI and AD dementia stage can be diagnosed solely on clinical symptoms, even in the absence of biomarker results (C. Yang & Xiao, 2015).

1.2.5 Neuropathological staging of AD

The 'ABC' scoring system for AD neuropathological changes has been outlined in the NIA-AA 2012 guideline, which acknowledges that the deposition of Aβ and NFT pathologies can develop prior to the clinical manifestation of cognitive deficit. The letter 'A' refers to the assessment of Aβ accumulation based on Thal phases, whereas 'B' denotes the deposition of NFTs based on Braak stages, and the letter 'C' scores the neuritic plaques based on Consortium to Establish a Registry for Alzheimer's Disease (CERAD) criteria (Ferrer, 2022).

This 2012 NIA-AA criteria is a revision of a former guideline established by the National Institute on Aging/Reagan Institute of the Alzheimer Association Consensus Recommendations for the Post-mortem Diagnosis of AD (NIA-Reagan criteria) in 1977 (Hyman et al., 2012).

1. **Stage A (Aβ accumulation based on Thal phases)**

The Thal staging, comprised of five phases (Table 1.2), is referred to when examining the anatomical localisation of Aβ deposits (Ferrer, 2022; Therriault et al., 2022). The neuropathological changes observed in phases 1 and 2 are mostly associated with asymptomatic individuals, whereas phases 4 and 5 are correlated to the presence of dementia (Trejo-Lopez, Yachnis, & Prokop, 2022) (Figure 1.11). The recommended method for Aβ detection is through highly sensitive silver staining or antibodies against Aβ immunohistochemistry staining (Deture & Dickson, 2019).

Table 1.2 Thal phases of Aβ accumulation. According to the Thal stages, the Aβ primarily localises in the neocortex and spreads into other brain regions until it reaches the cerebellum.

Aβ plaque score	Thal stage	Topography of Aβ deposition
A0	No Aβ plaques	
A1	Phase 1	Aβ accumulates exclusively in the neocortex
	Phase 2	Aβ spreads to isocortex (entorhinal and hippocampal cortices)
A2	Phase 3	Aβ is present in the striatum, diencephalon, and the cholinergic nuclei of the basal forebrain
A3	Phase 4	Aβ deposits in the brainstem nuclei
	Phase 5	Aβ is examined in the cerebellum

2. Stage B (NFT deposition based on Braak stages)

The original six-stage Braak and Braak system used to reference NFT deposition in the 1977 NIA-Reagan criteria was condensed into four-stage scoring system (B0, B1, B2, B3) as revised in the current NIA-AA guideline (Hyman et al., 2012; Trejo-Lopez et al., 2022) (Table 1.3). As the Braak stage escalates, the spread of the pathology and the number of neurons containing NFTs also increase with disease progression (Ferrer, 2022; Jouanne, Rault, & Voisin-Chiret, 2017; Therriault et al., 2022) (Figure 1.11). As such, the Braak stages show a parallel relationship with the cognitive symptoms, whereby Stage 1 and 2 are commonly related to clinically asymptomatic individuals, and stage 5 and 6 demonstrate strong correlation with demented patients (Trejo-Lopez et al., 2022). The suggested method for NFT detection is by using antibodies against tau or phospho-tau immunohistochemistry staining (Hyman et al., 2012).

Table 1.3 Braak staging of NFT deposition based on the anatomical distribution of tau NFT. Early Braak stages describe pathologies in the transenthorinal cortex, which later extends into primary sensory cortices. NFT scoring based on NIA-AA guidelines use the four-tiered staging formulated from condensed Braak stages.

NFT stage	Braak stage	Topography of NFT deposition
B0	No NFT	
B1	Stage 1	NFT deposition begins in the transentorhinal cortex
	Stage 2	NFT progresses to the entorhinal cortex and hippocampus
B2	Stage 3	NFT localised in the inferior temporal cortex
	Stage 4	NFT is found in most areas of the neocortex and the association cortices
B3	Stage 5	
	Stage 6	NFT spreads into primary sensory cortices

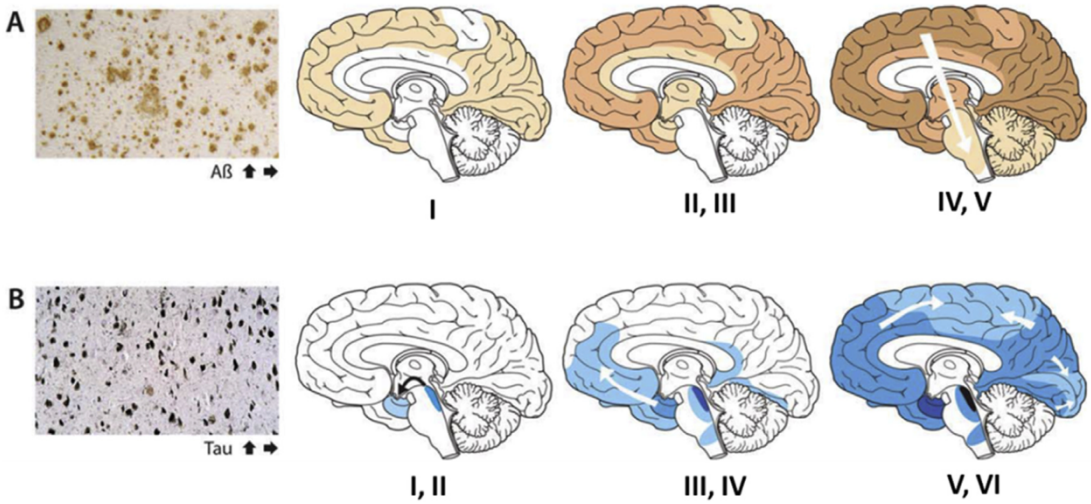


Figure 1.11 Spatio-temporal evolution of amyloid and NFT pathologies according to Thal and Braak stages. A: Amyloid deposits progression (Thal stages). B: NFT progression (Braak stages). Thal stages describe amyloid deposition in neocortex area (stage 1), before spreading to the entorhinal area, hippocampus and the cholinergic nuclei of the basal forebrain (stage 2 and 3). Finally, amyloid spreads to the brainstem nuclei and the cerebellum (stage 4 and 5). At the bottom part of the figure, Braak stages describe NFT accumulation to be first visualised in the transentorhinal cortex, entorhinal region and hippocampus (stage 1 and 2), extending to the inferior temporal, frontal, and parietal cortex (stage 3 and 4) and finally to the neocortical and primary sensory cortices (stage 5 and 6). Illustration retrieved from Jouanne et al (2017).

3. Stage C (neuritic plaques scoring based on CERAD)

The density of neuritic plaques is scored using the three stages outlined by CERAD (Table 1.4). The current NIA guideline emphasizes that the neuritic plaque that should be scored is the one that exhibits dystrophic neurites, as stained by thioflavin or silver staining techniques, whereas diffuse plaque should not be included (Doher et al., 2023; Hyman et al., 2012; Trejo-Lopez et al., 2022) (Figure 1.12).

Table 1.4 The CERAD scoring for neuritic plaque deposition. There are four stages of CERAD scores, ranging from no plaque, to frequent distribution of the neuritic plaque.

CERAD score	Neuritic plaque deposition
C0	No neuritic plaque
C1	Sparse neuritic plaque pathology
C2	Moderate density of neuritic plaque
C3	Frequent neuritic plaques

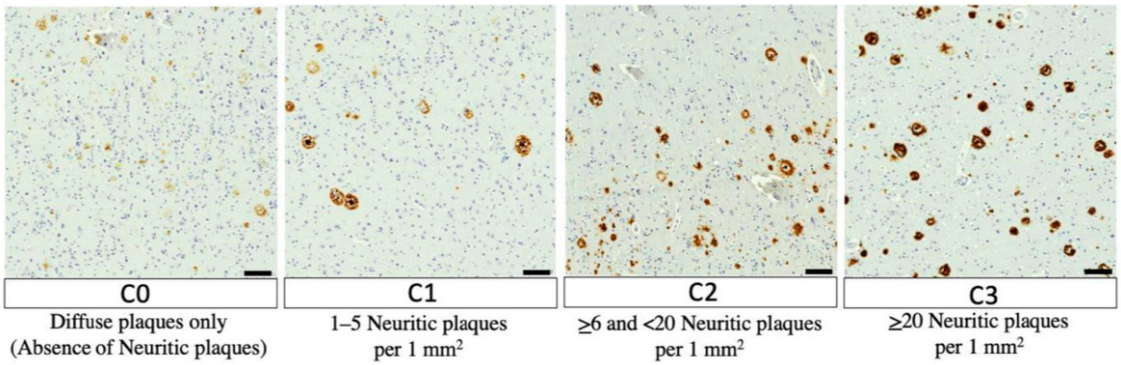


Figure 1.12 Neuritic plaque density and its CERAD scoring. Human brain section stained using mouse anti-human β-amyloid (6F3D) antibody, to investigate the senile plaque density. CERAD score was determined based on the neuritic plaque density in the neocortex region. Scale bars = 100 μm. Illustration retrieved from Doher 2023.

4. Reporting AD neuropathological changes result

Regardless of the individual's clinical history, a summary of the ABC staging score of the neuropathological changes will be reported from the range of "A0, B0, C0" to "A3, B3, C3". Examples of the scoring format are as follows (Hyman et al., 2012):

“Alzheimer’s Disease Neuropathologic Changes: A1, B0, C0”, or

“Alzheimer’s Disease Neuropathologic Changes: A2, B2, C1”.

The combination of these score would then be converted into levels of AD neuropathologic score, of either “not”, “low”, “intermediate”, or “high” (Hyman et al., 2012; Therriault et al., 2022) (Table 1.5).

Table 1.5 The combination of ABC scores is translated into "Not", "Low", "Intermediate" or "High" AD neuropathologic change level. The Aβ plaque scoring is determined by Thal phases, whereas neuritic plaque score and NFT score are assessed through CERAD and Braak stages respectively.

A: Aβ plaque score (Thal phases)	**C: Neuritic plaque score (CERAD)**	**B: NFT score (Braak stage)**		
		B0 or B1	**B2**	**B3**
A0	C0	Not	Not	Not
A1	C0 or C1 (none to sparse)	Low	Low	Low
	C2 or C3 (moderate to frequent)	Low	Intermediate	Intermediate
A2	Any C	Low	Intermediate	Intermediate
A3	C0 or C1 (none to sparse)	Low	Intermediate	Intermediate
	C2 or C3 (moderate to frequent)	Low	Intermediate	High

1.2.6 AD pharmacotherapies

There are limited pharmacotherapies available for AD, which has made it challenging for both patients and researchers alike. There are currently six FDA-approved drugs for AD management, with three being acetylcholinesterase inhibitors (AChEI), one NMDA blocker, and the other two anti-amyloid monoclonal antibodies (Behl et al., 2022; Grover & Jain, 2022).

Both AChEI and NMDA blocker are not disease-modifying therapies, as they only provide temporary symptomatic relief for patients. As such, pharmacotherapies under this classification do not alter the progression of the disease, the rate of cognitive decline or AD pathological burden. These drugs work by increasing and decreasing the level of two brain neurotransmitters, acetylcholine (ACh) and glutamate, respectively, which have become imbalanced in the AD condition (Husna Ibrahim et al., 2020). Conversely, the anti-amyloid monoclonal antibodies have shown an ability to slow the disease progression (Scheltens et al., 2021).

1. Acetylcholinesterase inhibitors

AChEIs are commonly used as the primary pharmacological intervention given to patients in the early and moderate stages of AD. Examples of AChEI include Donepezil, Galantamine and Rivastigmine (Husna Ibrahim et al., 2020; Soria Lopez et al., 2019). The development of AChEI drugs was driven by the observation that AD brain is deficient in cholinergic neurons, which play a crucial role in the formation of memory and learning (H. Ferreira-Vieira, M. Guimaraes, R. Silva, & M. Ribeiro, 2016). Decreased cholinergic function is therefore linked

to cognitive deficits seen in AD patients and is recognised as a late feature of the neurodegenerative cascade (Briggs et al., 2016; Grossberg, Tong, Burke, & Tariot, 2019).

Under physiologic condition, the synthesis of neurotransmitter ACh within the pre-synaptic neuron cytosol is mediated by choline acetyltransferase (ChAT). Once the neurotransmitter ACh is released into the synaptic cleft, acetylcholinesterase (AChE) helps to regulate its amount through periodic metabolism, which transforms ACh into its inactive form (H. Ferreira-Vieira et al., 2016) (Figure 1.13A). In AD pathological conditions, extensive cholinergic alterations were noted, where ChAT activity was reduced to 35-50% from that in healthy circumstances. As ChAT plays a crucial role in synthesizing ACh, alterations in the levels of this enzyme lead to reduced ACh levels in the synaptic cleft. The rate of metabolizing enzyme AChE in the synaptic cleft remains the same, despite the lower levels of ACh being produced. The reduced concentration of ACh, therefore, results in reduced cholinergic neurotransmission (Figure 1.13B). Indeed, it has been demonstrated that dementia severity is directly correlated to the decreased level of ACh synthesis (Francis, 2005).

AChEI pharmacotherapies work by blocking the action of AChE, preventing the degradation of the neurotransmitter ACh (Figure 1.13C). This results in an increased level of ACh in the synaptic cleft, potentiating cholinergic signaling and alleviating cognitive symptoms experienced by AD patients (Loi, Eratne, Kelso, Velakoulis, & Looi, 2018). All three AChEIs used in the current clinical setting display improved global, cognitive, and functional outcomes in AD

patients (Grossberg et al., 2019), but they are not disease-modifying over time. The side effects of AChEIs are generally mild and tolerable, with common gastrointestinal disturbances such as vomiting, nausea, and diarrhea (Joe & Ringman, 2019).

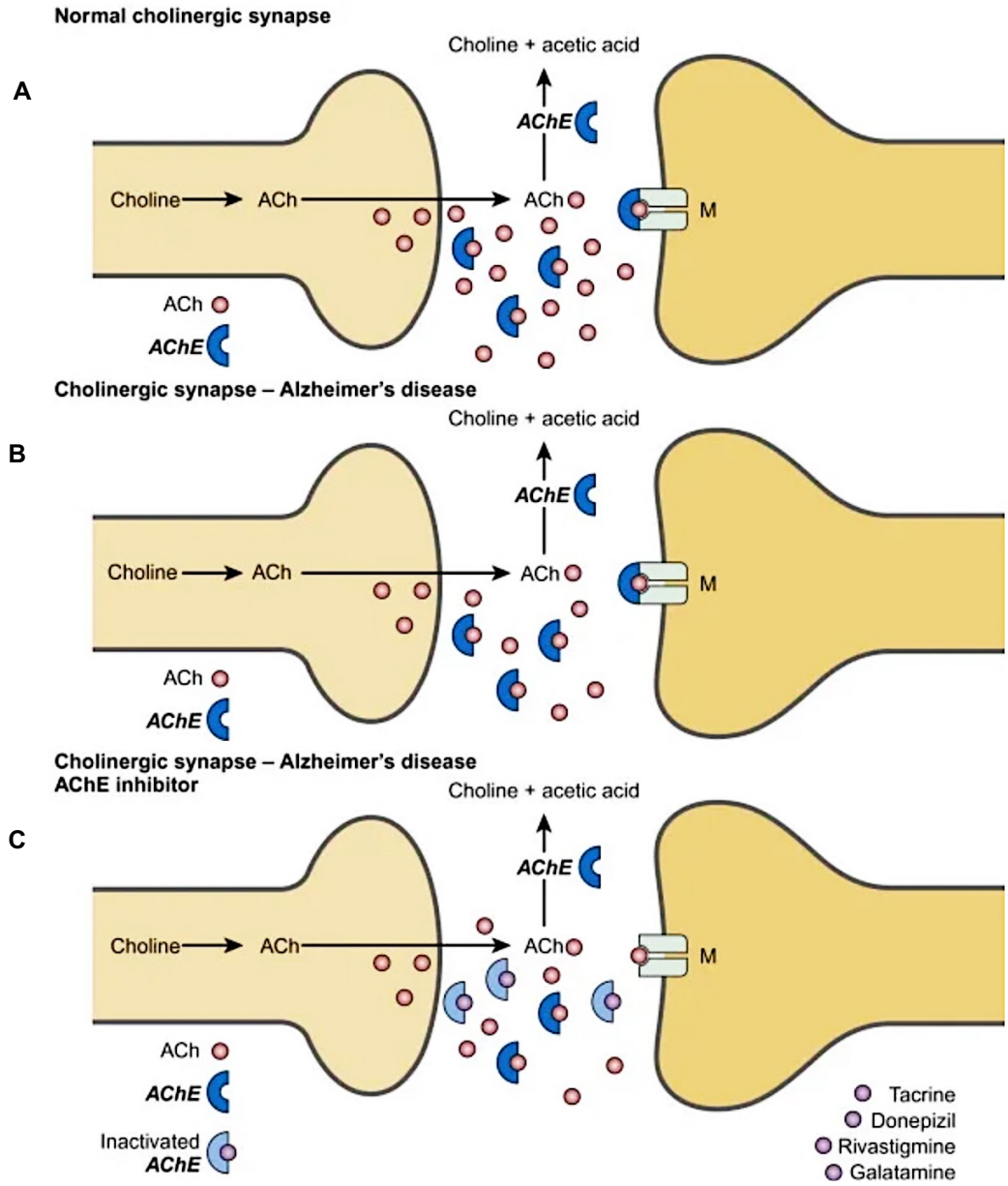


Figure 1.13 Acetylcholinesterase inhibitor mechanism of action. (A) Under physiologic condition, the synthesis of neurotransmitter acetylcholine (ACh) within the pre-synaptic neuron cytosol is mediated by choline acetyltransferase (ChAT). Large number of ACh molecules were present in the normal cholinergic synapse with muscarinic receptor (M). In the synaptic cleft, acetylcholinesterase (AChE) breaks down acetylcholine into choline and acetic acid. (B) In AD, ChAT activity was reduced to 35-50% from that in healthy circumstances leading to reduced ACh levels in the synaptic cleft. The rate of metabolizing enzyme AChE in the synaptic cleft remains the same, which resulted in reduced concentration of ACh available. (C) Acetylcholinesterase inhibitors (AChEI) pharmacotherapies work by blocking the action of AChE, preventing the degradation of the neurotransmitter ACh. This results in an increased level of ACh in the synaptic cleft, potentiating cholinergic signaling and alleviating cognitive symptoms experienced by AD patients. Image retrieved from https://neupsykey.com/cholinesterase-inhibitors/.

2. NMDA blocker

The NMDA blocker Memantine was approved by FDA in 2003 for the treatment of moderate-to-severe AD cases, showing modest effects on global impression, cognition, and activities of daily living (Joe & Ringman, 2019; Mendiola-Precoma, Berumen, Padilla, & Garcia-Alcocer, 2016). Memantine is rarely prescribed to mild AD patients, as AD trial results showed inconsistent benefits for this group (Grossberg et al., 2019). Additionally, a combination drug of AChEI and NMDA blocker, through the brand name Namzaric, is used for patients in the moderate-to-severe AD stage, as AChEI monotherapy was shown to be not as effective when prescribed to patients in that respective stage (Soria Lopez et al., 2019).

Memantine blocks glutamate access into the cell by binding uncompetitively to two sites of NMDA receptor (Briggs et al., 2016) (Figure 1.14). The NMDA receptor is an ion channel found on excitatory neurons, whose role is to regulate the passage of ions such as calcium into the cells. This ion channel is activated through glutamate binding to the receptor ligand site (Vyklicky et al., 2014). In AD, the Aβ oligomers are argued to induce the release of glutamate by astrocytes and downregulate the excitatory amino acid transporters 1 and 2, which function to reuptake the glutamate into astrocytes. This then lead to an excess of glutamate in the peri-synaptic space (Fani et al., 2021).

The overexposure of glutamate to the system results in overstimulation of the NMDA receptor, leading to glutamate-mediated excitotoxity (Briggs et al., 2016). This is because excessive glutamate influx into the neurons promotes mitochondrial dysfunction and nitric oxide generation, which, in turn, elicits

neuronal apoptosis and subsequent cognitive impairment (Mendiola-Precoma et al., 2016). Therefore, by blocking glutamate access into the cell, Memantine is argued to reduce neuronal loss and help to restore function in damaged neurons (Briggs et al., 2016). The adverse effects of this drug are generally well-tolerated, with reports of dizziness, confusion, and headache (Joe & Ringman, 2019).

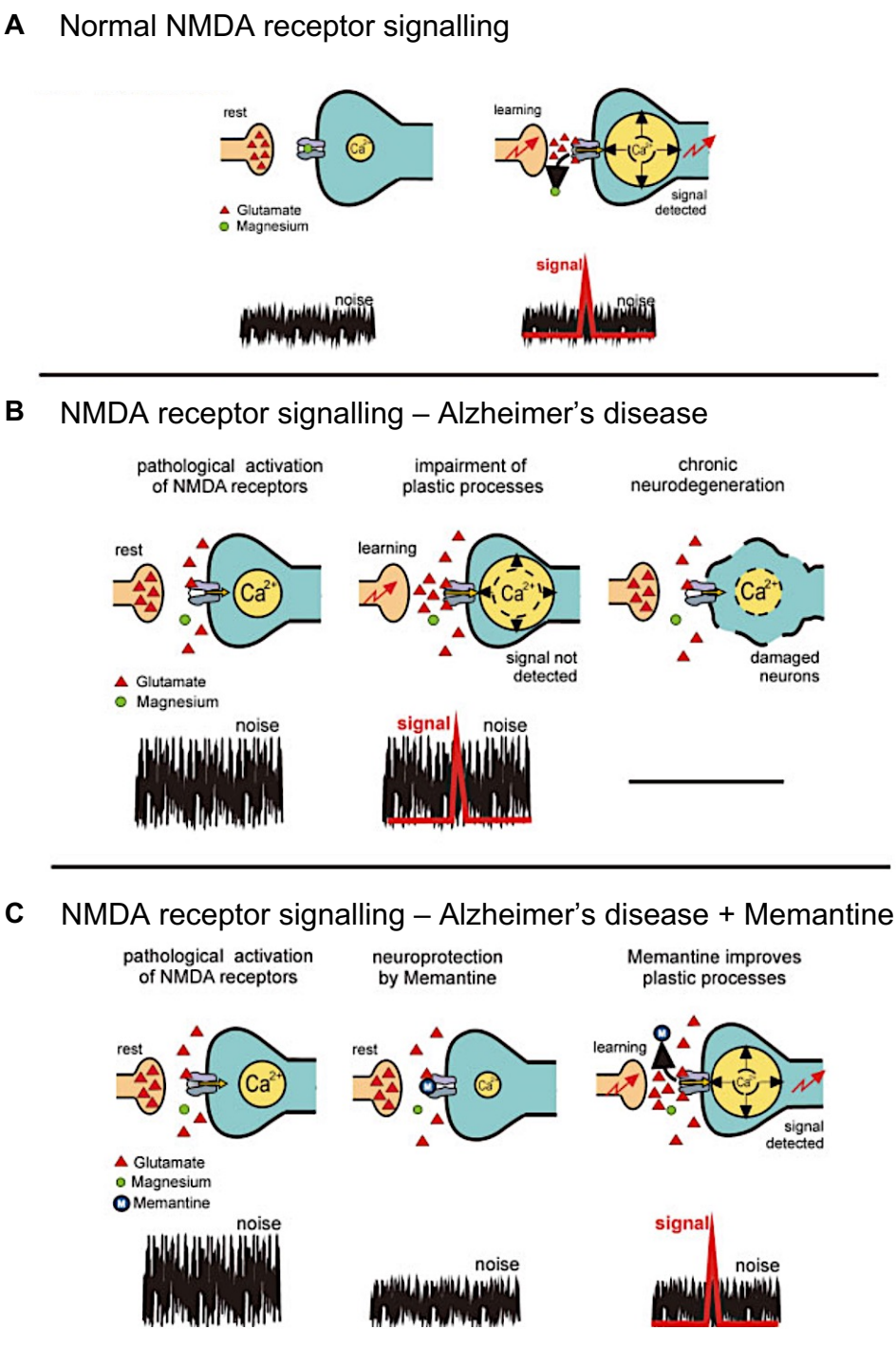


Figure 1.14 NMDA blocker mechanism of action. (A) Normal NMDA receptor signalling. Under physiologic condition, magnesium ion (Mg2+) acts as a filter to regulate the influx of calcium ion (Ca2+) into the cells. Learning occurs when NMDA receptor is activated, where Mg2+ ion is removed from the NMDA channel pore and replaced by glutamate binding to the receptor ligand site. This will result in a sufficiently strong signal over baseline activity (signal-to-noise ratio) is detected through Ca2+ ion fluctuations, and synaptic transmission can occur. (B) NMDA receptor signalling in AD. In AD condition, pathologic activation of NMDA receptor occurs due to the overactivation of glutamatergic system, and Mg2+ is

not effective enough to play its filtering role, causing excessive influx of Ca2+ ions. This in turn leads to impaired synaptic plasticity, elicits neuronal death and subsequent cognitive impairment. (C) NMDA receptor signalling in AD + Memantine. In AD condition, Memantine aids in blocking glutamate binding to the cell receptor. Memantine is argued to reduce neuronal loss and help to restore function in damaged neurons. Illustration retrieved from Danysz and Parsons (2003).

Table 1.6 Summary of AChEI and NMDA blocker pharmacotherapies available for the treatment of AD. These drugs helped to alleviate AD symptoms, but do not modify the course of disease. It is important to note that they demonstrated a modest effect on cognition, with a variable response rate. AChEI; acetylcholinesterase inhibitors; NMDA, N-methyl-D- aspartate.

Drug name (commercial name)	Drug classification	Drug effect	AD stage for drug prescription
Donepezil (Aricept)	AChEI	Blocks ACh neurotransmitter	Early and moderate AD
Rivastigmine (Exelon)	AChEI	Blocks ACh neurotransmitter	Early and moderate AD
Galantamine (Razadyne)	AChEI	Blocks ACh neurotransmitter	Early and moderate AD
Memantine (Namenda)	NMDA blocker	Blocks glutamate neurotransmitter and improves learning and memory	Moderate to severe AD
Donepezil and Memantine (Namzaric)	AChEI and NMDA blocker combination	Blocks ACh and glutamate neurotransmitter, improves learning and memory	Moderate to severe AD

3. Anti-Aβ directed monoclonal antibody

The human immunoglobulin gamma-1 monoclonal antibody (mAb) Aducanumab (Aduhelm) is the first disease-modifying agent to be approved by the FDA through the less common accelerated approval in June 2021, and is the first drug to be approved for AD since 2003 (Behl et al., 2022). Aducanumab is the first pharmacotherapy that explicitly targets the pathophysiology of the disease, the pathologic amyloid proteins (Rahman et al., 2023) (Figure 1.15). This drug is indicated for patients in the MCI stage or AD mild dementia stage (Grover & Jain, 2022). Initially, the development of this drug was stopped in 2019 after the results from two phase 3 trials were not promising. However, after researchers conducted further analysis of the data, significant plaque clearance was noted, signaling potential efficacy of Aducanumab. Hence, the development of this drug was continued until its recent approval in 2021 (Söderberg et al., 2022).

Several other mAbs have been developed and tested in clinical trials, such as Solanezumab, Bapineuzumab, and Ganterumab (Cummings, Tong, & Ballard, 2019). However, among these mAbs, Aducanumab was shown to be the most effective. In the clinical setting, Aducanumab is administered intravenously and has been shown to penetrate the blood-brain-barrier (BBB) to reach and target amyloid (Grover & Jain, 2022). Interestingly, this drug possesses higher affinity binding towards toxic oligomers and insoluble fibrillar aggregates in comparison to the non-pathogenic Aβ monomers (Grover & Jain, 2022). It was reported that this drug exhibits more than 10,000-fold selectivity for both soluble oligomers and Aβ fibrils when compared to monomers (Behl et al., 2022; Decourt et al., 2021). This selective binding results in a decrease of amyloid accumulation (Behl et al.,

2022; Grover & Jain, 2022; Scheltens et al., 2021). The mechanism of action of this drug was shown to be delivered through microglial-mediated removal, whereby the drug binds to fibrils and marks them for phagocytosis (Haddad et al., 2022).

Despite reduction in amyloid accumulation, clinical outcomes were conflicting, as EMERGE clinical trial suggested significant slowing of cognitive decline in high-dose Aducanumab administration, whereas ENGAGE trial reported no difference between high dose Aducanumab vs placebo (Synnott, Whittington, Lin, Rind, & Pearson, 2021). However, in a post-hoc analysis of ENGAGE trial, it was found that a subgroup of patients receiving high dose Aducanumab declined more slowly when compared to placebo, which supports the findings of EMERGE trial (Joseph, 2021). Aducanumab reaches maximal clinical benefit after approximately 5 months of administration due to its long half-life, reaching therapeutic levels after it crosses the BBB and continually destroys the amyloid aggregates (Haddad et al., 2022).

In late January 2024, Biogen, which was the manufacturing company for Aducanumab announced the discontinuation of this drug. The company mentioned that the decision was not due to concerns over safety or efficacy concerns but rather due to reprioritization of company resources to Lecanemab (Leqmbi) and other potential new treatment modalities such as antisense oligonucleotide therapy targeting tau (BIIB080) and oral small molecule inhibitor of tau aggregation (BIIB113) in the pipeline (Biogen, 2024).

A newly developed mAb, Lecanemab, delivered promising results in the phase 3 clinical trial, whereby it was deemed effective in lessening amyloid markers and delaying cognitive decline in the early AD cohort. This observation led to the accelerated approval granted by FDA in January 2023 for Lecanemab (Rahman et al., 2023). Lecanemab is a human monoclonal antibody that selectively targets Aβ soluble protofibrils with >1,000-fold and 10-15-fold affinity compared to the monomers and insoluble fibrils respectively. Data from phase 2 clinical trial demonstrated a robust and dose-dependent reduction of Aβ proteins in the AD patient brain. As a result, patients administered with Lecanemab exhibited a slower clinical deficit decline (McDade et al., 2022).

In the clinical setting, Lecanemab is FDA-approved to be prescribed only for patients in this early AD cohort only, as there are no efficacy details and safety data regarding the later stages of AD submitted (Rahman et al., 2023). Moreover, it is worth noting that there are multiple limitations in the phase 3 clinical study of Lecanemab, such as COVID19 pandemic, limited study population, and high dropout rate which warrants further investigation; an extension study is still ongoing for this drug (Rahman et al., 2023). Overall, however, the effects of all these interventions are modest at best, and new, more effective interventions are urgently required.

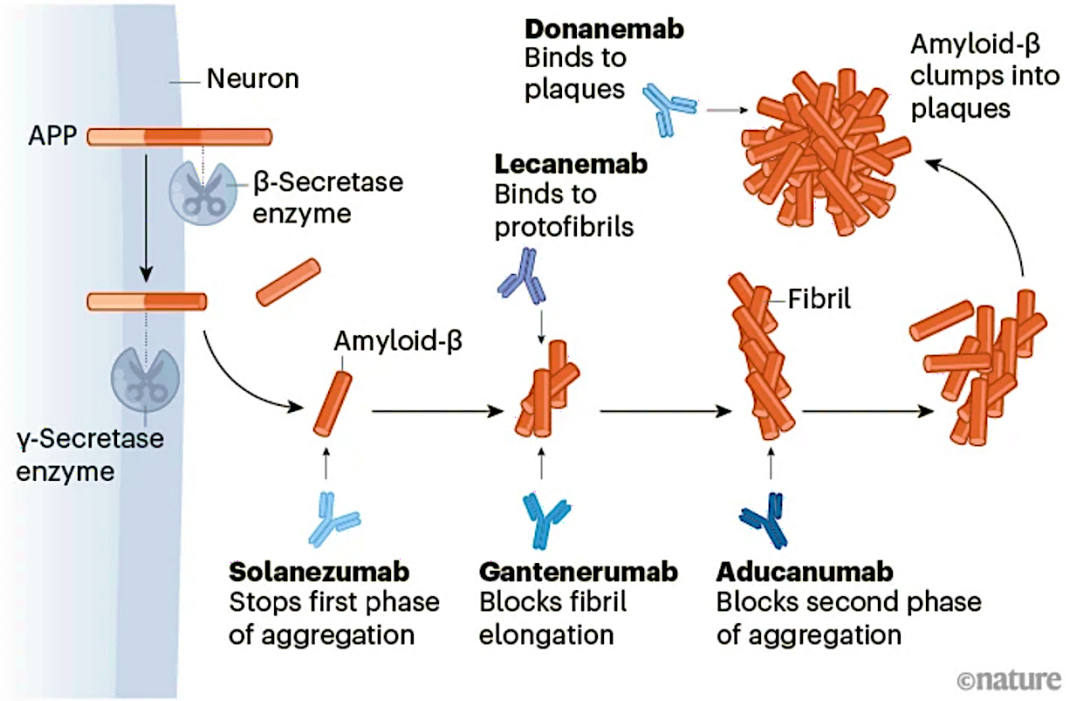


Figure 1.15 Monoclonal antibodies against amyloid. Aducanumab, Solanezumab, Ganterumab and Lecanemab all binds to amyloid, but the target species is different. Credit: Nik Spencer/Nature. Image retrieved from https://www.nature.com/articles/d41586-022-00651-0

1.2.7 Animal models of AD

In this thesis, two transgenic mouse models are adopted, which are the J20 and P301S mutants. Transgenic modeling in mouse is more widely available as compared to rats and is relatively inexpensive. Moreover, although the prevalence of LOAD is more dominant as compared to EOAD, the amyloid and NFT pathological expression of the disease is non-distinguishable. Henceforth, mutation of three common genes identified for EOAD including *APP* are employed to develop the transgenic models of AD (Elder, Sosa, & Gasper, 2010).

1.2.7.1 Transgenic J20 mutant (PDGF-APPSw,Ind)

The J20 mouse model overexpresses human APP (hAPP) with Indiana (717V-F) and Swedish (670/671KM-NL) double mutations in its brain. The transgene expression of this model is driven by the human platelet-derived growth factor β chain (*PDGF-β*) promoter in neurons and has been extensively used in preclinical studies to recapitulate amyloid deposition pathogenesis of AD (Tosh et al., 2018). Aside from amyloid deposition, this J20 mutant developed by Mucke and colleague in 2000 also displays other AD-like phenotypes such as synaptic loss, cognitive impairment and susceptibility to seizure (Mucke, Masliah, Yu, Mallory, & Rockenstein, 2000; Wright et al., 2013). Figure 1.16 shows hippocampal sections immunoperoxidase-stained for Aβ with 3D6 antibody, for APP-WT line I63 and APP-Swe,Ind line J20 respectively.

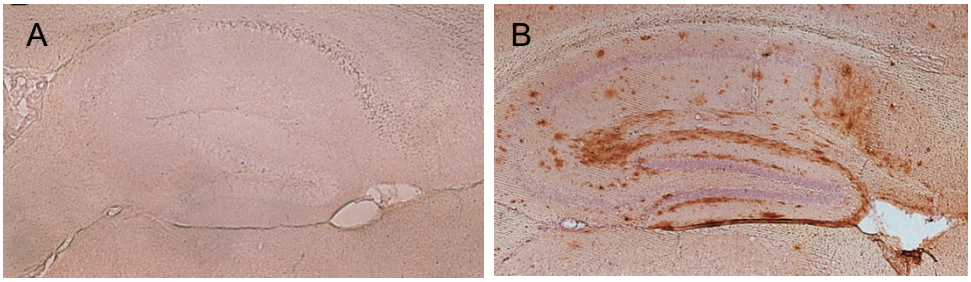


Figure 1.16 Hippocampal sections immunoperoxidase-stained for Aβ with 3D6 antibody. (A) APP-wild type line I63 (15 months), (B) APP-Sw,Ind line J20 (10 months). Sections viewed under light microscope of 4x magnifications. Pictures from Mucke et al (2000).

Time dependent changes of amyloid in hAPP-J20 mutant (Swe, Ind) was investigated by Shibly group (Shibly et al., 2023). Immunostaining of J20 brain section against Aβ was positive intracellularly in cortical and hippocampal neurons at 2 months old. At 3 months old and 6 months old, aside from intracellular deposition, vascular deposition of Aβ was also noted. However, obvious amyloid plaque deposition was only visualised at 9 months of age, both in the cortex and hippocampal region.

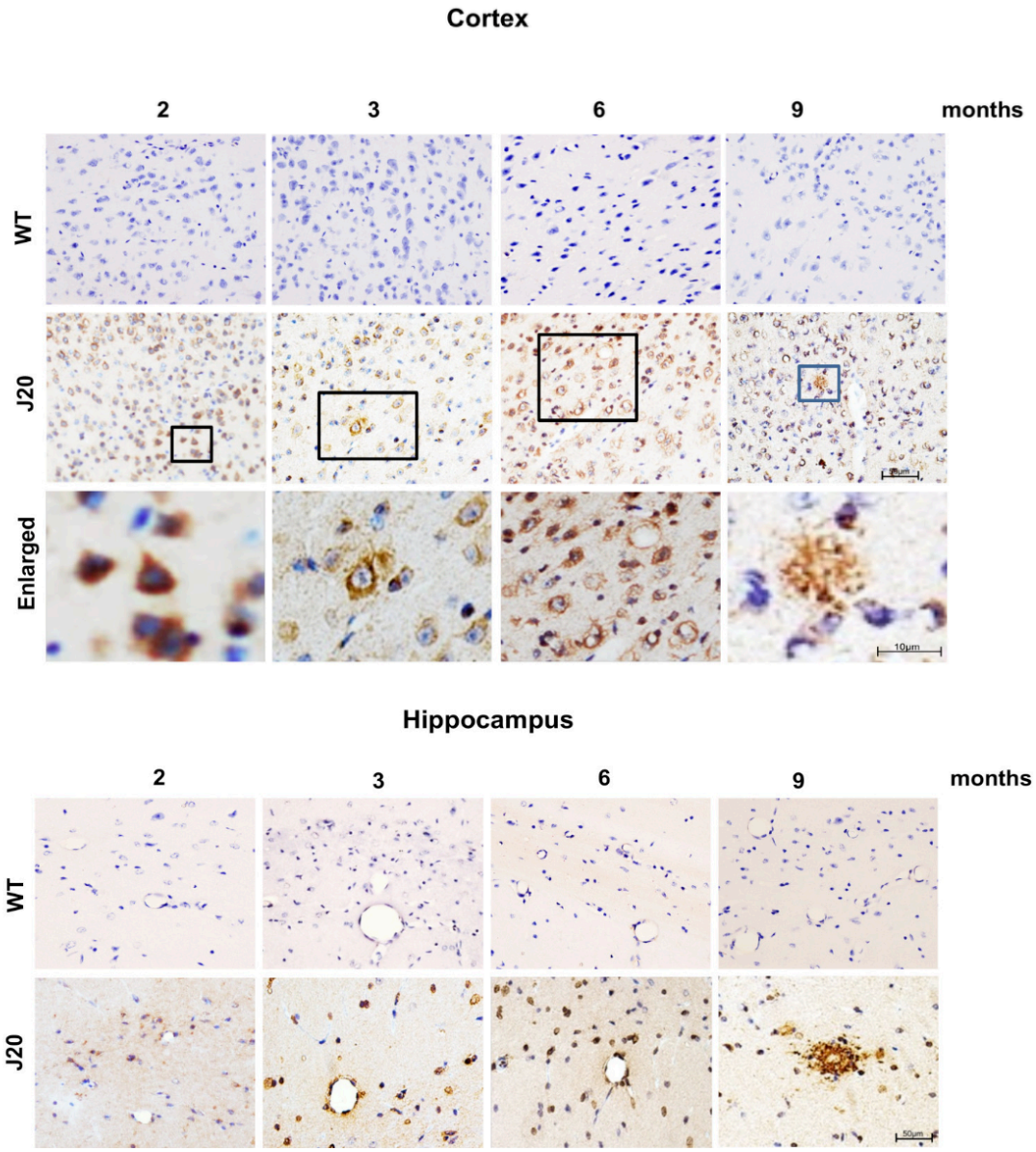


Figure 1.17 Aβ immunoreactivity in cortex and hippocampus region of J20 mice. Brain section of J20 and WT of 2, 3, 6 and 9 months of age were immunostained for Aβ. Intracellular Aβ within neurons of cortex and hippocampus area of J20 mice were observed at 2 months old, whereas vascular deposition of Aβ was noted together with intracellular Aβ in 3 and 6 months old J20 mice. Obvious amyloid plaque deposition was only noted in J20 mice at 9 months old. No Aβ deposits was visualised in WT mice at any age. Scale bar = 50 μm, magnified box scale bar = 10 μm. Figures retrieved from Shibly et al (2023).

1.2.7.2 Transgenic P301S mutant (hTau.P301S)

The development of transgenic mouse expressing human tau protein was made possible by the identification of *tau* gene mutations in frontotemporal dementia and parkinsonism linked to chromosome 17. The transgenic construct of this line was driven by the murine thy1 promoter, which produces the 383 amino acid isoforms of human tau commonly associated with tauopathies, with P301S mutation. In the cerebral cortex of this mutant, neuronal loss was seen apparent at 3 months old (Hampton et al., 2010) (Figure 1.18).

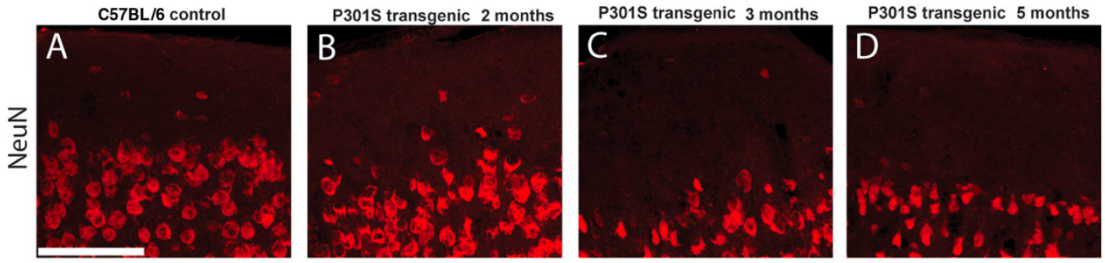


Figure 1.18 Progressive neuronal loss of transgenic P301S was observed in the cerebral cortex starting at 3 months old. Brain sections subjected to neuronal nuclei (NeuN) immunostaining. (A) WT C57BL/6 control, (B) P301S transgenic 2 months old, (C) P301S transgenic 3 months old, (D) P301S transgenic 5 months old. Scale bar = 100 μm. Images retrieved from Hampton et al (2010).

Furthermore, the mutation of P301S in exon 10 of *tau* leads to early onset of phenotypic and functional changes in this mutant, which was demonstrated by declined capability of microtubule assembly of mutated tau proteins, significant increase in tau filament assembly and apparent motor symptoms characterized by general muscle weakness, tremor and a severe paraparesis at 5-6 months of age (Allen et al., 2002). Due to the symptoms experienced by these transgenic

P301S mice at 5-6 months old, the requirement by the United Kingdom Home Office animal license regulations require humane killing when they reached that age (Hampton et al., 2010). Figure 1.19 shows brain section from transgenic P301S mutant stained for tau proteins using AT8 antibody. It should be noted that there are several P301S mutant lines available, and the one used for experiments conducted in this thesis and elaborated in this section is P310S line developed by Michel Goedert group. Phenotypic characterisation and the timeline of brain pathology development for this transgenic mutant is as illustrated in Figure 1.20 (Alzforum, 2024).

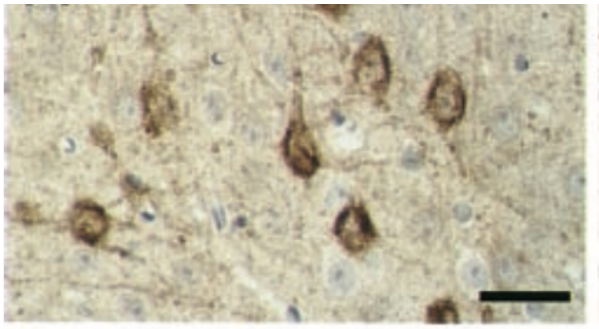


Figure 1.19 Tau proteins stained using AT8 antibody. Tau proteins immunoreactivity as seen in cortex. Transgenic mice of 5 months old was used. Scale bar 40 um. Figure retrieved from Allen et al, 2002.

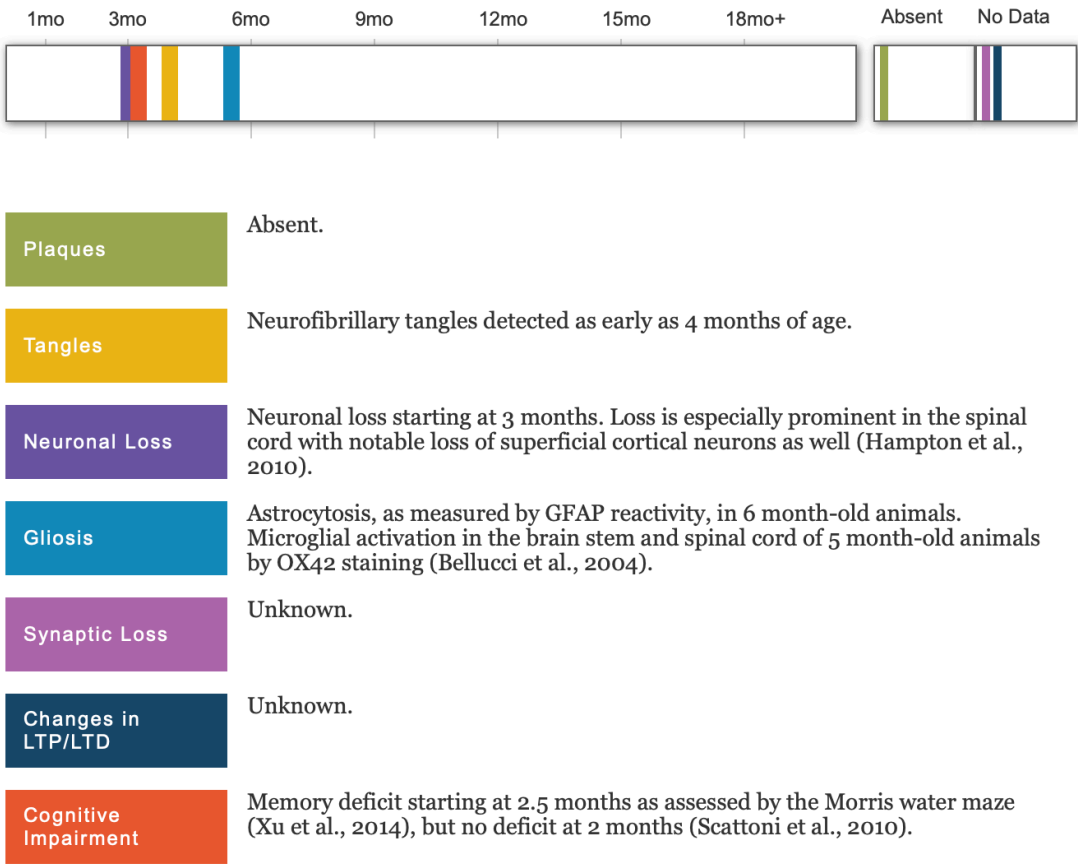


Figure 1.20 Brain pathology and phenotypic characterisation of transgenic P301S mice (developed by Michel Goedert). Neuronal loss is evident starting at 3 months old, whereas neurofibrillary tangles can be visualised as early as 4 months old. Timeline retrieved from https://www.alzforum.org/research-models/htaup301s (last updated: 11 June 2024).

1.3 Two-hit hypothesis

The premise that underlies Chapter 3 and Chapter 4 is associated with the two-hit hypothesis, whereby I sought to investigate whether the combination of AD pathologies in mutant animals (first hit) and traumatic brain injury (second hit) leads to an accelerated disease progress that is not observed if these hits are not concurrently present.

1.3.1 History

The two-hit hypothesis was first coined by geneticist and physician Alfred Knudson (August 9, 1922 – July 10, 2016) in 1971 through his observation of genetic mechanisms underlying retinoblastoma, which commonly affects young children. Under physiologic condition, the growth and division of retinoblasts are halted during embryogenesis. Subsequently, these cells later differentiate into photoreceptor and nerve cells. However, in pathologic condition, the retinoblasts failed to differentiate and hence continue to divide and results in tumour formation.

Between 1944 and 1969, Knudson studied 48 retinoblastoma patients and found that 40% of these patients inherited the disease through germ-line mutation. However, he also noticed that there was a portion of disease-free patients born to affected parents, which he found perplexing. These disease-free patients later give birth to children with retinoblastoma. This observation pointed out that the germ-cell mutation could be inherited without the accompanying phenotypic expression. Therefore, he came to an understanding that recessive mutation in

a single gene would not result in retinoblastoma, and thus for retinoblastoma to occur, mutation must happen in both copies of the gene. The first mutation inherited through germinal cells are considered as the “first hit”, whereas the second mutation occurred in the somatic cell denote the “second hit”. This phenomenon is known as the two-hit hypothesis (Knudson, 1971).

1.4 Traumatic brain injury

Traumatic brain injury (TBI) is a major cause of global morbidity and mortality. In England and Wales alone, TBI-related cases account for approximately 1.4 million hospital visit per year (Lawrence et al., 2016). Despite extensive studies for neuroprotective therapies and positive results in pre-clinical interventions, there are no successful clinical outcomes reported to date (Aertker, Bedi, & Cox, 2016; Khellaf, Khan, & Helmy, 2019). TBI can be divided into (i) open injuries where the brain parenchyma is punctured by external objects and (ii) closed injuries where focal tissue damage happens due to rapid brain movement inside the skull (Capizzi, Woo, & Verduzco-Gutierrez, 2020). Closed brain injuries are typically caused by blunt blow to the head, mainly acquired from falls, motor-vehicle accidents and sports activities (Ng & Lee, 2019).

TBI can be classified into mild, moderate, and severe cases depending on the location and severity of injury. The classification of TBI severity is based on (i) Glasgow Coma Scale score, (ii) duration of post-traumatic amnesia, and (iii) duration of unconsciousness (Julien et al., 2017) (Table 1.7, Table 1.8). Mild TBI is the most prevalent form of TBI, constituting 80-90% of all cases. Following mild TBI, brain function is acutely disrupted, with the presence or absence of brief loss of consciousness and confusion (Mira, Lira, & Cerpa, 2021). However, the majority of mild TBI patients recover without intervention, though an estimated proportion of 30-53% from overall mild cases reported debilitating conditions that persist at least up to one-year post-injury, which is referred as post-concussive syndromes (Dixon, 2017; Stocchetti & Zanier, 2016). The most common post

concussive symptom experienced by patient is headaches, followed by other complications such as sleep problem, cognitive dysfunction, and irritability. Furthermore, it has been estimated that more than 40% patients from moderate to severe injuries are inflicted with long-term neuropsychiatric disorders such as major depression, anxiety, post-traumatic stress disorders, psychosis, and aggression (Capizzi et al., 2020).

In addition, the neurochemical, metabolomics and cellular alterations following TBI that occur as a consequence of chronic microglial activation, persistent neuroinflammation, astrocytic gliosis, protein misfolding, loss of neurons and white matter degradation have been associated with an increased risk in the development of Alzheimer's disease in later life (Akamatsu & Hanafy, 2020; Kumar & Loane, 2012; Mira et al., 2021; Needham et al., 2019; Stocchetti & Zanier, 2016).

Table 1.7 Classification system for traumatic brain injury. The severity of traumatic brain injury is grouped according to the duration of unconsciousness, Glasgow coma scale score and the duration of post-traumatic amnesia.

Classification	Duration of unconsciousness	Glasgow coma scale	Post-traumatic amnesia
Mild	<30 minutes	13-15	<24 hours
Moderate	30 minutes – 24 hours	9-12	1-7 days
Severe	>24 hours	3-8	>7days

Table 1.8 Glasgow coma scale and score. The Glasgow coma scale score is determined by the total overall score rated from the eye, verbal, and motor response category.

Category	Response	Score
Eye opening	Open eyes spontaneously	4
	Open eyes in response to speech/ verbal command	3
	Open eyes in response to painful stimuli	2
	No eyes response	1
Verbal response	Oriented	5
	Able to answer questions but appeared confused	4
	Discernable words but inappropriate response	3
	Incomprehensible speech or sounds	2
	No verbal response	1
Best motor response	Able to move following commands	6
	Localised movement due to painful stimuli (purposed movement)	5
	Withdraws from pain in response to painful stimuli (non-purposed movement)	4
	Flexes upper extremities or extends lower extremities in response to painful stimuli (decorticate posture)	3
	Extends all extremities in response to painful stimuli (decerebrate posture)	2
	No motor response	1

1.4.1 Pathophysiology of traumatic brain injury

The pathophysiology of TBI is orchestrated by both primary and secondary mechanisms. Primary damage refers to the physical insult caused by the external force, which leads to tissue tearing, blood vessel damage, neuronal trauma, axonal shearing, and diffuse axonal injury (Prins, Greco, Alexander, & Giza, 2013). As a consequence of axonal shearing, the axonal transport becomes blocked which disrupts organelle trafficking and hence initiates intracellular injury (Mira et al., 2021). The secondary damage refers to the delayed cellular and molecular events that evolves following primary insult. The hallmarks of this delayed secondary CNS damage include further axonal degeneration and demyelination, mitochondrial and synaptic damage, neuroinflammation and protein accumulation, excitotoxicity, oxidative stress, as well as cellular damage and neuronal apoptosis (Mira et al., 2021; Ng & Lee, 2019) (Figure 1.21).

1.4.2 Neuroinflammation

Neuroinflammation plays a key role in the pathophysiology of traumatic brain injury (TBI) and has been shown to be both beneficial and detrimental. Its impact depends on whether the inflammation is well-controlled or abnormally sustained (Kumar & Loane, 2012). After TBI, neuroinflammation can be characterized by the activation of resident microglia and astrocytes, followed by the secretion of local pro-inflammatory cytokines and the infiltration of systemic leukocytes into the brain (Simon et al., 2017; Xiong, Mahmood, & Chopp, 2018). Indeed, elevated immunoreactivity towards the microglial marker ionized calcium-binding

adaptor molecule 1 (Iba-1) and the astrocytic marker glial fibrillary acidic protein (GFAP) has been reported post-TBI (Mira et al., 2021).

Soon after the primary injury impacts the brain, the damaged tissue releases danger-associated molecular patterns (DAMPs), which trigger ensuing inflammation. Examples of DAMPs include the S100 protein, heat-shock proteins, ATP, and high mobility group box-1 (HMGB1). A poor prognosis of TBI has been associated with high levels of S100β and HMGB1 in humans. The circulating DAMPs bind to pattern recognition receptors (PRRs) expressed on innate immune cells such as macrophages, monocytes, dendritic cells, and mast cells, as well as on non-immune cells like fibroblasts and epithelial cells (Azeem Alam, Hana, Jin, Suen, & Ma, 2018; Needham et al., 2019). The interaction between DAMPs and PRRs leads to the production of pro-inflammatory cytokines, either through direct intracellular signal transduction or through the formation of inflammasomes, resulting in leukocyte recruitment to the injury site (Aftab Alam et al., 2020; Needham et al., 2019).

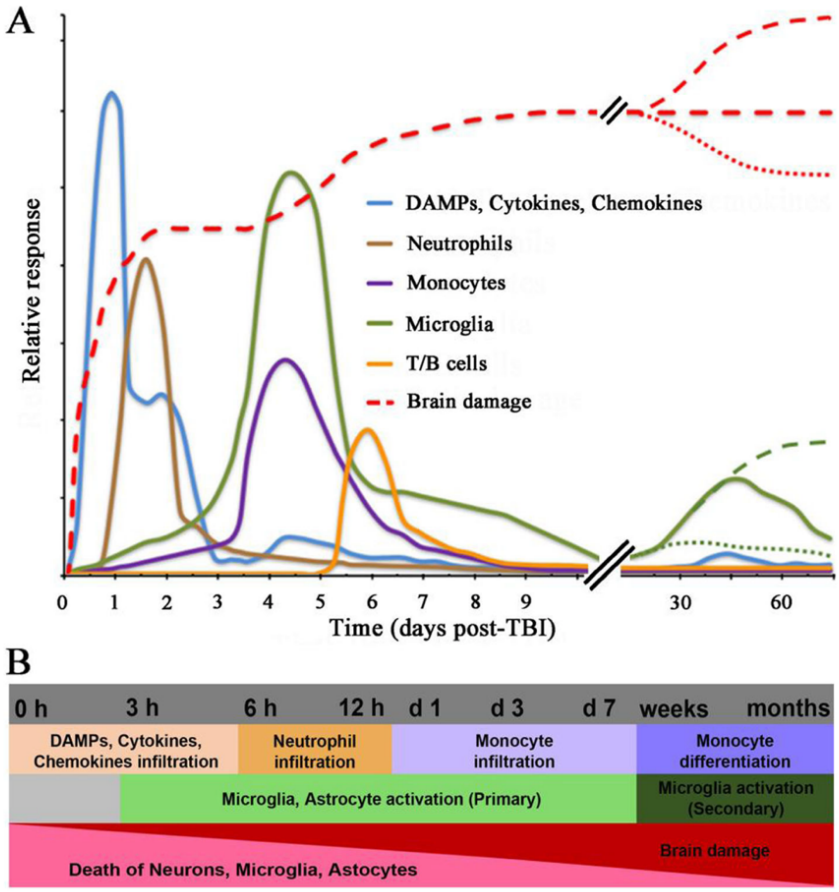


Figure 1.21 Pathophysiological cascades (secondary injury) following TBI. (A) Following primary injury, damaged cells release danger-associated molecular patterns (DAMPs), which trigger ensuing inflammation. Resident microglia and astrocytes were activated, followed by the secretion of local pro-inflammatory cytokines and the infiltration of systemic leukocytes to the injury site in the brain. The hallmarks of this secondary injury include further axonal degeneration and demyelination, mitochondrial and synaptic damage, neuroinflammation and protein accumulation, excitotoxicity, oxidative stress, as well as cellular damage and neuronal apoptosis. (B) Approximate timeline that highlights the behaviour of the cells following primary brain insult. Illustration retrieved from Aftab Alam et al (2020).

1.4.2.1 Microglia and astrocytes

1. Microglia

Microglia are the resident immune cells of the brain and are of myeloid origin, which make up 5-10% of total CNS cells (Jha, Jo, Kim, & Suk, 2019). These cells are characterized morphologically by a ramified appearance, with long, motile processes during resting state and are present throughout the CNS including the spinal cord. Moreover, they are found to be more densely populated in the white matter as compared to the grey matter (Liddelow, Marsh, & Stevens, 2020; Soulet & Rivest, 2008). Microglia originates from erythro-myeloid progenitors residing in the yolk-sac before embryonic day 8. Under physiologic condition, microglia are not replenished by peripheral blood-derived monocytes. Instead, they proliferate continuously to maintain a stable population in the brain throughout life (Schetters, Gomez-Nicola, Garcia-Vallejo, & Van Kooyk, 2018).

In health, the microglia constantly survey the cerebral microenvironment to eliminate pathogens and to restore homeostasis following neuronal death or tissue damage. These cells are equipped with phagocytic and antigen-presenting capabilities that allow them to phagocytose the dead cells, cellular debris, invading pathogens, and protein aggregates. Furthermore, the microglia also play a role in neuronal survival during development by producing neurotrophic factors, as well as helping in synaptic organization (Bachiller et al., 2018; Fricker et al., 2018).

Microglia are the first cell population to respond when TBI occurs, which then followed by astrogliosis (alternatively referred as reactive astrocytes) and persistent inflammation (Jha et al., 2019; Mira et al., 2021). In response to DAMPs binding following CNS injury, microglia become activated and undergo morphological changes from resting, ramified with long motile processes into the activated (also known as “primed” state), ameboid-shaped with enlarged cell body and retracted processes, which is a microglia phenotype that is almost identical to the peripherally-derived macrophages (Karve, Taylor, & Crack, 2016; Needham et al., 2019) (Figure 1.22). In addition, these activated microglia would express increased levels of major histocompatibility complex (MHC) antigens and become phagocytic (Y. S. Kim & Joh, 2006).

Microglia can produce a range of pro-inflammatory and anti-inflammatory molecules. Examples of pro-inflammatory molecules released by activated microglia are reactive oxygen species, nitrogen reactive species, and cytokines such as tumor necrosis factor-α (TNF-α), interleukin 1β (IL-1β) or interleukin 12 (IL-12). These pro-inflammatory mediators trigger inflammation and induce neurotoxicity (Bachiller et al., 2018; Guo, Wang, & Yin, 2022). In opposition, microglia were also discovered to play a role in neuroprotection by secreting anti-inflammatory mediators that induce tissue repair and stimulate growth. Examples of anti-inflammatory molecules produced by microglia include trophic factors like tumor growth factor-β (TGF-β) and brain derived neurotrophic factor (BDNF) (Bachiller et al., 2018; Needham et al., 2019).

Nonetheless, it is important to note that whilst the classification of cytokines or mediators into pro- or anti-inflammatory group would be a useful information in understanding its role in broad sense, the rigid categorisation of these cytokines might cause the complex nature of such molecules to be overlooked and missed (Needham et al., 2019). For instance, while IL-10 is generally considered as an anti-inflammatory cytokine based on its capability to suppress the activity of T-helper type 1 cells and natural killer cells which effectively interrupt the subsequent generation of pro-inflammatory cytokine IL-12 and lymphocyte activation. However, IL-10 is also considered to possess pro-inflammatory properties as it promotes the generation of cytotoxic T cells, and exerts immune stimulating effects such as promoting activation of B-cells, maturation and the synthesis of antibodies that can lead to detrimental B-cell mediated inflammation (Needham et al., 2019; Trinchieri, 2007).

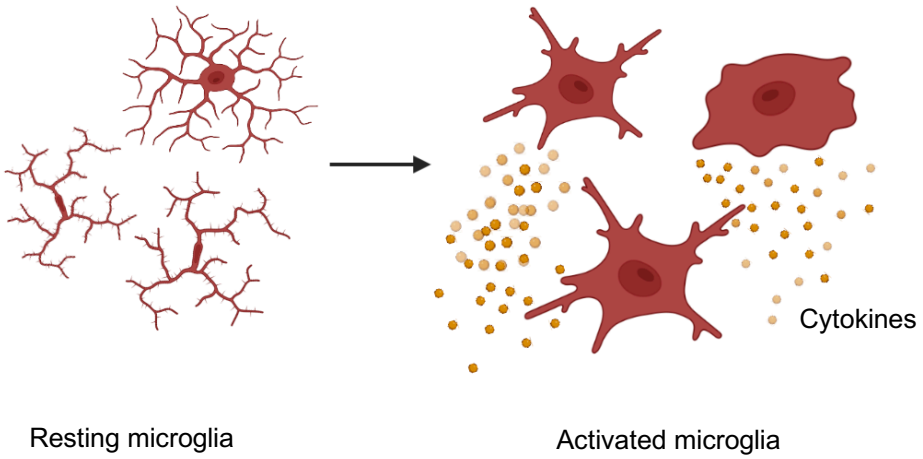


Figure 1.22 Resting and activated microglia. Following CNS injury, microglia become activated and undergo morphological changes from resting, ramified with long motile processes into the activated, ameboid-shaped with enlarged cell body and retracted processes. The M1 microglia phenotype release pro-inflammatory mediators such as cytokines which trigger the subsequent inflammation and induce neurotoxicity. The illustration was created using Bio-render website.

2. Astrocytes

Astrocytes are star-shaped cells with numerous thin processes that wrap blood vessels in the brain, contributing to the structure of the blood-brain barrier, and supply energy metabolites to neurons. However, it is becoming clear that their role in the CNS is more diverse than once thought (Kim, Park, & Choi, 2019). The term astrocyte was first used in 1893 by Michael von Lenhossek, which is attributed to the stellate morphology of these cells. Kolliker and Andriezen later classify these cells into fibrous and protoplasmic astrocytes (Oberheim, Goldman, & Nedergaard, 2012).

The fibrous astrocytes are found within the white matter, where they ensheathe blood capillary and contact axons. Conversely, the protoplasmic astrocytes are situated in the gray matter, where they make contact with both blood capillaries and the synapses (Kim et al., 2019) (Figure 1.23). These star-shaped cells play a crucial role in regulating brain homeostasis, such as controlling the extracellular pH, control the uptake and process of neurotransmitters, as well as delivering the nutrients from blood capillaries to neurons (Kubotera et al., 2019; Sahlender, Savtchouk, & Volterra, 2014).

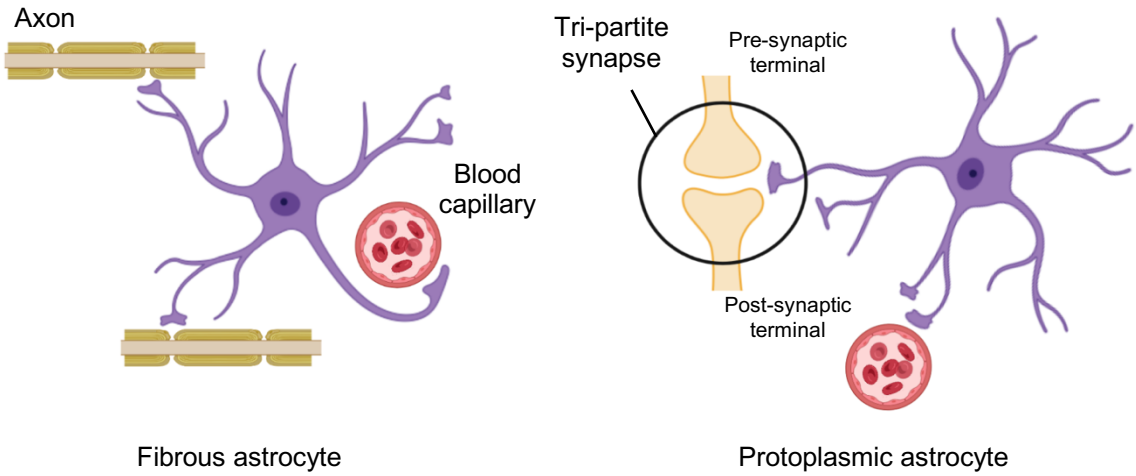


Figure 1.23 Two types of CNS astrocytes. The astrocytes are classified into two groups, which are (i) fibrous astrocytes of the white matter, and (ii) protoplasmic astrocytes of the grey matter. The fibrous astrocytes contact the blood capillaries and axons, whereas the protoplasmic astrocytes contact the blood capillaries and synapses. The illustration was created using Bio-render website.

In addition, together with the pericytes and endothelial cells, astrocytes construct the formation of BBB which functions as a highly selective membrane that protects the CNS from potentially harmful molecules and cells including the components of the immune system from the bloodstream, from translocating into the brain parenchyma (Harada, Kamiya, & Tsuboi, 2016) (Figure 1.24). The proximity between astrocytic end feet with the pre- and post-synaptic terminals of the neurons forms a tri-partite synapse structure. This strategic position of astrocytes allows them to modulate the synaptic function through gliotransmitter release such as glutamate, gamma-aminobutyric acid (GABA), ATP, D-serine, prostaglandins and neuropeptides (Harada et al., 2016; Kim et al., 2019; Mira et al., 2021; Sahlender et al., 2014).

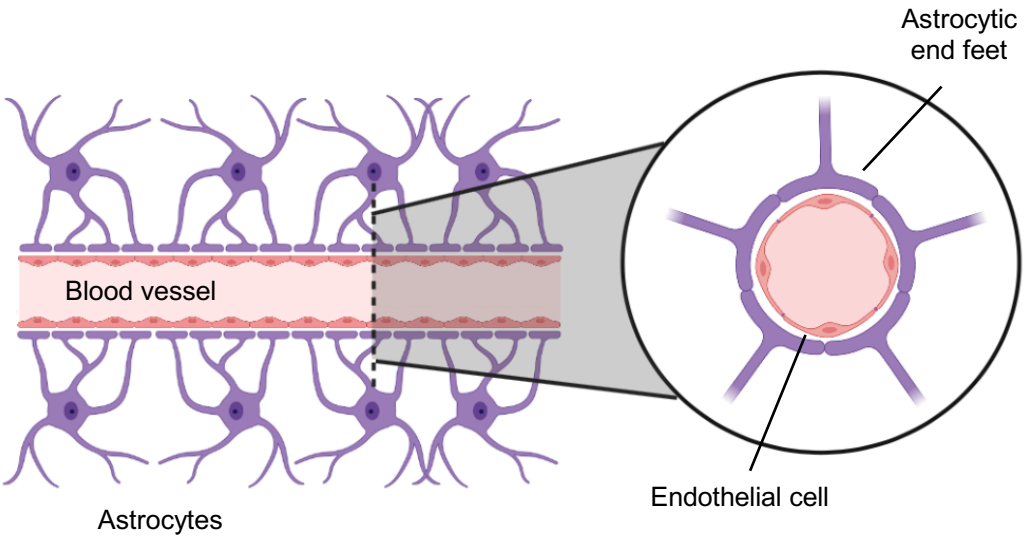


Figure 1.24 Astrocytes line the blood vessels with their end feet. The astrocytic end feet cover almost the entire surface of blood vessels, and they play important role in controlling the blood flow by regulating the dilation and constriction of the blood microvessels. The illustration was created using Bio-render website.

Moreover, as the human brain develops to maturity and adulthood, a large proportion of live synapses are eliminated to refine brain connectivity, that enables the surviving neurons to grow and strengthen. While microglia has been regarded as the main phagocytes in the CNS, the phagocytic capacity of astrocytes has increasingly been reported in the last decade (Konishi, Koizumi, & Kiyama, 2022). The phagocytic function possessed by astrocyte allow them to eliminate live synapses and clear synaptic debris, which contributes crucially to the formation and elimination of synapses (Kim et al., 2019). In light of brain trauma and inflammation, activated microglia influences astrocytes to become reactive and undergo changes in their morphology, roles, and protein expression (Kubotera et al., 2019; Mira et al., 2021). The immune function of astrocytes is

highly regulated by microglia, whereby activated microglia release factors that prompt intracellular signal transduction such as signal transducer and activator of transcription (STAT), NF-κB and mitogen and mitogen activated protein kinase (MAPK) pathways in astrocytes (Jha et al., 2019).

Neuroinflammation that ensues after microglial and astrocytic activation can be both helpful and harmful depending on circumstance, and may be considered as a double-edge sword (Bachiller et al., 2018; Guo et al., 2022). It was shown that the reactive astrocytes exert neuroprotective ability by forming scar formation at the lesion site to limit inflammation and thus protecting the surrounding brain tissue from further damage (Kubotera et al., 2019). The reactive astrocytes also generate growth factors, neurotrophic factors, and cytokines that encourage neurogenesis, neurite outgrowth and neuronal survival (Jha et al., 2019). However, they are also responsible for the release of neurotoxic levels of glutamate that are harmful to the neurons, and the production of cytokines and chemokines that trigger the ensuing pro-inflammatory response (Harada et al., 2016). The reactive astrocytes also secrete factors that increase BBB permeability, that results in the infiltration of peripheral leukocytes into the brain parenchyma (Zidarič, Gradišnik, & Velnar, 2022).

Although other CNS cells such as astrocytes, neurons, oligodendroglia and endothelial cells are capable of producing pro-inflammatory cytokines, microglia are the major contributor of cytokine release post-TBI (Needham et al., 2019). Pro-inflammatory cytokines secreted by microglia are not confined locally in the CNS, but also travel to the peripheral organs that in turn activate systemic APR.

The activation of this systemic response results in vascular dilation and upregulation of endothelial adhesion molecules that facilitate the infiltration of peripheral leukocytes into the brain (Anthony, Couch, Losey, & Evans, 2012; Xiong et al., 2018). The transmigration of these leukocytes to the site of injury leads to an exacerbated inflammatory response, as they add to the initial existing local neuroinflammation (Jha et al., 2019). It was shown that the peripheral neutrophils are the earliest circulating immune cells to be recruited into the CNS following TBI, and appears to be a crucial mediator for the subsequent secondary damage post-TBI (Anthony et al., 2012; Simon et al., 2017).

1.4.2.2 Systemic acute phase response

The systemic APR is an elemental response of the host to re-establish homeostasis and promote tissue repair following insult (Cray et al., 2009; Saber et al., 2013). The APR works through isolating and destroying pathogens, eradicating toxic molecules, and triggering host repair mechanism (Ceciliani, Giordano, & Spagnolo, 2002). APR is predominantly regulated by liver, although spleen and lung also participate in APR induction (Dickens et al., 2017; Villapol et al., 2015). The liver APR is coordinated by inflammatory mediators that can be classified into four main classes; (i) IL-1 type cytokines, (ii) IL-6 type cytokines, (iii) glucocorticoids, and (iv) growth factors (Ceciliani et al., 2002). During injury, the surface receptor of hepatocytes responds to the pro- and anti-inflammatory mediators released by the affected tissues, and subsequently stimulate the production or suppression of the acute phase proteins (Anglin, Rosebush, & Mazurek, 2010; Anthony et al., 2012; Ceciliani et al., 2002). Two major pathways that facilitates liver APR induction are the NF-kB and JAK-STAT pathways (Anthony et al., 2012; Lordan, Tsoupras, & Zabetakis, 2019).

The acute phase proteins are classified into positive or negative depending on whether they are upregulated or downregulated by at least 25% when inflammation ensues (C. C. Liu & Ahearn, 2004). Several examples of positive acute phase proteins include C-reactive protein, fibrinogen, haptoglobulin, and serum amyloid A (SAA) (Khalil & Al-Humadi, 2020). The production of positive acute phase proteins contributes to host defense by stimulating blood cell precursor egression from bone marrow to increase leukocyte supply in the

circulation, and mobilising circulating inflammatory cells such as monocytes to the site of injury. Once the blood-borne monocytes enter the tissues, they differentiate into tissue macrophages that helps attenuate injury by clearing cell debris and scavenging free radicals (McDonald et al., 2020; Serrano, Luque, & Aran, 2018). Conversely, the negative acute phase proteins such as albumin, pre-albumin, and transferrin show reduced production during APR (Khalil & Al-Humadi, 2020; Pepys, 2014). Although the mechanism by which the negative acute phase proteins work in APR is not entirely clear, it has been suggested that reduced production of these proteins help the liver to prioritise the amino acid reservoir for positive AP protein production (Liu & Ahearn, 2004; Serrano et al., 2018). Generally, the majority of inflammatory response will subside after 24-72 hours after initial insult (Liu & Ahearn, 2004), and the body will resolve to homeostasis at 3-7 days after injury (Ceciliani et al., 2002).

Bi-directional communication between the brain and the liver is clearly evident in the event of brain injury and has long been a major interest in my research group (Anthony et al., 2012; Couch et al., 2017) (Figure 1.25). Pro-inflammatory cytokines released by activated microglia do not only promote liver acute phase protein production but also stimulate further systemic cytokine release into the circulation (Lordan et al., 2019). This is evidenced through elevated chemokine C-C motif ligand 2 (*CCL-2*) gene expression in the liver and increased circulating CCL-2 after *TNF-a* is injected into the mouse brain. As CCL-2 is known to act as monocyte chemo-attractant, the increase in CCL-2 level is accompanied by increased circulating monocyte population in the blood and monocyte recruitment into the liver and the brain (Campbell et al., 2005). In addition, focal brain injury

in mice elevates neutrophil chemo-attractant CINC-1 production, which leads to increase in neutrophil numbers in the liver and within the circulation (Campbell et al., 2003).

Interestingly, it was shown that the magnitude of liver APR can reflect the severity of brain injury. The modulation of liver APR was shown able to regulate the intensity of focal brain injury. In an experimental neuroinflammation model, neutralisation of peripheral CINC-1 after brain injury inhibits recruitment of neutrophils to the brain, resulting on reduced brain damage (Campbell et al., 2003). Furthermore, specific inhibition of liver NF-κB pathway during APR by using adenoviral-delivered IκBα super-repressor was followed by marked reduction of neutrophil recruitment to the brain (Campbell et al., 2008). However, this observation appears to be age-dependent, as injection of peripheral inflammatory agents into young post-natal mice that were exposed to focal brain injury resulted in suppression of CNS inflammation instead (Sá-Pereira et al., 2018). Although it is evident that there is brain-liver crosstalk during APR, the mechanism by which information from the brain reaches the periphery has not been entirely clear. Nonetheless, it has been suggested that the extracellular vesicle (EV) in the blood could potentially act as the mediator between the two organs (Anthony et al., 2012; Couch et al., 2017).

1.4.2.3 Neutrophils, monocytes, and macrophages

1. Neutrophils

Neutrophils are the most abundant leukocytes and are the first blood-borne cell to respond to brain injury followed by monocytes (Jayaraj, Azimullah, Beiram, Jalal, & Rosenberg, 2019; Jian et al., 2019). Upon trauma, the DAMPS and chemokines released by the injured tissue recruit circulating neutrophils, and trigger the generation of granulocyte colony-stimulating factor that stimulate bone marrow to produce neutrophils (Yao & Kuan, 2020). After brain injury, increased expression of adhesion molecules are observed both on the BBB endothelial cells and on neutrophils that mediate the extravasation of neutrophils from the blood stream into the brain parenchyma (Brøchner & Toft, 2009). Subsequently, neutrophils migrate towards the site of injury following the chemokines concentration gradient signal (Jayaraj et al., 2019).

Although the activated neutrophils may exert neuroprotective effects by removing cell debris through phagocytosis and hence promote tissue healing, these activated neutrophils are also known by its destructive features that results in secondary injury to the surrounding tissues, including BBB impairment and brain edema (Jian et al., 2019). This pathogenic outcome was contributed by the release of pro-inflammatory factors such as inducible nitric oxide synthase (iNOS), ROS and matrix metalloproteinases (Jian et al., 2019). In addition, the transmigration of neutrophils may injure the endothelial cells through the neutrophil extracellular trap related mechanisms when they are sequestered within the microvasculature for an elongated period (Yao & Kuan, 2020). While

the infiltration of neutrophils to the site of injury can be detected as early as the first hour after trauma, the transmigration of peripheral monocytes took longer time to be recruited to the injured brain (Jian et al., 2019).

2. Circulating monocytes and tissue macrophages

The typical morphological features of monocytes are an irregular cell shape with oval- or kidney-shaped nucleus, with a high cytoplasm to nucleus ratio. Monocytes in the blood, bone marrow and the spleen constitute approximately 10% of total leukocytes number in human, and around 2-4% in mice (Italiani & Boraschi, 2014). The circulating monocytes are a subset of leukocytes that are produced in the bone marrow from long term hematopoietic stem cells (Rees, 2010). The circulating monocytes may remain in the circulation for up to 1 or 2 days, after which if there is no recruitment into tissues occur, these cells will die and be removed from the circulation (Italiani & Boraschi, 2014).

These monocytes exhibit surface pathogen recognition receptor and chemokine receptor that facilitate the transmigration of circulating monocytes to the site of damage during trauma, where they transform into macrophages and inflammatory dendritic cells when they localize in tissues (Jian et al., 2019). Monocytes, macrophages, and dendritic cells are classified under the mononuclear phagocyte system in the mid 1970s. The tissue macrophages are continually replenished by the circulating monocytes, where these monocytes undergo extensive transcriptional changes to mirror that of the resident macrophage and hence, adopt similar characteristics to them (Sreejit, Fleetwood, Murphy, & Nagareddy, 2020).

In the event of inflammation, activated resident macrophages release chemotactic mediators that attract circulating monocyte to facilitate the clearance of apoptotic cells and debris, as well as to occupy the available space. It was suggested that the engraftment efficiency of infiltrating monocytes into the tissue reflects the level of inflammation (Sreejit et al., 2020). It is noteworthy to mention that tissue macrophages are designated different names according to their location. For example, brain macrophages are called microglia, skin macrophages as Langerhans cells, and connective tissue macrophages as histiocytes (Italiani & Boraschi, 2015). The resident liver macrophages are referred as Kupffer cells (KC) and they represent 80-90% of the total tissue macrophages, making them to be the most abundant tissue macrophages in mammalian bodies (Nguyen-Lefebvre & Horuzsko, 2015; Shan & Ju, 2020).

Historically, the KCs were first recognized in 1876 by Karl Wilhelm von Kupffer through chloride-staining method. The KCs were previously termed as “Sternzellen” (star cells or hepatic stellate cells) and were inaccurately suggested to be part of the perivascular cells or the pericytes family. Nonetheless, after a thorough examination by Tadeusz Browicz in 1898, KCs were later identified as macrophages (Nguyen-Lefebvre & Horuzsko, 2015). These KCs localise within the lumen of the liver sinusoids towards the portal vein, where they adhere to the endothelial cells of the blood vessels (Li, Chang, & Li, 2022; Nguyen-Lefebvre & Horuzsko, 2015). Recent evidence pointed that KCs are originated from fetal yolk sac precursor and can self-renew throughout adult life (Shan & Ju, 2020). However, when there is a marked decrease in the number of KC, either through cell death or experimental depletion, the bone marrow–derived circulating

monocytes were observed to develop into KCs and maintain the KC pool. During inflammation, activated Kupffer cells secrete chemoattractant CCL-2 that promotes the infiltration of the circulating monocytes into the liver (Shan & Ju, 2020).

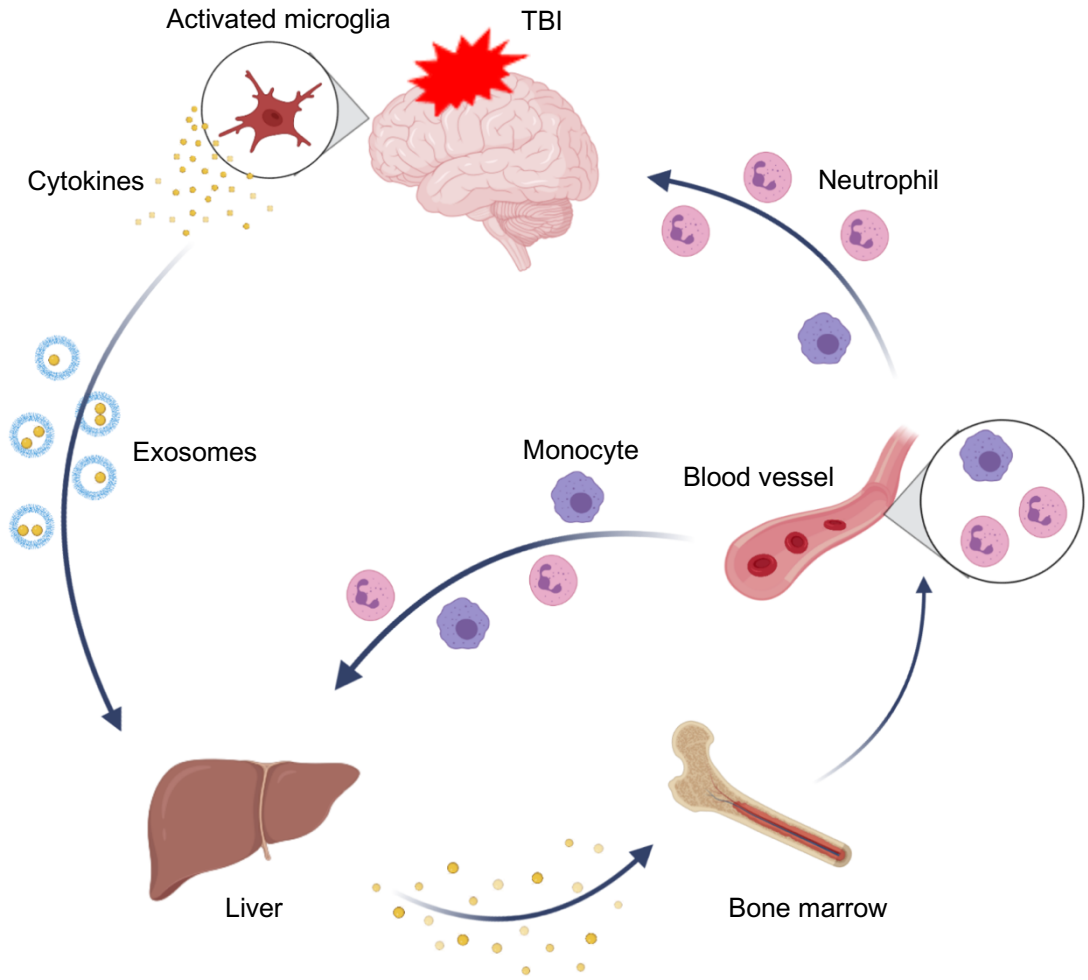


Figure 1.25 CNS - liver interplay during neuroinflammation. Microglia becomes activated after brain insult, and pro-inflammatory cytokines are released to local and systemic environment. Extracellular vesicles, specifically exosomes are potential mediator between the CNS and the peripheral system, by carrying pro-inflammatory cytokines as their cargo. Subsequently, liver responds by releasing cytokines and other acute phase proteins, which promotes egression of blood precursors from the bone marrow to increase leukocyte supply in blood circulation. Peripheral leukocytes such as neutrophils and monocytes then migrate to the liver and the brain. The illustration was created using Bio-render website.

1.4.2.4 Extracellular vesicles

During brain trauma, EV has been suggested to play a mediator role to transmit the signal between the CNS and the periphery (Anthony et al., 2012; Couch et al., 2017). EVs are released by almost every cell in the body and can be found circulating in bodily fluids such as blood including serum and plasma, CSF and urine (Hill, 2019; Urabe et al., 2020; Y. Zhang, Liu, Liu, & Tang, 2019). The term EV refers to the heterogenous membrane vesicles secreted by cells, that can be classified into three subtypes depending on their biogenesis nature; (i) exosomes (30-150nm), (ii) microvesicles (100-1000nm), and (iii) apoptotic bodies 50-4000nm) (Foers, Cheng, Hill, Wicks, & Pang, 2017; Lee & Kim, 2017; Urabe et al., 2020; Van Niel, D'Angelo, & Raposo, 2018). The exosomes and microvesicles are continually released by healthy cells, whereas apoptotic bodies are only released when cells undergo apoptosis (Foers et al., 2017). Therefore, the first two subtypes are the most widely studied EV population (Hill, 2019).

The exosomes originate from early endosome, through the inward budding of the plasma membrane. The early endosome later develops into late endosome that goes through a subsequent inward budding, leading to intraluminal vesicle (ILV) formation inside the lumen. At this stage, this late endosome transforms into multivesicular bodies (MVBs). MVBs will either be degraded upon lysosome fusion or be released into extracellular spaces upon merging with plasma membrane. The ILVs released into the extracellular spaces are termed exosomes (Vakhshiteh, Atyabi, & Ostad, 2019). On the contrary, biogenesis of microvesicles is more direct as compared to that of exosomes, whereby they are

formed through outward budding of the plasma membrane (Lee & Kim, 2017) (Figure 1.26).

It was initially presumed that the primary function of EVs is to discard unwanted cellular waste through their shedding. Therefore, little attention was given to them when their discovery was first reported in the late 80s (Urabe et al., 2020). However, this situation changed after Raposo et al (1996) showed that EVs are capable of initiating immune reaction, as incubation of cell culture with exosomes derived from human and murine B-cells triggers antigen-specific MHC class-II restricted T cell responses (Raposo et al., 1996). From then on, the interest on the role of EVs in immune system regulation in healthy and pathogenic condition has increased rapidly. The recognition of EV cargo such as genetic molecules, lipid and proteins has further revealed their roles in cell-to-cell communication and signaling, to local and distant cellular environment (Becker et al., 2016; Hill, 2019). The fusion of EVs containing these functional contents to their target cells was shown able to redirect the physiological state of the recipient cells (Becker et al., 2016; Vinaiphat & Sze, 2019).

During TBI, the binding of DAMPs to PPRs leads to a large protein complex assembly termed as inflammasome, which was first described by Martinon and colleagues in 2002. Different PPRs give rise to various inflammasome complexes. Pro-caspase 1 constitute one part of the protein complex that converts into caspase 1 upon activation. Cytokines such as IL-1β and IL-18 are subsequently produced following caspase 1 generation. One of the routes that

these cytokines released by the cells is through exosome secretion, as these substances were found in the exosome cargo (Noonin & Thongboonkerd, 2021).

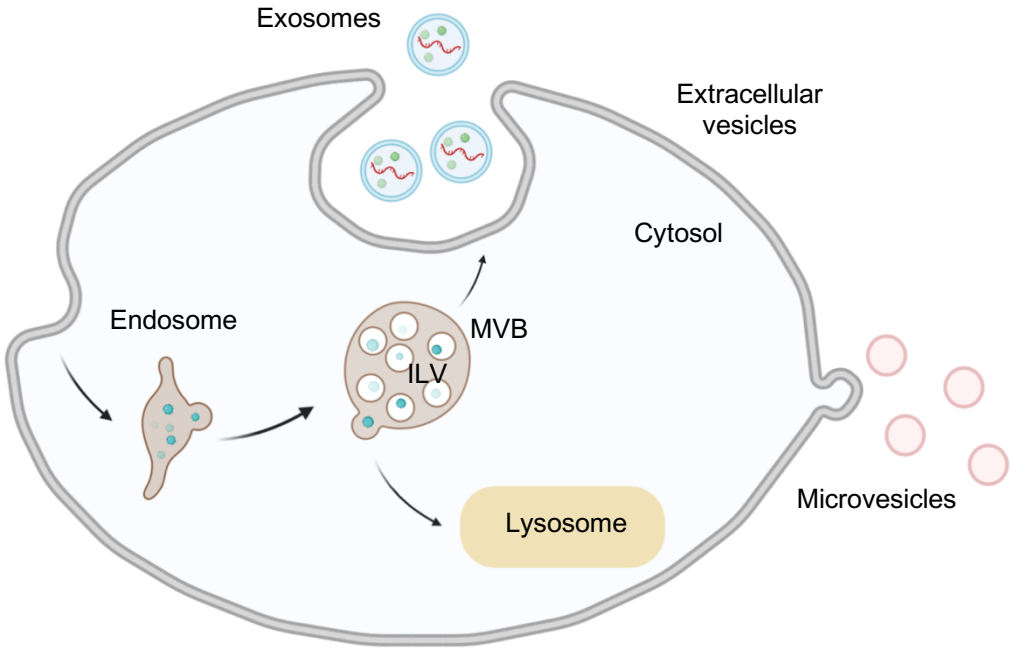


Figure 1.26 Biogenesis of exosomes and microvesicles. Inward budding of cellular plasma membrane produces early endosomes that later develops into multivesicular body (MVB) that contains intraluminal vesicles (ILV, late endosome). MVB either fuses with lysosome or plasma membrane, with the former results in MVB degradation, while the latter leads to ILV release into the extracellular space. ILV released into the extracellular space is termed as exosomes. Biogenesis of microvesicles is more direct as compared to that of exosomes, whereby they are formed through outward budding of the plasma membrane. The illustration was created using Bio-render website.

1.4.3 Animal models of TBI

Since 1980s, numerous animal models of TBI have been developed to replicate the pathological conditions of human TBI, to address the complex pathophysiology of the injury and to explore potential treatments (Cernak, 2005; C. Chen et al., 2022). Most experimental TBI studies are open-head injuries that require sterile surgical procedures under general anaesthesia. On the contrary, the closed-head injuries are less common employed although it can more closely mimic the human brain injury incidence. Nonetheless, no single animal model is able to simulate all aspects of TBI, henceforth the selection of animal model in the experimental research depends greatly on the goal of the study (Cernak, 2005; Iboaya, Harris, Arickx, & Nudo, 2019). It is important that the animal model selected to satisfy the following criteria, regardless of the research goal (Cernak, 2005; Sempere, Rodríguez-Rodríguez, Boyero, & Egea-Guerrero, 2019): (i) the mechanical force to induce the injury can be controlled, quantifiable and reproducible, (ii) the inflicted damage is quantifiable and able to mimic human clinical injury, (iiii) the injury outcome measured by behavioural, morphological, physiological, and biochemical parameters are the consequences of the mechanical force applied, and (iv) the injury severity can be predicted by the intensity of the mechanical force used.

At present, there are four most used TBI models in experimental research, which are fluid percussion injury (FPI), controlled cortical impact injury (CCI), impact acceleration injury, and blast injury. Among these, only FPI and CCI are used for aged animal models (Cernak, 2005; C. Chen et al., 2022; Iboaya et al., 2019). In

this thesis, the CCI method is chosen over FPI due to its advantage in offering precise control of mechanical factors such as the time, velocity, angle, and depth of impact as well as low mortality rate (Iboaya et al., 2019; Xiong, Mahmood, & Chopp, 2013). Thus, only the elaboration on CCI method will be discussed further in this section.

The CCI model uses a pneumatic or electromagnetic impact device (Figure 1.27) to deliver the mechanical force onto the exposed, intact dura following craniotomy under sterile surgical procedure. The most common craniotomy location is between bregma and lambda position. The mechanical force exerted by the rigid impactor controlled by a CCI software leads to cortical tissue loss, acute subdural haematoma, axonal injury, BBB dysfunction, oedema and neurobehavioral dysfunction (Iboaya et al., 2019; Xiong et al., 2013). Indeed, the cognitive deficits as observed with the Morris water maze test are highly related with the intensity of the mechanical force applied. Furthermore, CCI can induce emotional behaviour deficits as examined by elevated-plus maze and forced swim test in mice. Interestingly it was found that while cognitive deficits increase in relation to mechanical force intensity, the emotional deficits do not show the same association (Cernak, 2005; Xiong et al., 2013). In addition to mice, the CCI method has also been applied to other species such as rats, ferrets, swine, and monkeys. The focal injury caused by the impactor device onto the cortical region can have an associated widespread damage to other regions such as into the hippocampus and thalamus. Aside from the ease of control over mechanical factors and low mortality rate, CCI model also has a reduced risk of a rebound injury as compared to other types of TBI models (Xiong et al., 2013).

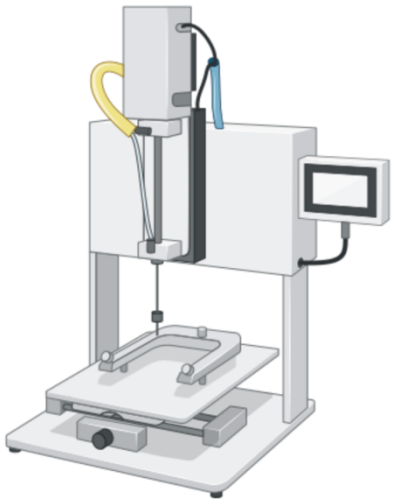


Figure 1.27 Controlled cortical impactor instruments. Mouse will be put under general anaesthesia and in stereotaxic position prior to the craniotomy. The impactor will then deliver mechanical force onto the exposed dura, generating CCI injury. The illustration was created using Bio-render website.

1.4.3.1 Limitations and advantages of rodent TBI model

Although the existing models of TBI can recapitulate most aspects of the functional and histopathological changes as seen in clinical injury, the non-human mammals still could not fully replicate human TBI in its entirety (C. Chen et al., 2022). This is because, despite the considerable physiological similarity of rodents to human brains, there is a notable difference in the structure and function such as the brain geometry, white-to-grey matter ratio, craniospinal angle as well as the absence of brain gyrus (Xiong et al., 2013). It has been suggested that the small lissencephalic brain of rodents are less suitable for modelling the complex structure of human brain anatomy. For instance, the lower brain mass of rodents are not able to replicate the angular acceleration and shearing forces as compared to that of human, thus the coup contrecoup injury

and diffuse axonal injury experienced in human may not able to be simulated in rodents (Cernak, 2005; Iboaya et al., 2019). Thus, these differences in structural characteristics may result in differing injury responses of comparable injury severity. Previous studies have also pointed of the variances of behavioural and histopathological outcomes to TBI when compared across different mouse and rat strains (Xiong et al., 2013).

Nonetheless, despite a variety of opinions on the ideal species to model human TBI, majority of researchers have regarded rodent models to be the most appropriate choice for neurotrauma studies. The small size and low costs of rodents allows investigators to conduct repetitive measurements and behavioral, morphological, cellular, and biochemical parameters that will entail a big number of animals. Henceforth, the adoption of other species aside from rodents, with higher phylogenetic characteristics to human are less achievable due to technical, ethical and/or financial constraints (Cernak, 2005). Thus, despite a better similarity of neurophysiological processes and functional impairments reflected by larger animal models towards human injury, rodent models are still most regularly employed in TBI research. Moreover, other advantages of rodent TBI are the availability of a vast option of genetically modified rodent strains and lower regulatory burden. Furthermore, the short life span of rodents which is up to 2-3 years provides a huge benefit for ageing studies (Iboaya et al., 2019).

1.5 Metabolomics

The concept of metabolomics was first proposed by Professor Jeremy Nicholson in 1999 (Q. Yang et al., 2019). As with other omics family such as genomics, proteomics and transcriptomics, metabolomics is the latest approach that explores the pathogenesis of human disease by distinguishing physiological from pathological pathways which may facilitate disease diagnosis and predicts prognosis (Aderemi, Ayeleso, Oyedapo, & Mukwevho, 2021; Y. Yang et al., 2019) (Figure 1.28). The metabolomics study identify and quantify low molecular weight molecules (<1500 Da) in the biological system, followed by the generation of data using high-throughput analytical techniques such as nuclear magnetic resonance (NMR) or mass spectrometry (MS) to gain insight of the system's metabolic state (Z. Liu, Waters, & Rui, 2022).

The quantitative and qualitative collection of global metabolites within a period of time is referred to as metabolomes, which is the downstream products following alterations that happen in the genome, proteome, and transcriptome (Aderemi et al., 2021; Y. Yang et al., 2019). Therefore, metabolomes are able to reflect the sensitive measure of the genetic, disease and environmental interaction which is an advantage that could not be captured by other omics family (Gowda & Raftery, 2019; Marshall & Powers, 2017). In addition, the capability of metabolomics application to detect subtle changes in a high output data with comprehensive metabolites quantification has made it to be a valuable tool in many fields, including biomarker study for early disease diagnosis, research on pathophysiology of disease, drug discovery, epidemiology study, as well as

monitoring cancer prognosis and diagnosis (Bharti & Roy, 2012; Letertre, Giraudeau, & de Tullio, 2021; Steuer, Brockbals, & Kraemer, 2019).

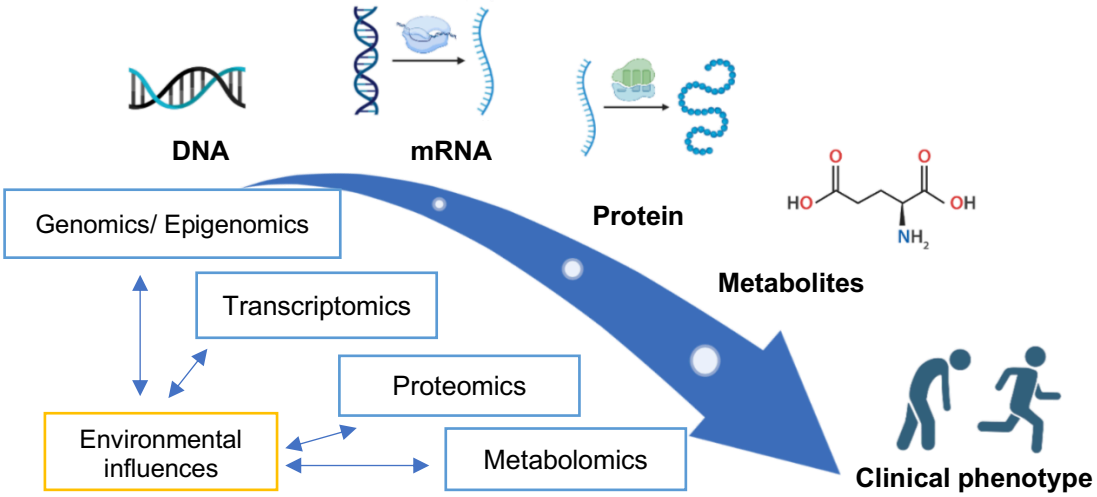


Figure 1.28 Overview of the omics family. Metabolomics are the biological end products of the upstream alterations in the genomics (genes), transcriptomics (mRNA), and proteomics (proteins), as well as the environmental influences. Example of environmental influences includes infection, drugs consumption, lifestyle, and nutrition. Therefore, metabolomes best reflect the clinical phenotype and is the best platform for biomarker discovery. The illustration was created using Bio-render website.

Various biological samples regardless of whether it is fluid or solid can be applied for metabolomics study such as tissues, serum, plasma, cells, CSF, urine, faeces, as well as exhaled gas (Ashrafian et al., 2021; Z. Liu et al., 2022). Example of metabolic information acquired from these biological samples include amino acids, carbohydrates, lipids, and hormones (Lombó, Ruiz-díaz, Gutiérrez-adán, & Sánchez-calabuig, 2021). The principle and workflow of metabolomics approach is practically straightforward. Firstly, the metabolomes are extracted from two or more groups comprising of control group and treated/ diseased

group(s). Then an analytical technique is employed for spectra acquisition from the biological samples, followed by multivariate statistical analysis such as principal component analysis (PCA) and orthogonal projections to latent structures (O-PLS). These statistical analyses enable user to identify clusters of metabolomes and ascertain group separations (Marshall & Powers, 2017).

1.5.1 Advantages of NMR spectroscopy

While the NMR and MS are two most common analytical modalities used in metabolic profiling, other methods such as gas chromatography (GC) and liquid chromatography (LC) may also be used (Marshall & Powers, 2017; Q. Yang et al., 2019). It is important to note that no single analytical platform is able to obtain complete profiling of all metabolites present in a biological sample, hence a combination with other techniques can be adopted (Emwas et al., 2019). Both NMR and MS techniques have their own strengths and weaknesses, though however the NMR approach is shown superior in many aspects (Gowda & Raftery, 2019).

The MS method is widely used when there is scarcity of sample volume, as the extreme sensitivity MS enable the detection of vast number of metabolites from as low as 10 µL of biofluid samples, of nanomolar and picomolar concentration (Vilca-Melendez, Uthaug, & Griffin, 2021). Furthermore, the use of a combined method such as LC-MS and GC-MS can yield the identification of more than 1000 metabolites from the sample of >1 µM concentration, as compared to 50-200 metabolites when NMR approach is used (Gowda & Raftery, 2019). MS also

delivers better spectral resolution and quality as compared to NMR (Marshall & Powers, 2017). However, although MS is better in terms of sensitivity as compared to NMR, MS approach requires the metabolites to be efficiently ionised for them to be detected. The procedure by which these metabolised are ionised destroys the sample and hence re-running of samples is not possible without having a significant batch effect as a consequence. The issue with ion suppression in MS is a well-known challenge. As MS is only able to detect readily ionised metabolites, this results in a number of metabolites to be overlooked (Marshall & Powers, 2017). However, these limitations are not present in NMR usage, making NMR to be a great approach when dealing with a huge number of samples (Vilca-Melendez et al., 2021).

In comparison to MS, NMR requires larger sample volume of approximately 30 to 600 µL, with micromolar to millimolar concentration. Metabolite detection using NMR modality does not require the sample to be ionised, which therefore non-destructive and results in excellent sample reproducibility and great sample recovery (Aderemi et al., 2021; Marshall & Powers, 2017). Moreover, NMR has simpler sample preparation method, easy method of metabolite quantification and requires shorter time for sample analysis. These advantages have made NMR modalities to be highly sought after in long-term experiments and large-scale clinical metabolomics studies (Aderemi et al., 2021; Emwas et al., 2019; Marshall & Powers, 2017; Steuer et al., 2019). In addition, NMR allows users to investigate the structure of molecules to a greater depth that is not offered by other approaches, as NMR has the capacity to evaluate numerous molecules at an atomic level through the excitation of isotopes such as 1H, 13C, 31P and 15N

(Emwas et al., 2019; Gowda & Raftery, 2019). The non-destructive nature of NMR sample preparation enable user to re-use the same biological samples to identify molecules containing different isotopes, which is a significant advantage of NMR (Gowda & Raftery, 2019). Therefore, given the advantages of NMR, the proton NMR (1H NMR) spectroscopy modality was employed in Chapter 5 of this thesis.

1.5.2 1H NMR spectroscopy

The 1H NMR spectroscopy has the widest application in the NMR metabolomics studies due to the abundance of hydrogen atom in the organic compounds (Emwas et al., 2019; Q. Yang et al., 2019). The fundamental concept of NMR spectroscopy is largely founded on the magnetic properties of specific atomic nuclei whereby it records the re-emission of pulsed electromagnetic frequency pattern of the nuclei when samples are placed in a strong magnetic field. When there is an absence of magnetic field, the nuclei are uniformly distributed in all direction (isotropic orientation) and hence there is no net magnetisation.

However, when an external magnetic field (B0) is applied, the motion of the charged particle will behave as a small magnet that causes them to align in the direction of B0, simulating the compass aligning in the north-south axis. As these charged particles spin, they develop a magnetic field creating a magnetic dipole (Gerothanassis, Troganis, Exarchoou, & Barbarossou, 2002; Kwan, Mobli, Gooley, King, & MacKay, 2011). Many magnetic nuclei have non-zero spin quantum number that will exhibit spin angular momentum. Nuclei with a

combination of odd and even protons and neutrons will have a half-integral spin (1/2), which signal can be detected in NMR. Examples include 1H, 13C, 31P and 15N. On the contrary, nuclei containing both even numbers of both protons and neutrons (for example: 4He, 12C, 16O and 32S), or both odd numbers of protons and neutrons (for example: 14N, 10B) cannot undergo NMR as they contain zero spin.

In 1H NMR spectroscopy, when the samples are exposed to the external magnetic field, the nuclei possess two orientations, either parallel (spin-up) or anti-parallel (spin-down) spins to the B0 (Figure 1.29). The spin-up nuclei have a lower energy level, whereas the spin-down nuclei have a higher energy level. The ratio of spin-up and spin-down nuclei are nearly equal, with a slight excess number of the spin-up orientations, thus generating a net macroscopic magnetisation in the same direction to the external magnetic field. The emission of energy in the same frequency occurs when the higher energy level nuclei return to their base level.

The frequency pattern translates into data that informs the structure, motion, and chemical environment of a particular molecule (Ashrafian et al., 2021). The specific frequency transmitted by each molecular nuclei is termed as chemical shift in the unit of parts per million (p.p.m) that enables the identification of chemical groups present within a molecule, structural information, and their bonding characteristics (Kwan et al., 2011; Simpson, Simpson, & Soong, 2012; Vilca-Melendez et al., 2021). The signals created by the transitions of atomic nuclei in a changing energy state produces one dimensional (1D) NMR spectrum

(Kwan et al., 2011). The area under the curve of each peak in the NMR spectrum corresponds to the concentration of the molecule (Vilca-Melendez et al., 2021). The metabolite assignment can be made through the information of their chemical shifts and splitting patterns, by comparing this information to the known literatures and metabolite database such as the human metabolome database (HMDB) (Wishart et al., 2018).

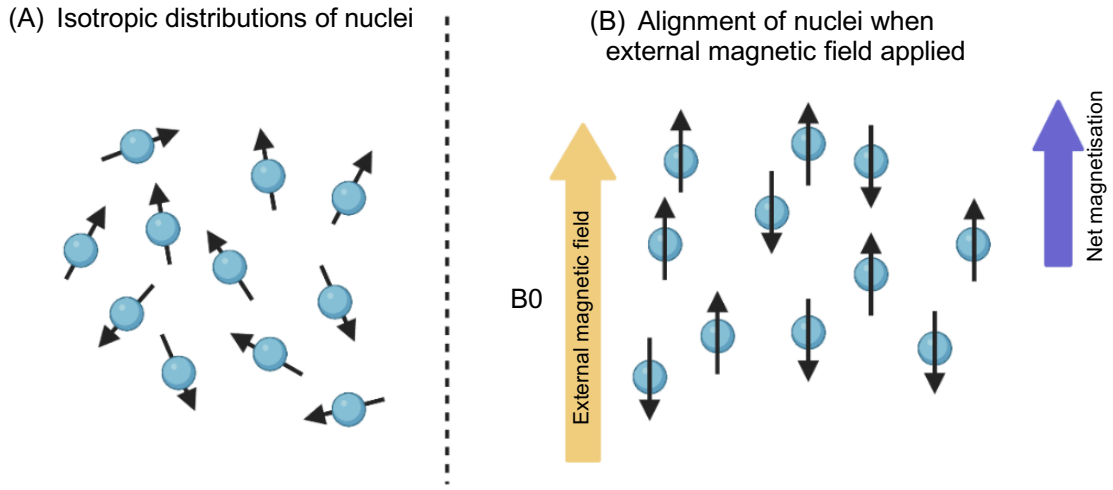


Figure 1.29 The orientation of nuclei with and without an external magnetic field. The number of possible orientations of a particular atomic nucleus is determined by the equation $2I + 1$, whereby I is the spin quantum number. Henceforth, in 1H NMR spectroscopy, 1H has the spin quantum number of 1/2 which will have two possible orientations – parallel (spin-up) and anti-parallel (spin-down) to the direction of external magnetic field (B0). The ratio of spin-up nuclei are slightly more than the spin-down nuclei, resulting in a net macroscopic magnetisation parallel to the direction of B0. The illustration was created using Bio-render website.

CHAPTER 2

METHODOLOGY

Chapter 2 : Methodology

2.1 Animals

Transgenic AD mouse overexpressing human APP (J20; Sw/Ind; heterozygous) and human neurofibrillary tangles (P301S; MAPT; homozygous) were used in this study. Breeding pairs for transgenic J20 and non-transgenic wild-type (WT) C57BL/6 mice were purchased from Charles River (UK) and were bred internally in the Biomedical Science building, University of Oxford under standard conditions with a 12-hour light/dark cycle with access to food and water ad libitum. Breeding pairs for transgenic P301S mice were obtained from Michel Goedert lab (UK). In all experiments, age-matched C57BL/6 littermates were used as controls. A mixture of male and female mice was used in all experimental groups to mimic gender diversity in AD patient population, which consists of both male and female. The age of mice used varies according to chapter/ experiments, which has been further detailed under experimental design in respective chapter methodology. All animal procedures were carried out in accordance with the UK Animals (Scientific Procedures) Act 1986.

2.1.1 Mutant genotyping

The ear clips of transgenic mutants were collected when they reached 3 weeks of age and were sent to Transnetyx (Cordova, USA) for genotyping. Probe APPsw.Tg was used to check for J20 strain, whereas probe Thy1-hTau.P301S was used for P301S strain respectively. Heterozygous J20 brain sections were further cross validated in-house using immunohistochemistry staining against

Aβ42 (Figure 2.1). Twenty-four-month-old J20 and WT brain sections were used as the positive and negative controls respectively.

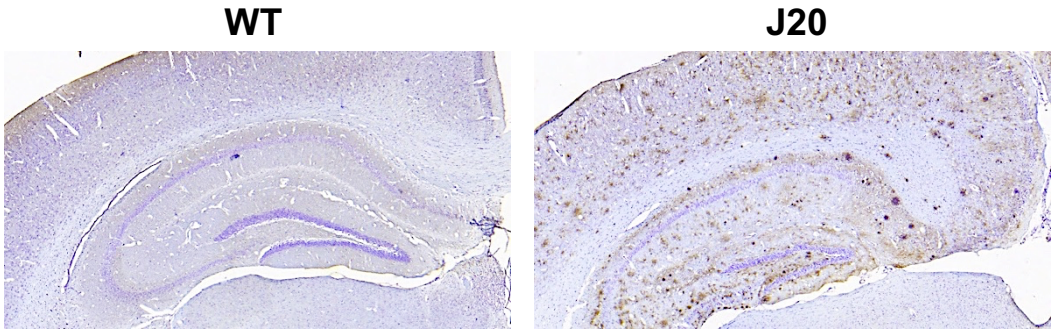


Figure 2.1 Brain sections immunostained against AB42 for amyloid detection. J20 brain section (24 months old) showed the presence of amyloid as represented through brown coloured staining, which was absent in its age-matched WT control. Staining procedure followed the protocol described in section 2.5.2.

2.2 Brain contusion

Animals were divided into naive and TBI groups; by which the latter was subjected to a single brain contusion using controlled cortical impactor device (Hatteras Instruments, Inc., Cary, NC). The brain surgery was performed under an operating microscope (Wild Heerbrugg, Switzerland) where the head of anaesthetized mice (3% isoflurane in oxygen) were shaved and positioned in a stereotaxic frame. Following a midline scalp incision, a 3-mm diameter craniotomy flap was excised at Bregma -2.5 mm anterior/posterior, -2.5 mm medial/lateral. The impact tip (1.1 mm diameter, round shape) of the controlled-cortical impactor device was lowered to the center of the exposed brain.

After the impactor was positioned at the dura surface, a single trauma was generated using an impact speed of 1.5 m/s, 0.5 mm impact depth, and an 85 ms dwell time. Linear injury device software (version 1.0.0; Erciyes) was used to control the impact specification, which enables the reproducibility of every contusion to be monitored. Any bleeding was allowed to resolve, and the skull flap was re-positioned and glued with VetBond (3M, St Paul, MN, USA), before the incision wound was closed with 6/0 Vicryl sutures (Ethicon, UK) and VetBond. Mice were allowed to recover in a heated chamber ($32^{o}C \pm 2$) before returning to their home cage. No post-surgical analgesia was administered in view of potential interference on inflammatory analysis. However, mice were carefully monitored daily for seven days post-surgery, with delicate care to ensure minimal distress following procedure. No mortality was observed in acute TBI cohort, while one mortality was noted in chronic TBI cohort. No procedure was performed in the naïve mice. It is worthwhile to mention that throughout this thesis, data comparisons were made between TBI and naïve groups, and no sham was included.

2.3 Behavioural test

Adhesive tape removal test was performed on the 12 months old J20 and WT cohort for acute TBI experiment, and result was reported in Chapter 3. Two-trial Y-maze, light-dark box, and spontaneous alternations assessments were carried out on the same day onto 4 months old P301S and WT cohort for chronic TBI experiment, and the results were reported in Chapter 4. For chronic TBI (chapter 4) experiment, the same mice were used throughout these three behavioural assessments. Mice were acclimatised to the test room for at least 30 minutes prior to the behavioural tests. The experimental timelines for these behavioural tests are as illustrated in Figure 2.2 and Figure 2.3.

2.3.1 Adhesive tape removal test

The sensorimotor deficit of the mice was assessed using adhesive tape removal behavioural test (L. Zhang, Chen, Li, Zhang, & Chopp, 2000). During the adhesive tape removal test, animals were placed in a transparent box and an adhesive tape strip (small, rectangular shape) was placed on both of mice forelimbs. Animal performance was examined by measuring the time taken to sense and remove the adhesive tapes. The time taken to sense the adhesive tape was noted as contact time, whereas the time taken to remove the adhesive tape was noted as removal time. First and second removal time was obtained, to which it refers to the adhesive tapes taken off from the first and second forepaws respectively.

The box was cleaned in between test sessions to remove urine and faeces from the previous animal. Animals were introduced to training every day for 5 days pre-TBI. Injury to the brain was performed on day 0. Following TBI (day 0), mice were assessed for sensorimotor deficit at day 1, day 2, day 4 and day 7. Schematic diagram for the experimental setup is as illustrated in Figure 2.2. The adhesive tape removal test data presented in Chapter 3 (section 3.2.1) was provided by Prof Daniel Anthony and Ross McLeod who carried out the experiment.

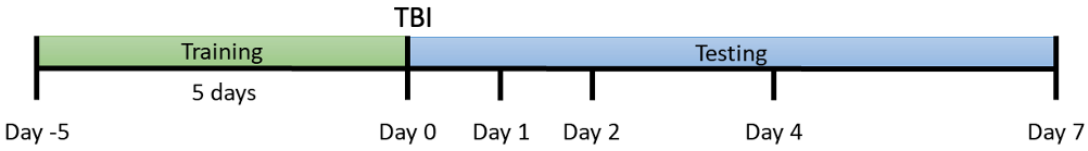


Figure 2.2 Experimental timeline for adhesive tape removal behavioural test. Animals were introduced to training every day for 5 days pre-TBI. Following TBI (day 0), mice were assessed for sensorimotor deficit at day 1, day 2, day 4 and day 7. Illustration was created using Microsoft PowerPoint.

2.3.2 Two-trial Y-maze

For two-trial Y-maze experiment, testing was accomplished by utilising a Y-shaped maze with light coloured, opaque arms oriented at 120-degree angles from each other. Visual cues were hung on the wall for all three arms. The room brightness was set at 27 lux during the acclimatisation period and throughout the two-trial Y-maze test. This testing measures the hippocampal function of the mice, by assessing its reference memory through novelty exploration assessment.

In this behavioural test, mice were introduced twice to the Y-maze. During the first introduction (acquisition period), one arm of the Y-maze was closed. Mice were allowed to explore the area for 5 minutes before they were returned to home cage (Herrera et al., 2020; Shavit-Stein et al., 2021). After 60 minutes interval, the mice were again introduced to the Y-maze (retrieval period) with all arms opened (Figure 2.4). The 60 minutes interval was chosen as per protocol by Kraeuter, Guest, & Sarnyai (2019). The newly opened arm was considered as novel arm, therefore the discrimination of familiarity versus novelty was measured by recording the time spent in the novel arm. Mice were allowed to roam freely in the Y-maze for 5 minutes (Herrera et al., 2020; Shavit-Stein et al., 2021) and graph was illustrated from the data collected from the first 2 minutes of retrieval period following previous protocol (Yau et al., 2007), as this is the phase where maximal exploratory activity happens.

During retrieval period, the mouse should remember that the novel arm was not previously available and would visit this novel arm more often (Kraeuter et al., 2019). Good reference memory was defined as longer time spent in the novel arm during the retrieval period, due to the instinctive nature of rodents to explore new territory. Mouse that did not show preference for any arms during the retrieval period may indicate impaired hippocampus function (Kraeuter et al., 2019) (Figure 2.5). The maze was thoroughly cleaned with 70% ethanol between sessions. During the acquisition and retrieval period, investigator was sat outside the sight of the mouse to reduce distraction. It should be noted that counterbalancing was not performed for this behavioural test, which is a limitation of this study.

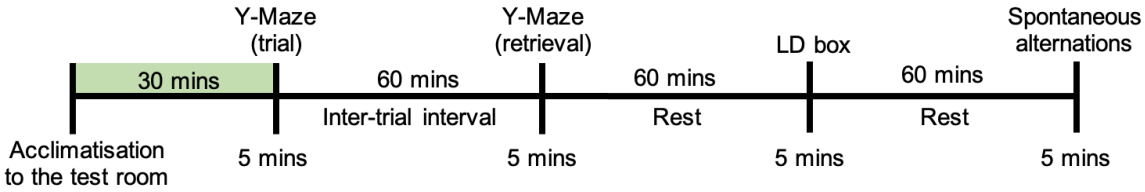


Figure 2.3 Experimental timeline for two-trial Y-maze, light dark box, and spontaneous alternations. Mice were acclimatised to the test room for at least 30 minutes prior to the behavioural tests. In two-trial Y maze test, mice were introduced twice to the Y-maze. During the first introduction (acquisition period), one arm of the Y-maze was closed. Mice were allowed to explore the area for 5 minutes before they were returned to home cage. After 60 minutes interval, the mice were again introduced to the Y-maze (retrieval period) with all arms opened. The newly opened arm was considered as novel arm, therefore the discrimination of familiarity versus novelty was measured by recording the time spent in the novel arm. Mice were allowed to roam freely in the Y-maze for 5 minutes. After 60 minutes rest, mice were then subjected to light-dark box test, where mice were initially put into the dark chamber and allowed to move freely between chambers for 5 minutes to test for anxiety-like behaviour. Subsequently, after another 60 minutes rest, mice were subjected to spontaneous alternations test, to measure the spatial working memory of the mice. The same mice were used throughout these three behavioural assessments. LD box, light dark box. Schematic diagram was created using Microsoft PowerPoint.

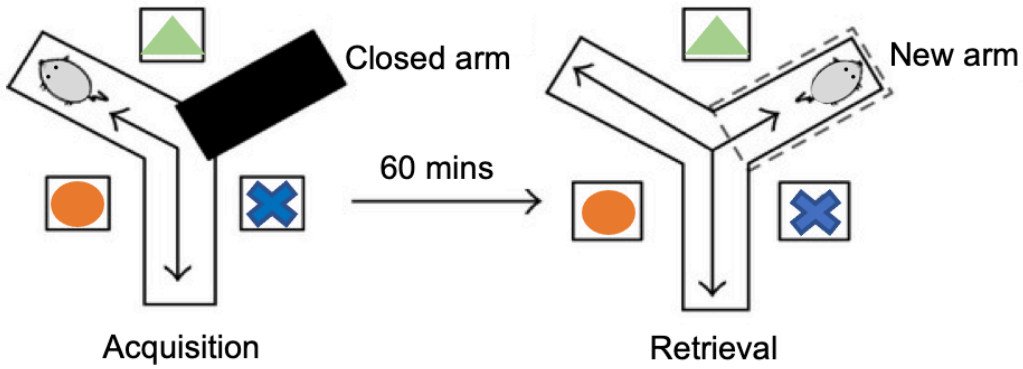


Figure 2.4 Two-trial Y-maze. Mice were introduced twice to the Y-maze, with a 60-minutes interval between the first (acquisition period) and second (retrieval period) session. One of the arms was closed in the acquisition period. This arm was later opened in the retrieval period and served as the novel exploratory area for the mouse. The illustration was created using Bio-render website and edited in Microsoft PowerPoint.

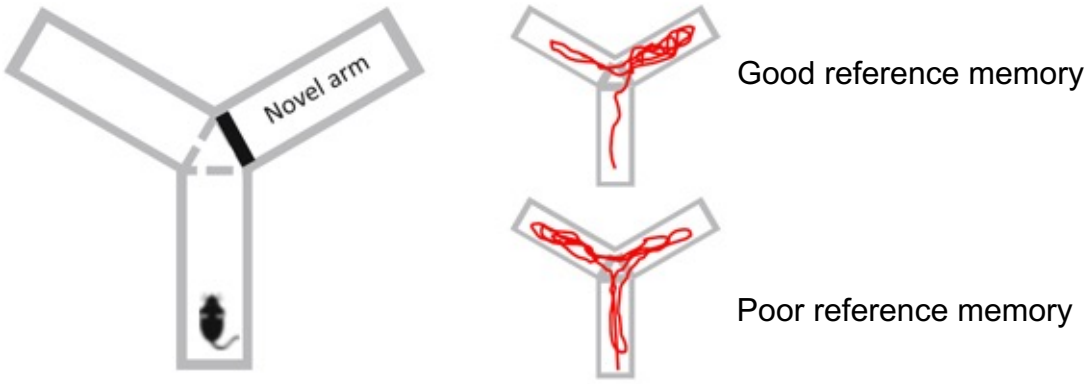


Figure 2.5 Good reference memory vs poor reference memory. During retrieval period, a mouse with good reference memory will show preference in exploring the novel arm, by spending more time in the previously unexplored arm. A mouse with poor reference memory will show no preference of arms, therefore may signify impaired hippocampal function. Illustration retrieved from Kraeuter et al., 2019.

2.3.3 Light-dark box

The light-dark box with a smaller dark compartment (one-third) and larger light compartment (two-third) was used in this study for anxiety assessment (Figure 2.6). The light chamber was illuminated with 119 lux brightness. Mice were initially put into the dark chamber (Takao & Miyakawa, 2006) and allowed to move freely between chambers for 5 minutes (Bourin & Hascoët, 2003). The time taken for the mice to enter the light chamber was described as latency to exit dark, whereas the time spent in the light chamber was defined as time in light chamber. The number of entries into the bright chamber was counted and reported as the number of transitions, which can also be used as a measure of locomotor activity. Rearing activity was defined when the rodent stands on the hind legs either supported or non-supported against the wall.



Figure 2.6 Light-dark box. A light-dark box with a smaller dark compartment (one-third) and a larger light compartment (two-third) was used in this study for anxiety assessment. The light chamber was illuminated with 119 lux brightness. Mice were initially put into the dark chamber and allowed to move freely between chambers for 5 minutes. The time taken for the mice to enter the light chamber was described as latency to exit dark, whereas the time spent in the light chamber was defined as time in light chamber. The illustration was created using Bio-render website.

2.3.4 Spontaneous alternations

Light coloured Y-maze with opaque arms oriented at 120-degree angles from each other was used for spontaneous alternations test. This behavioural test measures the spatial working memory of the mice that is driven by the natural curiosity of the rodents to explore new arms that were not previously visited. This activity requires the mice to remember which arm that they have and have not visited which necessitates the interaction between prefrontal cortex and hippocampus, two brain regions that governs the proper functioning of working memory (Kraeuter et al., 2019). Therefore, good spatial working memory indicates a good cognitive state and vice versa.

Protocol for spontaneous alternations was adopted from Kraeuter et al with slight modifications (Kraeuter et al., 2019). The arms were designated with A, B, and C for unique identifier prior to test period. Mice were placed in one arm (arm A)

and allowed to explore all three arms of the Y-maze for 5 minutes. It should be noted that counterbalancing was not performed for this behavioural test, which is a limitation of this study. Good working memory was denoted by high percentage alternations. An entry was counted when all four limbs of the mouse were within a single arm. An alternation was described as consecutive entries into all three arms (Figure 2.7). Poor working memory was represented by higher proportion of entering repeated arms. During the 5 minutes test duration, the number of arm entries and alternations were used to calculate the percentage of alternations, using the following formula (Miedel, Patton, Miedel, Miedel, & Levenson, 2017):

$$\% \text{ alternations} = (\text{number of alternations} / \text{total arm entries} - 2) \times 100$$

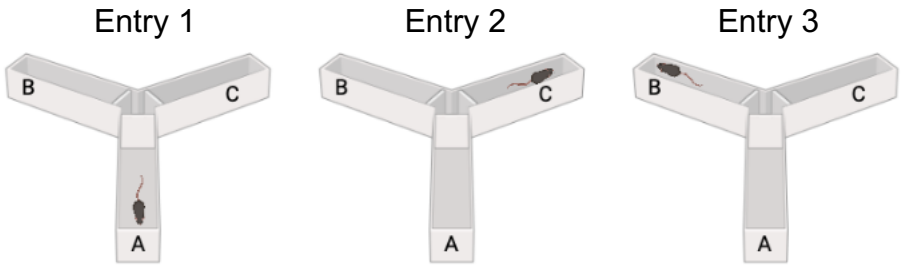


Figure 2.7 Representative figure illustrating an alternation. Each arm was labelled with either A, B or C. An alternation is defined as consecutive entry of into each of the three arms without any repeats, for example ABC, BCA, CBA and ACB. An entry was counted when all four limbs of the mouse were within a single arm. The illustration was created using Bio-render website.

2.4 Tissue sample collection

Animals were culled through cardiac puncture under general anesthesia (3% isoflurane in oxygen). The blood was collected into 2 mL heparin tubes (Teklab Ltd, UK) using sterile 1 mL syringe (Terumo; Leven, Belgium) connected to 23G x 1 ¼ inch blue needle (BD Microlance 3; Spain) pre-coated overnight (4°C) with heparin saline solution (5000 units heparin/L, 0.9% NaCl). Unless otherwise specified, the cardiac puncture performed in this thesis follows the above arrangement.

Immediately after cardiac puncture, mice abdomen was cut exposing the heart, and the right atrium was nicked to enable circulation flow-out. Mice were trans-cardially perfused with heparin saline solution (5000 units heparin/L, 0.9% NaCl) until the liver was cleared of blood. Fresh liver was collected and snap-frozen on dry ice for molecular analysis. Afterwards, the mice were trans-cardially perfused with 4% paraformaldehyde (PFA; made up with 0.1M phosphate buffer, pH 7.4), followed by brain and liver tissue collection for histology analysis.

2.5 Histology

The brain and liver tissues were post-fixed in 4% PFA for 24 hours (4°C), and cryoprotected in 30% sucrose for 48 hours (4°C) before being embedded in optimal cutting temperature medium (OCT; Thermo Scientific, UK). Aluminum foil molded into a small cup was used to contain the tissue. Isopentane bath on dry ice was used to freeze down the OCT, and samples were stored at -20°C until use.

2.5.1 Tissue sectioning

The OCT-embed tissues were sectioned on a pre-cooled cryostat (-19°C ± 2; Leica Microsystem, UK), set to cut at 10 μm thickness. The coronal section of fixed brains and livers were mounted on gelatin-coated microscope slides in a serial manner. The slides were then left to dry overnight at room temperature (RT) prior to storage at -20°C until further use.

2.5.2 Immunohistochemistry

Avidin-biotin complex method of immunohistochemistry (IHC) was used. Slides from the -20°C freezer were dried in an incubator (37°C, 15 mins), rehydrated briefly in phosphate buffered saline (PBS, Dulbecco A; pH 7.3 ± 0.2, Oxoid Ltd, UK) and quenched for endogenous peroxidase activity (1% hydrogen peroxide in methanol for 10 minutes; Sigma, UK). Where applicable (Table 2.1), an additional antigen retrieval step (citrate buffer, pH 6.0) was performed for brain sections prior to quenching (15 mins, 65°C). The citrate buffer solution was first heated in the microwave to reach the required temperature, and afterwards the sections were introduced into the hot citrate buffer solution for 15 minutes.

The sections were then washed by gentle shake in PBS solution (2 x 5 minutes, RT) and arranged into disposable Shandon sequenza clips (Thermo Scientific, UK). The liver sections were blocked for endogenous avidin and biotin (1:20 for 15 mins each at RT, 120 μL/ slide; Vector Laboratories, UK) with PBS washes (2 x 5 mins) in between. In the case of brain sections, the endogenous avidin and

biotin blocking step was not required and thus skipped. Therefore, the brain sections were directly blocked for non-specific Fc-dependent binding with normal serum for 1 hour at RT (10% serum diluted in PBS; 120 μL/ slide). The normal serum used was matched to the species in which the secondary antibody was raised in. Following serum blocking, sections were incubated overnight (4°C) with primary antibody (120 μL/ slide) against protein of interest (Table 2.1). Both primary and secondary antibodies chosen were diluted in either PBS, or a mixture of PBS added with 0.01% Tween-20 (PBS-T). The addition of detergent Tween-20 allows cell permeabilization which helps antibodies bind to endogenous nuclear antigens.

After overnight incubation with primary antibody, sections were washed with PBS (3 x 5 mins). This step was then followed by a 2-hour incubation with the biotinylated secondary antibody (RT; 120 uL/ slide) and 1-hour avidin-biotin-peroxidase complex solution (1:100 diluted in PBS, RT, 120 uL/ slide; Thermofisher). The avidin-biotin-peroxidase complex solution was prepared at least 30 minutes at RT prior to section incubation. After washing (2 x 5 mins with PBS) and racking the slides into 0.1 M phosphate buffer (PO_4), the sections were then developed in 3,3'-diaminobenzidine tetrahydrochloride (DAB diluted in 0.1 M PO_4; Sigma, UK) activated with hydrogen peroxide. For background counterstaining, the cresyl violet or Harris hematoxylin was used for brain and liver tissue respectively. Steps are as outlined in Table 2.2. After the final step where the sections were cleared in xylene 2, they were mounted with DPX medium and were left to dry at RT overnight. Positive control was included in every batch staining.

Table 2.1 Antibodies used for immunohistochemistry. The primary and secondary antibodies used for antigen detection. Different type of normal serum used for non-specific blocking was chosen depending on the host species of secondary antibody used. Some antibodies require antigen retrieval to optimize antigen-antibody binding. PBS-T is used in case of endogenous nuclear antigen target. Ab, antibody; AG, antigen retrieval; PBS, phosphate buffered saline; PBS-T, PBS added with Tween-20 detergent.

Target; Antibody [Manufacturer]	Dilution factor/ buffer [Antigen retrieval]	Secondary Ab	Normal serum
Microglia; Iba-1 [AbCam, ab178846]	1:1000/ PBS [No]	Goat anti-rabbit	Goat
Macrophages; Iba-1 [AbCam, ab178846]	1:2000/ PBS [No]	Goat anti-rabbit	Goat
Neutrophils; MBS [in-house production[2]]	1:10,000/ PBS-T [Yes]	Goat anti-rabbit	Goat
Tau tangles; AT8 [Invitrogen, MN1020]	1:1000/ PBS [No]	Horse anti-mouse	Horse
Amyloid plaques; Aβ1-42* [AbCam, ab201060]	1:1000/ PBS-T [Yes]	Goat anti-rabbit	Goat
Caspase-3; CASP3* [Bio-Techne R&D Systems, NB100-56113SS]	1:1000/ PBS-T [Yes]	Goat anti-rabbit	Goat

Note: 1% normal serum was used unless otherwise stated.
*5% normal serum added during primary and secondary Ab incubation, to reduce the intensity of unspecific background staining.

[2] Antibody produced and harvested by immunising rabbit with whole rat neutrophils and stimulant Megathura crenulata haemocyanin

Table 2.2 Steps for cresyl violet or Harris haematoxylin counterstaining. Cresyl violet is used to stain the background of brain tissue, whereas Harris haematoxylin is used to colour the liver tissue background. PO_4, phosphate buffer.

Cresyl violet staining	Harris haematoxylin
• 0.1 M PO_4 buffer • Acidified water (5 mins) • Cresyl violet (30 sec) • Distilled water (several gentle washes until the water is clear) • Graded alcohol (80%, 95%, 2x100%) • Xylene 1 and 2 (5 mins each)	• 0.1 M PO_4 buffer • Harris haematoxylin (30 sec) • Tap water (running slowly) • Acidified alcohol (until satisfactory mellow red) • Schott's tap water (until satisfactory grey blue) • Graded alcohol (80%, 95%, 2x100%) • Xylene 1 and 2 (5 mins each)

2.5.3 Cell quantification and histology analysis

Histological analysis was performed with the assessors being blinded to the identity of the sample group and culling timepoints.

2.5.3.1 Brain infarct size, brain atrophy and neuronal cell count

Brain sections stained with cresyl violet were used to measure brain atrophy, infarct size, and neuron cell count. Brain infarct area was defined as the area with reduced staining intensity accompanied by absence or damaged neuronal cells. The brain sections were scanned using Basler Microscopy software (version 1.3; Basler AG, Germany) under 4x magnification, followed by infarct area quantification by using tracing tool in Image J software (version 2.1.0; NIH, US). The same method was adopted for brain atrophy analysis. In addition, hippocampal CA1 neuronal counting was performed manually under light microscope (40x magnification; Leica Biosystem, GE), guided by 10x10 grid eyepiece. The average cell number was expressed as number of cells/ mm^2 area.

2.5.3.2 Brain plaque and tau tangles

Brain sections were stained against Aβ1-42 antibody for amyloid plaque detection, and AT8 antibody for tau tangles analysis. Brain sections were scanned using Basler Microscopy software (version 1.3; Basler AG, Germany) at 10x magnification, followed by the quantification of plaque and tangles using Image J software as per method above (section 2.5.3.1). The site of amyloid and

tau tangles quantification for acute and chronic TBI experiment are as illustrated in Figure 2.8.

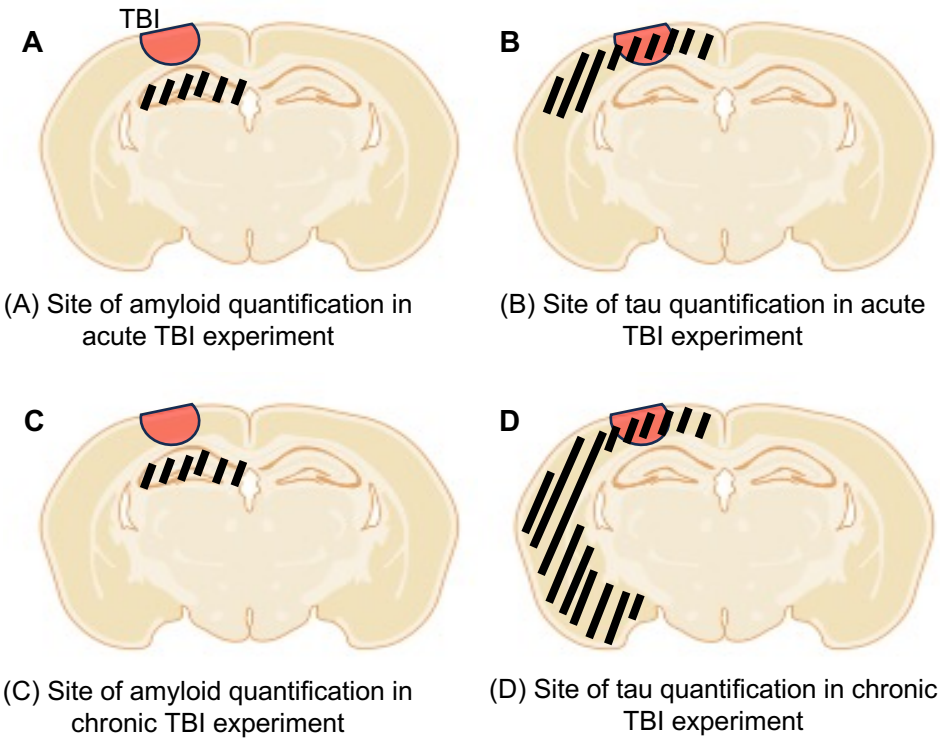


Figure 2.8 Quantification site for brain plaque and tau tangles. Two coronal sections with the largest lesion area between Bregma -2.2mm AP/ML to -2.5mm AP/ML was picked for amyloid and tau tangles analysis. In acute TBI experiment, (A) amyloid quantification was made in the hippocampus region (shaded), whereas (B) tau tangles quantification was made in the cortex area (shaded) around the TBI site (coloured in red). Different sites for amyloid and tau quantification were picked based on the distribution of the pathologies in each mutant respectively. For example, in acute TBI experiment, amyloid pathology was not seen in the cortex area and tau pathology was not observed in the hippocampus area. In chronic TBI experiment, (C) amyloid quantification was made in the hippocampus region (shaded). The distribution of tau tangles was seen more widespread in chronic TBI, therefore quantification was made within a larger area of the cortex (shaded). Illustration was created using Bio-render website and edited in Microsoft PowerPoint. AP, anterior-posterior; ML, medial-lateral.

2.5.3.3 MBS+ and Iba-1+ cells

Hepatic neutrophils and macrophages were counted from six representative fields across two tissue sections, under light microscope at 40x magnification (Leica Biosystem, GE). Two brain sections with the largest infarct area were selected for brain neutrophils and microglia analysis. The brain leukocyte populations were counted in eight representative fields within, and adjacent to, the infarct area (40x magnification; Leica Biosystem, GE) (Figure 2.9). A 10x10 eyepiece grid guide (0.28mm x 0.28 mm) was used, and the average cell number was expressed as number of cells/ mm^2.

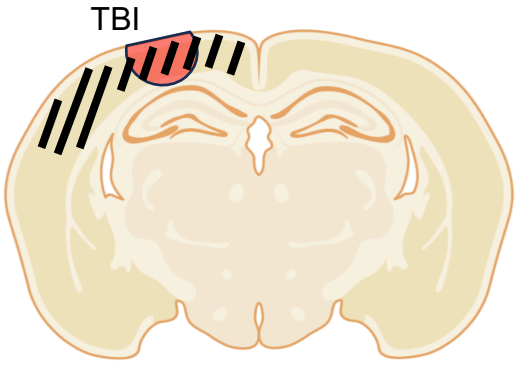


Figure 2.9 Site of brain MBS+ and Iba-1+ cells quantification. Two brain sections between Bregma -2.2mm AP/ML to -2.5mm AP/ML with the largest infarct area were selected for brain neutrophils and microglia analysis. The brain leukocyte populations were counted in eight representative fields within, and adjacent to the infarct area (shaded). Illustration was created using Bio-render website and edited in Microsoft PowerPoint.

2.6 Molecular biology

2.6.1 mRNA extraction and cDNA conversion

Liver extraction (fresh liver, 27-30 mg) was performed using RNeasy and QIAshredder mini kit (Qiagen, UK) following manufacturer's protocol. Brain extraction (fixed brain, 8 coronal sections of 10 μm thick) was achieved by using RecoverAll™ Total Nucleic Acid Isolation Kit for FFPE (ThermoFisher Scientific, UK). The extraction steps followed the protocol supplied on the manufacturer's website, except for the de-paraffinization step. In this thesis, clean PBS (Dulbecco A; pH 7.3 ± 0.2, Oxoid Ltd, UK) was used in place of xylene to isolate the sample from the embedding material, as my samples were embedded in OCT instead of paraffin.

Following tissue extraction, the eluted ribonucleic acid (RNA) concentration and quality were determined using NanoDrop 1000 Spectrophotometer (Thermo Scientific, UK). Absorbance ratio of ~2.0 at 260/280 was considered as 'pure' RNA. The RNA (1000 ng) was converted into complementary deoxyribonucleic acid (cDNA) using High-Capacity cDNA Reverse Transcription Kit (Applied Biosystems, UK) in a temperature-controlled thermocycler (Bio-Rad, UK). Thermocycler setting was set as follows: 10 mins at 25°C, 120 mins at 37°C, and 5 mins at 85°C. The produced cDNA was then stored at -20°C.

2.6.2 RT-qPCR

The gene of interest (GOI) level in the tissue was measured using real-time quantitative polymerase chain reaction (RT-qPCR). The samples were run in duplicate (10 ng/μL cDNA per well) using SYBR green master mix (Primerdesign, UK), on a Roche LightCycler 480 Real-Time PCR System (Roche Diagnostics, UK). Enzyme activation was set as 1 cycle, 2 minutes at 95°C, amplification for 40 cycles, denature for 10 seconds at 95°C and anneal for 1 minute at 60°C. The housekeeping genes ACTB (Primerdesign, UK), GAPDH (Primerdesign, UK), B2M (Bio-Rad, UK), or RPL13A (Sigma, UK) was used to calculate the relative expression of the GOI, which was determined using the 2-ΔΔCt method (Livak & Schmittgen, 2001).

The list of RT-qPCR primer sequence used is detailed in Table 2.3. The information on the components for RT-qPCR reaction can be found in Table 2.4 for Sigma primers, and Table 2.5 for Primerdesign and Bio-rad primers.

Table 2.3 RT-qPCR primers. Primer details used during RT-qPCR analysis to detect the level of GOI. The appropriate housekeeping gene was used to normalise the expression of GOI using the 2-ΔΔCt method. [F], forward primer sequence; GOI, genes of interest; [R], reverse primer sequence.

Gene	Manufacturer	Primer sequence/ details
CXCL-1	Sigma	**[F]** 5'-GCTGGGATTCACCTCAAGAAC-3' **[R]** 5'-TGTGGCTATGACTTCGGTTTG-3'
*CXCL-1*0	Sigma	**[F]** 5'-CATCCCGAGCCAACCTTCC-3' **[R]** 5'-CACTCAGACCCAGCAGGAT-3'
IL-1β	Sigma	**[F]** 5'-CAACCAACAAGTGATATTCTCCAT-3' **[R]** 5'-GGGTGTGCCGTCTTTCATTA-3'
RPL13a	Sigma	**[F]** 5'-AACGACCCCTTCATTGAC-3' **[R]** 5'-TCCACGACATACTCAGCAC-3'
SAA-2	Sigma	**[F]** 5'-TGGCTGGAAAGATGGAGACAA-3' **[R]** 5'-AAAGCTCTCTCTTGCATCACTG-3'
TNF-α	Sigma	**[F]** 5'-AGCCAGGAGGGAGAACAGA-3' **[R]** 5'-CAGTGAGTGAAAGGGACAGAAC-3'
B2M	Bio-Rad	**Unique Assay ID:** qMmuCID0040553
CCL-9	Bio-Rad	**Unique Assay ID:** qMmuCID0021820

Table 2.4 Components for RT-qPCR reaction for Sigma primers.

Component	**Volume (μL)**
SYBR green master mix	5.0
Forward primer (10 μM)	0.5
Reverse primer (10 μM)	0.5
DNase/ RNAse free water	1.5
cDNA	2.5
Total	**10**

Table 2.5 Components for RT-qPCR reaction for Primerdesign and Bio-rad primers.

Component	**Volume (μL)**
SYBR green master mix	5.0
Primer	0.5
DNase/ RNAse free water	2.0
cDNA	2.5
Total	**10**

2.7 Extracellular vesicles

2.7.1 Pellet isolation

Blood from cardiac puncture was centrifuged twice at 1,000 and 14,000 x g speed (10 mins per spin, 4°C; Hettich Mikro200R, Germany) to obtain platelet-free plasma (PFP). The supernatant was collected after the first spin and transferred into a new Eppendorf tube prior to the second spin. The final supernatant was stored at -80°C prior to use. On the day of the extracellular vesicle (EV) pellet isolation, the frozen PFP was thawed on wet ice and 40 μL of the sample was aspirated out to be diluted in 1,200 μL phosphate-buffered saline (PBS; pH 7.4; ThermoFisher). The diluted PFP was spun for 2 hours at 120,000 x g (4°C) using ultracentrifuge machine (Beckman Coulter, US). Without disturbing the EV pellet site, the supernatant was discarded, and pellet was vigorously resuspended in 200 μL PBS, which we referred to as 'EV solution'.

2.7.2 ZetaView nanoparticle tracking analysis

The ZetaView nanoparticle tracking analysis (NTA; Particle Metrix, Germany) machine was used to measure particle size and concentration. The EV solution was further diluted in clean PBS to achieve the ideal concentration of 50-200 particle/ frame in a final solution of 1 mL. The NTA machine uses the Stokes–Einstein equation and Brownian Motion principle to measure particle size. Brownian Motion is defined as the random movement of particles driven by their constant collision with each other in a moving fluid or gas. When 1 mL sample was inserted into the machine, the software captured the behaviour of moving

particles at 11 positions across the sample cell and calculated the mean square displacement. The Stokes-Einstein equation $D = k_B T / c\pi\eta R$ was then applied to calculate the hydrodynamic particle size, whereby D is diffusion coefficient, k_B is Boltzmann constant, T is temperature, η is viscosity and R is particle radius. The particle concentration in the sample was then determined by single particle count relative to the cell volume. The ZetaView software settings for EV measurement were selected following manufacturer's default protocol.

2.8 Statistical analysis and data presentation

Analysis for molecular, histology, and exosomes was performed with two-way ANOVA analysis on GraphPad Prism 9.5.0 software. In the cases where the main effect was significant (set at $p<0.05$ with 95% confidence interval), the post-hoc test Original FDR method of Benjamin and Hochberg set at 0.05 (to investigate the differences between control and experimental group at respective timepoints) was applied. Due to many pairwise comparisons in chapter 3 and 4, where multiple TBI timepoints and/or mutant groups were analysed in one graph, the FDR post-hoc test was preferred over Tukey's post-hoc test.

FDR post-hoc test has advantages when compared to family-wise error rate (FWER), such as Tukey's and Bonferroni test methods in scenarios involving multiple comparisons where there is a large datasets (Pawluk-Kołc, Zieba-Palus, & Parczewski, 2006). FDR post-hoc test has the ability to control the rate of false discoveries, tends to have higher statistical power and less conservative than FWER, therefore allowing a greater number of significant findings, which is beneficial in exploratory analyses (Pawluk-Kołc et al., 2006). Where appropriate,

Tukey's post-hoc test was employed in place of Original FDR method of Benjamin and Hochberg. All quantitative data are presented as mean ± standard error of the mean (SEM) unless otherwise stated. Analysis of adhesive removal tape behavioural test was measured through two-tailed Mann-Whitney test, and data were expressed in median with interquartile range. All data were subjected to Robust Regression and Outlier Removal (ROUT) method set at Q=1%, for outlier identification and removal. Digital illustrations were drawn through Microsoft PowerPoint and Bio-render website.

2.9 Metabolomics

2.9.1 Sample collection

Naïve J20 and WT animals (3 weeks – 50 weeks; total number of mice = 90) were culled through cardiac puncture under general anesthesia followed by collection of blood into 2mL Eppendorf tube. The blood was left to stand upright at RT for 30 minutes, and later subjected to centrifugation at 1,500xg for 10 minutes (19^{o}C) for serum collection. Serum was collected into a fresh Eppendorf tube and stored at -80^{o}C prior to use. The mice were then perfused with heparin saline for fresh tissues collection. Brain, liver, and spleen were snap-frozen onto dry ice and stored at -80^{o}C prior to sample extraction. I am grateful to Prof Daniel Anthony, Caroline Weglinski, Wenzheng Xiong, Dr Daniel Radford-Smith, and Daan Paget for helping with the sample collection from this large number of mice.

2.9.2 Sample extraction for fresh tissues

2.9.2.1 Brain

Brain samples were separated into prefrontal cortex (PFC) and hippocampus (HC) in -20C cryostat. The fresh frozen brain sample was mounted onto cryostat chuck using OCT and sectioned at 25-mm thickness on the cryostat to collect PFC-rich region. After the sectioning reach Bregma 1.70 mm (corpus callosum is apparent), the tissues were cut to waste until HC was observed. The HC block was removed using a pre-cooled scalpel for collection. Both PFC and HC were kept at -80 prior to acetonitrile double extraction. Acetonitrile was made fresh on

the day of extraction, diluted in ddH20 with 1:1 ratio and was kept cold on wet ice.

An amount of 10 μL/ mg acetonitrile was added to the PFC (18-35 mg) and HC samples (40-65 mg), followed by sample homogenisation. The PFC tissues and HC tissue blocks were homogenised using vortex and battery-powered pestle homogeniser respectively. The homogenous samples were then centrifuged at 12,000 x g for 10 minutes (4°C) before the supernatant (PFC, 170μL; HC, 350μL) was aspirated into a new Eppendorf tube. For double extraction, the acetonitrile (10 μL/ mg) was again added to the samples and pipette tip was used to disrupt the pellet at the bottom of the Eppendorf tube formed during the first extraction. This step was then followed by a period on the vortex so as to homogenise the samples thoroughly. The homogenised samples were then centrifuged as previously mentioned, followed by collection of the supernatant, yielding a total volume of 340μL for PFC and 700μL for HC respectively. The supernatant was lyophilised and stored at -80°C until the day of NMR analysis.

2.9.2.2 Liver and spleen

Liver (100-125 mg) and spleen (20-40 mg) samples were ground to fine powder using pestle and mortar on dry ice, before acetonitrile (8 μL/ mg) was added to the samples. Liver samples were vortexed and centrifuged at 12,000 x g for 10 minutes at 4°C. An amount of 750 μL liver supernatant was aspirated into a fresh Eppendorf tube and was kept upright on the dry ice. Spleen samples were homogenised using a battery-powered pestle homogeniser and centrifuged as

per liver's protocol. The grinding and homogenising process for spleen samples were performed by Caroline Weglinski. An amount of 200 μL spleen supernatant was collected into a new tube. Double extraction was performed for spleen samples thus yielding a total of 400 μL supernatant per sample. Liver and spleen supernatant was lyophilised and stored at -80°C until the day of NMR analysis.

2.9.3 Sample preparation and spectral acquisition

2.9.3.1 Serum

The frozen mice serum samples were thawed at room temperature, and 550 μL of ice-cold NMR buffer (75 mM phosphate buffer diluted in D20, pH 7.4) was added to 100 μL of serum. The solution was mixed thoroughly by gentle pipetting, and brief vortexing. The samples were then transferred to 5mm Borosilicate NMR glass tubes using glass pipette dropper. Spectral acquisition was performed by our collaborator in Numares AG, Regensburg, Germany using a 600-MHz Bruker AVIII 1H NMR spectrometer. The spin-echo Carr-Purcell-Meiboom-Gill (CPMG) spectra was acquired for metabolomic analysis. The CPMG spectra suppresses large molecular weight compounds for better metabolite visualisation.

2.9.3.2 Brain, liver, and spleen

On the day of NMR experiment, 600 μL NMR buffer was added to the frozen powdered lyophilants. The solution was pipetted up and down to ensure thorough mixing followed by centrifugation at 4000 x g for 5 mins (4^{o}C) to remove debris. Samples were transferred into glass NMR tube using glass pipette. Where applicable, air bubbles within the solution were removed by gentle flicking of the

NMR glass tube. The samples were kept chilled in the 4°C fridge prior to NMR run. Painless NMR spectra were acquired at 298K using a 700-MHz Bruker AVIII NMR Spectrometer (Department of Chemistry, University of Oxford) operating at 16.4 T equipped with a 1H TCI cryoprobe.

2.9.4 Spectra processing and multivariate analysis

All spectra were processed in TopSpin 3.6.1 software (Bruker, Germany), in which the spectra were visually inspected for spectral distortion and contamination, followed by manual phasing and baseline correction. The chemical shifts were referenced to the lactate doublet resonance centred at chemical shift 1.33 ppm. The spectra were later multiplied by an exponential function corresponding to a 0.3 Hz line broadening, and zero filled by a factor of 2. The processed spectra were exported to ACD/Labs Spectrus Processor Academic Edition 12.01 (Advanced Chemistry Development, Inc., Toronto, Canada) where the spectra were divided into small bins consisting of 0.02 ppm fixed-width segments. Water signal (4.20 – 5.20 ppm) and noise regions were marked as dark regions and removed from analysis. Sum-normalised bucket integrals were imported into RStudio 4.0.3 software (Vienna, Austria) for orthogonal partial-least square discriminant analysis (OPLS-DA).

2.9.4.1 Orthogonal partial-least square discriminant analysis

OPLS-DA is a supervised multivariate analysis that can generate separation of metabolic profiles between two groups. To generate OPLS-DA model, the metabolomics data was first corrected for unequal class sized, followed by

random assignation of data into ten partitions, whereby nine partitions were classified into training set (90%) and one partition was used as the test set (10%). The training set was used to build the OPLS-DA models that can learn the underlying discriminatory patterns between the classes under consideration using 7-fold internal cross validation procedure. To build the predictive ability of the models, the training set was cross-validated with the independent test set using a 10-fold external cross-validation procedure with 100 iterations, creating an ensemble of 1,000 models. This validation scheme ensures that any discrimination of experimental groups generated in the model is a true separation and does not occur by chance, and therefore also generates the accuracy, sensitivity, and specificity of the models.

2.9.4.2 Statistical analysis and metabolite assignment

The graph of variable importance in projection (VIP) scores generated by the RStudio was examined for the inflection point that signify the cut-off point for the discriminatory metabolites that were important in driving the group separation. Selected VIP bins were then analysed with two-way analysis of variance (ANOVA) analysis on GraphPad Prism 9.5.0 software. Results were considered significant at $p<0.05$ with 95% confidence intervals. Tukey's post-hoc test was employed where appropriate and quantitative data was expressed as mean ± standard deviation (SD). Metabolites were assigned by referring to the 2D total correlation spectroscopy TOCSY, literature papers and HMDB platform.

CHAPTER 3

ACUTE TBI

Chapter 3 : The effect of acute TBI on J20 and P301S mutants

3.1 Introduction

AD is characterised by the presence of amyloid plaques and tau tangles in the brain, accompanied by an irreversible deterioration of cognitive abilities and reduction in brain size over time (De Strooper & Karran, 2016). In the late stage of AD, patients experience a loss of motor functions, which causes difficulty walking, an inability to regulate bowel movements, and failure of the respiratory system, eventually resulting in death (Della Sala et al., 2004). AD can be classified into three broad stages: pre-clinical, MCI/ prodromal, and AD dementia (mild, moderate, and severe AD). Differences in the rate of AD progression have been noted across patients, with a subgroup progressing faster than others, as measured by accelerated cognitive decline (Thalhauser & Komarova, 2012) and a higher whole-brain atrophy rate (Sluimer et al., 2008). The variation in the speed of disease course has made finding a cure for AD difficult.

There has been extensive research into understanding AD pathobiology since its discovery in 1906, with the intent to find a cure to this debilitating disease. Recent discovery of disease-modifying drugs, such as Aducanumab and Lecanemab, are at the cornerstone of the field's achievement (Behl et al., 2022; McDade et al., 2022; Rahman et al., 2023). However, the usage of these drugs is still in its infancy, and they are associated with serious adverse effects such as cerebral oedema and microhaemorrhage (Ramanan & Day, 2023). The well-established AD treatments are AChEI and NMDA blockers that increase ACh and reduce

glutamate, respectively. These pharmacotherapies are not disease-modifying therapies, as they only provide temporary symptomatic relief for the patients (Husna Ibrahim et al., 2020). All these drugs focus on targeting the brain; therefore, it is impertinent to broaden our target location to enable more choices that can reduce or halt AD progression aside from the brain.

Previous findings have drawn associations between the brain and peripheral organs, particularly the liver, which serves as the main APR organ (Campbell et al., 2008; Dickens et al., 2017; Sá-Pereira et al., 2018). The severity of brain inflammation was shown to be reflected in the degree of liver inflammation, and the suppression of liver inflammation has yielded neuroprotective effects (Anthony, Walker, & Perry, 2005; Campbell et al., 2010; Villapol et al., 2015). EVs in the blood are one potential mediator for brain-liver interplay (Hazelton et al., 2018). Exosomes, in particular, displayed the ability to pass the BBB due to their small size and may play a critical role in information exchange between organs (Budnik, Ruiz-Cañada, & Wendler, 2016; Kang, Zuo, Hong, Tang, & Geng, 2019).

Gilbert and colleagues noticed that AD patients with a history of TBI (AD-TBI) experience faster disease progression, as evidenced by hastened cognitive decline compared to AD patients without a history of TBI (Gilbert et al., 2014). Nonetheless, the mechanism underlying this phenomenon is not fully elucidated. Shishido group observed that TBI-associated cognitive and histopathological changes were only pronounced in triple-transgenic AD mouse model but were not significant in wild-type animals (Shishido et al., 2019). This finding pointed

towards the possible interaction between AD pathology and TBI, resulting in the accelerated disease outcome observed. However, it is not clear as to which of the two key AD pathologies – amyloid plaques or tau tangles – influences the observed outcome. Therefore, to gain an understanding of this phenomenon, I investigated the histological and molecular changes in the AD-TBI group in comparison to AD or TBI only controls.

I hypothesized that the underlying pathobiology is associated with the two-hit theory, wherein the systemic APR orchestrated by the liver is excessively triggered in the AD-TBI group, leading to a massive recruitment of peripheral immune cells into the injured AD brain. The infiltration of these immune cells may result in the secretion of inflammatory mediators that can further exacerbate the primary damage caused by the TBI. I predicted that the increase in brain inflammation would be accompanied by an increase in neuronal death, which may underlie the decline in cognitive ability seen in AD patients. Furthermore, I assessed the EV and exosome quantification of these control and experimental groups to observe if there are any changes to their profile following TBI, which may signify their contribution as the mediators in the brain-periphery cross-talk during neurotrauma. The findings from this chapter may provide insight into whether the presence of AD pathology in the brain can contribute to the higher systemic APR response and hence the accelerated AD progression, as well as providing a basis for whether the liver is a suitable target for AD pharmacotherapies for future studies. This approach may involve targeting liver molecules that may be upregulated only during AD-TBI double hits and are either not present or not enhanced in AD or TBI only controls.

3.1.1 Chapter aims

The aims of this chapter are as follows:

1- To investigate whether the presence of amyloid pathology in the brain can affect the level of systemic APR after TBI.

2- To ascertain whether the degree of plaque burden in the brain results in different liver APR outcomes, as measured through molecular RT-qPCR and immunohistochemistry assessments.

3- To determine whether EV acts as the mediator in the brain-periphery interplay during TBI by inspecting EV and exosome profiles.

4- To explore whether the presence of tauopathy in the brain yields similar systemic APR, as seen in J20 cohort after TBI, by using P301S mutants.

3.1.2 Experimental design

In the first part of this chapter, the J20 mouse model is used to investigate the effect of acute TBI when subjected to amyloid pathology. Transgenic J20 mice aged 12 and 6 months, along with their corresponding age-matched WT controls, were used to explore the outcome of TBI exposure with differing amyloid burdens in the J20 mutant. In the second part of this chapter, the P301S mouse model (2 months old) was used to study the effect of acute TBI when subjected to tauopathy. Brain, liver, and blood samples were collected to examine histopathological, molecular and exosome profile changes after TBI. The experimental design for this chapter is illustrated in Figure 3.1.

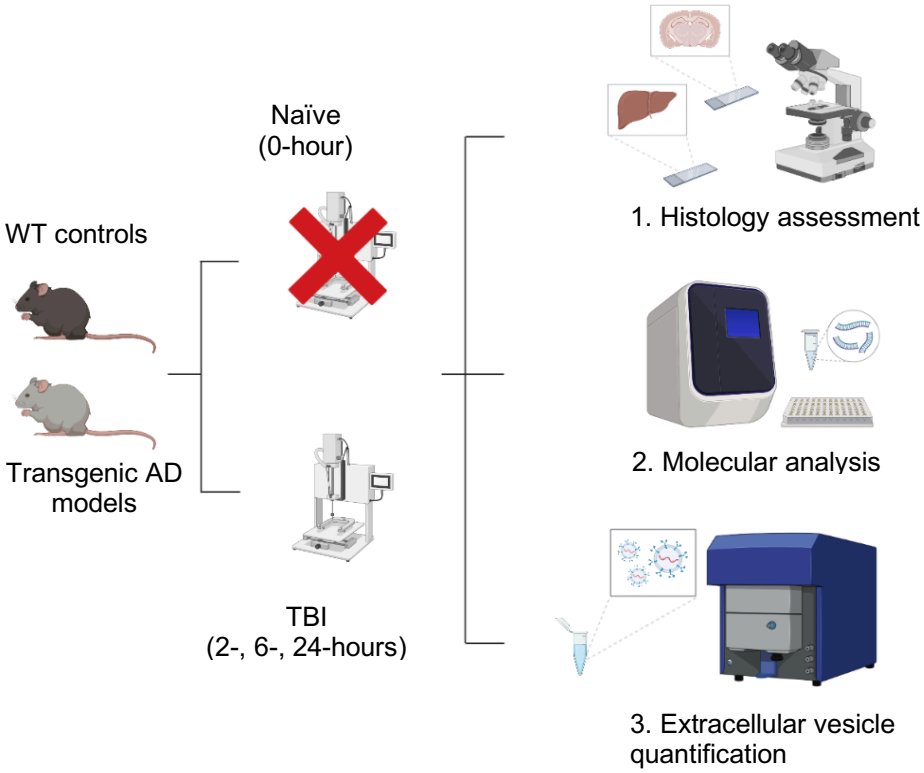


Figure 3.1 Experimental design for acute TBI study. Transgenic AD models and their corresponding WT controls were classified into naïve and TBI experimental groups. The mice in TBI groups received a single contusion and were divided into several groups which were culled at 2-, 4- and 24-hours timepoints post-contusion respectively. The brain, liver, and plasma samples were subsequently collected for histology, molecular and EV assessments. The illustration was created using Bio-render website.

3.2 Results

3.2.1 J20 mice exhibit sensorimotor deficit following TBI

To validate if there is a functional outcome difference in this J20 mutants as compared to controls due to the presence of amyloid pathology in the brain, I investigated the functional deficit after TBI through adhesive removal test. This behavioural test was performed prior to histology, molecular and EV assessment.

Briefly, adhesive tape strips were placed on the mice forepaws, and animal performance was assessed by measuring the time needed to sense (contact time) and to remove the tape strips (removal time). It was hypothesized that the J20 group will require longer time to sense and remove the tape strips, which reflects longer recovering time from brain injury. I also hypothesized that the J20 group may develop sensorimotor deficit following the contusion due to the pathogenic effect of amyloid plaque, which may not be observed in the WT group. Mice (n=9/ group, 12 months old) were introduced to training period for 5 days before brain contusion, with 1 trial per day. Following TBI, mice were allowed to rest, and the actual test was performed at 24 hours, 48 hours, 4 days, and 7 days post-injury (Figure 3.2A; study design).

No difference in contact time was noted between WT (8.23 sec, IQR=7.53) and J20 group (11.65 sec, IQR=49.99) at 24 hours (Figure 3.2B; Mann-Whitney test). However, at 48 hours, J20 mice (16.62 sec, IQR=32.75) required significantly longer time to sense the presence of the adhesive tape as compared to WT mice (8.23 sec, IQR=11.09), suggesting sensory deficit (Figure 3.2C; Mann-Whitney

test, $p<0.05$). At 4 days (Figure 3.2D; WT 10.6 sec, IQR=6.52; J20 21.89 sec, IQR=15.61) and 7 days (Figure 3.2E; WT 8.09 sec, IQR=9.19; J20 19.81 sec, IQR=19.73) time points, the differences in contact time between the groups were not statistically significant.

The time taken to remove adhesive tape reflects the motor function of the mice (Figure 3.2, F-M). The first and second removal time refers to the adhesive tapes taken off from the first and second forepaws respectively. In the first removal cohort, there is negligible difference between J20 (14.49 sec, IQR=54.79) and WT (10.77 sec, IQR=9.13) at 24 hours timepoint (Figure 3.2F; Mann-Whitney test). At 48 hours and 4 days post-TBI, the J20 mice took two times longer to remove the first strip as compared to WT, with statistical significance of $p<0.01$ for both timepoints. At 48 hours timepoint, the time taken for J20 was 36.49 sec, IQR=99.57 as compared to WT with 16.41 sec, IQR=12.10 (Figure 3.2G; Mann-Whitney test, $p<0.01$). At 4 days timepoint, J20 mice spent 24.77 sec, IQR=44.96 to remove the strip as opposed to WT with 12.33 sec, IQR=5.60 (Figure 3.2H; Mann-Whitney test, $p<0.01$).

The overall pattern in the WT group showed a downward trend from 16.41 sec, IQR=12.10 at 48 hours, 12.33 sec, IQR=5.60 at 4 days and later 11.93 sec, IQR=17.01 at 7 days post-TBI (Figure 3.2I). However, in the case of J20, although there is a downward trend from 48 hours (36.49 sec, IQR=99.57) to 4 days post-TBI timepoint (24.77 sec, IQR=44.96), it becomes plateau afterwards with 25.74 sec, IQR=9.46 at 7 days post-TBI (Figure 3.2I). This may imply a faster motor recovery in WT animals, which was not the case for J20 mice.

In the second removal time, no statistical difference between groups was observed at 24 hours (Figure 3.2J; WT 47.48 sec, IQR=90.41; J20 120 sec, IQR=80.72) and 48 hours (Figure 3.2K; WT 82.63 sec, IQR=93.19; J20 120 sec, IQR=64.99). At 4 days post-TBI, J20 (120 sec, IQR=86.89) required four times longer than WT (28.73 sec, IQR=17.93) to remove the adhesive strip (Figure 3.2L; Mann-Whitney test, $p<0.05$). At 7 days post-TBI, the statistical difference between groups remained at $p<0.05$ with J20 requiring 47.54 sec, IQR=89.00 to remove the second strip as compared to WT at 28.67 sec, IQR=46.92 (Figure 3.2M; Mann-Whitney test). The overall observation infers sensorimotor deficits in J20 mice post-TBI that persist up to 7 days.

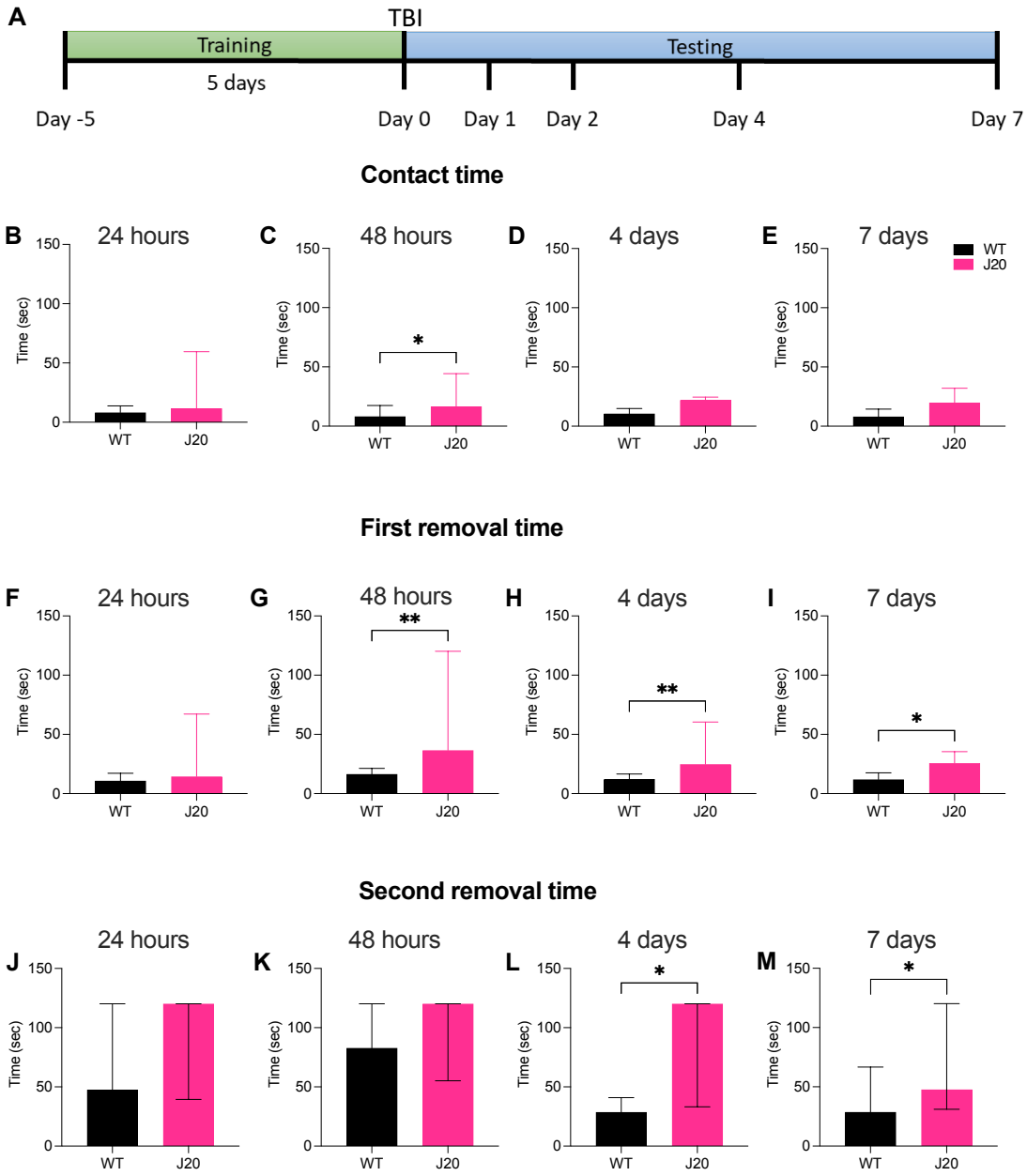


Figure 3.2 Adhesive tape removal behavioural assessment in 12 months old J20/ WT mice cohort. Littermate WT C67BL/6 controls were used in this experiment. (A) The experimental design for adhesive tape removal test that explore the sensorimotor deficit following brain injury. Twelve-month-old WT and J20 mice were subjected to 5 days training period pre-TBI, and they were tested at 24 hours, 48 hours, 4 days, and 7 days post-injury. (B-E) The time taken for mice to sense and contact the adhesive tape on their forepaws. Increased contact time was noted in the J20 mice at 48-hour timepoint signifying sensory deficit, with $p<0.05$ significance level. (F-I) The time taken to remove the adhesive tape from the first forepaw. J20 mice required noticeably longer time to remove the tape from the first paw as compared to WT mice, which signifies motor deficit following TBI. (J-M) The time taken to remove the adhesive tape from the second forepaw. Data are presented as median with interquartile range (IQR). Mann-Whitney test; *$p\leq0.05$, **$p<0.01$. The timeline diagram was created using Microsoft PowerPoint.

Number of mice per group; n=9 (WT), n=9 (J20).

3.2.2 Increased CASP3+ apoptotic neurons in J20 mice at 24 hours post-TBI

To investigate if the functional deficit displayed by J20 post-TBI was related to the acute phase reaction that occurs within 24 hours post-injury, the histopathological and molecular changes in the brain and liver were examined. Samples were collected from mice (12 months old) at 0-, 2-, 6- and 24-hour post-TBI.

To explore if the TBI causes alteration to the brain Aβ42 burden, fixed brain sections are immuno-stained against Aβ42 and quantification were made in the hippocampus which is the primary memory hub. In J20 mice cohort, amyloid plaque quantification was not done in the cortex region as no deposition was seen in other areas aside from hippocampus (figure not shown). Similarly, no plaque burden was noted in the cortex area of WT naïve and WT TBI mice (figure not shown).

No plaque was observed in the hippocampus of WT mice at any point before and after TBI (Figure 3.3A(i), Figure 3.3B(i), Figure 3.3D). Two-way ANOVA was performed, and result showed interaction $p=0.1589$, TBI $p=0.1589$, genotype $p=0.0004$ (Figure 3.3D). At 0-hour, the J20 mice was presented with Aβ42 burden of 0.22% $\pm$ 0.11 (Figure 3.3A-ii). At 2-hour post-injury, the Aβ42 burden was shown increased to 1.63% $\pm$ 0.40 (Figure 3.3B-ii) with statistical significance of $p<0.05$ when compared against 0-hour J20 group (Figure 3.3D; two-way ANOVA, FDR post-hoc test). After the 2-hour timepoint, the Aβ42 graph showed a

downward trend with 0.68% ± 0.50 at 6-hour and 0.75% ± 0.47 at 24-hour post-TBI although it is not statistically significant (Figure 3.3D).

To evaluate the extent of brain damage following TBI, cortical infarct size and apoptotic CA1 neurons was measured. Brain sections were stained with cresyl violet for assessment. Example pictures for naïve brain section and TBI brain section were exhibited in Figure 3.3C(i) and Figure 3.3C(ii) respectively. In figure 3.3C(ii), dotted line shows the brain infarct area, represented by reduced cresyl violet staining. For brain infarct size, two-way ANOVA revealed interaction p=0.0162, TBI p=0.1286, and genotype p=0.0542 (Figure 3.3E). No difference was distinguished between WT (3.27 mm^2 ± 0.28) as compared to J20 (2.58 mm^2 ± 0.25) at 2-hour timepoint. Interestingly, the infarct size was shown increased in the WT (4.01 mm^2 ± 0.24) as opposed to J20 (2.92 mm^2 ± 0.11) at 6-hour with significance value of $p<0.05$ (Figure 3.3E; two-way ANOVA). However, this difference became negligible at 24-hour, with 3.02 mm^2 ± 0.39 for WT and 3.50 mm^2 ± 0.01 for J20 respectively.

Neurons in the hippocampal CA1 region were stained for apoptotic neuronal marker caspase-3 (CASP3), as CASPS3 is responsible for most proteolytic process during cell death. The CASP3 positive (CASP+) neurons were only counted at 24 hours post-TBI, as the neuronal apoptotic neurons are most apparent between 24 hours to 48 hours after CCI-implicated contusion (Akamatsu and Hanafy, 2020). Two-way ANOVA analysis for CASP3+ neurons revealed interaction p=0.1706, TBI p=0.0057, genotype p=0.0609 (Figure 3.3F).

There was no CASP3+ neurons detected in WT and J20 group at 0-hour. Nonetheless, a stark increase of CASP3+ number in the J20 mice was observed at 24-hour timepoint, with 66.23 ± 16.92 against 15.08 ± 11.82 in WT, which was a 4-fold difference in comparison (Figure 3.3F; two-way ANOVA; $p<0.05$).

Collective findings from brain histopathological assessment following acute TBI in 12 months old mice showed an excessive neuronal death in the J20 hippocampus at 24-hours timepoint when compared against its WT control. However, significant difference between groups was not found in the Aβ42 burden and cortical infarct size parameters at the same timepoint.

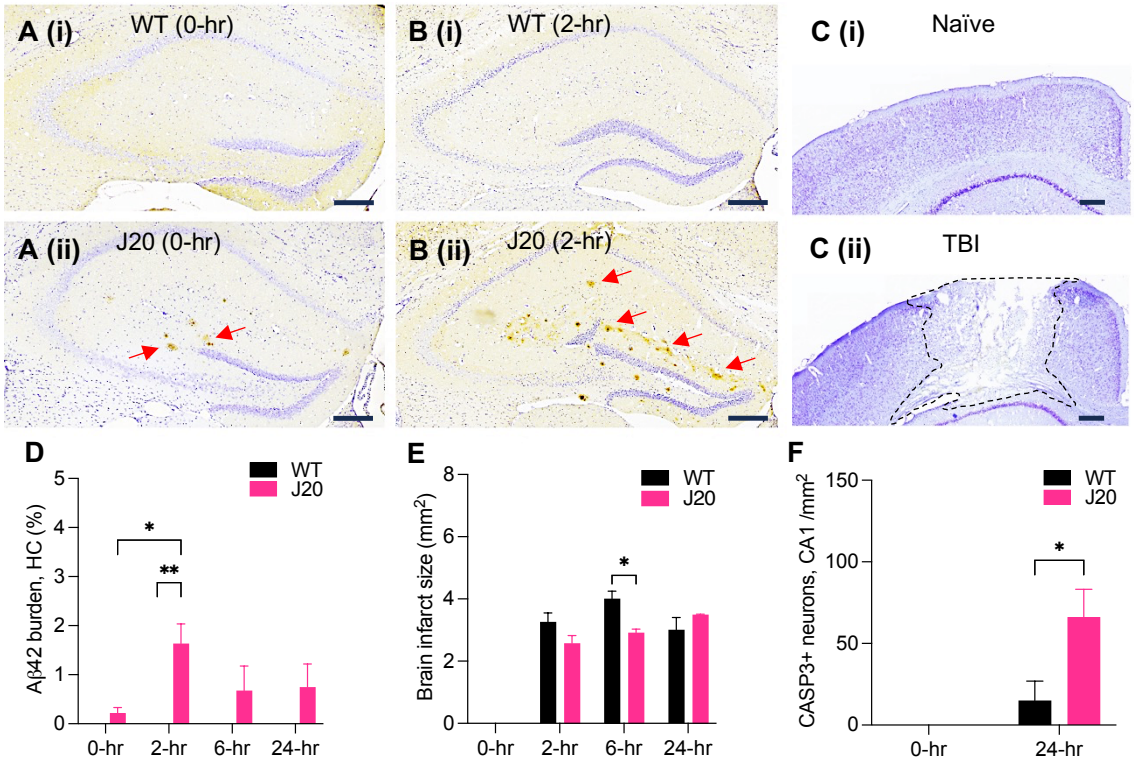


Figure 3.3 Brain histopathological assessment following acute TBI in 12 months old J20/ WT mice cohort. (A-B) Brain sections stained for Aβ1-42 immunostaining for amyloid detection showed clumps of proteins in the hippocampus region in J20 mice. (C) Brain section stained with cresyl violet to investigate the extent of brain infarct post-TBI. (C-i) Naïve brain section. (C-ii) TBI brain section. Dotted line shows the brain infarct area, represented by reduced cresyl violet staining. (D) Aβ42 burden in J20 hippocampus was shown elevated at 2-hr timepoint as compared to 0-hr timepoint with $p<0.05$ significance. (E) Quantification of brain infarct size. (F) Quantification of apoptotic neuronal cells in the CA1 hippocampal region through CASP3 staining were performed using t-test analysis. Data are presented as mean ± SEM. Scale bar = 200 μm; 4x magnification. Aside from figure 3.3F, all analyses were performed with two-way ANOVA with FDR post-hoc set at 0.05; *p≤0.05, **p<0.01. Identified outliers using ROUT method set at Q=1% were removed.

Number of mice per group for Aβ42 burden; WT 0-hour (n=6), J20 0-hour (n=4), WT 2-hour (n=4), J20 2-hour (n=3), WT 6-hour (n=5), J20 6-hour (n=5), WT 24-hour (n=5), J20 24-hour (n=5).

Number of mice per group for brain infarct size; WT 0-hour (n=6), J20 0-hour (n=4), WT 2-hour (n=5), J20 2-hour (n=4), WT 6-hour (n=5), J20 6-hour (n=5), WT 24-hour (n=5), J20 24-hour (n=4).

Number of mice per group for CASP3+ neurons; WT 0-hour (n=3), J20 0-hour (n=3), WT 2-hour (n=3), J20 2-hour (n=3), WT 6-hour (n=4), J20 6-hour (n=3), WT 24-hour (n=3), J20 24-hour (n=3).

3.2.3 No difference in brain neutrophils and microglia

To investigate if there are differences in brain inflammatory level in TBI-AD vs TBI-WT group, neutrophil and microglia number was counted. Figure 3.4A(i-ii) and Figure 3.4B(i-ii) showed representative brain sections stained for neutrophil and microglia correspondently. No neutrophil was noted in naïve brain section (Figure 3.4A-i), whereas brown staining indicating neutrophils were seen in blood vessels and brain parenchyma after TBI (Figure 3.4A-ii). Low number of microglia in resting state was observed in naïve brain section (Figure 3.4B-i), whereas an increased microglia number in activated state was noted in the brain section after TBI (Figure 3.4B-ii).

There are no neutrophils in the brain at 0-hour in both J20 and WT groups. Following acute brain injury, the neutrophils count irrespective of WT or J20 groups showed a marked increase, with $p<0.001$ significance level for TBI main effect as analysed with two-way ANOVA. However, interaction ($p=0.7726$) and genotype ($p=0.4336$) results were shown not significant (Figure 3.4C; two-way ANOVA). At 2-hour timepoint, the number of neutrophils raised to 108.60 ± 23.24 in WT and 134.0 ± 49.15 in J20. At 6-hour timepoint, the neutrophil counts were 132.83 ± 20.71 and 126.0 ± 31.37 for WT and J20 respectively. At 24-hour timepoint, the neutrophil number in WT went down to 95.80 ± 26.69 whereas the J20 went up to 141.40 ± 37.73. When assessed with Original FDR method of Benjamini and Hochberg post-hoc test set at 0.05, none of the timepoints showed significance between groups.

The microglia count was analysed using two-way ANOVA, and the result revealed interaction p=0.8493, TBI p<0.0001, genotype p=0.7533 (Figure 3.3D). At 0-hour timepoint, microglia count showed 156.60 ± 16.89 for WT and 185.25 ± 19.62 for J20. After 2 hours post-injury, the number was elevated to 258.60 ± 28.29 and 245.0 ± 44.51 for WT and J20 respectively. The numbers continued to show an upward trend at 6-hour timepoint with 302.0 ± 20.39 for WT and 306.0 ± 20.40 for J20 group. At 24-hour timepoint, both groups showed a downward trend with the numbers reduced to 270.40 ± 7.43 for WT and 272.20 ± 25.26 for J20 respectively. The Original FDR method of Benjamini and Hochberg post-hoc test revealed no statistical significance between groups at all timepoint.

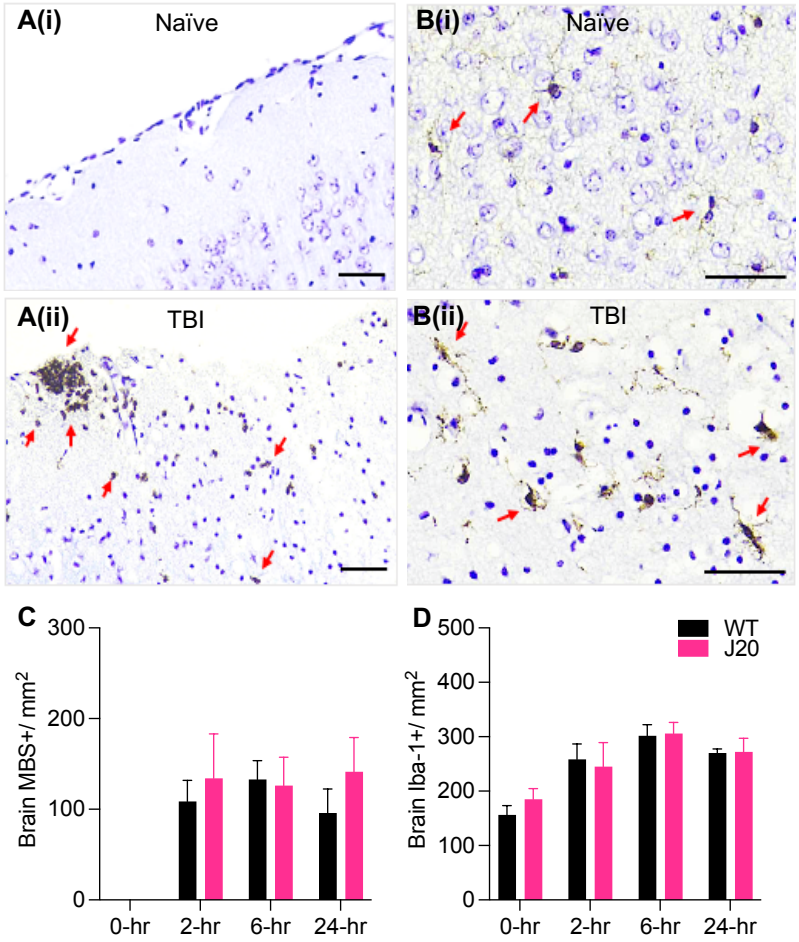


Figure 3.4 Brain neutrophils and microglia counts after acute TBI in 12 months old J20/ WT mice cohort. Fixed brain slices were immuno-stained with antibody against (A) MBS for neutrophils and (B) Iba-1 for microglia respectively. Number of positive cells were quantified from four representative fields across two tissue sections at 40x magnification. Bar graphs represent brain (C) MBS+ and (D) Iba-1+ stained cells. Scale bar = 50µm; 20x magnification. Results are analysed through two-way ANOVA and expressed as mean ± SEM. Original FDR method of Benjamini and Hochberg post-hoc test set at 0.05 was used. Identified outliers using ROUT method set at Q=1% were removed. Iba-1, anti-macrophage ionized calcium binding adaptor molecule; MBS, anti-neutrophils.

Number of mice per group for brain MBS+; WT 0-hour (n=4), J20 0-hour (n=4), WT 2-hour (n=5), J20 2-hour (n=4), WT 6-hour (n=6), J20 6-hour (n=4), WT 24-hour (n=5), J20 24-hour (n=5).

Number of mice per group for Iba-1+; WT 0-hour (n=5), J20 0-hour (n=4), WT 2-hour (n=5), J20 2-hour (n=3), WT 6-hour (n=6), J20 6-hour (n=4), WT 24-hour (n=5), J20 24-hour (n=5).

3.2.4 Plaque deposition increases systemic APR through increased liver *CCL-9*, *SAA-2*, and *CXCL-10* molecules post-TBI

To explore if brain injury in the presence of amyloid plaque in the brain gives a different systemic APR profile, the relative expression of molecule panels commonly affected during APR in the liver was measured.

Two-way ANOVA analysis of chemokine *CCL-9* expression revealed interaction p=0.2326, TBI p<0.001, genotype p=0.0609 (Figure 3.5A). The expression of chemokine *CCL-9* was shown not significant between groups at 0-hour to 6-hour timepoints. However, at 24-hour timepoint, a marked increase was shown in J20 group as compared to WT. The relative expression in J20 group is 1.5-fold higher than that of WT, with 1.74 ± 0.18 and 1.18 ± 0.16 respectively (Figure 3.5A; two-way ANOVA, original FDR method of Benjamini and Hochberg post-hoc test; p<0.05).

Figure 3.5B illustrates serum amyloid A 2 (*SAA-2)* molecule that elevates slowly throughout time. Two-way ANOVA analysis revealed interaction: p=0.0002, TBI p<0.0001, genotype p=0.0067 (Figure 3.5B). At 2 hours post-TBI, the relative expression of *SAA-2* in WT was 2.56 ± 0.84 as opposed to 0.59 ± 0.15 for J20. At 6-hour timepoint, the expression level increased to 30.99 ± 15.86 and 27.23 ± 10.67 for WT and J20 respectively. The *SAA-2* expression level in J20 at 24-hour timepoint (271.22 ± 63.12) showed a 10-fold stark increase as compared to its level at 6-hour timepoint (27.23 ± 10.67), whereas only 2-fold increase was reported for WT group at 24-hour timepoint (63.42 ± 28.15) as compared to its 6-

hour timepoint (30.99 ± 15.86). The original FDR method of Benjamini and Hochberg post-hoc test analysis between WT and J20 group at 24-hour timepoint revealed statistical significance of $p<0.0001$.

The relative expression level of chemokine *C-X-C motif ligand 1* (*CXCL-1*; Figure 3.5C) and *ligand 10* (*CXCL-10*; Figure 3.5D) was measured. Two-way ANOVA analysis for *CXCL-1* expression revealed interaction $p=0.0756$, TBI $p<0.0001$, genotype $p=0.3998$ (Figure 3.5C). The expression of *CXCL-1* was low in both WT and J20 at 0-hour timepoint. Interestingly, marked increase in *CXCL-1* expression was seen in WT at 2-hour post-injury, with a reading of 18.33 ± 2.73. The WT reading showed a 2-fold difference when compared against J20 of 7.81 ± 2.50 expression level at 2-hr timepoint, with a significance value of $p<0.05$ (Figure 3.5C; two-way ANOVA, original FDR method of Benjamini and Hochberg post-hoc test). However, as the time progressed, the difference between groups was negligible at 6-hour timepoint (WT; 11.38 ± 2.73, vs J20; 14.41 ± 3.03). At 24-hour, the readings were near baseline with 2.56 ± 0.61 and 2.22 ± 0.69 for WT and J20 respectively.

In addition, two-way ANOVA analysis for *CXCL-10* expression revealed interaction $p<0.05$, TBI $p=0.4633$, genotype $p=0.5712$ (Figure 3.5D). There was no difference in *CXCL-10* relative expression at 0-hour and 2-hour between groups. At 6-hour timepoint, the difference between WT (0.82 ± 0.20) and J20 (1.89 ± 0.56) was evident with the significance level of $p<0.05$ (Figure 3.5D; two-way ANOVA, original FDR method of Benjamini and Hochberg post-hoc test).

Both groups then showed downwards trend towards 24-hour, and no difference between groups was noted.

Two-way ANOVA analysis for *IL-1β* expression revealed interaction p=0.3072, TBI p=0.8232, genotype p=0.5894 (Figure 3.5E), whereas *TNF-α* showed interaction: p=0.2656, TBI p=0.5615, genotype p=0.6910 (Figure 3.5F). As the two-way ANOVA did not reveal significance, the original FDR method of Benjamini and Hochberg post-hoc test was not applied onto these inflammatory molecules *IL-1β* and *TNF-α.* Altogether, the RT-qPCR findings showed an excessive expression of *CCL-9*, *SAA-2*, and *CXCL-1*0 in J20 when compared to WT following acute TBI.

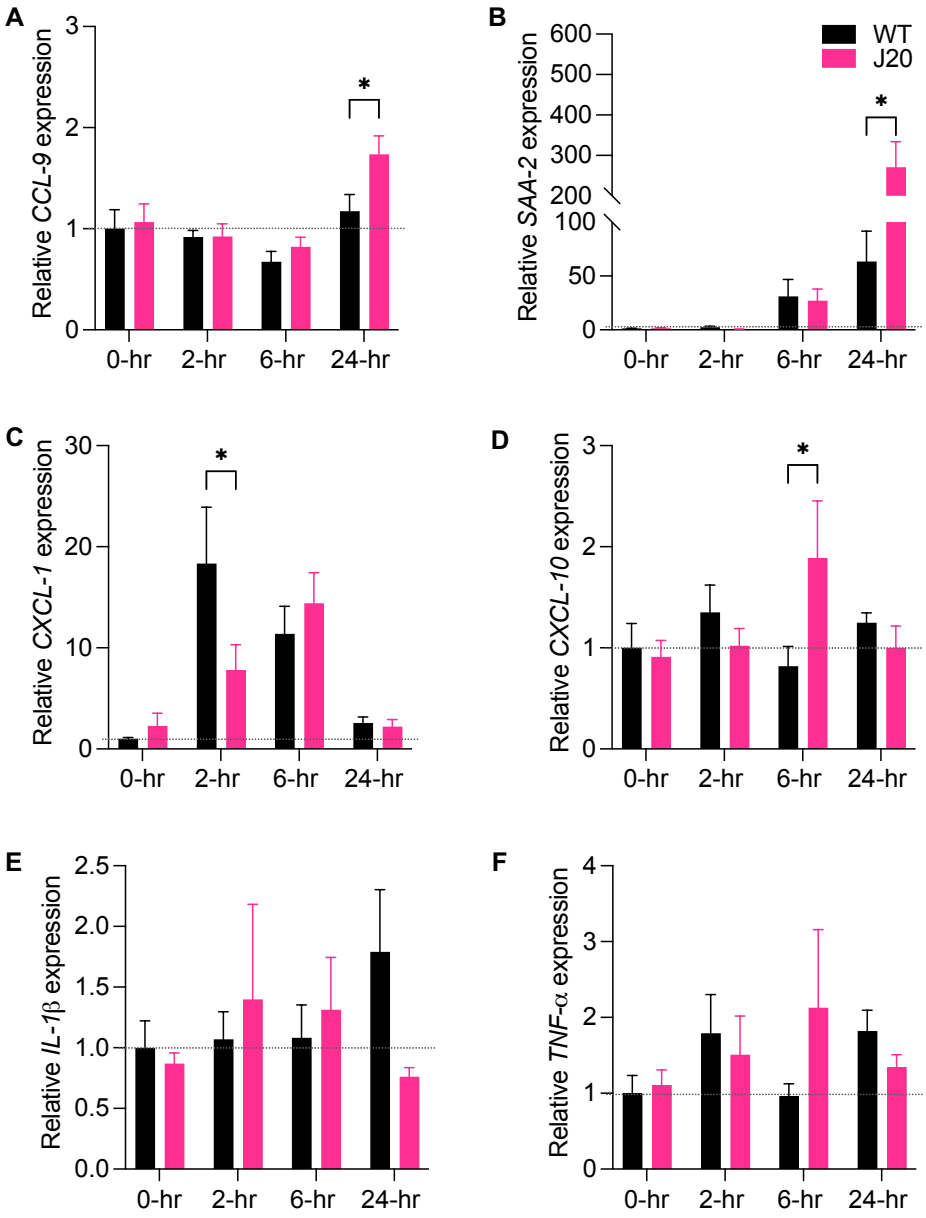


Figure 3.5 Liver molecular expression as measured through RT-qPCR in 12 months old J20/ WT mice cohort. cDNA from fresh liver samples were analysed by RT-qPCR for chemo-attractants and inflammatory cytokines. Hepatic (A) *CCL-9*, (B) *SAA-2*, (C) *CXCL-1*, (D) *CXCL-10*, (E) *IL-1β*, and (F) *TNF-a* expression level was normalised against reference gene *ACTB*. Molecule *CCL-9* and *SAA-2* showed marked increase at 24-hours timepoint in J20 mice with $p<0.05$ and $p<0.0001$ against WT of corresponding timepoint. Interestingly, *CXCL-1* was increased in WT at 2-hr timepoint as compared to J20 with $p<0.05$ significance, whereas *CXCL-10* was shown to be higher in J20 at 6-hr timepoint in comparison to WT with $p<0.05$ difference. Results are expressed as mean ± SEM. Two-way ANOVA with FDR post-hoc; *$p<0.05$, ****$p<0.0001$.

Number of mice per group; WT 0-hour (n=5), J20 0-hour (n=5), WT 2-hour (n=5), J20 2-hour (n=5), WT 6-hour (n=7), J20 6-hour (n=5), WT 24-hour (n=5), J20 24-hour (n=5).

3.2.5 Liver MBS and Iba-1 counts of J20 mutants are indifferent to WT controls

Liver neutrophils and Kupffer cells were counted to evaluate the extent of liver inflammation. The liver sections were stained for MBS marker for neutrophils detection (Figure 3.6A) and Iba-1 marker for Kupffer cells detection respectively (Figure 3.6B).

Two-way ANOVA analysis for MBS positive (MBS+) counts revealed interaction $p=0.2121$, TBI $p<0.05$, genotype $p=0.8676$ (Figure 3.6C). At 0-hour timepoint, the MBS+ counts between groups were shown low with 16 ± 2 for WT and 17 ± 3 for J20 group. Following acute TBI, the MBS+ number increased to 43 ± 12 for WT and 53 ± 12 for J20 at 2-hour timepoint. However, no notable difference was ascertained between groups. At 6-hour timepoint, the number of MBS+ in WT group remained at 43 ± 8 while the number was shown reduced in J20 25 ± 9. At 24-hour timepoint, the MBS+ number in WT went down to near baseline with a reading of 20 ± 4. However, in J20, the number of neutrophils remained high with 30 ± 5 which was 1.5-fold higher than WT. Nonetheless, although the two-way ANOVA revealed $p<0.01$ for TBI main effect, the original FDR method of Benjamini and Hochberg post-hoc test set at 0.05 showed no statistical difference between groups at all timepoints.

The liver Iba-1 positive (Iba-1+) cells was counted and analysed. The two-way ANOVA revealed no statistical significance across timepoints, with interaction $p=0.7157$, TBI $p=0.3988$, genotype $p=0.7233$ (Figure 3.6D).

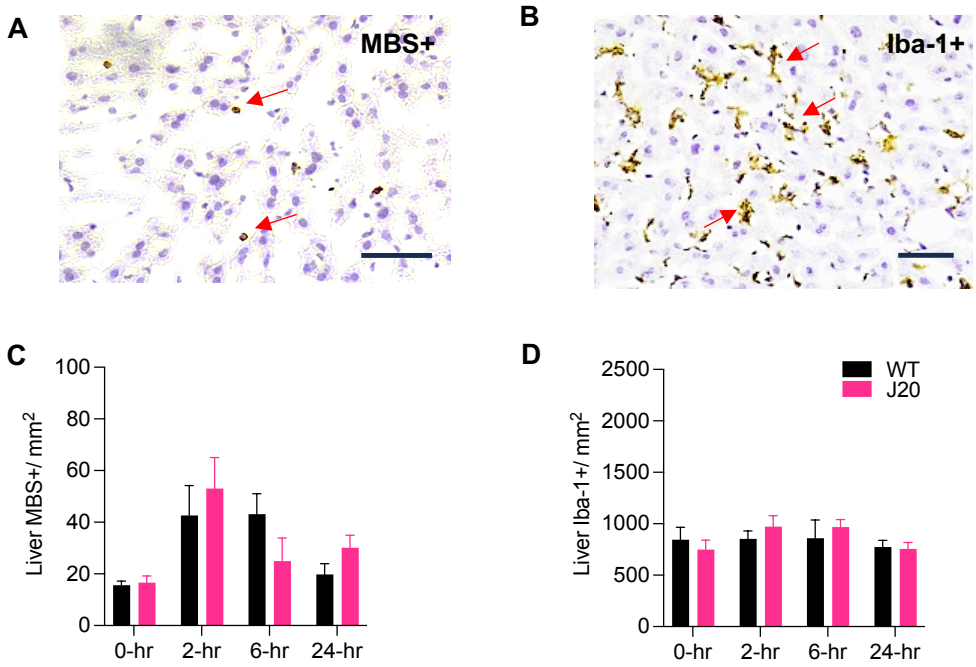


Figure 3.6 Peripheral inflammatory response post-acute TBI in 12 months old J20/ WT mice cohort. The number of neutrophils and Kupffer cells in the liver twelve-month-old WT and J20 animals were compared to investigate the hepatic APR on translational level following increased hepatic RNA transcription of chemo-attractants and inflammatory molecules. Fixed liver samples were immuno-stained with antibody against (A) MBS and (B) Iba-1 for neutrophils and macrophages respectively. Significant increase in the (C) liver neutrophil count was evident at $p<0.01$ for TBI timepoint main effect, though however no statistical significance was achieved at FDR post-hoc analysis. (D) Liver Iba-1 count showed no statistical difference across groups. Analysis was performed using two-way ANOVA, followed by original FDR method of Benjamini and Hochberg post-hoc test set at 0.05 where applicable. Results are expressed as mean ± SEM. Scale bar = 50µm; 20x magnification. Identified outliers using ROUT method set at Q=1% were removed. Iba-1, anti-macrophage ionized calcium binding adaptor molecule; MBS, anti-neutrophils; TBI, traumatic brain injury.

Number of mice per group for liver MBS+; WT 0-hr (n=5), J20 0-hr (n=5), WT 2-hr (n=5), J20 2-hr (n=5), WT 6-hr (n=7), J20 6-hr (n=5), WT 24-hr (n=5), J20 24-hr (n=5).

Number of mice per group for liver Iba-1+; WT 0-hr (n=5), J20 0-hr (n=5), WT 2-hr (n=5), J20 2-hr (n=5), WT 6-hr (n=6), J20 6-hr (n=5), WT 24-hr (n=5), J20 24-hr (n=5).

3.2.6 Brain RT-qPCR profile of J20 is indifferent to WT control

To explore the correlation between the hepatic inflammatory response and brain inflammatory status, brain mRNA level of pro-inflammatory molecules was assessed. Due to limited sample, only 24-hour timepoint was examined. This timepoint was chosen as we observed increased CASP3+ neuronal death (Figure 3.3) and higher liver mRNA expression in J20 group as compared to WT, at 24-hour timepoints (Figure 3.5)

Inflammatory molecule *IL-1*β did not show statistical difference after two-way ANOVA analysis (Figure 3.7A; interaction p=0.23, TBI p=0.13, genotype p=0.22), whereas *TNF-*α showed a significant TBI main effect of $p<0.05$ (Figure 3.7B; interaction p=0.47, genotype p=0.51). However, the original FDR method of Benjamini and Hochberg post-hoc analysis set at 0.05 did not find any meaningful difference between WT and J20 at 24-hour timepoint.

In addition, *CXCL-1* displayed significant TBI main effect of $p<0.01$ (Figure 3.7C; interaction p=0.98, genotype p=0.24). No significant difference was found between groups following original FDR method of Benjamini and Hochberg post-hoc analysis. The *SAA-2* expression did not reach significance with interaction p=0.18, TBI main effect p=0.75 and genotype main effect p=0.61 (Figure 3.7D).

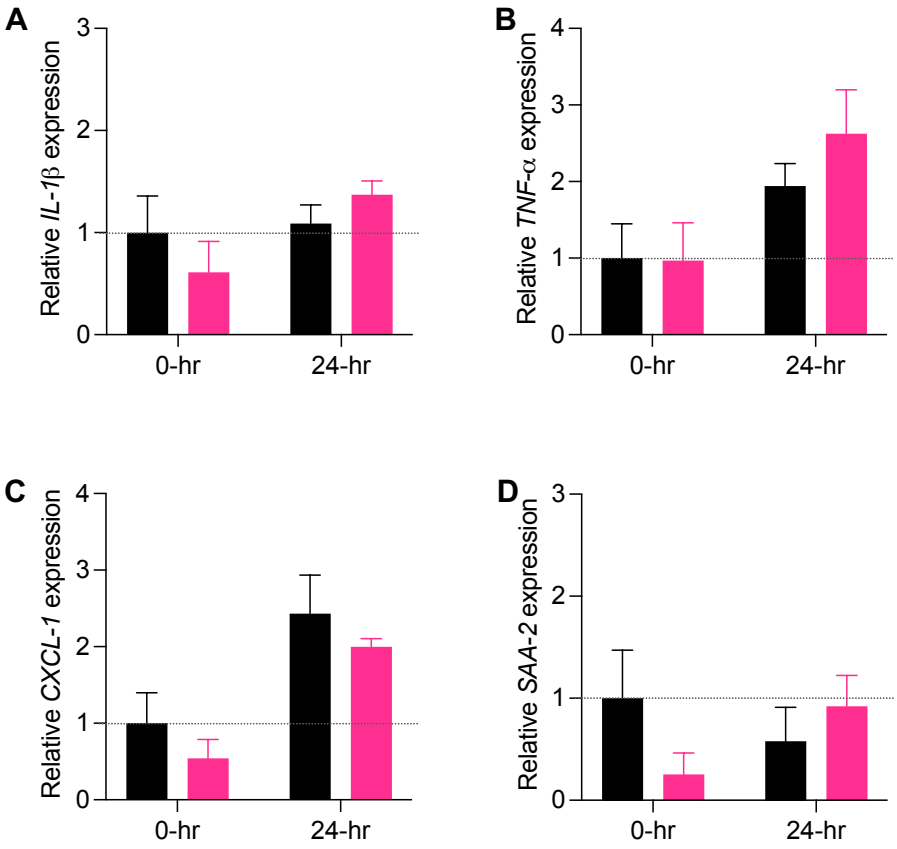


Figure 3.7 Brain mRNA expression of pro-inflammatory molecules at 24-hr timepoint in 12 months old J20/ WT mice cohort. cDNA from fixed brain sections were analyzed by RT-qPCR for (A) *IL-1β,* (B) *TNF-α* (C) *CXCL-1* and (D) *SAA-2* relative expression against housekeeping gene ACTB. No differences in pro-inflammatory molecules expression between J20 and WT group were seen at 24-hr timepoint as analysed through two-way ANOVA with original FDR method of Benjamini and Hochberg post-hoc test set at 0.05. Results are expressed as mean ± SEM. Identified outliers using ROUT method set at Q=1% were removed.

Number of mice per group for IL-1β and TNF-α; WT 0-hr (n=5), J20 0-hr (n=4), WT 24-hr (n=4), J20 24-hr (n=5).

Number of mice per group for CXCL-1; WT 0-hr (n=5), J20 0-hr (n=4), WT 24-hr (n=4), J20 24-hr (n=4).

Number of mice per group for SAA-2; WT 0-hr (n=5), J20 0-hr (n=3), WT 24-hr (n=5), J20 24-hr (n=5).

3.2.7 EV profile and exosomes quantification of J20 mutants are indifferent to WT controls

To visualise the EV profile, size distribution graph was generated for each timepoints (Figure 3.8A-D) and total EV quantification was performed (Figure 3.8E).

Total EV quantification revealed no significant interaction (p=0.94), TBI (p=0.54) and genotype (p=0.99) main effects following two-way ANOVA analysis. Median EV size was investigated (Figure 3.8F) and the interaction (p=0.78), TBI (p=0.11) and genotype (p=0.97) main effects did not reach statistical significance. Further, the total exosome concentration was evaluated, and no differences was noted across groups (Figure 3.8G; interaction p=0.78; TBI p=0.81, genotype p=0.21).

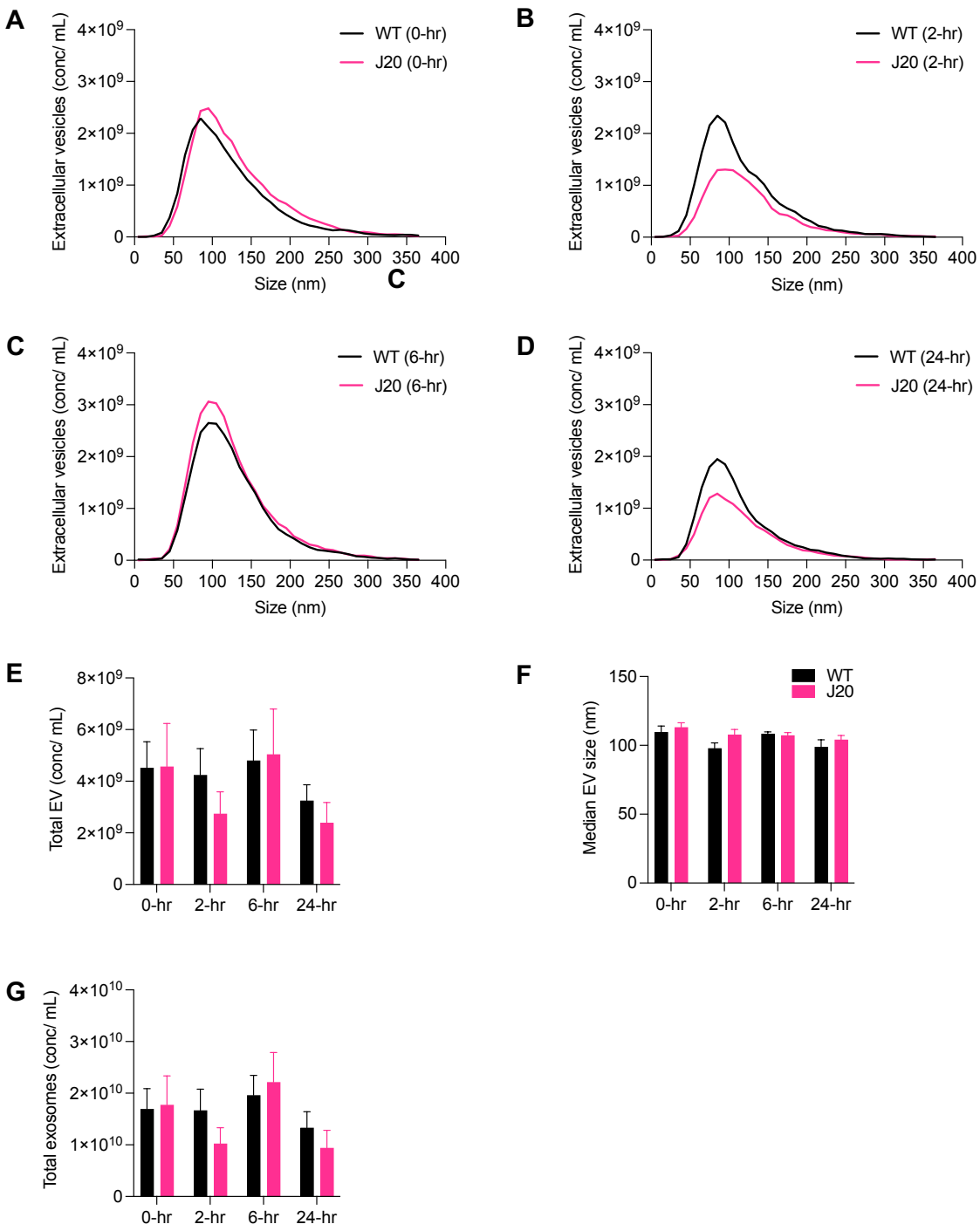


Figure 3.8 EV profile and total exosome quantification in 12 months old J20/WT cohort following acute TBI. Line graph depicts EV size distribution profile of WT and J20 at (A) 0-hour, (B) 2-hour, (C) 6-hour, and (D) 24-hour timepoints (size range 0-350 nm). The (E) total EV concentration, (F) median EV size, and (G) total exosomes concentration across timepoints (size range 30-150) were measured. No differences between J20 and WT was observed across timepoints. Results are expressed as mean ± SEM; two-way ANOVA. Identified outliers using ROUT method set at Q=1% were removed.

Number of mice per group; WT 0-hr (n=5), J20 0-hr (n=7), WT 2-hr (n=5), J20 2-hr (n=5), WT 6-hr (n=7), J20 6-hr (n=4), WT 24-hr (n=5), J20 24-hr (n=7).

3.2.8 Brain injury profile of 6 months old J20/ WT mice

The 6 months old J20 cohort with their age-matched WT controls (n=4-6/ group) were employed to investigate if the differing plaque burden deposition would affect the APR outcome following acute TBI. Brain sections of WT and J20 mice were stained against Aβ42. As expected, no plaque was seen in WT controls (Figure 3.9A - WT). Although amyloid plaque was not observed in these 6 months old mice (Figure 3.9A - J20), positive tissue genotyping results for amyloid pathology in these J20 mice denoted that the amyloid pathology is present in these mice. IHC findings from other studies reported that amyloid plaque deposition was only apparent in J20 mice starting 9 months of age (Shibly et al., 2023; Wright et al., 2013). However, intraneuronal amyloid was shown present in the J20 brain as early as 3 months old (Shibly et al., 2023). Please refer to section 1.2.7.1 for further information on transgenic J20 brain pathology development. Following acute TBI, brain sections from WT and J20 from 2-hour, 6-hour, and 24-hour timepoints were examined for plaque deposition, and no amyloid plaque was observed (figures not shown).

Two-way ANOVA analysis of brain infarct size reported interaction p=0.0108, TBI p=0.0056, genotype p=0.6872 (Figure 3.9B). At 2-hour timepoint, bigger infarct size was noted in J20 (3.13 ± 0.30) when compared to WT (2.21 ± 0.31). The infarct size was negligible between groups at 6-hour, with the reading of 3.55 ± 0.18 for J20 and 3.84 ± 0.46 for WT. Surprisingly, the infarct volume in J20 mice went down to 2.74 ± 0.21 whereas WT remained high at around 3.66 ± 0.24 (Figure 3.9B; two-way ANOVA with original FDR method of Benjamini and

Hochberg post-hoc test; $p<0.05$). However, the neuronal death count as reflected by CASP+ number at 24-hour were shown higher with 131.53 ± 13.87 in J20 as compared to 24.42 ± 18.00 for WT (Figure 3.9C; two-way ANOVA; interaction $p=0.1823$, TBI $p<0.0001$, genotype $p=0.0504$).

Leukocyte infiltration into the brain was assessed through neutrophils and microglial counts. The two-way ANOVA for brain MBS+ revealed interaction $p=0.8572$, TBI $p=0.0001$, genotype $p=0.6321$ (Figure 3.9D). In addition, two-way ANOVA for brain Iba-1+ revealed interaction $p=0.9212$, TBI $p<0.0001$, genotype $p=0.7183$ (Figure 3.9E). However, Original FDR method of Benjamini and Hochberg post-hoc test set at 0.05 reported no significance between groups throughout timepoints.

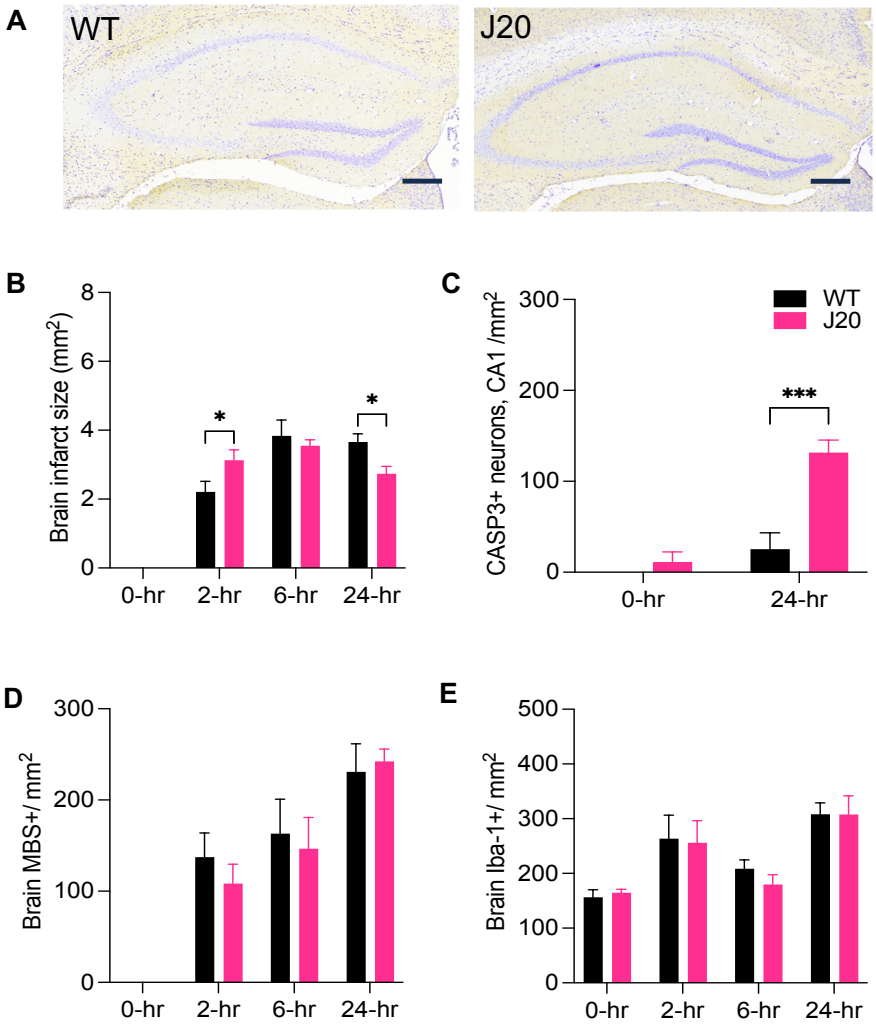


Figure 3.9 Brain infarct size and inflammatory profile following acute TBI in 6 months old J20/ WT mice cohort. (A) Brain slices stained for Aβ1-42 immunostaining for amyloid detection, showed no presence of amyloid in the 6 months old J20 cohort, which is denoted as prodromal stage. This J20 cohort was tested positive for AD genotype, however the plaque burden has yet to reach observable amount. (B) Brain infarct size analysis showed bigger lesion area in J20 at 2-hr timepoint that does not resolve over time. At 24-hr timepoint, WT group depicted higher lesion area, although (C) CASP+ stained neurons indicated higher density of dead neuronal cells in the J20 at 24-hr timepoint in hippocampal area. (D) Brain MBS+ cell and (E) Iba-1+ cell count was significant post-TBI with $p<0.001$ and $p<0.0001$ respectively for main effect of TBI across timepoints, although post-hoc test revealed negligible difference between groups. Results are expressed as mean ± SEM; two-way ANOVA. Scale bar = 200 μm; 4x magnification. Identified outliers using ROUT method set at Q=1% were removed. Iba-1, anti-microglia ionized calcium binding adaptor molecule; MBS, anti-neutrophils.

Number of mice per group for brain infarct size; WT 0-hour (n=5), J20 0-hour (n=5), WT 2-hour (n=4), J20 2-hour (n=5), WT 6-hour (n=4), J20 6-hour (n=6), WT 24-hour (n=5), J20 24-hour (n=5).

Number of mice per group for CASP3+ neurons; WT 0-hour (n=4), J20 0-hour (n=3), WT 2-hour (n=3), J20 2-hour (n=4), WT 6-hour (n=3), J20 6-hour (n=5), WT 24-hour (n=4), J20 24-hour (n=3).

Number of mice per group for brain MBS+; WT 0-hour (n=5), J20 0-hour (n=5), WT 2-hour (n=4), J20 2-hour (n=5), WT 6-hour (n=5), J20 6-hour (n=5), WT 24-hour (n=5), J20 24-hour (n=5).

Number of mice per group for brain Iba-1+; WT 0-hour (n=5), J20 0-hour (n=4), WT 2-hour (n=4), J20 2-hour (n=5), WT 6-hour (n=4), J20 6-hour (n=5), WT 24-hour (n=5), J20 24-hour (n=5).

3.2.9 *SAA-2* and *CXCL-1* upregulation in 6 months old J20 mice following acute TBI

To investigate the systemic APR in 6 months old mice, the same array of molecules measured in the liver of 12 months old cohort (section 3.2.4) was run for RT-qPCR. We have observed notable difference in 4 molecule arrays in the 12 months old cohort, namely *CCL-9*, *SAA-2*, *CXCL-1*, and *CXCL-10*. Interestingly, in this 6-month-old cohort, only *SAA-2* (Figure 3.10B) and *CXCL-1* (Figure 3.10C) reported significance when analysed with post-hoc analysis.

Two-way ANOVA for liver *CCL-9* (Figure 3.10A) reported interaction p=0.3543, TBI p=0.0645, and genotype p=0.4165. The *SAA-2* molecule in 6 months old group (Figure 3.10B; two-way ANOVA; interaction: $p<0.05$, TBI $p<0.0001$, genotype p=0.0962) showed the same trend as that of 12 months old group, with J20 peaked the highest at 24-hour timepoint. Following TBI at 2-hour and 6-hour timepoints, the relative expression of WT was comparable to that of J20, with 2.58 ± 1.09 (WT) against 4.09 ± 1.50 (J20) at 2-hour timepoint, and 78.83 ± 16.92 (WT) against 71.72 ± 33.26 (J20) at 6-hour timepoint respectively. However, at 24-hour timepoint, the J20 group had 3-fold higher expression as compared to WT with the reading of 176.96 ± 50.11 (J20) and 54.05 ± 34.23 (WT), with $p<0.01$ significance (Figure 3.10B; two-way ANOVA with original FDR method of Benjamini and Hochberg post-hoc test set at 0.05).

Additionally, *CXCL-1* was reported to be significant for interaction ($p<0.01$), as well as TBI ($p<0.0001$) and genotype ($p<0.05$) main effects when assessed with

two-way ANOVA (Figure 3.10C). Before any injury was inflicted onto the brain (0-hour), the baseline for WT was 1.00 ± 0.25, whereas for J20 was 0.56 ± 0.05. At 2-hour timepoint, the reading in WT went slightly up to 2.69 ± 0.72, while J20 went up 25-fold higher to 13.74 ± 2.88. Analysis with original FDR method of Benjamini and Hochberg post-hoc test revealed significance at $p<0.001$. The expression level of *CXCL-1* in both groups were slowly reclining from 6-hour towards 24-hour timepoint where the reading reached near baseline.

Two-way ANOVA analysis for *CXCL-10* expression revealed interaction p=0.2601, TBI p=0.0511, genotype p=0.1249 (Figure 3.10D). Furthermore, two-way ANOVA analysis for *IL-1*β showed interaction p=0.2281, TBI $p<0.05$, and genotype p=0.7923 (Figure 3.10E). Analysis with original FDR method of Benjamini and Hochberg post-hoc test did not reveal significance between groups across timepoints. Two-way ANOVA analysis for *TNF-*α reported interaction p=0.2878, TBI $p<0.01$, genotype p=0.2114 (Figure 3.10F). Similarly to *IL-1*β*,* no marked difference was noted between groups following original FDR method of Benjamini and Hochberg post-hoc analysis.

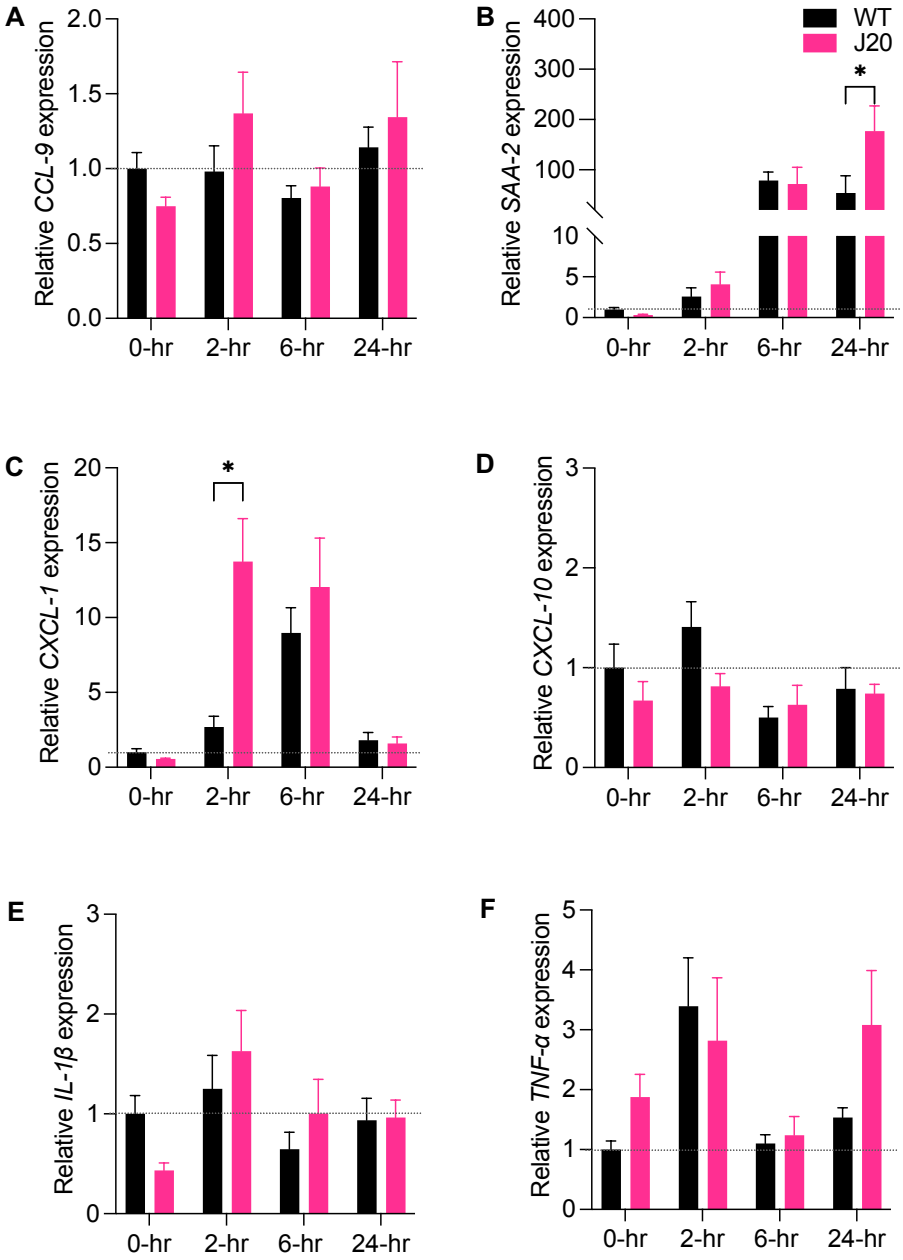


Figure 3.10 Liver molecular expression as measured through RT-qPCR following acute TBI in 6 months old J20/ WT mice cohort. Mice were subjected to acute TBI, and fresh liver samples were collected at 2-, 6-, and 24-hours timepoints post-injury. cDNA from the fresh liver samples were analyzed by RT-qPCR for a range of chemo-attractants and inflammatory cytokines. Hepatic (A) *CCL-9*, (B) *SAA-2*, (C) *CXCL-1*, (D) *CXCL-1*0, (E) *IL-1β*, and (F) *TNF-α* expression level was normalised against reference gene *ACTB*. Molecule *SAA-2* showed marked increase at 24-hours timepoint in J20 mice with $p<0.01$ in comparison to its WT counterparts. *CXCL-1* level was elevated sharply as opposed to WT at 2-hour timepoint with $p<0.001$ significance. Results are expressed as mean ± SEM. Two-way ANOVA with original FDR method of Benjamini and Hochberg post-hoc test set at 0.05; *$p<0.05$, **$p<0.01$, ***$p<0.001$.

Number of mice per group; WT 0-hour (n=7), J20 0-hour (n=5), WT 2-hour (n=5), J20 2-hour (n=5), WT 6-hour (n=7), J20 6-hour (n=6), WT 24-hour (n=5), J20 24-hour (n=5).

3.2.10 Liver MBS+ counts increased in 6 months old J20 mice at 6-hour post-TBI

Liver histological outcomes were investigated in 6 months old cohort to evaluate the APR profile in prodromal stage of AD. Liver MBS+ showed significant interaction at $p<0.05$, TBI main effect of $p<0.0001$ and genotype $p=0.1442$ (Figure 3.11A; two-way ANOVA). At 0-hour timepoint, the reading for WT when there was no brain insult was 14 ± 3, and J20 was 22 ± 4. At 2-hour post-TBI, the WT counts increased to 65.52 ± 13.32 whereas the reading for J20 was 44 ± 8. At 6-hour, WT went down to 34 ± 7, while J20 continued to increase and showed the reading of 67 ± 14. The original FDR method of Benjamini and Hochberg post-hoc test set at 0.05 showed significant difference between groups at $p<0.05$ (Figure 3.11A). At 24-hour timepoint, both WT and J20 showed a downward trend with the readings of 17.68 ± 2.65 and 33.28 ± 6.06 respectively.

On the other hand, liver Iba-1+ cells analysis reported a significant TBI main effect of $p<0.05$, with interaction $p=0.0735$, and genotype $p=0.6436$ (Figure 3.11B; two-way ANOVA). At 0-hour timepoint, the WT group had 1134 ± 118 Iba-1+ cells whereas J20 had 1081 ± 120 counts. After 2-hour TBI, there was negligible difference between WT (1208 ± 65) and J20 (1008 ± 68) cell counts. At 6-hour timepoint, the original FDR method of Benjamini and Hochberg post-hoc test set at 0.05 reported a near significant difference with $p=0.067$. The reading for J20 was comparably higher with 1617 ± 198 counts as compared to WT with 1249 ± 68. At 24-hour timepoint, both groups showed approximately

similar reading with 1236.40 ± 81.09 against 1267.00 ± 75.10 for WT and J20 respectively.

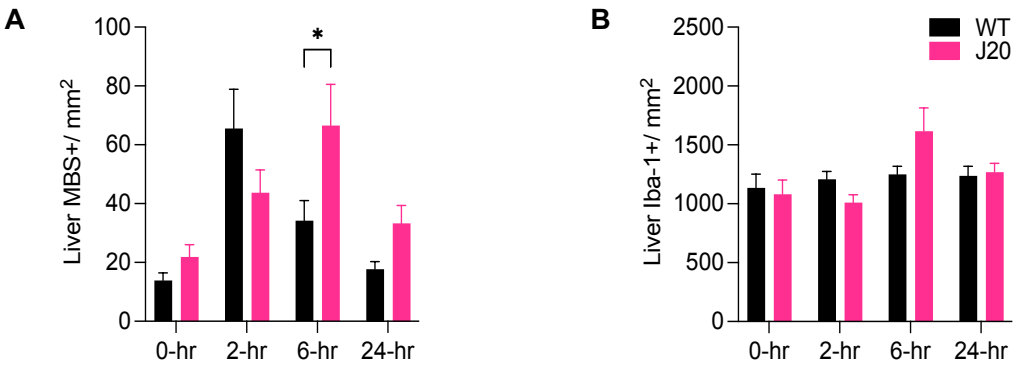


Figure 3.11 Liver neutrophils and Kupffer cells count following acute TBI in 6 months old J20/ WT mice cohort. Mice were subjected to acute TBI and were allowed to survive for 2-, 6- and 24- hour post-injury. Fixed liver samples were immuno-stained with antibody against liver MBS and Iba-1 for neutrophils and Kupffer cells respectively. Number of positive cells were quantified from six representative fields across two tissue sections at 40x magnification. Liver (A) MBS+ number was markedly higher in J20 6-hour timepoint with $p<0.05$, whereas (B) Iba-1+ stained cells showed a near significant increase with $p=0.067$. Results are analysed through two-way ANOVA and expressed as mean ± SEM. The original FDR method of Benjamini and Hochberg post-hoc test set at 0.05 was used where applicable. Identified outliers using ROUT method set at Q=1% were removed.

Number of mice per group for liver MBS+; WT 0-hr (n=6), J20 0-hr (n=5), WT 2-hr (n=5), J20 2-hr (n=5), WT 6-hr (n=7), J20 6-hr (n=5), WT 24-hr (n=5), J20 24-hr (n=5).

Number of mice per group for liver Iba-1+; WT 0-hr (n=8), J20 0-hr (n=5), WT 2-hr (n=5), J20 2-hr (n=5), WT 6-hr (n=8), J20 6-hr (n=5), WT 24-hr (n=5), J20 24-hr (n=5).

3.2.11 *IL-1β* level in J20 brain is higher in contrast to WT control at 6-hour timepoint

Furthermore, to investigate the inflammatory level in the brain, injury-related molecules *IL-1β, TNF-α, CXCL-1,* and *SAA-2* were analysed. Due to limited number of samples, only one timepoint was examined. The 6-hour timepoint was chosen in consideration of the histological outcomes in the brain (Figure 3.9) and liver (Figure 3.11) of the 6 months old J20/ WT cohort.

Two-way ANOVA analysis reported TBI main effect of $p<0.0001$, interaction $p=0.0866$, and genotype $p=0.0882$ for cytokine *IL-1β,* with Original FDR method of Benjamini and Hochberg post-hoc test set at 0.05 revealed significance of $p<0.05$ at 6-hour timepoint (Figure 3.12A). The relative expression of J20 group was 14.25 ± 3.47, which is 2-fold higher than WT (7.35 ± 0.69). On the contrary, the cytokine *TNF-α* (Figure 3.12B; two-way ANOVA; interaction $p=0.9752$, TBI $p<0.05$, genotype $p=0.5633$) revealed no statistical significance following original FDR method of Benjamini and Hochberg post-hoc analysis, with 4.63 ± 1.58 and 3.92 ± 1.33 for J20 and WT respectively at 6-hour timepoint (Figure 3.12B).

Two-way ANOVA analysis for *CXCL-1* reported interaction $p=0.32$, TBI $p=0.25$, genotype $p=0.97$ (Figure 3.12C). As there was no significance observed, the post-hoc analysis was not performed. Two-way ANOVA analysis of *SAA-2* molecule revealed stark difference of TBI main effect with $p<0.0001$, with interaction $p=0.83$, genotype $p=0.21$ (Figure 3.12D). However, original FDR

method of Benjamini and Hochberg post-hoc test did not reveal meaningful distinction between groups at 6-hour timepoint.

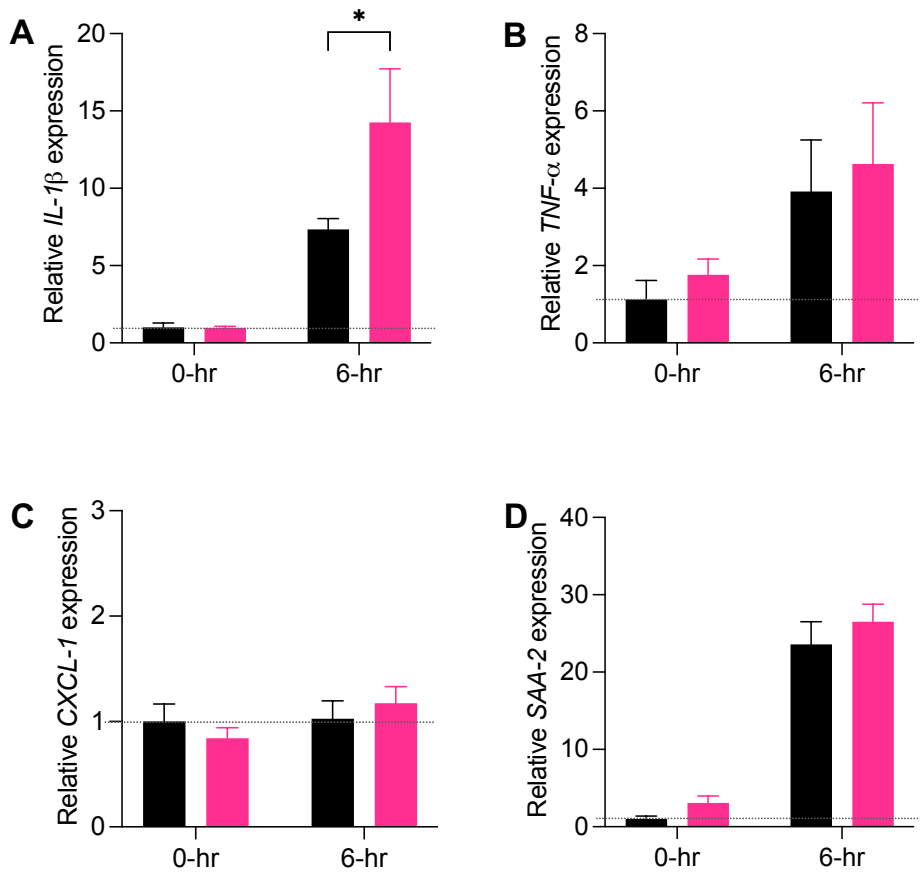


Figure 3.12 Brain mRNA expression of pro-inflammatory molecules at 6-hour timepoint in 6 months old J20/ WT mice cohort. cDNA from fixed brain sections were analyzed by RT-qPCR for (A) *IL-1β,* (B) *TNF-α,* (C) *CXCL-1*, and (D) *SAA-2* relative expression against housekeeping gene *RPL13A*. Pro-inflammatory cytokine (A) *IL-1β* level was shown elevated in J20 group at 6-hour timepoint, while no difference was noted in *TNF-a, CXCL-1* and *SAA-2 expression*. Results are expressed as mean ± SEM. Two-way ANOVA with original FDR method of Benjamini and Hochberg post-hoc test set at 0.05. *p<0.05. Identified outliers using ROUT method set at Q=1% were removed.

Number of mice per group for IL-1β, TNF-α, CXCL-1; WT 0-hr (n=4), J20 0-hr (n=5), WT 6-hr (n=5), J20 6-hr (n=5).

Number of mice per group for SAA-2; WT 0-hr (n=5), J20 0-hr (n=5), WT 6-hr (n=5), J20 6-hr (n=5).

3.2.12 EV profile and exosomes quantification of J20 mutants were indifferent to WT controls

To investigate EV profile in 6 months old cohort, EV size distribution (Figure 3.13A-D), total EV concentration (Figure 3.13E), median EV size (Figure 3.13F) and total exosome concentration (Figure 3.13G) was examined.

Negligible EV size distribution was visualised between WT and J20. Two-way ANOVA analysis on total EV concentration was found to be insignificant, with interaction $p=0.89$, TBI $p=0.31$, genotype $p=0.56$ (Figure 3.13E). Two-way ANOVA analysis of median EV size showed significant TBI main effect of $p<0.05$, with interaction $p=0.50$, genotype $p=0.09$ (Figure 3.13F). However, no difference was seen between groups following original FDR method of Benjamini and Hochberg post-hoc analysis. In addition, no difference was observed in total exosome concentration across timepoints, as two-way ANOVA test revealed interaction $p=0.72$, TBI $p=0.14$, genotype $p=0.58$ (Figure 3.13G).

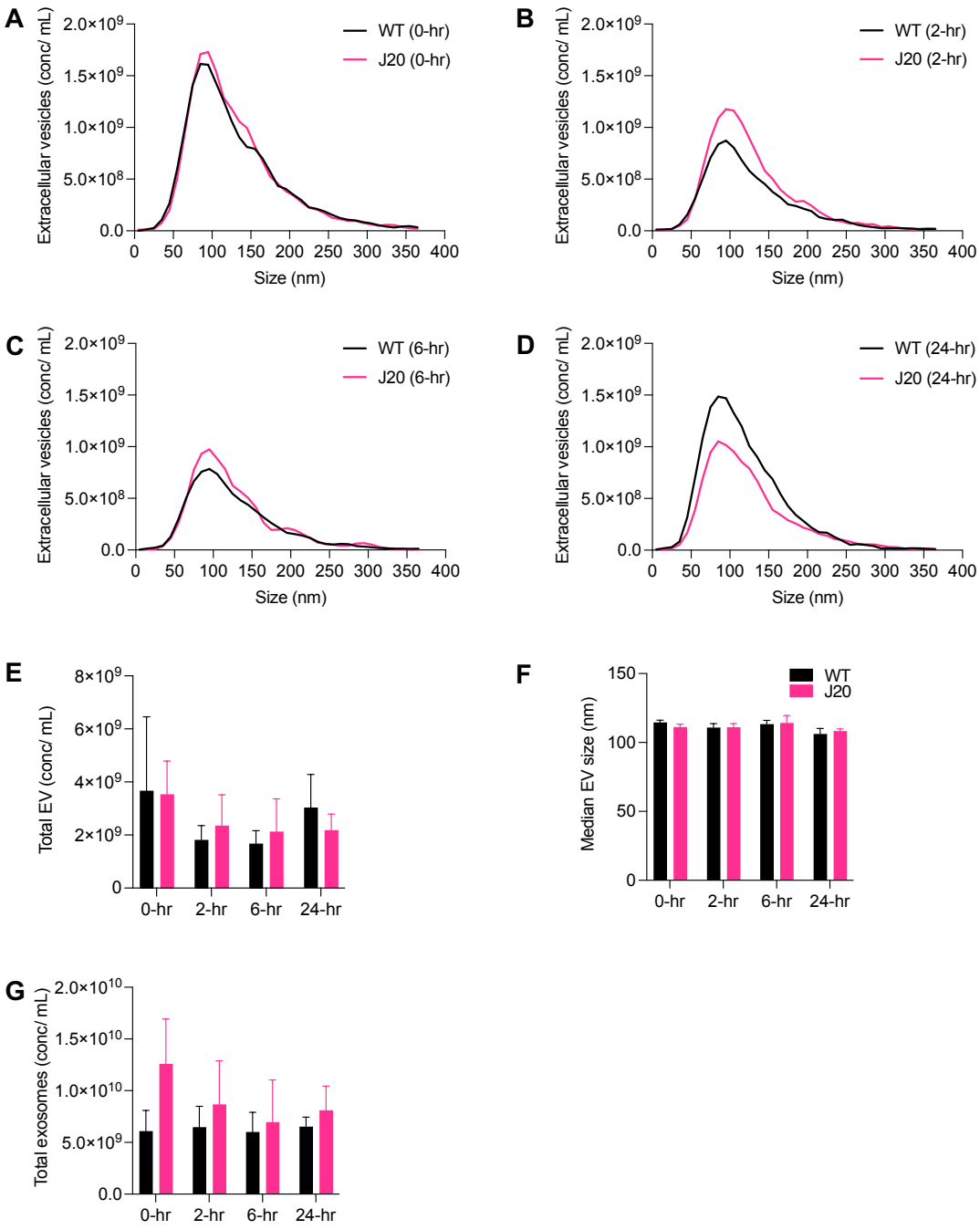


Figure 3.13 EV profile and exosome quantification following acute TBI in 6 months old J20/ WT mice cohort. Line graph depicts EV size distribution profile of WT and J20 at (A) 0-hour, (B) 2-hour, (C) 6-hour, and (D) 24-hour timepoints (size range 0-350 nm). The (E) total EV concentration, (F) median EV size, and (G) total exosomes concentration across timepoints (size range 30-150) were measured. No differences between J20 and WT was observed across timepoints. Results are expressed as mean ± SEM; two-way ANOVA. Identified outliers using ROUT method set at Q=1% were removed.

Number of mice per group; WT 0-hr (n=8), J20 0-hr (n=5), WT 2-hr (n=5), J20 2-hr (n=5), WT 6-hr (n=9), J20 6-hr (n=5), WT 24-hr (n=5), J20 24-hr (n=5).

3.2.13 Brain histological outcomes at 6-hour post-TBI in P301S mutant

Transgenic P301S mouse model (2 months old, n=6-7/ group) was used to investigate the local and systemic APR profile when TBI was applied in the presence of tauopathy in the brain. Due to limited sample availability, the 6-hour timepoint was chosen in consideration of the earlier J20 findings. Brain sections from homozygous P301S mice was stained against AT8 immunoreactivity to visualise abnormally phosphorylated tau proteins (Figure 3.14A). Two-way ANOVA analysis on AT8 burden reported interaction $p<0.01$, TBI $p<0.01$, genotype $p<0.01$ (Figure 3.14B). The original FDR method of Benjamini and Hochberg post-hoc test set at 0.05 revealed AT8 burden increased significantly at 6-hour post-TBI (Figure 3.14B).

Brain infarct size was measured, and two-way ANOVA analysis reported interaction $p=0.9607$, TBI $p<0.0001$, genotype $p=0.9607$ (Figure 3.14C). The original FDR method of Benjamini and Hochberg post-hoc test set at 0.05 revealed no meaningful difference for WT and P301S groups at 6-hour post-TBI (Figure 3.14C). In addition, when brain MBS+ cells readings were analysed, two-way ANOVA reported interaction at $p<0.01$ significance level, with TBI and genotype main effect of $p<0.0001$ and $p<0.01$ respectively (Figure 3.14D). As expected, no MBS+ cells were found in both WT and P301S brain sections at 0-hour. At 6-hour post-TBI, the MBS+ cell count in WT was 55 ± 11, whereas the reading for J20 was 134 ± 25. The original FDR method of Benjamini and Hochberg post-hoc test set at 0.05 revealed marked difference between groups

at 6-hour timepoint with $p<0.01$ significance (Figure 3.14D). Furthermore, two-way ANOVA analysis on brain Iba-1+ cells reported significant TBI main effect of $p<0.05$. However, interaction ($p=0.1566$) and genotype ($p=0.1045$) were shown insignificant (Figure 3.14E). The Iba-1+ cell counts for WT and J20 at 0-hour timepoint was 99 ± 3 and 102 ± 10 respectively. At 6-hour timepoint, there was an insignificant increase in numbers for both groups, with 111 ± 25 for WT and 157 ± 16 for J20. The original FDR method of Benjamini and Hochberg post-hoc test set at 0.05 showed no significant difference between groups at 6-hour post-TBI (Figure 3.14E).

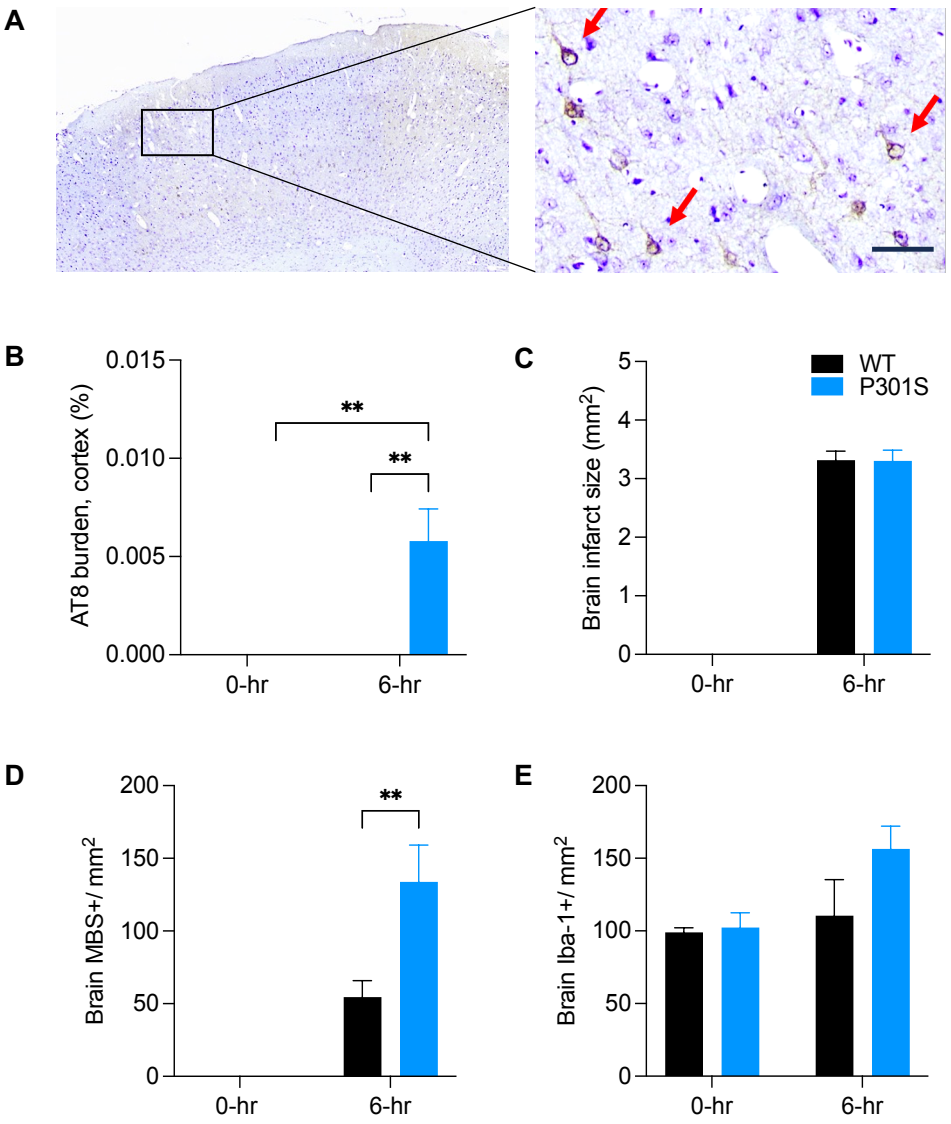


Figure 3.14 Brain histopathological assessment following acute TBI in WT and P301S mutants following 6-hour TBI. (A) Fixed brain slices from P301S TBI immuno-stained with AT8 antibody against tau tangles (dark brown protein pointed with red arrows). (B) Quantification of AT8 burden in cortex region showed significant increase in tau protein at 6-hour timepoint as compared to 0-hour timepoint, in P301S group. No difference was seen in the WT groups at corresponding timepoints. (C) Brain infarct size showed negligible difference between WT and P301S at 6-hour post-TBI. Fixed brain slices were immuno-stained with (D) anti-MBS antibody for neutrophil quantification and (E) anti-Iba-1 antibody for microglia counts respectively. Marked increase in the neutrophil numbers was seen in P301S groups at 6-hour timepoint, whereas no difference was noted in Iba-1+ cell counts. Results are analysed using two-way ANOVA, and expressed as mean ± SEM. Scale bar = 50 μm; 10x magnification. The original FDR method of Benjamini and Hochberg post-hoc test set at 0.05 was used where applicable. Identified outliers using ROUT method set at Q=1% were removed. Schematic illustration of the brain area examined for tau burden quantification can be found under Methodology section 2.5.3.2.

Number of mice per group for AT8 burden; WT 0-hr (n=3), P301S 0-hr (n=3), WT 6-hr (n=3), P301S 6-hr (n=3).

Number of mice per group for brain infarct size; WT 0-hr (n=4), P301S 0-hr (n=4), WT 6-hr (n=4), P301S 6-hr (n=4).

Number of mice per group for brain MBS+; WT 0-hr (n=6), P301S 0-hr (n=5), WT 6-hr (n=4), P301S 6-hr (n=5).

Number of mice per group for brain Iba-1+; WT 0-hr (n=5), P301S 0-hr (n=5), WT 6-hr (n=4), P301S 6-hr (n=4).

3.2.14 No heightened APR response was seen in P301S group as compared to WT control

The same panel of molecules were analysed in P301S models following acute TBI at 6-hour timepoint, which are *CCL-9, SAA-2, CXCL-1, CXCL-10, IL-1β,* and *TNF-α.*

Two-way ANOVA analysis of *CCL-9* reported interaction p=0.3385, TBI timepoints p<0.001, genotype p=0.3765 (Figure 3.15A). Further analysis using the original FDR method of Benjamini and Hochberg post-hoc test set at 0.05 was performed, and no differences was noted between groups at 0-hour and 6-hour timepoints (Figure 3.15A). Two-way ANOVA analysis of *SAA-2* expression level reported interaction p=0.4492, TBI p<0.05, genotype p=0.4483 (Figure 3.15B). However, post-hoc analysis of *SAA-2* indicated no difference between groups (Figure 3.15B; two-way ANOVA, original FDR method of Benjamini and Hochberg post-hoc test set at 0.05).

In addition, two-way ANOVA analysis of *CXCL-1* reported interaction p=0.1209, TBI p<0.001, genotype p=0.1053 (Figure 3.15C). At 0-hour timepoint, the baseline expression level of *CXCL-1* in WT group was 1.00 ± 0.19, whereas P301S had the basal expression level of 0.77 ± 0.10. At 6-hour post-TBI, both groups showed an increased molecule expression, although the WT group displayed higher level with 18.19 ± 6.04 as compared against P301S at 8.36 ± 1.56. Post-hoc analysis of *CXCL-1* relative expression denotes significant difference of p<0.05 between groups at 6-hour post-TBI (Figure 3.15C; original

FDR method of Benjamini and Hochberg post-hoc test set at 0.05). Two-way ANOVA analysis of *CXCL-10* reported interaction p=0.5923, TBI p<0.01, genotype p=0.5807 (Figure 3.15D). The original FDR method of Benjamini and Hochberg post-hoc test revealed no meaningful difference between groups at any timepoints. Two-way ANOVA analysis of *IL-1β* reported interaction p=0.3335, TBI p=0.9555, genotype p=0.1752 (Figure 3.15E). As there was no significance reported, a follow-up post-hoc test was not performed. Two-way ANOVA analysis of *TNF-α* reported interaction p=0.6027, TBI p<0.0001, genotype p=0.0680 (Figure 3.15F). The original FDR method of Benjamini and Hochberg post-hoc test revealed no meaningful difference between groups at any timepoints.

Besides that, liver MBS+ and Iba-1+ counts were performed. Two-way ANOVA analysis on liver MBS+ reported interaction p=0.6668, TBI p<0.05, genotype p=0.4015 (Figure 3.15G). At 0-hour, the MBS+ count in WT was roughly similar to P301S, with 29 $\pm$ 5 against 26 $\pm$ 5. After TBI, the MBS+ numbers were shown higher in the WT with 50 $\pm$ 10, when compared to P301S of 41 $\pm$ 7 at 6-hour timepoint. It is noteworthy to point that the graph pattern of liver MBS+ followed that of *CXCL-1* graph, which was expected due to *CXCL-1* neutrophil chemoattractant feature. Nonetheless, no significant difference was noted between groups in liver MBS+ counts when the original FDR method of Benjamini and Hochberg post-hoc test was performed. Furthermore, two-way ANOVA analysis of liver Iba-1+ revealed interaction p=0.7632, TBI p=0.8834, genotype p=0.3894. Post-hoc analysis was not performed due to insignificant result reported by two-way ANOVA (Figure 3.15H).

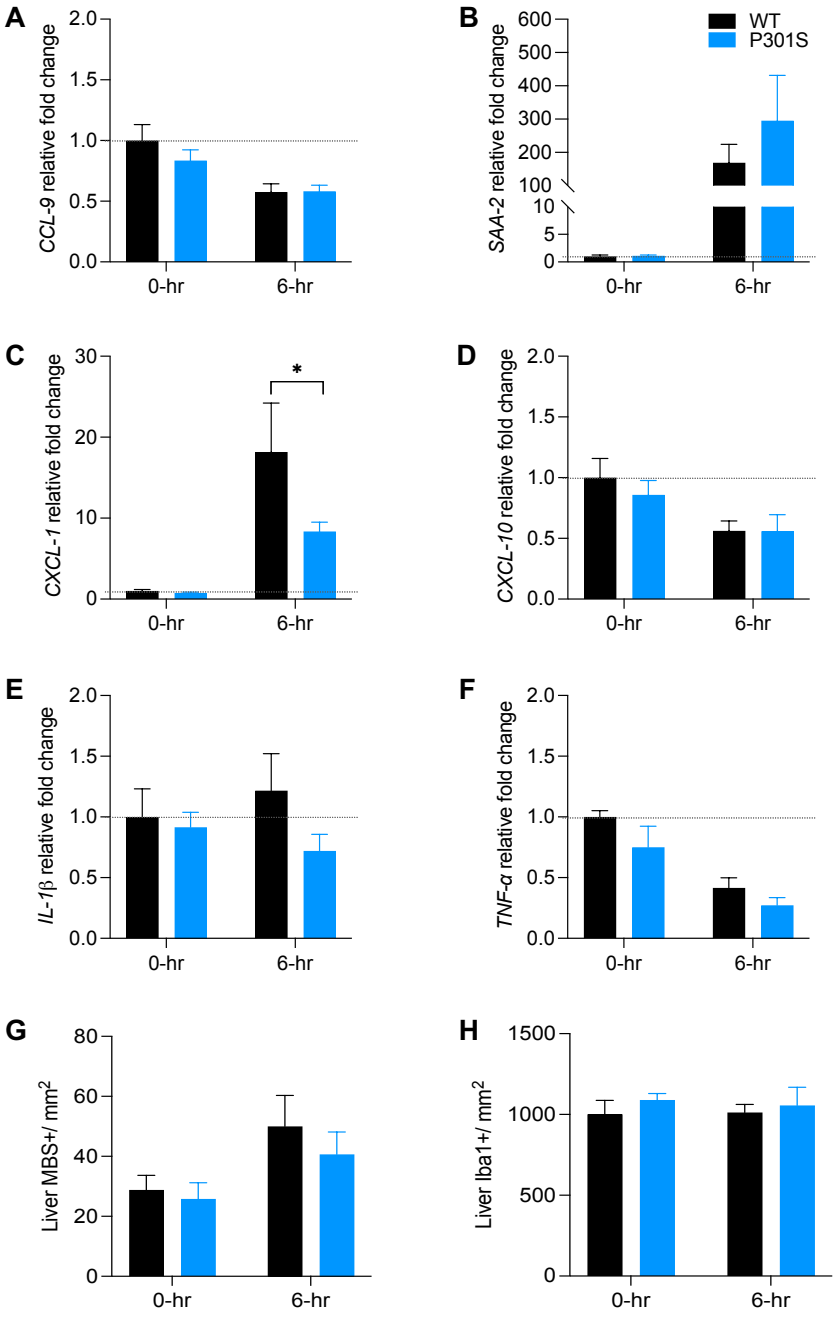


Figure 3.15 Hepatic RT-qPCR and histology profile of WT and P301S mutants at 6-hour post-injury. WT and P301S mice were subjected to TBI, and fresh liver tissues were collected at 6-hour following trauma. cDNA from the fresh liver samples were analyzed by RT-qPCR for a range of chemo-attractants and inflammatory cytokines. Hepatic (A) *CCL-9*, (B) *SAA-2*, (C) *CXCL-1*, (D) *CXCL-10*, (E) *IL-1β*, and (F) *TNF-α* expression level was normalised against reference gene *ACTB*. Fixed liver slices were immuno-stained for antibody against (G) neutrophils and (H) Kupffer cells respectively. No significant difference was noted across groups. Results are analysed using two-way ANOVA, and expressed as mean ± SEM. Original FDR method of Benjamini and Hochberg post-hoc test was performed where applicable. Identified outliers using ROUT method set at Q=1% were removed. *p<0.05. Iba-1, anti-microglia ionized calcium binding adaptor molecule; MBS, anti-neutrophils; TBI, traumatic brain injury.

Number of mice per group for CCL-9, SAA-2, CXCL-1, CXCL-10, IL-1β, and TNF-α; WT 0-hr (n=6), P301S 0-hr (n=6), WT 6-hr (n=6), P301S 6-hr (n=7).

Number of mice per group for liver MBS+; WT 0-hr (n=6), P301S 0-hr (n=5), WT 6-hr (n=5), P301S 6-hr (n=6).

Number of mice per group for liver Iba-1+; WT 0-hr (n=6), P301S 0-hr (n=6), WT 6-hr (n=5), P301S 6-hr (n=4).

3.2.15 Increased EV concentration in P301S mice at 6-hour timepoint

Size distribution graph was generated for 0-hour (Figure 3.16A) and 6-hour timepoints (Figure 3.16B). Total EV quantification (Figure 3.16C) revealed significant interaction ($p<0.05$) and TBI main effect ($p<0.01$), but the genotype main effect was not significant ($p=0.12$). Post-hoc test using original FDR method of Benjamini and Hochberg reported meaningful difference at 6-hour timepoint between P301S and WT at $p<0.05$ (Figure 3.16C).

Median EV size examination (Figure 3.16D) showed interaction at $p<0.01$, but the TBI ($p=0.26$) and genotype ($p=0.89$) main effects were not significant. Original FDR method of Benjamini and Hochberg post-hoc test was applied, and no difference was seen between groups at respective timepoints.

In addition, two-way ANOVA analysis on total exosome concentration (Figure 3.16E) reported significant TBI ($p<0.001$) and genotype ($p<0.05$) main effects, but insignificant interaction ($p=0.33$). Original FDR method of Benjamini and Hochberg post-hoc test revealed near significant difference between groups at 6-hour timepoint with $p=0.063$ (Figure 3.16E).

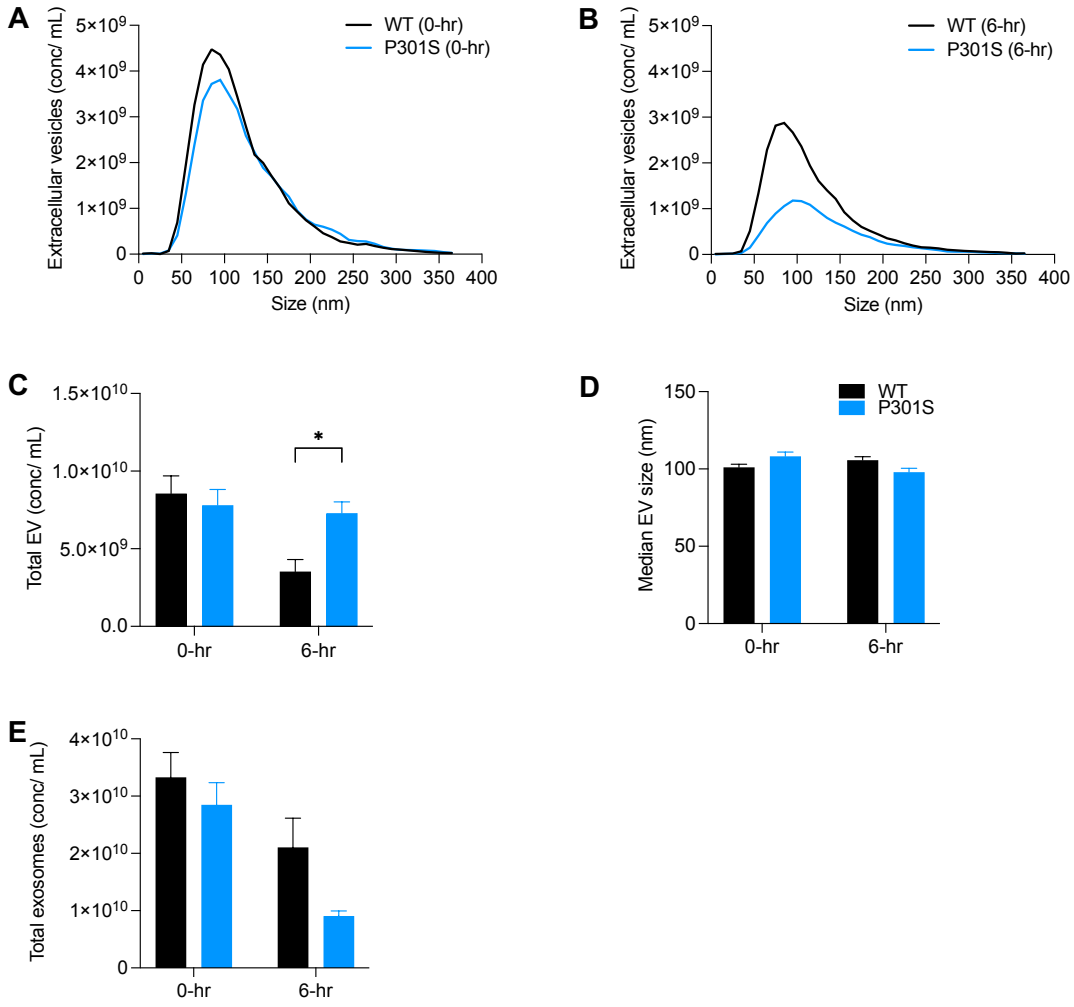


Figure 3.16 EV profile and exosome quantification of WT and P301S mutants at 6-hr post-injury. Line graphs illustrate EV size distribution at (A) 0-hr and (B) 6-hr timepoints. P301S displayed higher (C) total EV concentration at 6-hr timepoint when compared to WT control. No difference in (D) median EV size and (E) total exosome concentration was observed between groups. Results are analysed using two-way ANOVA with original FDR method of Benjamini and Hochberg post-hoc test, and expressed as mean ± SEM.

Number of mice per group; WT 0-hr (n=6), P301S 0-hr (n=6), WT 6-hr (n=6), P301S 6-hr (n=7).

3.3 Discussion

3.3.1 Principal findings

In this chapter, I demonstrated that the presence of amyloid pathology in the brain can alter the level of systemic APR following brain injury compared to WT controls in both 6-month-old and 12-month-old J20 cohort. However, the degree of amyloid pathology in the brain was shown to affect the APR profile. Differences in liver molecular expression and histology outcomes in 12-month-old J20 group when compared to 6-month-old J20 group. The APR profile in 12-month-old J20 group was delayed and of lower intensity than that in the 6-month-old cohort. In this discussion section, 6-month-old J20 mice will be interchangeably referred to prodromal AD or the younger J20 group, while 12-month-old J20 mice may be referred to AD dementia or the older J20 group. The term 'prodromal' or 'AD dementia' is assigned based on their amyloid pathology deposition status.

In the 6-month-old cohort, J20 mice exhibited a larger lesion size (Figure 3.9B) along with a 5-fold increase in liver chemokine *CXCL-1* expression compared to WT at 2-hour timepoint (Figure 3.10C). At the 6-hour timepoint, J20 mice showed elevated neutrophil infiltration into the liver (Figure 3.11A) accompanied with increased brain cytokine *IL-1β* (Figure 3.12A). The persistent inflammatory response in J20 mice was evidenced by a marked increase in liver *SAA-2* expression at the 24-hour timepoint, showing a 3-fold difference in contrast to WT control (Figure 3.10B). This liver inflammation was associated with excessive neuronal death in hippocampal CA1 region at the 24-hour timepoint (Figure

3.9C). The principal findings of the 6-month-old J20 group are as illustrated in Figure 3.17.

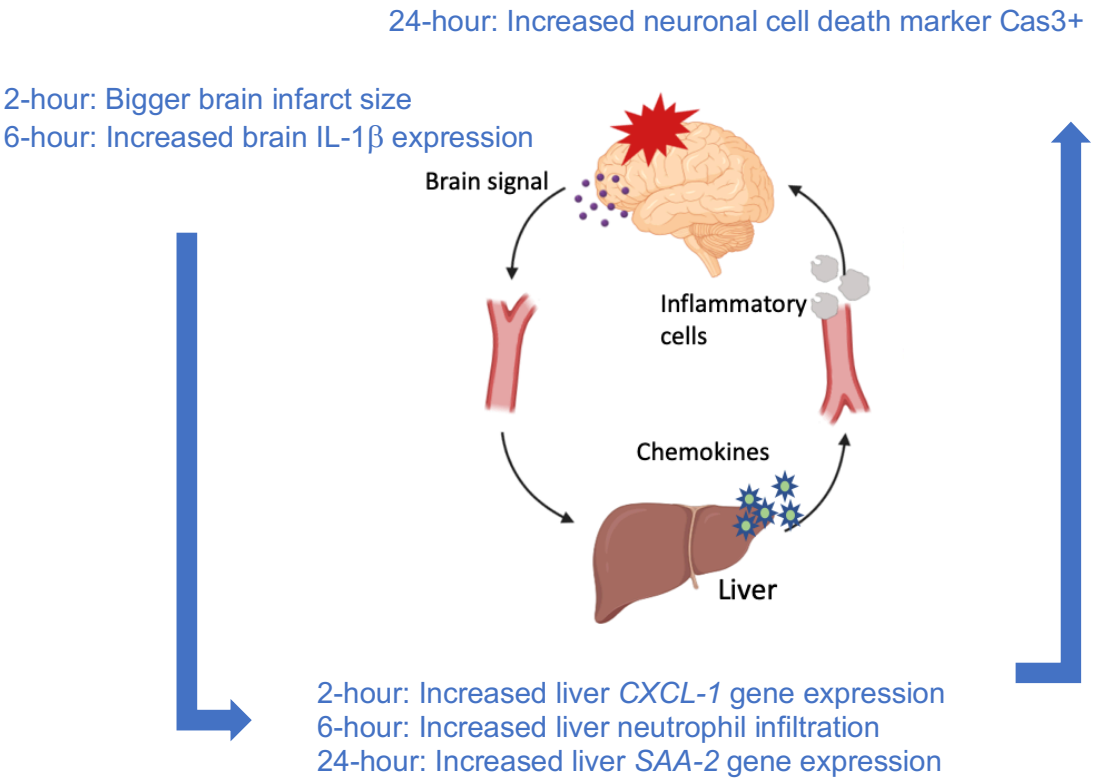


Figure 3.17 Principal findings for the 6-month-old J20 cohort when compared against age-matched WT control. The illustration was created using Bio-render website.

In the 12-month-old cohort, J20 mice showed an increased Aβ42 burden at 2-hour post injury (Figure 3.3D), followed by a subsequent elevation in liver chemokine *CXCL-1*0 expression (Figure 3.5D) at the 6-hour timepoint when compared to WT controls. At the 24-hour timepoint, J20 group exhibited a marked increase in liver *CCL-9* and *SAA-2* expression (Figure 3.5A-B), accompanied with high count of neuronal apoptosis in the CA1 hippocampal region (Figure 3.3F). No distinct liver neutrophil or Kupffer cell count was observed in the J20

group in comparison to WT control at any timepoint. The principal findings of the 12-month-old J20 group are as illustrated in Figure 3.18.

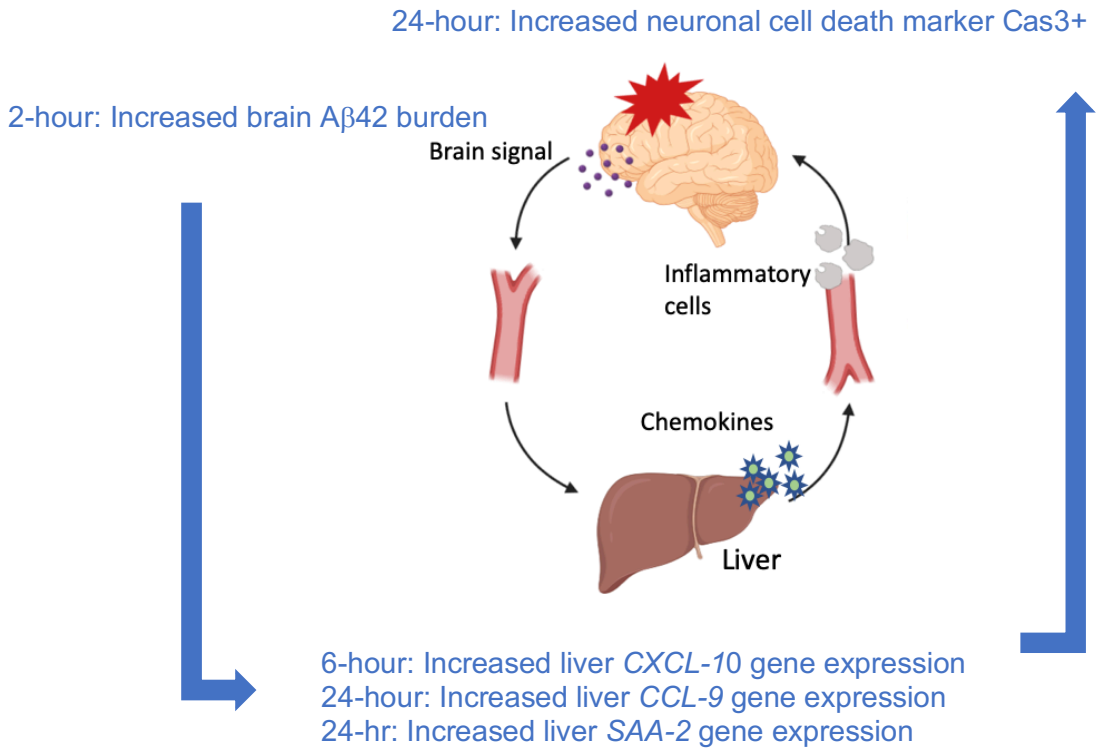


Figure 3.18 Principal findings of the 12-month-old J20 cohort when compared against age-matched WT control. The illustration was created using Bio-render website.

In the second part of this chapter, I investigated the effect of acute TBI in the presence of tau pathology using the P301S mutant and its corresponding age-matched WT controls. The mice were divided into naïve and TBI groups, and the brain contusion procedure along with subsequent assessments was conducted similar to the J20 cohort. I explored liver immunohistochemistry and molecular expression outcomes at 6-hour timepoint post-injury. Interestingly, I found no difference in the hepatic APR response between P301S mutants against WT controls. However, following TBI at the 6-hour timepoint, there was an increase

in brain tau burden accompanied by elevated recruitment of neutrophils into the brain, along with raised plasma EV concentration.

3.3.2 Heightened hepatic APR and brain injury observed in the 6 months old J20 cohort

Sensorimotor assessment was conducted in the 12-month-old cohort using the adhesive removal tape test. At the 48-hour timepoint, J20 mice exhibited a prolonged time to sense the presence of the tape (Figure 3.2C), indicating sensory deficits. Notably, motor deficits in J20 mice were evident as early as 48 hours and persisted up to 7 days post-injury (Figure 3.4G-I). These findings align with human and rodent findings that have demonstrated enhanced cognitive impairments in AD-TBI subjects (Gilbert et al., 2014; Shishido, Kishimoto, Kawai, & Toyota, 2016; Shishido et al., 2019).

Previous studies have reported high level of pro-inflammatory cytokines in the AD brain, released by primed microglia due to their continuous contact with amyloid clumps (Mandrekar & Landreth, 2010; Stock, Kasus-Jacobi, & Pereira, 2018). Examples of these cytokines include IL-1β and IL-6, TNF-α, and interferon-γ (Hoeijmakers, Heinen, Dam, & Lucassen, 2016), which are known to strongly influence the initiation of APR response in the periphery (Sá-Pereira et al., 2018; Webster et al., 2017). Interestingly, the same set of pro-inflammatory molecules has been reported to be released during brain trauma (Gyoneva & Ransohoff, 2015; Minter, Taylor, & Crack, 2016), suggesting an overlap of downstream pathobiology cascades in these two conditions.

Trauma to the brain involves a complex interplay between the CNS, peripheral organs, and the immune system. Microglia, the resident immune cells in the brain, serve as the CNS's first line of defense and are rapidly activated in response to insults. Activated microglia initiates local and systemic immune response through the secretion of pro-inflammatory cytokines, resulting in the recruitment of peripheral immune cells (leukocytes) such as neutrophils and macrophages to the site of injury (Xiong et al., 2018). The activation of immune response serves the purpose of resolving inflammation, restoring homeostasis, and promoting healing. However, uncontrolled activation of immune system due to polytrauma can cause detrimental effects and further exacerbate CNS condition through secondary injury. Pre-existing conditions such as AD (first hit) can cause the microglia to be chronically active (primed state). Therefore, the introduction of additional insults such as TBI (second hit) can cause the primed microglia to become over-activated and hence, secrete massive level of cytokines resulting in immune response dysregulation.

The production of these pro-inflammatory molecules by activated glial cells and leukocytes in the brain will trigger oxidative stress, excitotoxity and progressive neuronal death after TBI (Bye et al., 2007). Among these cytokines, IL-1β is believed to be the key mediator for both central and peripheral inflammatory response by regulating the release of other cytokines. IL-1β has been found to exert effects on BBB disruption, adhesion of leukocytes to endothelial cells, brain oedema, and cellular apoptosis (Woodcock & Morganti-Kossmann, 2013). In human, IL-1β is generated within 24-hour following injury, as observed through raised concentration in blood, CSF, and brain extracellular space. Furthermore,

increased mRNA and protein IL-1β expression was detected in human post-mortem brain samples within minutes to hours following TBI (Helmy, De Simoni, Guilfoyle, Carpenter, & Hutchinson, 2011). Studies in rodent TBI models have demonstrated that the administration of IL-1 receptor antagonist is able to attenuate neurotoxic function exerted by IL-1β through reduced neuronal damage and contusion volume (Helmy et al., 2011; Woodcock & Morganti-Kossmann, 2013). Therefore, in the case of AD-TBI phenomenon, an excessive amount of pro-inflammatory molecules generation is expected which will lead to more extensive damage to the brain.

In the present study, brain histological results displayed an increase in amyloid burden peaking at 2-hour post-TBI in 12 months old J20 mice (Figure 3.3D). In conformation with this finding, previous study in human subject has found that 30% of TBI brains were presented with acutely formed diffuse cortical Aβ deposits that share properties akin to AD-like pathology, detected as early as 2-hour following TBI (Ikonomovic et al., 2004; G. W. Roberts et al., 1994). In the 6 months old cohort, a larger brain infarct size was observed at 2-hour timepoint (Figure 3.8B), suggesting greater tissue damage contributed by the AD and TBI double insults. Hepatic response was seen elevated in 6 months old J20 mice at 2-hour timepoint, with liver mRNA expression of *CXCL-1* was shown markedly higher against WT with 5-fold difference (Figure 3.9C). *CXCL-1* is a chemoattractant and plays a pivotal role in mediating neutrophils recruitment during inflammation. The mRNA *CXCL-1* expression is believed to be translated into functional protein as observed through subsequent neutrophil infiltration into the liver at 6-hour timepoint (Figure 3.10A), inferring heightened APR response

in the 6 months old J20 mutants in contrast to the WT controls. *CXCL-1* mediates function by signalling via CXC-receptor-2 (CXCR-2) on neutrophils (Sawant et al., 2016), aiding neutrophil extravasation through blood endothelial cells to the site of inflammation (Dembic, 2015). During APR, neutrophils are the first cell of the innate immune system to respond to brain injury followed by monocytes (Jayaraj et al., 2019; Jian et al., 2019; Rosales, 2018). *CXCL-1* induction in the liver was governed by the IL-1β released by the CNS (Campbell et al., 2005). Thus, the expression of hepatic *CXCL-1* and liver neutrophil counts have been adopted as the surrogate marker of APR intensity. Surprisingly, the 12 months old J20 cohort exhibited 2-fold lower *CXCL-1* expression when compared to WT control, suggesting defective innate system capacity and lower APR response following TBI.

In the 12 months old cohort, *CXCL-10* expression was seen peaking at 6-hour timepoint with 2-fold higher concentration in contrast to WT control (Figure 3.5D), an outcome that was not observed in its younger J20 counterpart. Ageing was suggested to cause dysregulation of CXCL-10 production, as aged rodents displayed raised peripheral level of CXCL-10 in contrast to young rodents, and was correlated with poor performance of working memory (Bradburn et al., 2018). Furthermore, the high expression of *CXCL-10* level observed in this study may also be contributed by the higher burden of AD pathology in 12 months old mice, as the findings in human revealed 90% higher blood level of CXCL-10 in AD patients when compared to controls (Zhou, Sun, Xie, & Zhao, 2023). The level of CXCL-10 in CSF has been linked to cognitive deficits severity in human AD (Galimberti et al., 2006). CXCL-10 is predominantly produced by astrocytes

during neurotrauma (Phares, Stohlman, Hinton, & Bergmann, 2013) and AD, as the elevation of CXCL-10 was demonstrated in human AD patients (Xia, Bacskai, Knowles, Qin, & Hyman, 2000) and transgenic AD mutants (Duan et al., 2008; Zaheer et al., 2013). CXCL-10 binds to chemokine CXC-motif-receptor-3 (CXCR3) and its production was shown to co-localise with Aβ plaques in rodents (Duan et al., 2008; Zaheer et al., 2013). Moreover, CXCL-10/CXCR3 has been suggested to play a critical role in AD pathology generation as mouse deficient in CXCR3 exhibited significant reduction of Aβ plaque formation and associated with amelioration of behavioural impairments (Krauthausen et al., 2015).

The chemokine CXCL-10 is also termed as inhibitory protein-10, known to promote T helper 1 cell recruitment that represents a small fraction of the infiltrating leukocytes during TBI. These T cells play a role in secreting monocyte-attracting chemokine such as CCL-2 (Gyoneva & Ransohoff, 2015). Therefore, an increase in Kupffer cell in the liver is expected following increased *CXCL-10* expression in J20 mice. However, contrary to my prediction, no changes in J20 Kupffer cell count in contrast to WT control was observed at either 6- or 24-hour post-TBI (Figure 3.6). There is a possibility that the *CXCL-10* mRNA was not translated into functional proteins due to translational mechanism error. Although unrelated to *CXCL-10*, previous study has revealed the occurrence of dysregulated mRNA translational ability in AD mutants as they age (Ghosh et al., 2020). Indeed, the foundation of neurodegenerative disease development including AD revolves around misfolded protein generation due to an enhanced level of error-prone translations (Brilkova et al., 2022). Therefore, the likelihood that there is defective translational machinery and thus *CXCL-1*0 was not

translated in these 12 months old J20 cohort is high. A follow-up experiment is needed to ascertain this possibility.

Moreover, the 12 months old J20 cohort displayed a 1.5-fold higher expression of *CCL-9* as compared to control (Figure 3.5A). CCL-9 is homologous to mouse CCL-6 and carry an alternative name as the macrophage inflammatory protein 1γ (MIP-1γ). CCL-9 exerts its effect through chemokine receptor 1 (CCR1) (Apostolakis, Chalikias, Tziakas, & Konstantinides, 2011; Dembic, 2015; Kanno et al., 2005), and is highly involved in myeloid progenitor cells recruitment, monocyte activation and transmigration into the tissue where they mature into macrophage (LaFleur, Lukacs, Kunkel, & Matsukawa, 2004; H. Yan et al., 2015). Despite higher *CCL-9* expression, no changes were seen in Kupffer cells count between J20 and WT at 24-hour. However, another possible explanation for this outcome may be attributed to the time needed for mRNA to be translated into functional proteins before a higher Kupffer cell numbers can be visualised. Further investigation needs to be undertaken to examine if there is indeed production of functional protein and monocyte recruitment into the liver after 24-hour timepoint. Nonetheless, it is noteworthy to point that the heightened APR response in 12 months old J20 vs age-matched WT control is delayed when compared to 6 months old cohort as no increased leukocyte infiltration was seen in the J20 liver within the first 24-hour post-TBI.

These murine CCL-9 and CCL-6 cytokines are akin to human CCL23 and CCL15 and have been suggested to be an indicator of brain ischemia, as the level of CCL-23 and CCL-6 in human plasma and rodent neurons respectively were

observed to increase and remained high within the first 24 hours after injury (Simats et al., 2018). Increased level of CCL15 in the blood level of AD patients (29–35% higher) was seen in opposition to controls (Zhou et al., 2023). CCR-1 was recognized as a biomarker for AD (Halks-Miller et al., 2003), although how this receptor contributes to the disease aetiology warrants further investigation. Both microglia and astrocytes express CCR-1, and they exhibited a strong affinity towards CCL-6 as demonstrated through an in vitro study conducted by Kanno and colleagues (Kanno et al., 2005). The same study provided the evidence that the CCL-6 effects seen was mediated through PI3- kinase/Akt signalling pathway (Kanno et al., 2005) recognized to promote cell growth, proliferation, and migration (Popiolek-Barczyk & Mika, 2016).

In addition, persistent inflammation in J20 mice was displayed through a 10-fold increase and 3-fold increase in mRNA expression of hepatic *SAA-2* in 12 months old cohort (Figure 3.5B) and 6 months old cohort (Figure 3.10B) respectively at 24-hour timepoint. SAA protein is acute phase reactants that are encoded by *SAA1* and *SAA2* genes and is synthesized predominantly in the liver during APR in response to injury or infection. The level of *SAA* can increase by 1000-fold during APR when compared to basal concentration during in vivo inflammation (Thorn, Lu, & Whitehead, 2003). The mRNA expression of *SAA* can be induced principally by cytokines IL-1 and IL-6. In vitro experiment demonstrated an enhanced *SAA* induction following synergistic combination of IL-1 and IL-6 pro-inflammatory stimuli. Other cytokines that can affect SAA production either directly or indirectly includes IL-2, TNF-α, interferon-γ and ciliary neutrophic factor (Uhlar & Whitehead, 1999). It was observed that mice deficient in IL-6 or

TNF-α was not able to generate SAA serum protein to the level seen in WT control following lipopolysaccharide challenge. Furthermore, mice deficient of both IL-6 and TNF-α had almost completely absent SAA production (Uhlar & Whitehead, 1999). SAA has been suggested to function as monocyte and T cell chemoattractant and have the ability to elicit the release of IL-8 from neutrophils (Thorn et al., 2003). The stark increase of *SAA-2* expression in 12 months old J20 might be a result of higher concentration of pro-inflammatory cytokine released by primed microglia in response to high amyloid burden in the brain and TBI insult. This is because the mRNA level of *SAA* has been reported to rise continuously in dose-dependent manner in correlation to raised pathogen load or increasing doses of IL-1, IL-6, and TNF-α (Dowton, Peters, & Jestus, 1991; Uhlar & Whitehead, 1999). Nonetheless, it is noteworthy to mention that the elevated *SAA* mRNA expression may not yield a proportionally equivalent amount of protein synthesis. A study found that the treated human PLC/PRF/5 hepatoma cells exhibited a 76-fold increase in *SAA* mRNA expression by 24-hour, but only resulted in 4- to 6-fold increase in SAA protein synthesis (Steel, Rogers, DeBeer, DeBeer, & Whitehead, 1993).

To test the hypothesis that the elevated systemic APR led to potentially exacerbating AD progression, molecular and histological assessments were performed on brain tissue. Pro-inflammatory cytokine *IL-1β* was elevated in 6 months old J20 brain at 6-hour timepoint (Figure 3.12A). Previous study reported association of *IL-1β* mRNA levels within 24 hours of injury with injury severity (Bye et al., 2007), which may suggest an intensified injury in the J20 brain compared to the control. However, it must be noted that further study is needed

to ascertain this assumption. Increased *IL-1β* in the 6 months old J20 brain may be a downstream implication of the exponential increase of hepatic *CXCL-1*, as its receptor CXCR2 is vastly expressed in microglia (Zhou et al., 2023). CASP+ neuronal death count revealed higher cell death in J20 mice, in both 6- and 12-months old cohort. However, younger J20 ($p<0.001$ vs control) showed more prominent cellular death intensity compared to older J20 ($p<0.05$ vs control) at 24-hour timepoint (Figure 3.3F and 3.9C). This observation further strengthens the premise that the 6-month-old J20 mice displayed a more intense level of APR accompanied by increased brain tissue damage. There was no difference shown in *TNF-α* level in J20 and WT in the 6 months old cohort (Figure 3.12B). This observation is in accordance to the previous studies that revealed that focal TBI using CCI did not show increased *TNF-a* within 24-hour (Bye et al., 2007; Semple, Bye, Rancan, Ziebell, & Morganti-Kossmann, 2010; Woodcock & Morganti-Kossmann, 2013). On the contrary, rodent TBI studies using other injury methods such as the lateral fluid percussion technique showed an increase of *TNF-α* peaking at 4-hour to 6-hour and resolved by 24-hour (Fan et al., 1996; Knoblach, Fan, & Faden, 1999).

The systemic immune response is regulated primarily by the liver, through the action of NF-κB transcription factors upon CNS cytokine release into the periphery. This bi-directional communication between the brain and the periphery has been suggested to be mediated by the EVs in the blood (Hazelton et al., 2018). To ascertain if the brain-periphery communication was mediated through EVs, perhaps by carrying cytokines from the brain to the liver, total EV concentration, median EV size and total exosome concentration was measured.

I predicted that the J20-TBI group would release a higher amount of EVs or exosomes in relation to higher amount of cytokine released by the microglia. However, no difference was noted between J20 and WT in the 6- and 12-months old cohorts in all EV-exosome parameters (Figure 3.7 and Figure 3.11). It may be possible that a distinct concentration between J20 and WT may be proven if these exosomes could be further identified using brain-origin specific biomarker, as the exosomes quantified in this study did not investigate such differences.

Brain contusion subjected to P301S mice showed an increase in AT8 tau burden (Figure 3.14B), consistent with previous study done by Edwards and colleagues (Edwards, Zhao, Dash, Soto, & Moreno-Gonzalez, 2020). The present finding is accompanied by increased brain neutrophils to the brain and increased EV concentration at 6-hour timepoint (Figure 3.16C). However, liver molecular and histological outcomes did not indicate raised APR level in the P301S-TBI group. Taken both J20 and P301S findings altogether, in the event where both amyloid and tau pathologies are concurrently present, it seems heightened systemic APR may be initiated by the amyloid pathology, but the increase in EV and brain neutrophil recruitment to the brain during AD may be predominantly driven by the presence of tau in the brain.

In summary, the presence of amyloid pathology in the brain has a discernible impact on the systemic APR, characterised by increased hepatic *CXCL-1* expression and neutrophil recruitment into the liver. This heightened APR was shown associated with elevated levels of brain *IL-1β* and neuronal cell death, suggesting an exacerbation of brain injury. Notably, there was no observable

increase in brain neutrophils in the J20 mice, although further studies could explore potential neutrophil recruitment post 24-hour timepoint. The introduction of tauopathy using the P301S model did not yield similar systemic APR outcomes as observed in the J20 model. However, intriguingly, higher brain neutrophil levels and extracellular vesicle (EV) concentrations were noted in the P301S group compared to the WT at the 6-hour timepoint. Future studies could delve into exploring systemic APR in the P301S model across extended timepoints, which was not covered in this study due to limited sample size.

CHAPTER 4

CHRONIC TBI

Chapter 4 : The effect of chronic TBI exposure onto J20 and P301S mutants

4.1 Introduction

It is widely acknowledged that TBI stands as a prominent environmental risk factor contributing to the onset of dementia-related neurodegenerative disorders such as AD, Parkinson's disease, and chronic traumatic encephalopathy (CTE) (Ramos-Cejudo et al., 2018; Xiong et al., 2018). Individuals subjected to repeated brain injury, in contact sports such as boxing, predispose players to an increased susceptibility to post-traumatic dementia in later life. This phenomenon was initially termed as 'punch drunk syndrome' in 1928, and later replaced by 'dementia pugilistica' terminology in 1937, before ultimately being referred as CTE (Castellani & Perry, 2017). Dementia pugilistica has been associated with intense NFT formation in the cortex and was claimed to be absent of amyloid plaque formation as determined by standard silver and Congo red histochemistry (Corsellis, Bruton, & Freeman-Browne, 1973). However, this finding was shown to be incorrect as Roberts and team (1990) reinvestigated the brain samples of boxers with dementia pugilistica using a more sensitive immunocytochemical method and found that the samples were positive against an antibody raised to the β-amyloid protein present in AD plaques (G. W. Roberts et al., 1994; Gareth W Roberts, Allsop, & Bruton, 1990). This observation showed the detrimental effect of TBI towards AD development in later life, through the generation of both AD-like pathologies; amyloid and NFT formation long term after post TBI.

Moreover, Nandoe and colleagues (2002) described a case report on a previously healthy patient who developed AD following mild TBI. A 55-year-old lady was diagnosed with minor concussion after she bumped her head against the front car window in a traffic accident and experienced a brief loss of consciousness. She had prior TBI histories of similar severity at the age of 9 and 32 years old. This lady came to the outpatient clinic 1.5 years later as she complained of having progressive forgetfulness. Neurophysiological examination showed global cognitive impairments, and routine brain MRI revealed mild cortical and moderate hippocampal atrophy. Therefore, she was diagnosed with dementia syndrome with probable AD according to NINCDS-ADRDA criteria. During the follow up period of 3 years, this patient showed symptoms deterioration which include anxiety and vivid delusions. The patient was then treated with neuroleptics and later admitted to nursing home (Nandoe, Scheltens, & Eikelenboom, 2002).

In addition, brain samples from 152 patients (age range; 8 weeks to 81 years) who died within 2 weeks following a single incidence of TBI demonstrated diffuse Aβ plaques in 30% of the cases, with striking similarities to plaques seen in early AD stage. Plaque accumulation post-TBI was observed indiscriminately in all age groups, including children. By contrast, plaque accumulation in control brains collected from non-neurological death reasons were found almost exclusively in aged individuals (V. E. Johnson, Stewart, & Smith, 2010; G. W. Roberts et al., 1994). It is intriguing that despite similarities in plaque features, TBI-induced plaques develop in a very rapid manner, as they are observed as early as 2 hours post-TBI, whereas plaques in AD develop slowly, which is the reason they are

pre-dominantly observed in the elderly (V. E. Johnson et al., 2010). Linear correlation between TBI and AD has been proposed, whereby more severe injury possess greater risk to develop AD (Collins-Praino & Corrigan, 2017; Johnson et al., 2010). Indeed, studies on the association between previous history of TBI with AD development as well as earlier AD-onset has long been pursued (Collins-Praino & Corrigan, 2017; Kokiko-cochran & Godbout, 2018; Lobue et al., 2019). However, there are limited studies available that explore the long-term consequences of a single moderate TBI on AD subjects, when there is an existing AD pathology. Henceforth, in this chapter I sought to investigate the chronic effect of TBI to J20 and P301S models, focusing on the histological and molecular perspective in the brain and liver, as well as characterising the EV and exosome concentration in the plasma post-TBI.

4.1.1 Chapter aims

The aims for this chapter are as follows:

1- To investigate if chronic TBI in J20 and P301S mutants accelerate amyloid and tau pathology development in the brain.
2- To examine if there is elevated inflammation in J20 and P301S brains following chronic TBI through neutrophil and microglia quantification.
3- To explore if there is persistent hepatic inflammation level in J20 and P301S mutants after chronic TBI by measuring the pro-inflammatory cytokines using RT-qPCR assessment.
4- To ascertain if the hepatic neutrophil and Kupffer cell numbers in J20 and P301S cohorts are increased following chronic TBI.

5- To characterise the EV and exosome profile in J20 and P301S groups in comparison to WT controls following chronic TBI.

4.1.2 Experimental design

In this chapter, J20 and P301S mouse mutants were used to investigate the effect of chronic TBI on amyloid-like pathology and tauopathy respectively. Transgenic J20 and P301S mice of 2 months of age with their corresponding age-matched WT controls were subjected to TBI and were left to recover in the heated chamber, before allowed to return into their home cage. The mice were housed in the animal care facility with water and food *ad libitum*. After 8 weeks, mice were culled when they reach 4 months old followed by sample collection.

The 2-month-old age group was chosen for TBI induction based on the AD-like pathology timeline whereby at this timepoint, the pathology has developed but the burden is not yet accumulated or widely spread in both mutant models. Therefore, this characteristic would enable better pathology visualisation when they reach 4 months old, should there is an accelerated pathology development following chronic TBI. For clarification, in this chapter, mice in both naïve and TBI groups were 4 months old when culled, and their pathologies were compared.

An additional set of behavioural experiment was performed for P301S/ WT cohort at 8 weeks post-TBI before culling was performed to explore their neurological and functional outcomes, as we observed increased AT8 tau burden in P301S cohort. This behavioural experiment is not the major focus of this chapter, and it

only serves as a pilot study due to small sample size [number of mice per group: WT naïve (n=6), WT chronic TBI (n=4), P301S naïve (n=7), P301S chronic TBI (n=6)]. This behavioural experiment was not performed onto J20 cohort as we did not see any plaque formation in their brain following chronic TBI. The experimental design for this chapter is as illustrated in Figure 4.1.

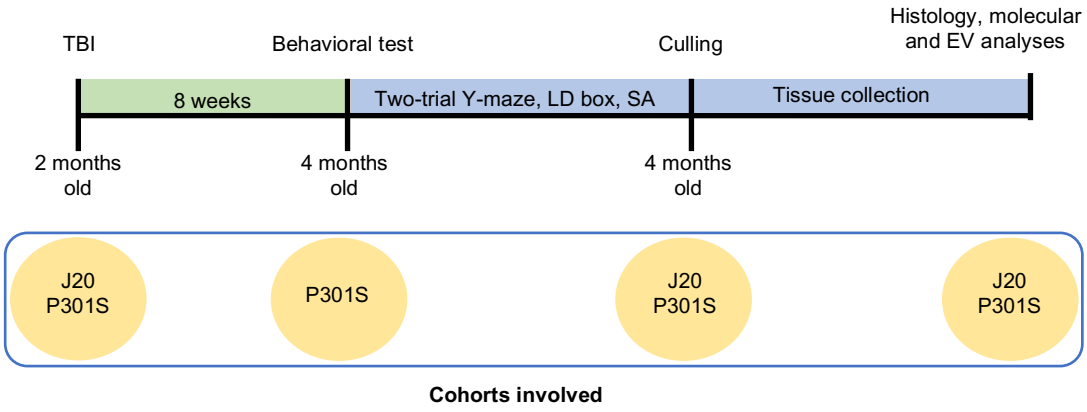


Figure 4.1 Experimental design for chronic TBI using transgenic J20 and P301S mutants. Mice were subjected to TBI at 2 months old and the P301S cohort was later assessed for neurological and functional deficit through a set of behavioural tests at 4 months old. The mice were subsequently culled followed by sample collection for histology, molecular and EV analysis. LD box, light dark box; SA, spontaneous alternations. The timeline diagram was created using Microsoft PowerPoint.

4.2 Results

4.2.1 Chronic TBI increases AT8 tau burden in the brain

To ascertain if chronic TBI leads to an accelerated amyloid plaque or abnormal phosphorylated tau accumulation, both J20 and P301S brain sections were immunostained against Aβ42 (amyloid plaque) and AT8 (hyperphosphorylated tau) antibodies.

To investigate if chronic TBI leads to an accelerated amyloid plaque development, J20 brain sections were immunostained against Aβ42 antibody. Naïve and week 8 J20 brain sections revealed no positive staining when checked against amyloid plaque (figures not shown). To determine if chronic TBI may induce abnormal phosphorylated tau accumulation in the J20 mutants, naïve and week 8 J20 brain sections were tested against AT8 antibody, and no positive staining was observed (figures not shown).

Furthermore, to investigate if cross-pathology exists in P301S mutant, brain sections of naïve and week 8 P301S mice were subjected to amyloid Aβ42 staining. No amyloid plaque was seen in P301S naïve and week 8 brain sections (figures not shown). Additionally, naïve and week 8 P301S brain sections were also checked against AT8 antibody to examine the impact of chronic TBI on hyperphosphorylated tau accumulation. A significant increase in AT8 burden in P301S brain sections was demonstrated following chronic TBI (Figure 4.2A-C). Global increase in the AT8 burden was demonstrated in both ipsilateral (Figure 4.2D) and contralateral brain sections of P301S (Figure 4.2E).

Two-way ANOVA analysis of AT8 burden in ipsilateral brain sections of P301S vs WT revealed significant interaction ($p<0.05$), TBI ($p<0.05$) and genotype ($p<0.0001$) main effects. Original FDR method of Benjamini and Hochberg post-hoc test set at 0.05 reported marked increase in AT8 accumulation ($p<0.01$) between P301S week 8 (0.110 ± 0.011) vs P301S naïve (0.057 ± 0.018). Furthermore, there was no AT8 burden observed in WT in both naïve (P301S naïve vs WT naïve, $p<0.01$) and week 8 (P301S week 8 vs WT week 8, $p<0.0001$) cohorts (Figure 4.2D).

In addition, two-way ANOVA analysis on AT8 burden in contralateral brain sections also described significant interaction ($p<0.05$), TBI ($p<0.05$) and genotype ($p<0.0001$) main effects (Figure 4.2E). Original FDR method of Benjamini and Hochberg post-hoc analysis showed discernible elevation of AT8 burden ($p<0.05$) between P301S week 8 vs P301S naïve. In agreement with ipsilateral results, there was also no AT8 burden observed in contralateral WT brain sections, both in naïve (P301S naïve vs WT naïve, $p<0.01$) and Week 8 (P301S week 8 vs WT week 8, $p<0.0001$) cohorts (Figure 4.2E).

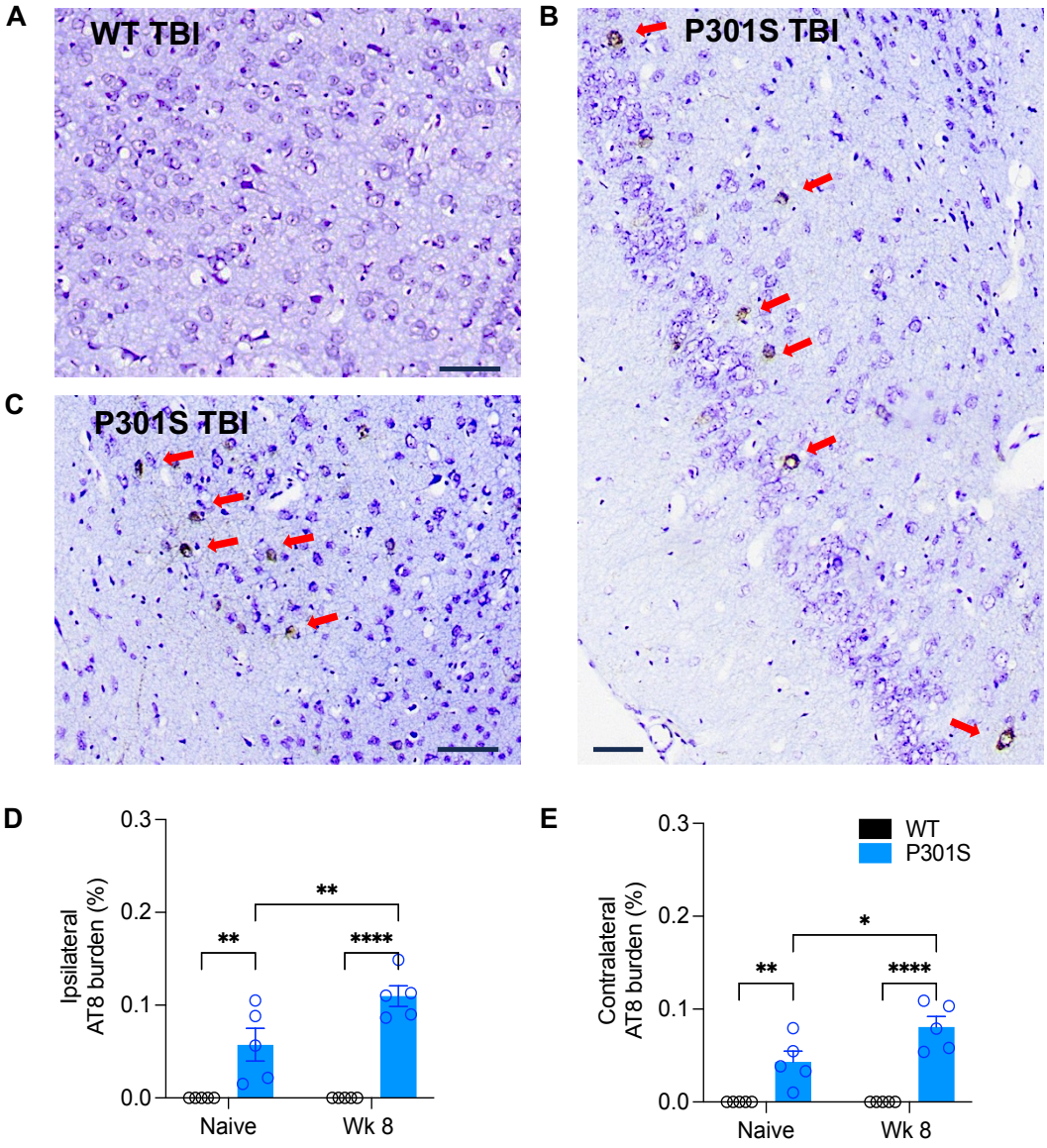


Figure 4.2 Abnormal hyperphosphorylated tau burden. Figures showing brain sections of (A) WT TBI and (B-C) P301S TBI immunostained against AT8 antibody. No AT8 tau was seen in WT brain sections. AT8 localisation was demonstrated in P301S group as seen through dark brown staining guided by red arrows. (D) Ipsilateral and (E) contralateral tau burden was quantified in the cortex region and analysed with two-way ANOVA, with FDR post-hoc test. Analysis was done on the brain sections taken from naïve and TBI mice at 4 months of age. Wk 8, week 8. Scale bar = 50 μm; 10x magnification. Schematic illustration of the brain area examined for tau burden quantification can be found under Methodology section 2.5.3.2.

Number of mice per group; WT naïve (n=5), P301S naïve (n=5), WT week 8 (n=5), P301S week 8 (n=5).

4.2.2 Increased impulsivity in both P301S and WT mice after chronic TBI

To investigate the long-term neurological effect of TBI, the mice were subjected to two-trial Y-maze, light dark box, and spontaneous alternations analyses. The behavioural assessment experimental design is as illustrated in Figure 4.3A.

The hippocampal function of the mice was assessed through its reference memory performance by using two-trial Y-maze behavioural test. The test was termed as “two-trial” as the mice were introduced twice to the Y-maze. During the first introduction (acquisition period), one arm of the Y maze was closed, and the mice were allowed to explore the area. After 1 hour interval, the mice were again introduced to the Y-maze (retrieval period), at this time with all arms opened. Thus, the previously closed arm would be considered as the novel arm, a new area for the mice. Mice with good reference memory would be indicated by longer time spent in the novel arm, due to the instinctive nature of rodents to explore new territory (Figure 4.3B).

For two-trial Y-maze, the two-way ANOVA analysis revealed strong genotype main effect ($p<0.001$), but insignificant interaction ($p=0.3871$) and TBI main effect ($p=0.4085$) (Figure 4.2C). WT naïve group (44.72 ± 3.48 sec) spent markedly longer time in novel arm when compared to P301S naïve (29.05 ± 2.80 sec), with significance of $p<0.01$ (Figure 4.2C; two-way ANOVA, original FDR method of Benjamini and Hochberg post-hoc test). After chronic TBI, WT week 8 mice spent 39.58 ± 3.13 sec in the novel arm, which was notably higher than P301S week 8

of 29.17 ± 1.94 sec, with significance difference of $p<0.05$ (Figure 4.2C; two-way ANOVA, original FDR method of Benjamini and Hochberg post-hoc test). Additionally, the effect of chronic TBI on the anxiety-like behaviour was investigated through light-dark box test (Figure 4.3D). Briefly, the mice were first put into the dark chamber and allowed to exit into the light chamber and the mice activity was assessed for 5 minutes. As mentioned earlier, the instinctive nature of mice would be to explore new area, which in this case is the light region. Thus, anxious animals would exhibit tendency to spend more time in the dark chamber and thus having higher latency to exit dark.

Figure 4.3E illustrates the latency to exit dark, whereby two-way ANOVA revealed significant TBI main effect ($p<0.05$), with interaction ($p=0.9686$) and genotype ($p=0.6842$) reported not significant. WT naïve stayed for 130.33 ± 47.97 sec in the dark chamber before exiting, whereas P301S naive spent 149.86 ± 53.42 sec. The findings on latency to exit dark on week 8 was interesting and contrary to my initial expectation. Instead of showing anxiety-like behaviour by spending more time in the dark before exiting into light chamber, both WT week 8 and P301S week 8 groups showed impulsive behaviour which was demonstrated through shorter time taken to exit dark as compared to naive. After 8 weeks post-TBI, there was a massive decrease in latency to exit dark, with WT demonstrating 22.75 ± 14.66 sec (6-fold difference as compared to WT naive) and P301S exhibiting 38.33 ± 10.01 sec (4-fold difference as compared to P301S naïve). Nonetheless, the post-hoc test was not significant between groups

(Figure 4.3E; original FDR method of Benjamini and Hochberg post-hoc test set at 0.05).

Explorative activity in light chamber was measured through time spent in light chamber. Two-way ANOVA analysis reported interaction p=0.4613, TBI p=0.9603, genotype p=0.6702 (Figure 4.3F). Post-hoc analysis was not performed since the two-way ANOVA results was shown not significant. Furthermore, the number of rears was also measured and analysed with two-way ANOVA, which found significant genotype main effect ($p<0.05$) but insignificant interaction (p=0.5340) and TBI (p=0.2603) (Figure 4.3G). It was noted that P301S consistently showing lower rearing number as compared to WT in both naive and week 8 timepoints. P301S naïve group showed 4 ± 2 rear counts as compared to WT naïve of 14 ± 5 (genotype p=0.09), and 2 ± 2 as compared to 8 ± 2 at week 8. To ascertain that this observation was not due to locomotor issues in P301S, the number of transitions between dark and light chamber was inspected (Figure 4.3H). Two-way ANOVA analysis revealed interaction p=0.8110, TBI p=0.6942, genotype p=0.7714. No significance was noted between groups thus inferring negligible movement restriction bias.

Moreover, the function of both prefrontal cortex and hippocampus (working memory) of the mice was assessed through spontaneous alternation test (Figure 4.3I). An alternation is defined as consecutive entries into all three arms. Therefore, mice with good working memory were indicated by high percentage alternations, whereas mice with poor working memory were represented by higher proportion of entering repeated arms (Figure 4.3J-K). Two-way ANOVA

on spontaneous alternations revealed interaction p=0.7812, TBI p=0.6269, genotype p=0.2829, inferring no significant difference between groups (Figure 4.3L).

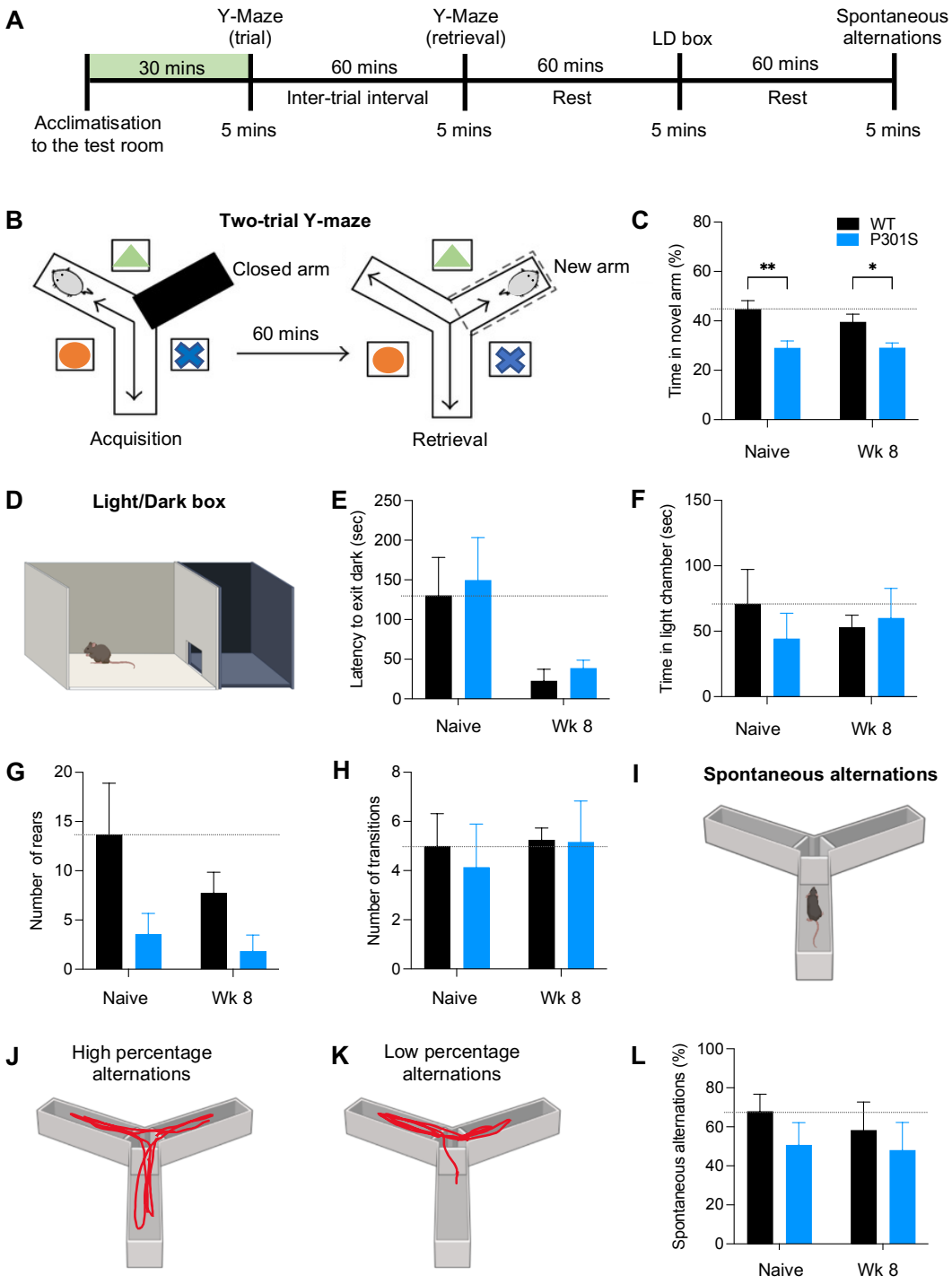


Figure 4.3 Behavioural assessments after chronic TBI in P301S mice. Mice were subjected to behavioural experiments according to the (A) timeline

described. (B) Two-trial Y-maze were carried out to gauge long-term memory ability by investigating (C) the time taken to explore the novel arm. Anxiety-like disorder was explored using (D) light-dark box test. (E) Latency to exit dark, (F) time in light chamber, (G) number of rears and (H) number of transitions were noted. Working memory performance was examined through (I) spontaneous alternations test whereby (J) high percentage alternations is indicative of good working memory and (K) low percentage alternations is indicative of poor working memory. An alternation is defined as consecutive entries into all three arms. Graph (L) illustrates spontaneous alternation analysis using the formula of % alternations = (number of alternations/ total arm entries – 2) x 100. Data was analysed using two-way ANOVA followed by original FDR method of Benjamini and Hochberg post-hoc test set at 0.05 where applicable. Identified outliers using ROUT method set at Q=1% were removed. Dotted lines are parallel to WT naïve (control group), thus the line acted as a reference baseline for the transgenic P301S naïve and WT TBI /P301S TBI groups. Wk 8, week 8. The illustration was created using Bio-render website.

Number of mice per group: WT naïve (n=6), WT week 8 (n=4), P301S naïve (n=7), P301S week 8 (n=6).

4.2.3 Brain microglia basal number is unchanged post-TBI in both J20 and P301S mutants

Figure 4.4A illustrates brain MBS graph with significant TBI effect with $p<0.0001$ (Figure 4.4A; two-way ANOVA). However, the statistical difference for interaction ($p=0.93$) and genotype ($p=0.94$) main effect was not meaningful. Original FDR method of Benjamini and Hochberg post-hoc analysis set at 0.05 showed significant increase of MBS+ cells in WT week 8 vs WT naive (29 ± 13 vs 0 ± 0; $p<0.01$), J20 week 8 vs J20 naive (25 ± 7 vs 0 ± 0; $p<0.01$), and P301S week 8 vs P301S naive (27 ± 9 vs 0 ± 0; $p<0.01$). No meaningful statistical difference between genotypes within week 8 cohorts was observed.

Statistical analysis for brain Iba-1 (Figure 4.4B) demonstrated significant TBI ($p<0.0001$) and genotype ($p<0.05$) main effects, with non-significant interaction ($p=0.75$). Original FDR method of Benjamini and Hochberg post-hoc analysis revealed marked increase of Iba-1+ cells in WT week 8 vs WT naive (241 ± 23 vs 110 ± 25; $p<0.01$), J20 week 8 compared to J20 naive (240 ± 16 vs 145 ± 30; $p<0.05$) and P301S week 8 vs P301S naive (295 ± 29 vs 188 ± 21; $p<0.05$). No meaningful statistical difference between genotypes within week 8 cohorts was noted. In addition, two-way ANOVA analysis showed no significant result for CA1 neurons (Figure 4.4C) with interaction $p=0.792$, TBI main effect $p=0.574$ and genotype main effect of $p=0.955$.

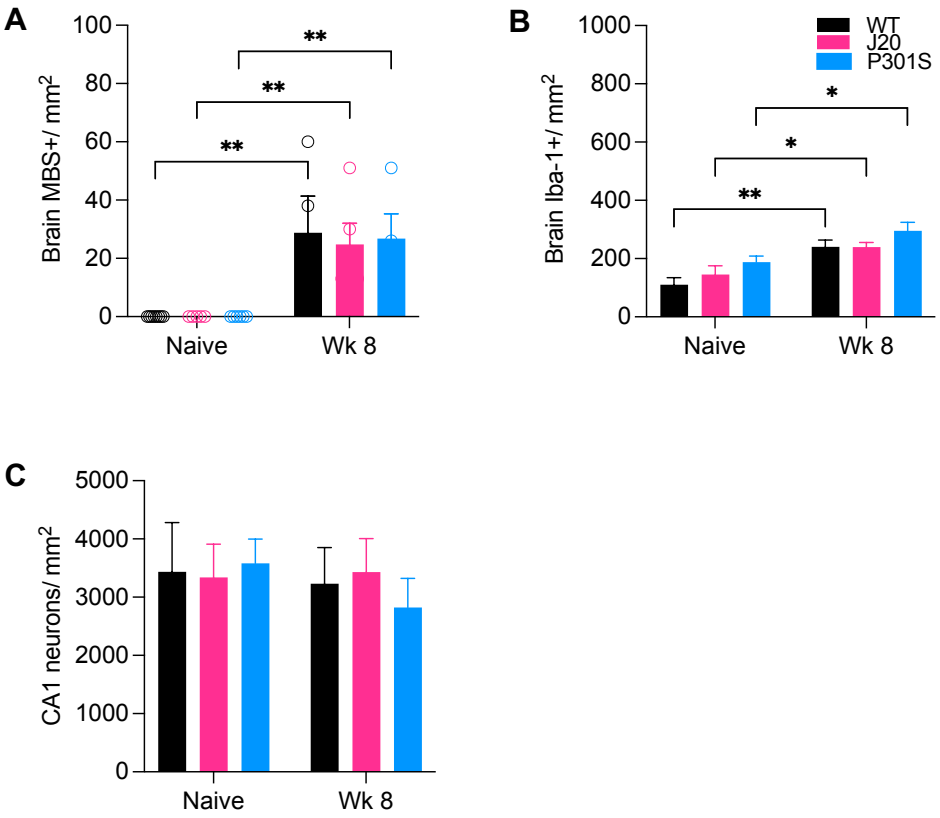


Figure 4.4 Brain histological outcome after chronic TBI. Graphs show (A) brain MBS+, (B) brain Iba-1+, and (C) CA1 neurons quantification. No difference was noted across groups at Week 8. Two-way ANOVA with original FDR method of Benjamini and Hochberg post-hoc test set at 0.05. *p<0.05, **p<0.01. Identified outliers using ROUT method set at Q=1% were removed. Wk 8, week 8.

Number of mice per group for brain MBS+; WT naïve (n=8), WT week 8 (n=5), J20 naïve (n=5), J20 week 8 (n=5), P301S naïve (n=6), P301S week 8 (n=4).

Number of mice per group for brain Iba-1+; WT naïve (n=5), WT week 8 (n=5), J20 naïve (n=5), J20 week 8 (n=5), P301S naïve (n=5), P301S week 8 (n=5).

Number of mice per group for CA1 neurons; WT naïve (n=4), WT week 8 (n=4), J20 naïve (n=4), J20 week 8 (n=3), P301S naïve (n=5), P301S week 8 (n=3).

4.2.4 Chronic TBI resulted in increased hepatic *IL-6* expression in P301S group

A range of hepatic pro-inflammatory molecules were analysed using RT-qPCR. Two-way ANOVA reported no significance for relative *IL-1β* expression (Figure 4.5A; interaction p=0.548, TBI main effect p=0.791, genotype main effect p=0.253). Genotype main effect ($p<0.05$) was revealed significant for *IL-6* expression level, when analysed using two-way ANOVA. However, interaction (p=0.132) and TBI main effect (p=0.660) was revealed not significant (Figure 4.5B). Original FDR method of Benjamini and Hochberg post-hoc test demonstrated higher *IL-6* level in P301S (1.905 ± 0.644) when compared to WT (0.521 ± 0.072) at week 8 with $p<0.01$ significance, with 3.7-fold difference.

Two-way ANOVA analysis of *TNF-α* reported no meaningful statistical result with interaction p=0.097; TBI p=0.395, genotype p=0.311 (Figure 4.5C). Furthermore, two-way ANOVA analysis of *GFAP* revealed significant TBI main effect $p<0.05$, with insignificant interaction p=0.320, and genotype main effect p=0.259 (Figure 4.5D). Original FDR method of Benjamini and Hochberg post-hoc test showed significant difference between J20 naïve (1.666 ± 1.040) vs J20 week 8 (0.164 ± 0.025) with $p<0.05$ (Figure 4.5D).

Two-way ANOVA analysis of *SAA-2* reported insignificant interaction p=0.093, TBI main effect p=0.156, and genotype main effect p=0.088 (Figure 4.5E). Due to insignificant main effects, post-hoc test was not performed for *SAA-2* molecule. Moreover, two-way ANOVA analysis for *SAP* expression reported significant

interaction ($p<0.05$) and TBI main effect ($p<0.05$), but insignificant genotype main effect ($p=0.170$) (Figure 4.5F). Post-hoc analysis revealed markedly higher ($p<0.05$) WT naïve expression (1.000 ± 0.116) when compared to J20 naïve (2.310 ± 0.414). After chronic TBI, no significant difference was noted between week 8 groups, albeit the *SAP* expression of WT week 8 (2.760 ± 0.432) vs P301S week 8 (1.594 ± 0.212) showed a near significance ($p=0.059$). However, WT week 8 (2.760 ± 0.432) showed an elevated *SAP* expression when compared to WT naïve (1.000 ± 0.116) with $p<0.05$ (Figure 4.5F; two-way ANOVA, original FDR method of Benjamini and Hochberg post-hoc test set at 0.05).

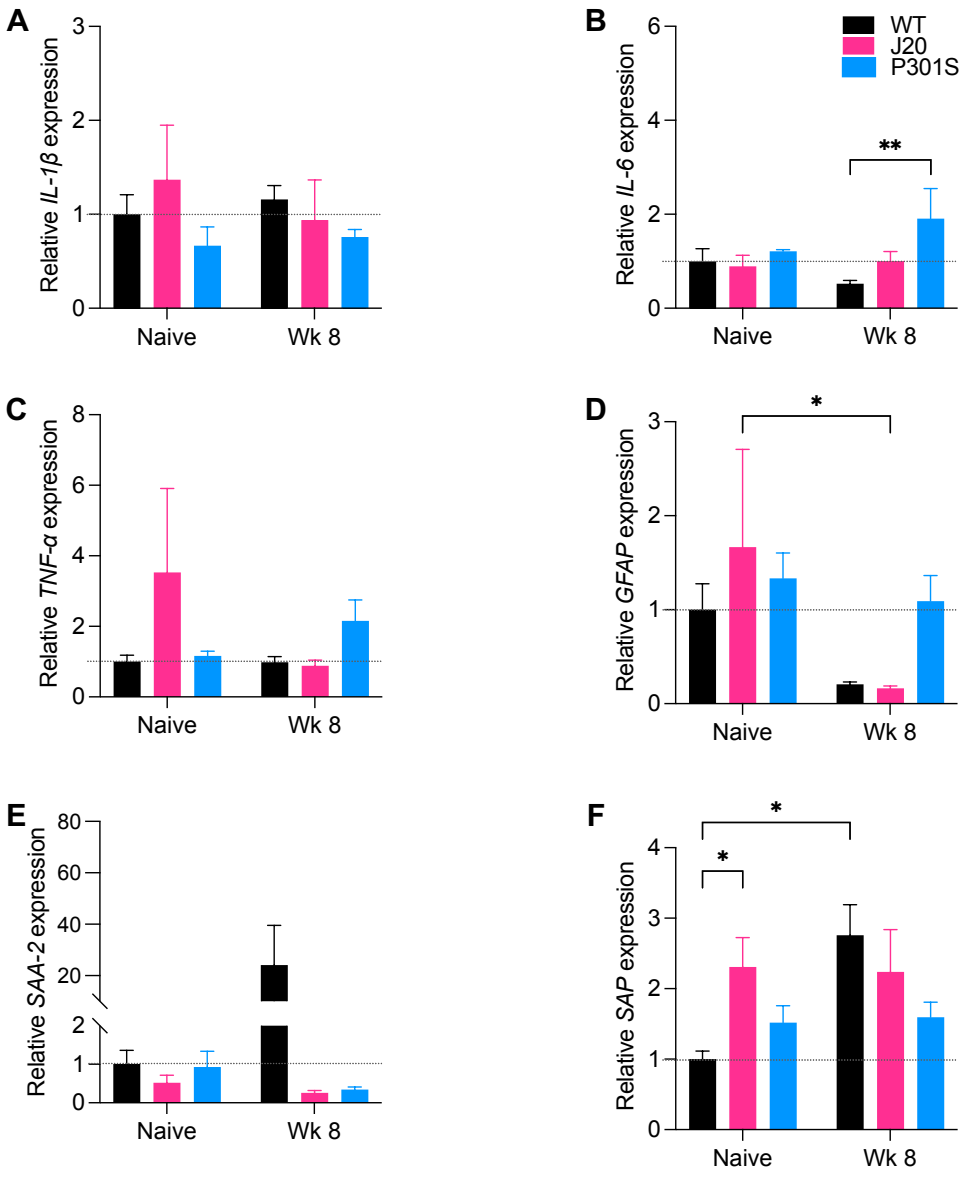


Figure 4.5 Relative expression of pro-inflammatory molecules in the liver as examined by RT-qPCR. Graphs represent the relative expression of (A) *IL-1β,* (B) *IL-6,* (C) *TNF-α,* (D) *GFAP*, (E) *SAA-2* and (F) *SAP*. The pro-inflammatory genes were normalised against housekeeping gene *B2M*. Two-way ANOVA with original FDR method of Benjamini and Hochberg post-hoc test was performed where applicable. P301S mutants expressed markedly higher IL-6 when compared to WT controls at Week 8. *p<0.05, **p<0.01. Identified outliers using ROUT method set at Q=1% were removed. Wk 8, week 8.

Number of mice per group for IL-1β, IL-6, TNF-α, GFAP, SAP; WT Naïve (n=8), WT Week 8 (n=8), J20 Naïve (n=5), J20 Week 8 (n=5), P301S Naïve (n=7), P301S Week 8 (n=6).

Number of mice per group for SAA-2; WT naïve (n=8), WT week 8 (n=7), J20 naïve (n=5), J20 week 8 (n=5), P301S naïve (n=7), P301S week 8 (n=6).

4.2.5 No changes in liver neutrophils and Kupffer cell number after chronic TBI

A set of chemokines that may play a role in neutrophil and Kupffer cells recruitment were analysed by RT-qPCR. Four chemokines were chosen namely *CCL-3*, *CCL-9*, *CXCL-1*, and *CXCL-10*.

Two-way ANOVA analysis of *CCL-3* expression level reported interaction $p=0.082$, TBI $p=0.429$, genotype $p<0.05$ (Figure 4.6A). Original FDR method of Benjamini and Hochberg post-hoc test was applied, and significant difference was seen between WT naïve (1.000 ± 0.165) vs J20 naïve at $p=0.01$, as well as J20 naïve (2.246 ± 0.832) vs P301S naïve (0.730 ± 0.064) at $p<0.01$. No meaningful difference was noted between groups after chronic TBI at week 8.

Two-way ANOVA analysis of *CCL-9* expression level revealed no significant results, with interaction $p=0.471$, TBI $p=0.553$, genotype $p=0.920$ (Figure 4.6B), Similarly, two-way ANOVA analysis of *CXCL-1* (Figure 4.6C; interaction $p=0.464$, TBI main effect $p=0.409$, genotype main effect $p=0.404$) and *CXCL-1*0 (Figure 4.6D; interaction $p=0.230$, TBI main effect $p=0.087$, genotype main effect $p=0.374$) were also shown not significant.

Furthermore, the quantification for liver MBS+ (Figure 4.6E; two-way ANOVA; interaction $p=0.133$, TBI main effect $p=0.787$, genotype main effect $p=0.461$) and Iba-1+ (Figure 4.6F; two-way ANOVA; interaction $p=0.641$, TBI main effect $p=0.765$ genotype main effect $p=0.08$) cells were made and no difference was seen between groups after chronic TBI at week 8.

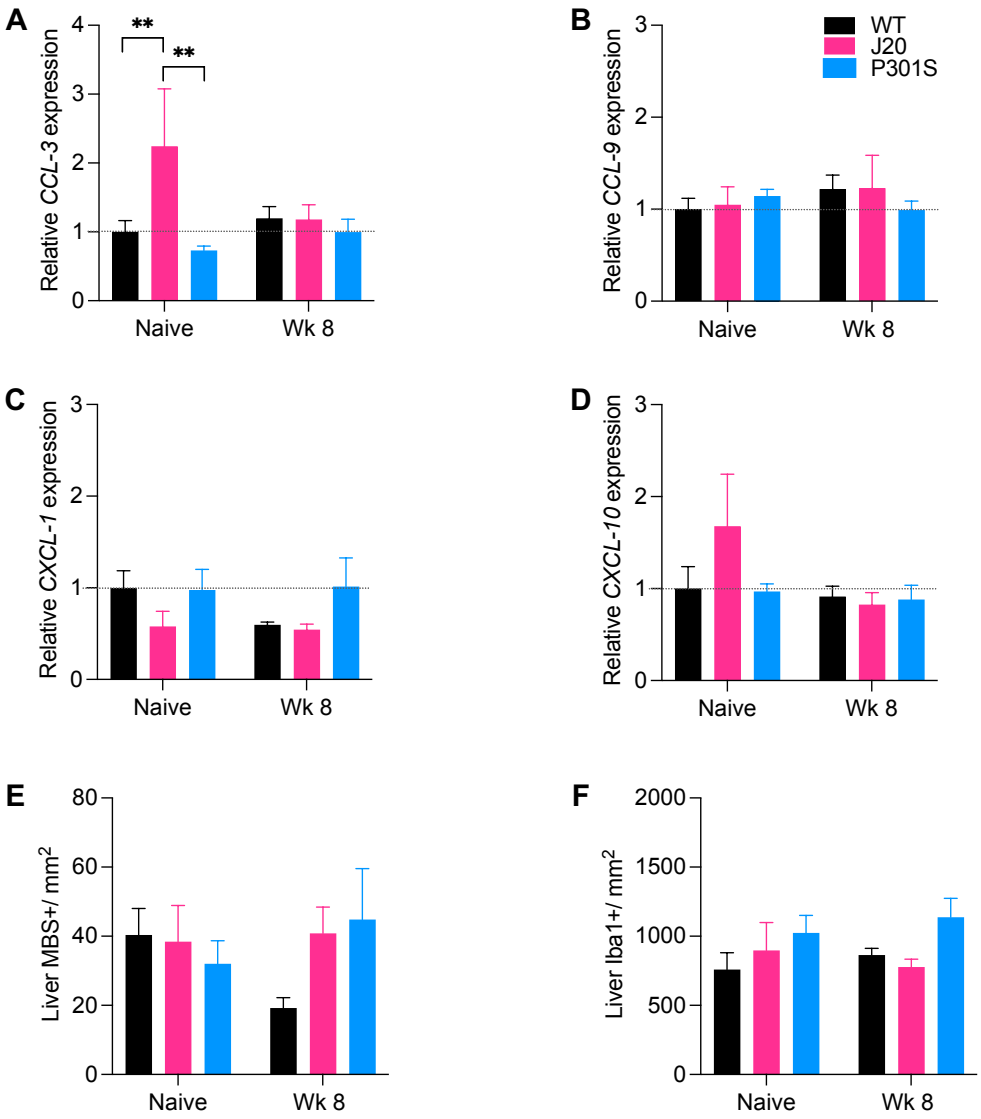


Figure 4.6 Relative expression of hepatic chemokines and histological outcomes. Graphs illustrate relative expression of (A) *CCL-3*, (B) *CCL-9*, (C) *CXCL-1*, and (D) *CXCL-1*0. No difference was found between groups at Week 8. Histological outcomes on (E) liver MBS+ and (F) liver Iba-1+ revealed negligible difference between groups after chronic TBI. Results are expressed as mean ± SEM. Two-way ANOVA with Original FDR method of Benjamini and Hochberg post-hoc test. **p≤0.01. Identified outliers using ROUT method set at Q=1% were removed. Wk 8, week 8.

Number of mice per group for CCL-3, CCL-9 and CXCL-10; WT naïve (n=8), WT week 8 (n=8), J20 naïve (n=5), J20 Week 8 (n=5), P301S naïve (n=7), P301S week 8 (n=6).

Number of mice per group for CXCL-1; WT naïve (n=8), WT week 8 (n=6), J20 naïve (n=5), J20 week 8 (n=5), P301S naïve (n=7), P301S week 8 (n=6).

4.2.6 Decreased total EV and exosome concentration after chronic TBI in P301S group

To investigate the EV profile after chronic TBI, EV size distribution (Figure 4.7A) was plotted, followed by assessment of total EV concentration (Figure 4.7B), median EV size (Figure 4.7C) and total exosome concentration (Figure 4.7D).

Chronic TBI was shown to have genotype main effect on total EV concentration (Figure 4.7B; two-way ANOVA; interaction $p=0.434$, TBI main effect $p=0.610$, genotype $p<0.01$). Original FDR method of Benjamini and Hochberg post-hoc test reported significance between WT week 8 (5.42×10^9) vs P301S week 8 (1.64×10^9) at $p<0.05$, and J20 week 8 (6.06×10^9) vs P301S week 8 (1.64×10^9) at $p<0.05$. WT Two-way ANOVA analysis on median EV size showed no effect on interaction ($p=0.723$), TBI ($p=0.686$) and genotype ($p=0.956$) (Figure 4.7C).

Two-way ANOVA analysis for total exosome concentration revealed significant genotype main effect of $p<0.01$, but the interaction ($p=0.289$) and TBI ($p=0.395$) was shown to be not significant (Figure 4.7D). Original FDR method of Benjamini and Hochberg post-hoc test reported significance between WT week 8 (1.94×10^{10}) vs P301S week 8 (6.11×10^9) at $p<0.05$, and J20 week 8 (2.26×10^{10}) vs P301S week 8 (6.11×10^9) at $p=0.01$.

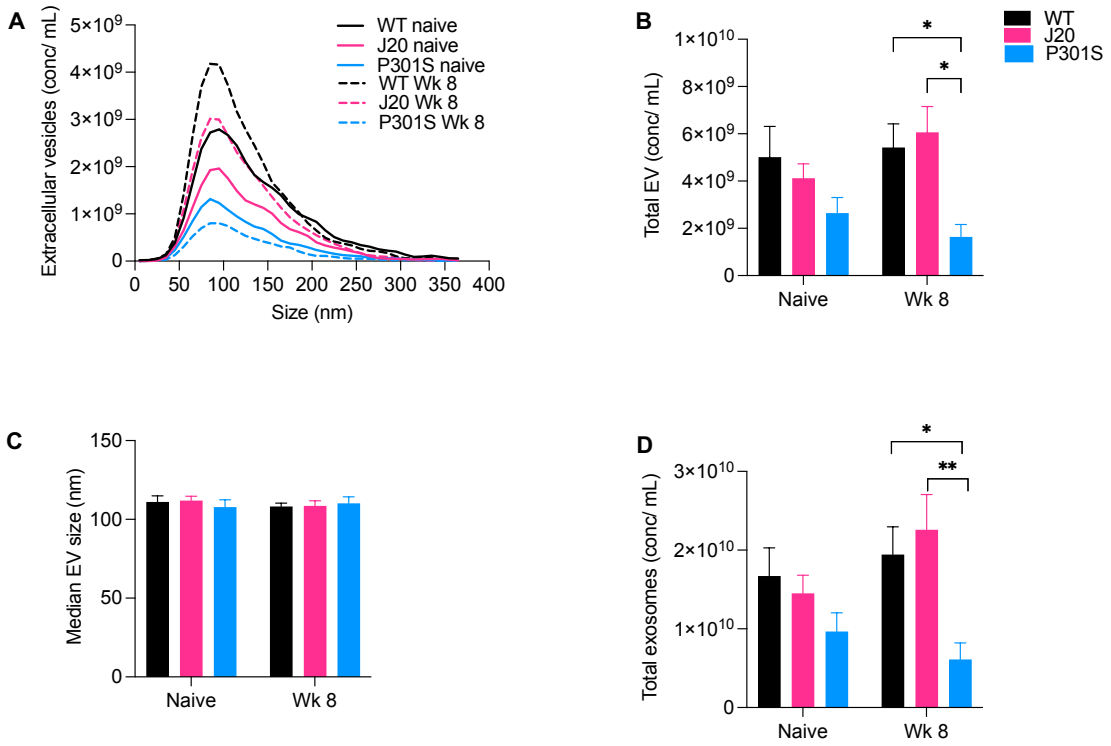


Figure 4.7 EV profile and exosome quantification following chronic TBI. Line graph depicts (A) EV size distribution profile of WT, J20 and P301S for naive and week 8 timepoints (size range 0-350 nm). (B) Total EV concentration, (C) median EV size, and (D) total exosomes concentration (size range 30-150) were measured. No difference between groups was observed post-chronic TBI. Results are expressed as mean ± SEM; two-way ANOVA. Identified outliers using ROUT method set at Q=1% were removed. Wk 8, week 8. *$p<0.05$, **$p\leq0.01$.

Number of mice per group for size distribution profile, total EV and total exosome concentration; WT naïve (n=9), WT week 8 (n=7), J20 naïve (n=5), J20 week 8 (n=5), P301S naïve (n=7), P301S week 8 (n=5).

Number of mice per group for median EV; WT naïve (n=10), WT week 8 (n=8), J20 naïve (n=5), J20 week 8 (n=5), P301S naïve (n=7), P301S week 8 (n=5).

4.3 Discussion

4.3.1 Principal findings

In this chapter I investigated the effects of chronic TBI in J20 and P301S models from molecular and histological perspective by comparing these AD mutants to age-matched WT control. In the P301S mutant cohort, significant increase in brain AT8 tau burden was visualised following chronic TBI (Figure 4.2D-E). Tau or amyloid deposition was not observed in WT and J20 groups, neither in the naive nor TBI groups respectively. Two-trial Y-maze showed significant difference between P301S week 8 vs WT week 8 (Figure 4.3C), however, it should be noted that the effect was not due to chronic TBI ($p=0.4085$), rather it was due to genotype difference ($p<0.001$). Light-dark box behavioural test demonstrated increased impulsivity in both P301S and WT after chronic TBI ($p<0.05$), as seen through reduced time spent in the dark chamber when compared to naive (Figure 4.3E). Nonetheless, no difference between P301S and WT was seen at week 8

Brain MBS+ and Iba-1+ densities were shown elevated in all groups after chronic TBI, but J20 and P301S mutants did not show notable difference when compared to WT control (Figure 4.4A-B). RT-qPCR assessment on hepatic pro-inflammatory molecules revealed elevated *IL-6* expression in P301S when compared to WT at week 8 (Figure 4.5). The level of hepatic MBS+ and Iba-1+ cells at week 8 were not significant against naive (Figure 4.6E-F). Total EV (Figure 4.7B) and exosome (Figure 4.7D) quantification showed significant

reduction in P301S group at week 8 when compared to WT week 8 and J20 week 8 respectively.

4.3.2 Higher AT8 burden in the brain after chronic TBI is correlated with higher *IL-6* expression in the liver

Brain histological analysis indicates accelerated AT8 accumulation in P310S TBI when compared against P301S naive. This finding is in accordance with previous study that observed an increase in AT8 burden in cortex and brainstem area in transgenic tauopathy mice model, both ipsilateral and contralateral to the CCI site after 1-2 months post-injury (Edwards et al., 2020). The same study also observed higher ipsilateral hippocampal tau burden. The mechanism by which secondary injury potentiate the development of tauopathy was investigated by Lucke-Wold and team (2017) which described that endoplasmic reticulum (ER) stress and oxidative stress may play an active role.

They found that dying cells and the cells with pathologic tau accumulation showed higher ER stress, with accompanying markers of tau hyperphosphorylation AT100 (specific antibody against phosphorylated tau at threonine 212 and serine 214), CP-13 (specific antibody against phosphorylated tau at serine 202), and paired helical filaments. TBI is suggested to cause tau acetylation that catalyses tau disengagement from tubulin, resulting in tau hyperphosphorylation and aggregation (B. Lucke-Wold et al., 2017; Trzeciakiewicz et al., 2017). Indeed, an enhanced acetylated-tau level was discovered in human AD with prior TBI history when compared to human AD

cohort without TBI experience (Shin et al., 2021). On the contrary, Flavin and colleagues (2023) proposed that tauopathy is caused by conformational shift of tau towards cis isomeric orientation, causing destabilisation of microtubule binding which potentiates tau aggregation (Flavin et al., 2023).

Previous epidemiology study have implied that approximately 80-85% people affected with mild TBI experienced post-concussion symptoms and recovers within 3 months (Belanger, Curtiss, Demery, Lebowitz, & Vanderploeg, 2005), while a proportion of patients may take up to a year or longer to recover (Cnossen et al., 2018; Haarbauer-Krupa et al., 2021). The post-concussion symptoms reported by patients involve cognitive and somatic alterations such as memory problems, experiencing headache and feeling nauseous, as well as emotional changes such as irritability and depression (Cnossen et al., 2018).

On the contrary, the majority of people who experienced moderate-to-severe TBI experienced long-term adverse health outcomes, and therefore TBI has increasingly been described as a chronic health condition (Haarbauer-Krupa et al., 2021). 30% of moderate TBI survivors experienced worsening symptoms over a 5 year period, especially in memory and learning capacity (N. H. Johnson, de Rivero Vaccari, Bramlett, Keane, & Dietrich, 2023). Furthermore, prospective observational study of adult patients with severe TBI reported persistent impairments that interfere with social integration and participation at 8 years after injury (Ruet et al., 2019), demonstrating long-term consequences of TBI.

In the present study, the memory and anxiety aspects of these P301S mutants after chronic TBI were explored. Surprisingly, no significant difference was found in P301S TBI when compared to WT TBI. These findings are in line with the findings of Bailes and team that observed dysfunctional permeability of BBB, altered neuronal soma, and discernible damage to corticospinal tract axons that extend to areas away from the cortical impact site in the rodent models of mild TBI, without any accompanying behavioural changes (Bailes, Petraglia, Omalu, Nauman, & Talavage, 2013). Interestingly, I discovered that both P301S TBI and WT TBI cohorts displayed increased impulsivity and disinhibition behaviour when compared to naive (Figure 4.3E; TBI main effect $p<0.05$). Spontaneous alternation test was also performed to investigate the function of prefrontal cortex and hippocampus, and no significant difference was reported between groups (Figure 4.3I). It is noteworthy to remark that, as the spontaneous alternations test was done on the same day as the two-trial Y-maze, a carry-over bias might have been introduced to the mice from their prior exposure to the Y-maze setting, which could contribute to the insignificant outcome observed.

In accordance to the disinhibition behaviour observed in TBI groups as compared to naïve (Figure 4.3E), human studies reported that 30% of TBI patients develop disinhibition post-injury (Jang & Kwon, 2017). Behavioural symptoms after TBI such as increased impulsivity, poor cognitive inhibition, aggression, and depression are long-term outcomes associated with TBI, which are risk factors for suicides. Literature review revealed that individuals with TBI history have 3-4 times higher likelihood to die from suicide when compared to general population, with suicidal ideation reported in over 10% patients after TBI (Juengst, Kumar,

Arenth, & Wagner, 2014). A case study on a 27-year-old male with 30 days loss of consciousness and post-traumatic amnesia showed severe disinhibition and violence post-TBI (Jang & Kwon, 2017). It has been suggested that this behaviour is related to injuries of the amygdala, orbitofrontal cortex and anterior cingulate cortex (Jang & Kwon, 2017).

Post-mortem human brains with TBI history showed the presence of prolonged activation of microglia and phagocytic macrophages up to 18 years after a single moderate-to-severe injury (V. E. Johnson et al., 2013). Similarly, in an experimental TBI using CCI mouse model, chronically activated microglia with increased Iba-1, CD68 and MHC Class II molecule CR3/43 were demonstrated in TBI group against control when examined at 1 year post-injury (Loane, Kumar, Stoica, Cabatbat, & Faden, 2014). In confirmation with these studies, I discovered higher brain Iba-1+ cells in the TBI cohort at week 8 when compared to naïve (Figure 4.4B; TBI main effect $p<0.0001$). Pursuant to this discovery, FDR post-hoc test was applied to explore if the presence of AD-like pathology would prompt higher Iba-1+ numbers when compared to control. However, no significant difference was found between groups following chronic TBI.

To my astonishment, peripheral molecular assessment revealed marked increase in *IL-6* level in P301S TBI when compared against WT TBI (Figure 4.5B). Nonetheless, at week 8 negligible differences were observed in liver histological findings (Figure 4.6E-F). The liver histological outcome was expected as the statistical evaluation of hepatic chemo-attractants that are responsible for leukocyte recruitment were shown not meaningful after chronic TBI (Figure 4.6A-

D). Total EV and exosome quantification in P301S was shown significantly reduced after chronic TBI when compared to both WT week 8 and J20 week 8 groups (Figure 4.7). The trend for total EV in P301S chronic TBI cohort was shown opposite to its P301S 6-hour acute TBI cohort (Chapter 3, Figure 3.16). In acute TBI, total EV concentration in P301S TBI was shown elevated when compared to WT TBI (Figure 3.16C, $p<0.05$). Accumulating evidence has suggested that primary and secondary injuries of TBI can influence the concentration level and characteristics of EVs. Because EVs can carry a variety of cargo such as RNA, lipids, proteins, they may serve as regulators of neuroinflammation (X. Liu et al., 2023). EVs were observed to trigger anti-inflammatory or pro-inflammatory effects on the receptor cells that they interact to, depending on their parental origin, and the cargo they carry (Kolonics et al., 2020). Therefore, a follow-up experiment is needed to ascertain the information regarding their parental cell and the cargo they carry in P301S TBI animals, both in acute and chronic TBI cohorts.

There is a scarcity of information regarding *IL-6* expression in the liver during chronic AD-TBI phenomenon from literature findings. In non-TBI human samples, elevated peripheral IL-6 has been suggested as predictor of cognitive decline in late midlife (Singh-Manoux et al., 2014). During brain injury, IL-6 was shown to be secreted principally by astrocytes in the brain (Van Wagoner, Oh, Repovic, & Benveniste, 1999), and in vitro exposure of IL-6 to astrocytes demonstrated mitogenic effect on astrocytes which may contribute to astrogliosis (Kossmann, Hans, Imhof, Trentz, & Morganti-Kossmann, 1996; Selmaj, Farooq, Norton, Raine, & Brosnan, 1990). Activation of astrocytes after mild or moderate focal

TBI was suggested to offer neuroprotection by restricting inflammation and preserving neural tissue (Myer, Gurkoff, Lee, Hovda, & Sofroniew, 2006).

Astrocyte hypertrophy was shown prominent in the cerebral cortex at 28 days post-injury, with reactive astrocytes intermingled with well-preserved neurons beneath the site of injury (Myer et al., 2006). Dual nature of astrogliosis has been ascribed to neuroprotective and neurodegenerative characteristics. Increased secretion of pro-inflammatory chemokines including IL-6 is associated with increased BBB breakdown (Takeshita et al., 2021). Experimental evidence from CCI and closed head injury model exhibited biphasic pattern of BBB breakdown after injury, with increased permeability observed in primary phase in hours post-TBI, followed by a secondary delayed phase at 3–7 days following injury (Karve et al., 2016). In between primary and secondary phase is a period where BBB permeability was shown decreased. Higher permeability of BBB would permit infiltration of peripheral immune cells that may contribute to injury repair, but could also play a role in exacerbating the secondary injury (Karve et al., 2016).

Intriguingly, astrocytes activation and high level of IL-6 have been implicated in disinhibition, impulsivity, and depression symptoms in many studies. For example, the activation of astrocytes in the corpus collosum, motor, and somatosensory cortex after TBI has been suggested to underlie the symptoms of impulsive behaviour and altered cognitive function (B. P. Lucke-Wold et al., 2014). Preliminary findings from other study described white matter changes, frontal lobe dysfunction, and axonal damage in monoaminergic pathways that follow after TBI are linked to disinhibition behaviour, likely to be triggered by

inflammation (Juengst et al., 2014; Yurgelun-Todd et al., 2011). In particular, altered level of inflammatory cytokines IL-2, IL-6, IL-8, TNF-α and vascular endothelial growth factor (VEGF) are associated with suicidal behaviour (Serafini et al., 2013). Lindqvist and team investigated both plasma and CSF IL-1β, IL-6, IL-8, TNF-α in 63 suicide attempters and found that increased IL-6 is correlated to symptom severity, as violent suicide attempters showed the highest IL-6 (Lindqvist et al., 2009).

In the present study, RT-qPCR investigation on molecular expression of inflammatory cytokines in the brain were not performed, and the outcomes from behavioural study were gained from a small sample size [number of mice per group: WT naïve (n=6), WT chronic TBI (n=4), P301S naïve (n=7), P301S chronic TBI (n=6)]. Therefore, given lack of research on *IL-6* expression in the brain and liver during chronic AD-TBI, it may be a thought-provoking approach for future studies to take in the direction of investigating IL-6 brain-periphery crosstalk in AD-TBI mutants, astrocyte histology profile, and their correlation with behavioural changes in a larger sample size.

CHAPTER 5

J20 METABOLITE PROFILE

Chapter 5 : The metabolite profile of J20 mutant using untargeted approach

5.1 Introduction

Metabolomics approaches have gained increasing importance in the medical field due to their enormous potential in providing insights into alterations in genetics, transcripts, proteins, and external environmental influences that occur within an individual (Wilkins & Trushina, 2018). Metabolite profiling involves the quantitative detection of a vast number of small-molecule metabolites, capturing the information on the biochemical reactions during metabolism in tissues and body fluids. Differences in the metabolomic fingerprints resulting from the body operating under different circumstances such as diseased and healthy can lead to identification of novel biomarkers for disease diagnosis, prognosis, treatment, and progression (Aderemi et al., 2021; Yin, Harms, Hankemeier, Kindt, & de Lange, 2023). The two widely used analytical techniques for metabolomics study are NMR spectroscopy and MS. The NMR spectroscopy is most commonly utilised for multiple tissues investigation due to its advantages such as requiring little to no sample preparation, non-destructive to samples as well as yielding highly reproducible outcomes (Gowda et al., 2008).

Metabolomics methodologies can be divided into targeted and untargeted approach. Targeted metabolomics measure a select group of a known metabolites that have been biochemically characterised to explore specific metabolic pathways. Targeted approach is typically more quantitative, can be employed for measuring the influence of therapeutics in drug pharmacokinetic

study, and can also be used to validate biomarkers recognised using untargeted metabolomic study (Bodnar, Roberts, Higgins, & Bachstetter, 2019; Yin et al., 2023; X. Zhang, Zhu, Wang, Zhang, & Cai, 2016). Conversely, the untargeted metabolomics is an unbiased and global comprehensive analysis of all measurable small-molecule metabolites in the sample including unknown analyte. Due to high abundance of analytes and the identity of the molecules are often unknown, the measurement is commonly performed through relative quantification of metabolites. This approach may aid hypothesis building through novel biomarker and metabolic pathway discovery, as well as providing basis for future targeted metabolomics studies (Yin et al., 2023). Metabolic pathways are largely conserved between species, hence the biomarker discovery from animal preclinical studies offers valuable translational potential into human clinical care and medical field advancement (Wilkins & Trushina, 2018).

AD is a debilitating neurodegenerative disease characterised by amyloid plaque and NFT pathologies. While these two proteins are the hallmarks of this progressive disease, other pathologies that may contribute to the production of these pathogenic proteins may have begun 20 years or more before the manifestation of cognitive symptoms in AD patients. Example of these pathologies include induction of oxidative stress and inflammatory cascades, mitochondrial dysfunction, impaired synaptic transmission and cell signalling, as well as altered calcium and lipid homeostasis (Hunsberger et al., 2020; Wilkins & Trushina, 2018). There is a scarcity of literature reporting on metabolite alterations in both the brain and periphery, as rodent AD metabolomics studies are mostly focused on only brain tissues and/or plasma (Yin et al., 2023). It is

important to explore the metabolite profile of peripheral tissues and bodily fluids in relation to the CNS, as metabolic dysfunction linked to AD pathology is not limited to CNS but also extends systemically (Muntsant & Giménez-Llort, 2022; Van Der Velpen et al., 2019). In this chapter, transgenic J20 mutant and its age-matched WT control of varying ages from 3 to 50 weeks were classified into early and late AD, representing the pre-clinical AD phase and MCI-AD dementia phase, respectively. The untargeted metabolomics approach using 1H NMR modality was adopted, and the OPLS-DA multivariate analysis, which can discern the differences in diseased as opposed to healthy groups was employed. The outcome of this chapter will provide a comprehensive brain-periphery metabolite profiling, comprising PFC, HC, liver, spleen, and serum components of the J20 mutant. As AD is a complex disease, there is a need for a continuous search for new biomarkers to better recognise individuals at risk for AD. Therefore, at the end of this chapter, a list of potential peripheral biomarkers will be generated.

5.1.1 Chapter aims

The aims for this chapter are as follows:

1- To investigate the metabolite signature of early AD (pre-clinical AD) and late AD (MCI-AD dementia) stage
2- To identify top discriminatory metabolites of J20 mutant that are present in both brain (PFC, HC) and periphery (liver, spleen, serum) samples
3- To generate a list of potential peripheral biomarkers

5.1.2 Experimental design

Naive J20 and WT animals (3 - 50 weeks; total n=90) were used in this study. Mice were grouped into early (n=36) and late AD (n=54) at 19 weeks cut-off point. This cut-off point was chosen as it indicates the mark where the progression in AD pathology is more nuanced (Alzforum, 2019), as the spatial memory and learning deficit is apparent as measured by radial arm maze (Wright et al., 2013) and Morris water maze (Cheng et al., 2007) (Figure 5.1). In this hAPP-J20 mutant, neuronal loss and neuroinflammation were shown to precede Aβ plaque deposition (Wright et al., 2013). Neuronal loss from hippocampal CA1 region was exhibited as early as 12 weeks old, correlated to increased number of activated microglia and astrogliosis as the mice age increases. Although intraneuronal Aβ was observed throughout the hippocampus as early as 6 weeks old, the deposition of Aβ plaque was only observed in the hippocampus at 36 weeks old (Shibly et al., 2023; Wright et al., 2013).

The early AD group corresponds to pre-clinical phase of disease progression, whereas the late AD group relates to the MCI-AD phase. PFC (n=81), HC (n=90), liver (n=83), spleen (n=84), and serum (n=80) samples were investigated for top discriminatory metabolites using 1H NMR modalities coupled with OPLS-DA untargeted approach.

It should be noted that although a total of n=90 mice was culled for this NMR study, the number of samples included during analysis varies according to tissues, as some samples were excluded due to small sample volume or weight,

that did not meet the minimum inclusion criteria set for each tissue; PFC (18-35 mg), HC (40-65 mg), liver (100-125 mg), spleen (20-40 mg) and serum (100 μL). Figure 5.1 outlines a simplified timeline of J20 phenotypic changes across disease progression, with the 19 weeks cut-off point where the mice in this chapter were classified into early AD or late AD group, which represented pre-clinical AD and MCI-AD phase respectively.

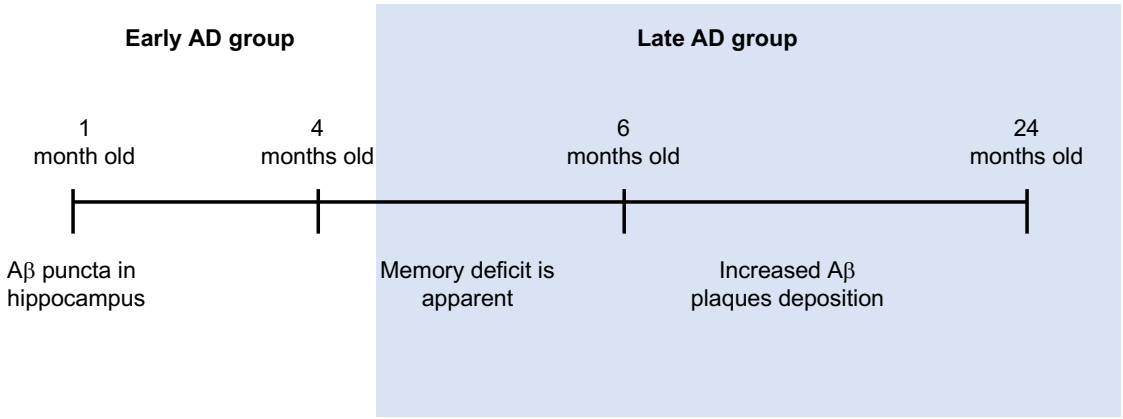


Figure 5.1 J20 mutant phenotypic timeline. Mice (n=90) were classified into early AD (n=36) or late AD (n=54) group at 19 weeks old cut-off where the spatial memory and learning deficit is apparent as measured by radial arm maze (Wright et al., 2013) and Morris water maze (Cheng et al., 2007). In this chapter, the early AD group corresponds to pre-clinical AD and late AD group corresponds to MCI-AD phase respectively. Timeline adapted and simplified from Alzforum website: https://www.alzforum.org/research-models/j20-pdgf-appswind

5.2 Results

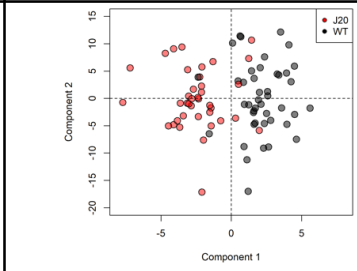
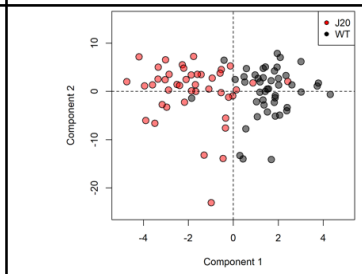
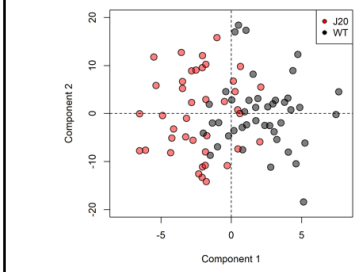
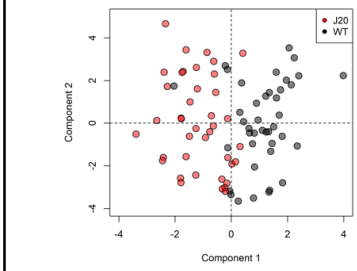
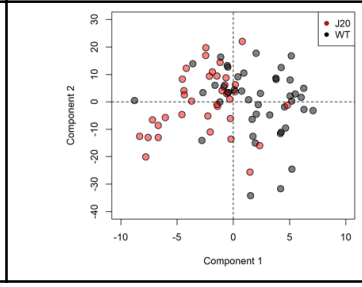
5.2.1 J20 metabolomics profile is different to WT

To validate that the in-house OPLS-DA script can discern J20 metabolites against WT control, OPLS-DA analysis was run on PFC, HC, liver, spleen, and serum samples regardless of age classification. In Table 5.1, the OPLS-DA plots illustrated distinct separation between J20 (represented by red circles) and WT (represented by black circles) across samples. The accuracy, specificity and sensitivity of samples showed more than 60% confidence with $p<0.0001$ when the OPLS-DA model of the samples was compared against random chance, when analysed through t-test. The accuracy described in Table 5.1 for each tissue type was displayed as boxplots in Figure 5.2.

The PFC samples of J20 vs WT OPLS-DA model displayed a significantly higher value of mean predictive accuracy when compared against the mean predictive accuracy of random chance (model created through random class assignments) (Figure 5.2A; mean ± SD, 79 ± 3% vs 51 ± 7%). The HC samples showed a great separation for J20 vs WT OPLS-DA model as opposed to random chance model with mean predictive accuracy of 74 ± 4% vs 49 ± 6% (Figure 5.2B). Moreover, the J20 vs WT liver samples showed a distinct separation with mean predictive accuracy of 64 ± 4% when compared to random chance model of 50 ± 7% (Figure 5.2C). The mean predictive accuracy of J20 vs WT OPLS-DA model for spleen samples is higher than the random chance model with 73 ± 3% vs 49 ± 6% (Figure 5.2D). The serum samples showed a great separation of J20 vs WT, with

the mean predictive accuracy of 64 ± 4% when compared to the random chance OPLS-DA model of 51 ± 7% (Figure 5.2E).

Table 5.1 OPLS-DA plots of J20 vs WT (all age). The sample number, mean predictive accuracy, sensitivity, specificity details for J20 vs WT (all age) are outlined for PFC, HC, liver, spleen, and serum samples. In the OPLS-DA plot, J20 samples are represented by red circle whereas WT samples are represented by black circles. ****p<0.0001 by Kolmogorov-Smirnov test.

Sample	WT vs J20 (all age)	Details	
PFC		Sample number	Total (n= 81) J20 (n=38) WT (n=43)
		Accuracy ± SD (%)	79 ± 3 ****
		Specificity ± SD (%)	84 ± 6 ****
		Sensitivity ± SD (%)	75 ± 5 ****
HC		Sample number	Total (n= 90) J20 (n=43) WT (n=47)
		Accuracy ± SD (%)	74 ± 4 ****
		Specificity ± SD (%)	73 ± 5 ****
		Sensitivity ± SD (%)	75 ± 4 ****
Liver		Sample number	Total (n= 83) J20 (n=40) WT (n=43)
		Accuracy ± SD (%)	64 ± 4 ****
		Specificity ± SD (%)	63 ± 5 ****
		Sensitivity ± SD (%)	65 ± 6 ****
Spleen		Sample number	Total (n=84) J20 (n=41) WT (n=43)
		Accuracy ± SD (%)	73 ± 3 ****
		Specificity ± SD (%)	77 ± 5 ****
		Sensitivity ± SD (%)	70 ± 4 ****
Serum		Sample number	Total (n=80) J20 (n=37) WT (n=43)
		Accuracy ± SD (%)	64 ± 4 ****
		Specificity ± SD (%)	67 ± 5 ****
		Sensitivity ± SD (%)	63 ± 8 ****

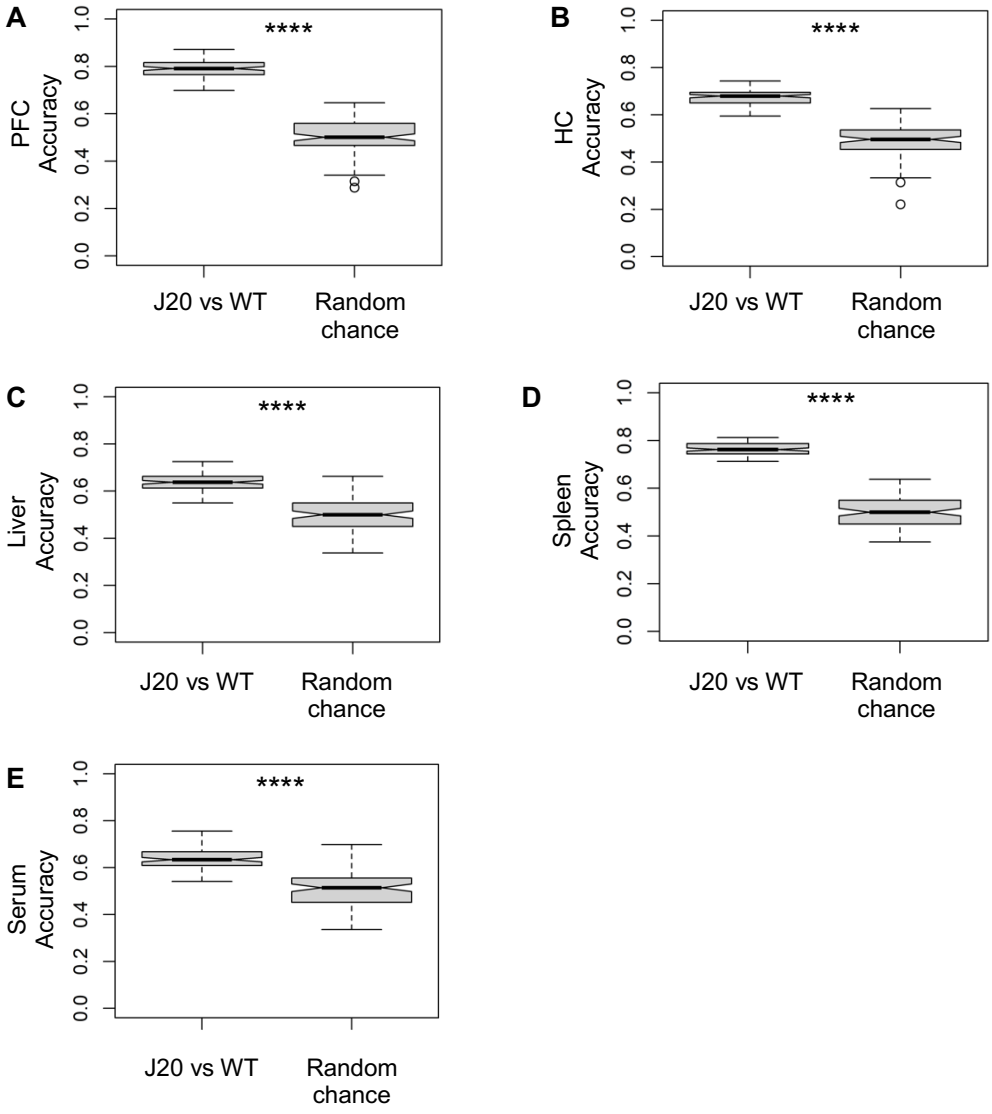
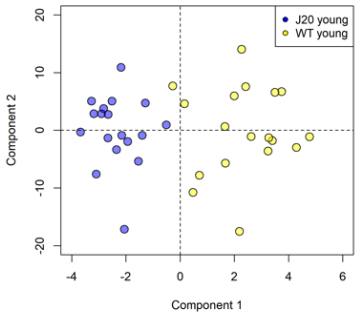
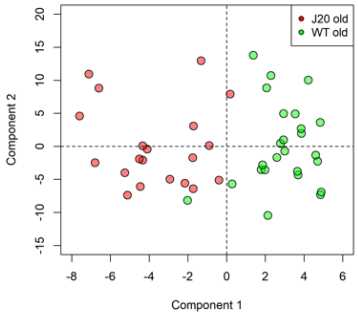


Figure 5.2 Box plots of predictive accuracies from the OPLS-DA models of J20 vs WT (all age) against random chance. Figures illustrate the box plots for (A) PFC, (B) HC, (C) liver, (D) spleen, and (E) serum samples. ****indicates $p<0.0001$ by Kolmogorov-Smirnov test.

5.2.2 Prefrontal cortex

To investigate PFC metabolite changes throughout the course of AD, a total of 81 PFC samples were grouped into early and late AD. To identify metabolite separation between J20 mutant and WT control, OPLS-DA was used to construct predictive model of J20 young vs WT young (Table 5.2; early AD) and J20 old vs WT old (Table 5.2; late AD). The representative OPLS-DA scores plot displayed a great distinction between J20 and WT in both early and late AD group.

Table 5.2 Prefrontal cortex OPLS-DA plots illustrated a distinct separation for J20 vs WT samples in early and late AD stage. The predictive accuracy, specificity, and sensitivity of the models are expressed in mean ± SD. ****p<0.0001 by Kolmogorov-Smirnov test. Purple = J20 young, yellow = WT young, red = J20 old, green = WT old.

PFC samples	OPLS-DA plot	Details	
Early AD (J20 young vs WT young)		Sample number	Total (n = 36) J20 young (n=18) WT young (n=18)
		Accuracy ± SD (%)	75 ± 5 ****
		Specificity ± SD (%)	70 ± 7 ****
		Sensitivity ± SD (%)	81 ± 7 ****
Late AD (J20 old vs WT old)		Sample number	Total (n=45) J20 old (n=20) WT old (n=25)
		Accuracy ± SD (%)	72 ± 5 ****
		Specificity ± SD (%)	78 ± 7 ****
		Sensitivity ± SD (%)	67 ± 8 ****

The mean predictive accuracy of J20 young vs WT young OPLS-DA model (75 ± 5%) is significantly higher than the mean predictive accuracy of random chance (50 ± 9%) (Figure 5.3A). Besides that, the mean predictive accuracy of J20 old vs WT old OPLS-DA model (72 ± 5%) also exhibited higher value when compared to the mean predictive accuracy of random chance (50 ± 9%) (Figure 5.3B).

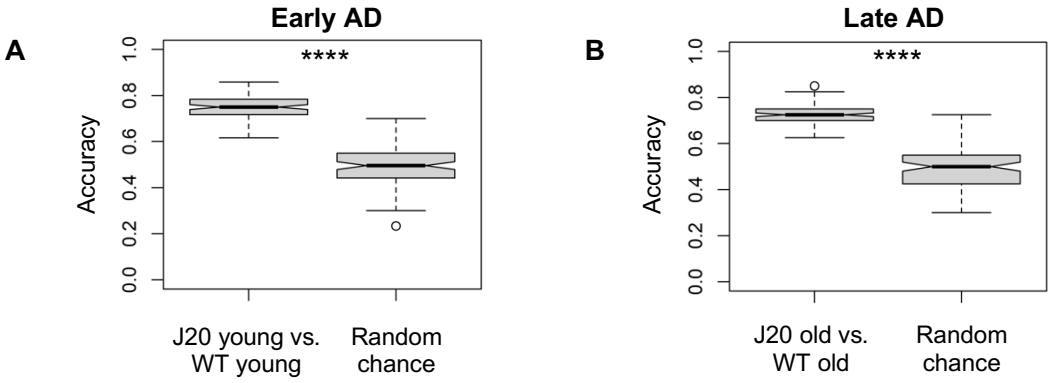


Figure 5.3 Box plots of predictive accuracies from the PFC OPLS-DA models of J20 vs WT against random chance. Figures illustrate the box plots for (A) early AD and (B) late AD stage. ****indicates p<0.0001 by Kolmogorov-Smirnov test.

5.2.2.1 Identifying the top discriminatory metabolites between early AD and late AD

To identify the discriminatory metabolites from the J20 vs WT OPLS-DA models of early and late AD, VIP scores were generated (Figure 5.4). The VIP score cut-off at 1.63 and 1.71 for early and late AD respectively was determined by identifying a 'drop-off' on the VIP ranking plot. Top discriminatory metabolite is defined as the metabolite with the VIP score above this cut-off point, and PFC top metabolites are detailed in Table 5.3.

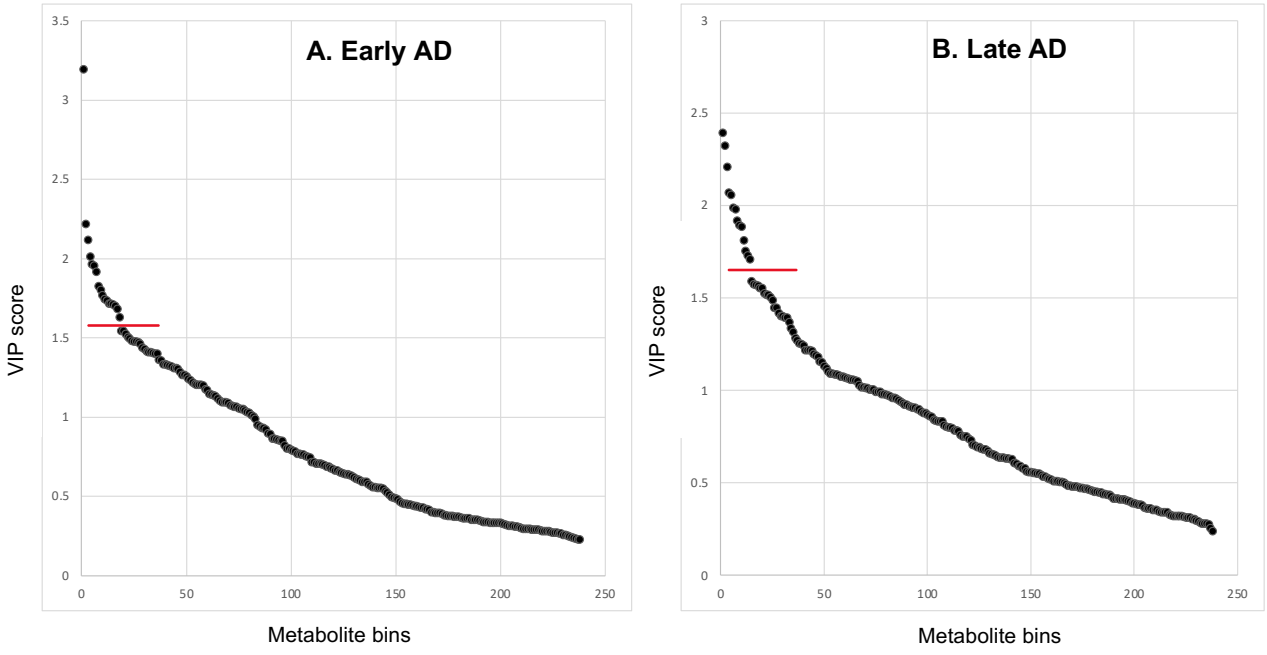


Figure 5.4 VIP ranking plot for PFC samples. The VIP ranking plot identifies the top discriminatory metabolites in (A) early AD and (B) late AD OPLS-DA models. The red line indicates the VIP score cut-off at 1.63 for early AD and 1.71 for late AD respectively, before a 'drop-off' in the VIP score.

Table 5.3 List of top discriminatory metabolites in PFC samples. Table below detailed the top discriminatory metabolites and their corresponding chemical shifts (spectral bins), VIP scores and rank for early and late AD group.

Early AD: J20 young vs WT young			
Top discriminatory metabolites	**Bin (ppm)**	**VIP score**	**VIP rank**
citrate	2.68....2.70.	3.19	1
	2.66....2.68.	2.22	2
fatty acyl chain =CH-CH2-CH=	2.78....2.80.	2.12	3
	2.82....2.84.	1.97	5
glucose	3.42....3.44.	2.01	4
	3.44....3.46.	1.80	9
	3.84....3.86.	1.70	16
lactate	1.32....1.34.	1.83	8
	4.08....4.10.	1.74	11
	4.10....4.12.	1.63	18
sphingomyelin	3.22....3.24.	1.77	10

Late AD: J20 old vs WT old			
Top discriminatory metabolites	**Bin (ppm)**	**VIP score**	**VIP rank**
fatty acyl chain =CH-CH2-CH=	2.82....2.84.	2.40	1
	2.78....2.80.	2.32	2
citrate	2.64....2.66.	2.07	4
	2.66....2.68.	1.98	7
	2.50....2.52.	1.89	9
	2.68....2.70.	1.81	11
glucose	3.86....3.88.	2.06	5
lactate	1.32....1.34.	1.92	8
	4.10....4.12.	1.89	10
glutamine	2.48....2.50.	1.73	13
lysine	1.90....1.92.	1.71	14

5.2.2.2 Concentration of top PFC metabolites during early and late AD phase

Next, to explore the concentration level of the top discriminatory metabolites, two-way ANOVA was performed, and six metabolites were shown significant namely citrate, fatty acyl chain, lactate, glucose, glutamine, and lysine.

Citrate showed genotype main effect of $p<0.0001$ (Figure 5.5A), and Tukey's post-hoc revealed $p<0.01$ differences in early AD cohort. The J20 young group showed lower level of citrate (0.0144 ± 0.0004) when compared to WT young (0.0151 ± 0.0006; $p<0.01$). Similarly in late AD stage, J20 old (0.0146 ± 0.0007) demonstrated lower citrate level in comparison to WT old (0.0154 ± 0.0006) with $p<0.001$.

The fatty acyl analysis reported age and genotype main effects at $p<0.0001$ significance (Figure 5.5B). Genotype difference was prominent in late AD cohort, with J20 old (0.0082 ± 0.0013) having notably lower fatty acyl level than WT old (0.0097 ± 0.0009), with significance value of $p<0.0001$. Age difference was prominent in WT young vs WT old (1.23-fold difference; $p<0.0001$) and J20 young vs J20 old (1.14-fold difference; $p<0.05$), with old cohort displaying raised fatty acyl value in comparison to young cohort.

In addition, lactate (Figure 5.5C) exhibited genotype main effect of $p<0.001$, with Tukey's post hoc reporting differences between J20 old vs WT old with 0.0889 ± 0.0103 and 0.0979 ± 0.0073 respectively ($p<0.05$). Furthermore, analysis of glucose (Figure 5.5D) revealed interaction ($p<0.01$) and age main effect

($p<0.05$). Late AD cohort showed notably lower glucose level ($p<0.05$) in J20 old (0.0026 ± 0.0002) when compared to WT old (0.0028 ± 0.0002). Ageing effect was remarkable in WT cohort with WT old displaying increased glucose level in comparison to WT young (0.0026 ± 0.0002; $p<0.01$). Nonetheless, ageing did not impose any effect to the glucose level within J20 cohort, as the glucose level stayed the same throughout the course of AD with 0.0026 ± 0.0002 for both J20 young and J20 old.

Figure 5.5E illustrates glutamine (interaction $p<0.05$) analysis, with J20 old (0.0064 ± 0.0007) had higher glutamine level when compared against WT old (0.0059 ± 0.0007). Besides that, genotype ($p<0.01$) and age ($p<0.0001$) main effects were reported for lysine (Figure 5.5F). WT old (0.0133 ± 0.0014) was shown to exhibit higher lysine level in comparison to J20 old (0.0117 ± 0.0021) with significance level of $p<0.01$ (1.14-fold difference). Moreover, ageing effect was seen in WT cohort, with WT old have marked increase in lysine level when compared to WT young (0.0107 ± 0.0018) with 1.24-fold difference ($p<0.0001$). No difference was reported when lysine level in J20 young was measured against J20 old.

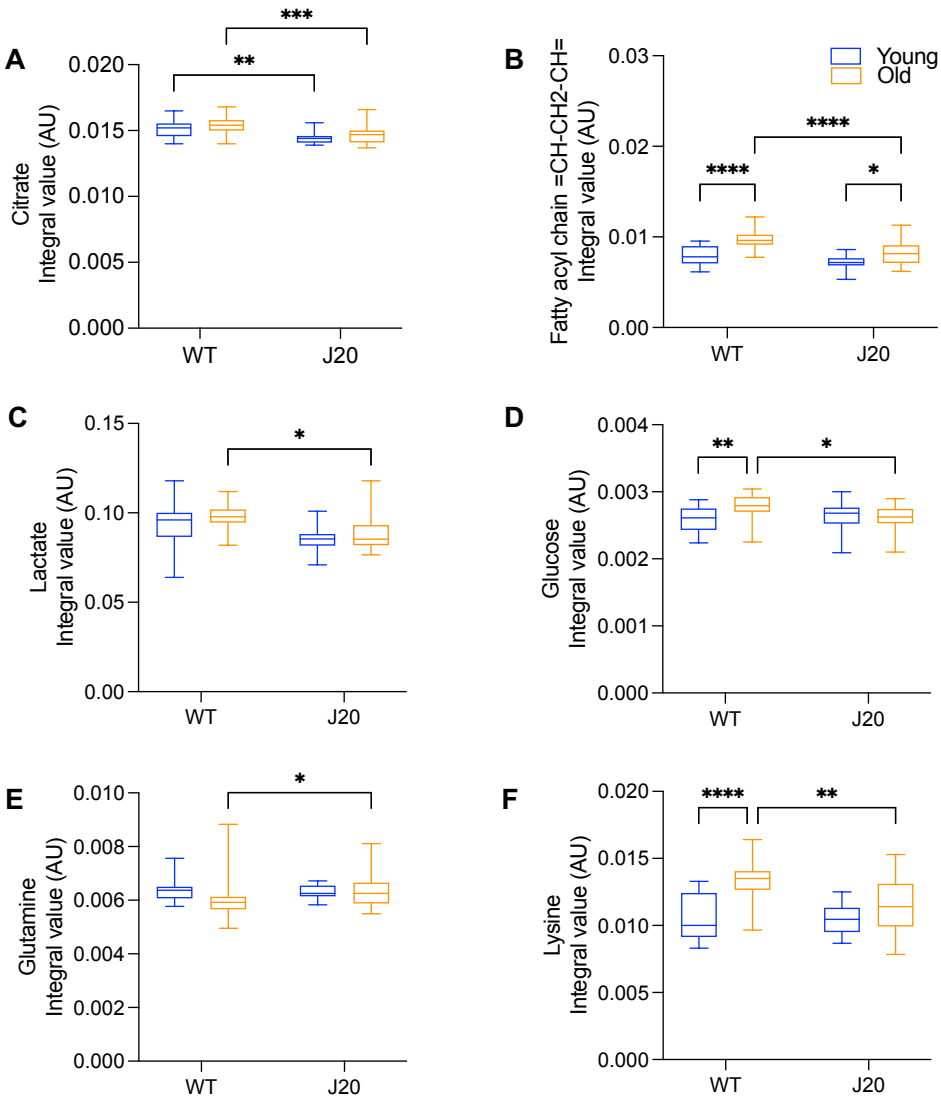


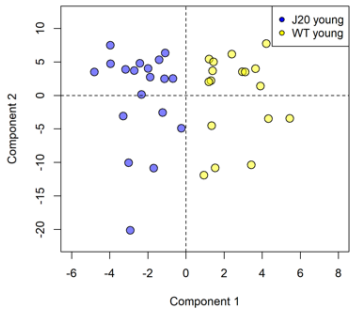
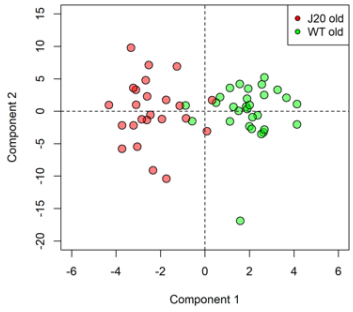
Figure 5.5 PFC VIP metabolites. Statistical analysis revealed six significant discriminatory metabolites in the PFC, which are (A) citrate, (B) fatty acyl chain =CH-CH2-CH=, (C) lactate, (D) glucose, (E) glutamine, and (F) lysine. Analysis was carried out through two-way ANOVA with Tukey's post-hoc. Data are expressed as mean ± SD. *p<0.05, **p<0.01, ***p<0.001, ****p<0.0001.

Early AD (total n=36; J20 young n=18; WT young n=18). *Late AD* (total n=45; J20 old n=20; WT old n=25)

5.2.3 Hippocampus

To ascertain hippocampal metabolite separation between J20 mutant and WT control, OPLS-DA was used to construct predictive model of J20 young vs WT young (Table 5.4; early AD) and J20 old vs WT old (Table 5.4; late AD). The representative OPLS-DA scores plot displayed a clear clustering of the J20 mutants and WT controls in both early and late AD group (Table 5.5).

Table 5.4 Hippocampus OPLS-DA plots illustrated a great separation for J20 vs WT samples in early and late AD stage. The predictive accuracy, specificity, and sensitivity of the models are expressed in mean ± SD. ****p<0.0001 by Kolmogorov-Smirnov test. Purple = J20 young, yellow = WT young, red = J20 old, green = WT old.

HC samples	OPLS-DA plot	Details	
Early AD (J20 young vs WT young)		Sample number	Total (n= 36) J20 young (n=19) WT young (n=17)
		Accuracy ± SD (%)	73 ± 4 ****
		Specificity ± SD (%)	82 ± 8 ****
		Sensitivity ± SD (%)	77 ± 6 ****
Late AD (J20 old vs WT old)		Sample number	Total (n=53) J20 old (n=24) WT old (n=29)
		Accuracy ± SD (%)	74 ± 4 ****
		Specificity ± SD (%)	80 ± 7 ****
		Sensitivity ± SD (%)	70 ± 7 ****

The mean predictive accuracy for the J20 young vs WT young OPLS-DA model (73 ± 4%) is significantly higher than the mean predictive accuracy of the random chance model (51 ± 12%) (Figure 5.6A). The OPLS-DA model generated for J20 old vs WT old revealed higher predictive mean of 73 ± 4% as compared to random chance model of 49 ± 10% (Figure 5.6B).

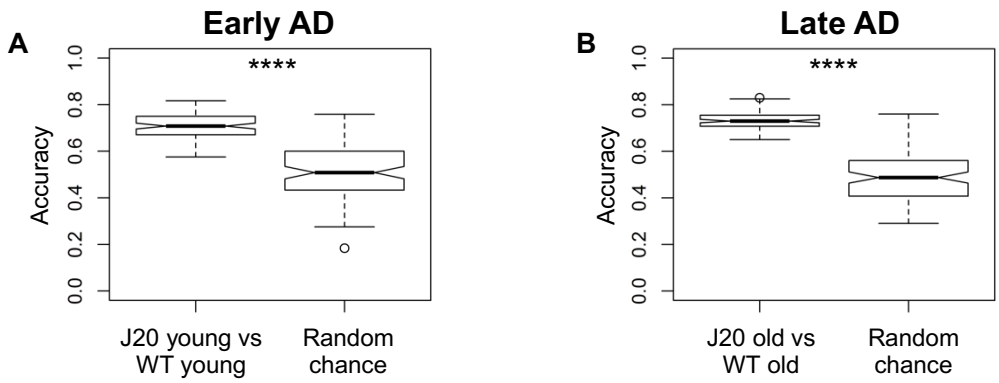


Figure 5.6 Box plots of predictive accuracies from the HC OPLS-DA models of J20 vs WT against random chance. Figures illustrate the box plots for (A) early AD and (B) late AD stage. ****indicates p<0.0001 by Kolmogorov-Smirnov test.

5.2.3.1 Identifying HC top discriminatory metabolites

To identify the top HC discriminatory metabolites during early AD and late AD, VIP scores from the OPLS-DA models were computed and the VIP ranking plot was generated (Figure 5.7). Cut-off point at 1.45 was selected for early AD group, whereas cut-off point at 1.32 was chosen for late AD group. The list of top metabolites is described in Table 5.5. The discriminatory metabolite in the first VIP rank was identified to be phosphocholine in early AD, and taurine for late AD. However, the two-way ANOVA analysis reported that these metabolites did not show significance, thus they were not considered as one of the principal metabolites. In early AD, statistical analysis revealed meaningful difference for only lactate, whereas lactate and choline were identified as the principal metabolites for late AD group.

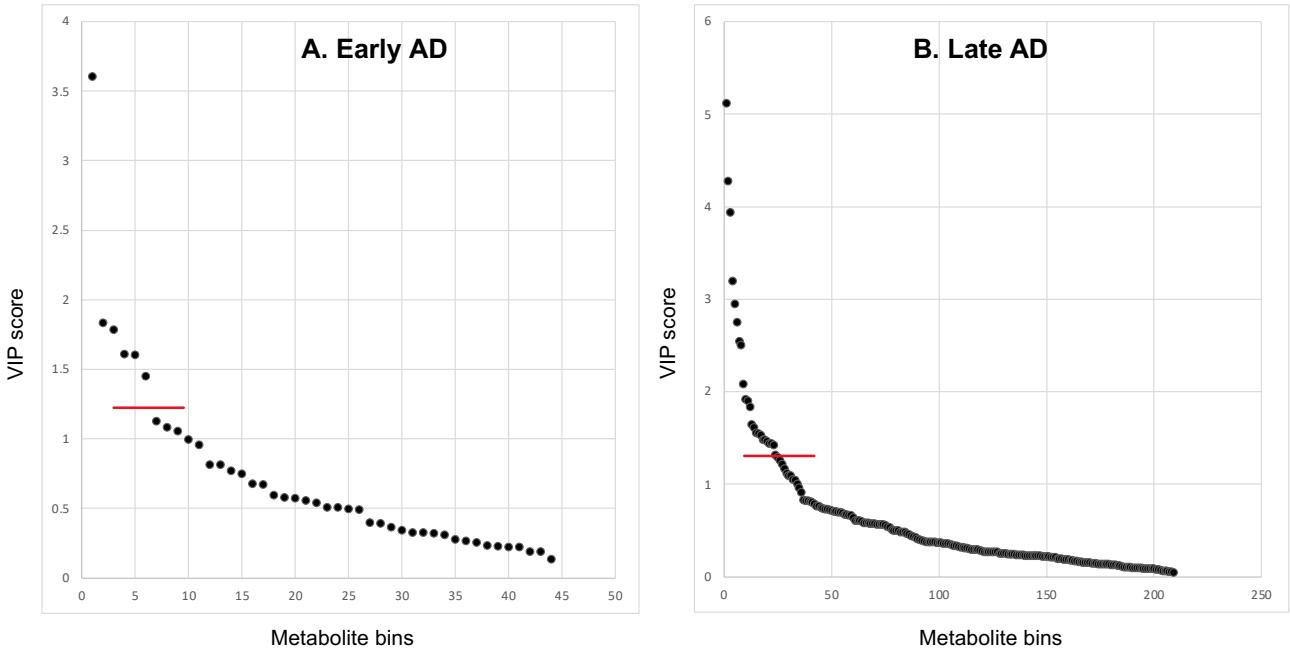


Figure 5.7 VIP ranking plot for HC samples. The VIP ranking plot identifies the top discriminatory metabolites in (A) early AD and (B) late AD OPLS-DA models. The red line indicates the VIP score cut-off at 1.45 for early AD and 1.32 for late AD respectively, before a 'drop-off' in the VIP score.

Table 5.5 List of top discriminatory metabolites in HC samples. Table below detailed the top discriminatory metabolites and their corresponding chemical shifts (spectral bins), VIP scores and rank for early and late AD group.

Early AD: J20 young vs WT young			
Top discriminatory metabolites	**Bin (ppm)**	**VIP score**	**VIP rank**
phosphocholine	3.21....3.23.	3.60	1
taurine	3.39....3.41.	1.83	2
	3.43....3.45.	1.79	3
	3.25....3.27.	1.61	4
lactate	1.33....1.35.	1.60	5
	1.31....1.33.	1.45	6

Late AD: J20 old vs WT old			
Top discriminatory metabolites	**Bin (ppm)**	**VIP score**	**VIP rank**
taurine	3.41....3.43.	5.12	1
	3.25....3.27.	4.28	2
lactate	1.31....1.33.	3.94	3
	1.33....1.35.	2.95	5
	4.11....4.13.	1.55	15
creatine	3.03....3.05.	3.19	4
choline	3.19....3.21.	2.75	6
phosphocholine	3.21....3.23.	2.55	7
taurine	3.27....3.29.	2.50	8
	3.39....3.41.	2.08	9
glutamine	2.13....2.15.	1.90	11
N-acetyl-aspartate	2.01....2.03.	1.64	13
serine-PETA	3.97....3.99.	1.47	20
glutamate	2.05....2.07.	1.43	23

5.2.3.2 Concentration of top metabolites during early and late AD phase

Two-way ANOVA was performed to investigate the changes in concentration of HC top metabolites across groups. Lactate showed genotype main effect (Figure 5.8A; $p<0.01$), with Tukey's post hoc revealed differences within early AD and late AD cohorts. In early AD, J20 young (0.0965 ± 0.0088) displayed reduced lactate level when compared to WT young (0.1035 ± 0.0138; $p<0.01$). Similarly in late AD, J20 old (0.0998 ± 0.0100) exhibited lower lactate level when compared to WT old (0.1035 ± 0.0138). In addition, genotype main effect was observed for choline with $p<0.01$ (Figure 5.8B). Tukey's post hoc reported marked elevation ($p<0.05$) of choline in J20 old (0.0063 ± 0.0008) in comparison to WT old (0.0058 ± 0.0008).

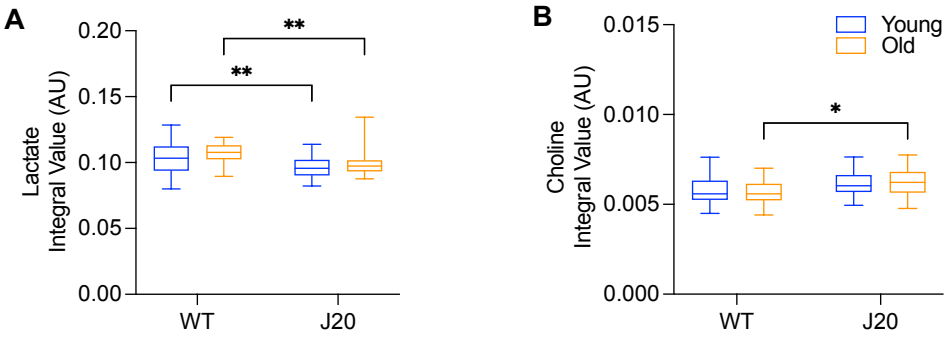


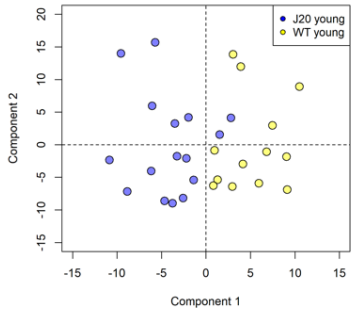
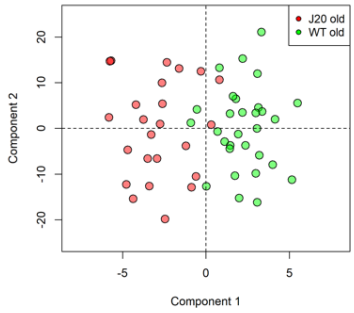
Figure 5.8 HC VIP metabolites. Statistical analysis reported two significant discriminatory metabolites in the HC, which are (A) lactate and (B) choline. Analysis was performed through two-way ANOVA with Tukey's post-hoc. Data are expressed as mean ± SD. *p<0.05, **p<0.01.

Early AD (total n=36; J20 young n=19; WT young n=17). *Late AD* (total n=53; J20 old n=24; WT old n=29)

5.2.4 Liver

To identify liver metabolite separation between J20 mutant and WT control, OPLS-DA was used to construct predictive model of J20 young vs WT young (Table 5.6; early AD) and J20 old vs WT old (Table 5.6; late AD). The representative OPLS-DA scores plot displayed significant clustering of J20 vs WT only in the late AD OPLS-DA model, but not in the early AD OPLS-DA model.

Table 5.6 Liver OPLS-DA plots illustrated a great separation for J20 vs WT samples late AD stage, but not in the early AD stage. The predictive accuracy, specificity, and sensitivity of the models are expressed in mean ± SD. ****p<0.0001 by Kolmogorov-Smirnov test. Purple = J20 young, yellow = WT young, red = J20 old, green = WT old.

Liver samples	OPLS-DA plot	Details	
Early AD (J20 young vs WT young)		Sample number	Total (n = 29) J20 young (n=16) WT young (n=13)
		Accuracy ± SD (%)	40 ± 7 (ns)
		Specificity ± SD (%)	30 ± 8 (ns)
		Sensitivity ± SD (%)	51 ± 11 (ns)
Late AD (J20 old vs WT old)		Sample number	Total (n=54) J20 old (n=24) WT old (n=30)
		Accuracy ± SD (%)	71 ± 5 ****
		Specificity ± SD (%)	74 ± 8 ****
		Sensitivity ± SD (%)	69 ± 7 ****

The mean predictive accuracy for the J20 young vs WT young OPLS-DA model showed no difference to the random chance model with 40 ± 7% vs 50 ± 13% (Figure 5.9A). The OPLS-DA model generated for J20 old vs WT old reported significantly higher predictive mean of 71 ± 5% as compared to random chance model of 50 ± 9% (Figure 5.9B).

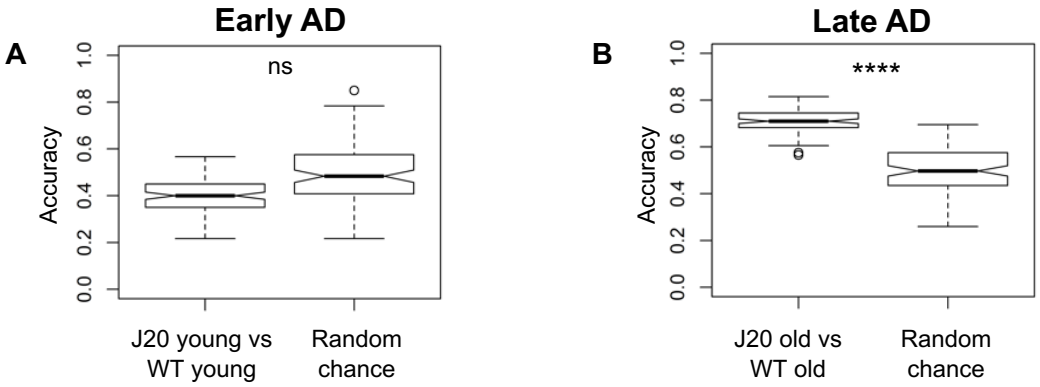


Figure 5.9 Box plots of predictive accuracies from the liver OPLS-DA models of J20 vs WT against random chance. Figures illustrate the box plots for (A) early AD and (B) late AD stage. ****indicates p<0.0001 by Kolmogorov-Smirnov test.

5.2.4.1 Identifying liver discriminatory metabolites

To identify the top discriminatory metabolites for the separation during late AD stage, VIP scores from the OPLS-DA models were computed and the VIP ranking plot was produced (Figure 5.10). No VIP ranking plot was generated for early AD as the mean predictive accuracy between J20 young vs WT young was not significant. The cut-off point was selected at 1.70, and the top metabolites for late AD are as listed in Table 5.7. Out of these metabolites, 4 metabolites were shown significant in liver which are citrate, glutamine, lysine, and histidine.

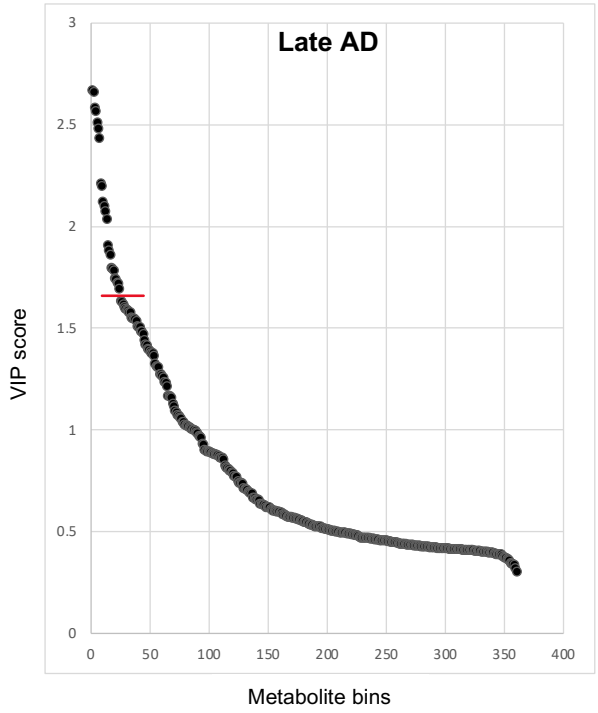


Figure 5.10 VIP ranking plot for liver samples. The VIP ranking plot identifies the top discriminatory metabolites in late AD OPLS-DA models, with the cut-off point at 1.70 as indicated by the red line. Top discriminatory metabolites are recognised as the metabolites with the VIP scores above this cut-off point.

Table 5.7 List of top discriminatory metabolites in liver samples. Table below detailed the top discriminatory metabolites and their corresponding chemical shifts (spectral bins), VIP scores and rank for late AD group.

Late AD: J20 old vs WT old			
Top discriminatory metabolites	**Bin (ppm)**	**VIP score**	**VIP rank**
citrate	2.54....2.56. 2.64....2.66. 2.52....2.54.	2.67 2.66 2.04	1 2 13
glutamine	2.16....2.18.	2.58	3
glucose	3.78....3.80.	2.20	9
lysine	2.98....3.00.	2.12	10
lipoprotein	2.92....2.94.	2.08	12
fatty acyl =CH-CH2-CH=	2.72....2.74.	1.88	15
histidine	3.32....3.34.	1.80	17

5.2.4.2 Concentration of top liver metabolites during early and late AD phase

To investigate the change of concentration across early and late AD phases in the liver top metabolites, two-way ANOVA analysis was performed. Interaction was observed for citrate (Figure 5.11A; $p<0.05$), though both age ($p=0.069$) and genotype ($p=0.064$) main effect was not significant. Tukey's post hoc analysis revealed higher ($p<0.01$) citrate level in J20 old (0.014 ± 0.002) when compared to WT old (0.013 ± 0.003). Furthermore, ageing was shown to have impacted the level of citrate in WT cohort, with WT old (0.013 ± 0.003) had notably reduced level in comparison to WT young (0.015 ± 0.002), with significance of $p<0.05$.

Glutamine analysis showed an age main effect (Figure 5.11B; $p<0.05$), with Tukey's post-hoc test reported higher ($p<0.05$) glutamine level in J20 old (0.013 ± 0.002) as opposed to WT old (0.012 ± 0.003). Moreover, two-way ANOVA reported interaction ($p<0.05$) and age ($p<0.05$) main effect for lysine (Figure 5.11C). Ageing main effect was apparent in WT cohort with WT old (0.001 ± 0.0004) displaying reduced ($p<0.01$) lysine level in contrast to WT young (0.002 ± 0.0003). Nonetheless, no difference was noted when J20 old was compared against J20 young, as the lysine value was consistent (0.002 ± 0.0003) throughout ageing.

In addition, for histidine, age main effect was observed (Figure 5.11D; $p<0.01$). The post-hoc test reported reduction ($p<0.05$) of histidine level in WT old (0.0007 ± 0.0002) when compared to WT young (0.0009 ± 0.0002), with $p<0.05$

significance. However, the difference between J20 old (0.0008 ± 0.0002) and J20 young (0.0009 ± 0.0002) was not significant.

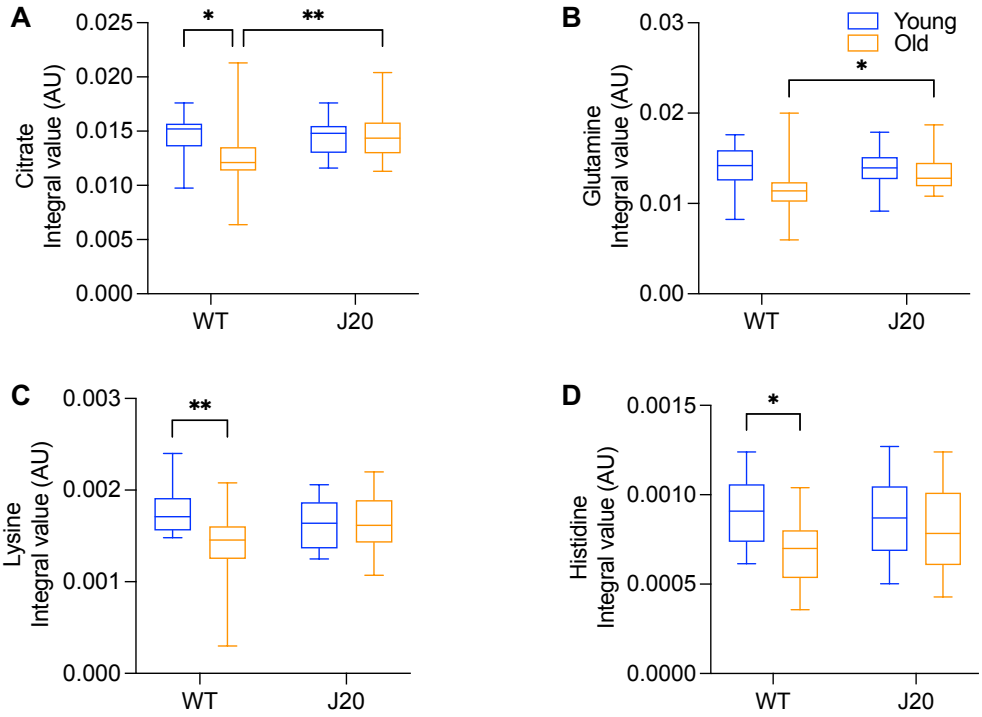


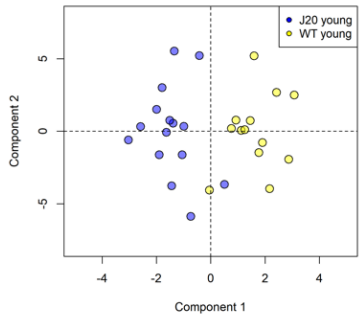
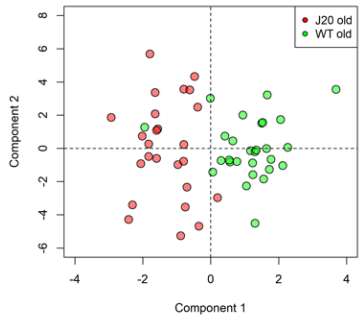
Figure 5.11 Liver VIP metabolites. Statistical analysis revealed four significant discriminatory metabolites in the liver, which are (A) citrate, (B) glutamine, (C) lysine, and (D) histidine. Analysis was performed through two-way ANOVA with Tukey's post-hoc test. Data are expressed as mean ± SD. *p<0.05, **p<0.01.

Early AD (total n=29; J20 young n=16; WT young n=13). *Late AD* (total n=54; J20 old n=24; WT old n=30)

5.2.5 Spleen

To identify spleen metabolite separation between J20 mutant and WT control, OPLS-DA was used to construct predictive model of J20 young vs WT young (Table 5.8; early AD) and J20 old vs WT old (Table 5.8; late AD). The representative OPLS-DA scores plot displayed significant distinction in both early and late AD OPLS-DA models.

Table 5.8 Spleen OPLS-DA plots illustrated a great separation for J20 vs WT samples early and late AD stage. The predictive accuracy, specificity, and sensitivity of the models are expressed in mean ± SD. ****p<0.0001 by Kolmogorov-Smirnov test. Purple = J20 young, yellow = WT young, red = J20 old, green = WT old.

Spleen samples	OPLS-DA plot	Details	
Early AD (J20 young vs WT young)		Sample number	Total (n = 28) J20 young (n=13) WT young (n=15)
		Accuracy ± SD (%)	67 ± 5 ****
		Specificity ± SD (%)	73 ± 8 ****
		Sensitivity ± SD (%)	63 ± 8 ****
Late AD (J20 old vs WT old)		Sample number	Total (n=53) J20 old (n=25) WT old (n=28)
		Accuracy ± SD (%)	75 ± 4 ****
		Specificity ± SD (%)	77 ± 6 ****
		Sensitivity ± SD (%)	74 ± 7 ****

The mean predictive accuracy for the J20 young vs WT young OPLS-DA model showed displayed significantly higher value when compared to the random chance model with 67 ± 5% against 49 ± 10% (Figure 5.12A). The OPLS-DA model generated for J20 old vs WT old also reported significantly higher predictive mean of 75 ± 4% as compared to random chance model of 49 ± 9% (Figure 5.12B).

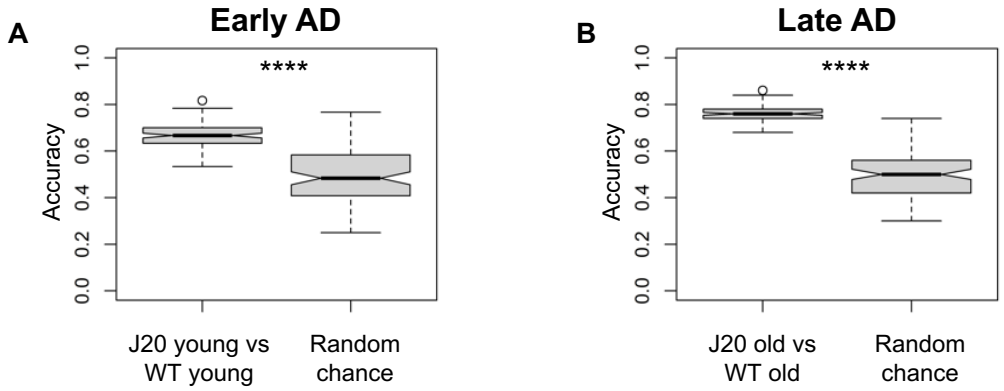


Figure 5.12 Box plots of predictive accuracies from the spleen OPLS-DA models of J20 vs WT against random chance. Figures illustrate the box plots for (A) early AD and (B) late AD stage. ****indicates p<0.0001 by Kolmogorov-Smirnov test.

5.2.5.1 Identifying spleen discriminatory metabolites

To identify the discriminatory metabolites from the J20 vs WT OPLS-DA models of early and late AD, VIP ranking plots were generated (Figure 5.13). The VIP score cut-off was determined at 1.84 and 1.93 for early and late AD respectively and the top metabolites are detailed in Table 5.9. The principal metabolites driving the separation between J20 and WT in spleen were revealed by two-way ANOVA analysis. Six metabolites were discovered, which are unsaturated lipids, lipoprotein, glucose, glutamine, threonine, and polyunsaturated fatty acid (PUFA).

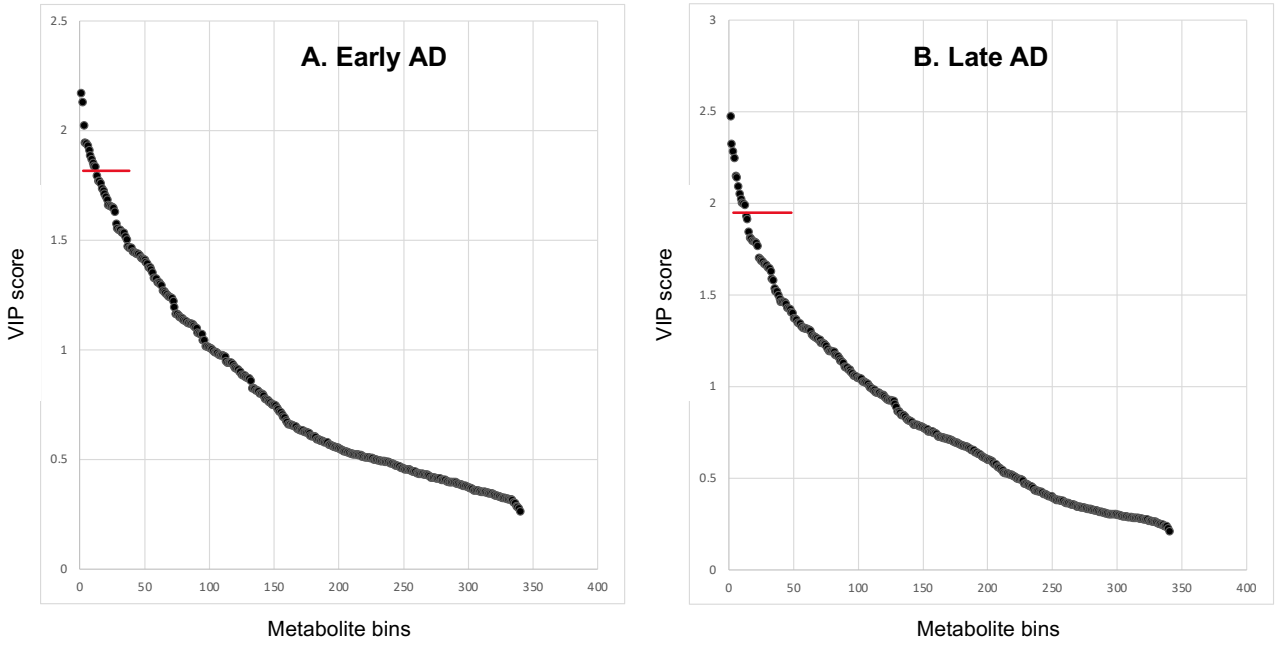


Figure 5.13 VIP ranking plot for spleen samples. The VIP ranking plot identifies the top discriminatory metabolites in (A) early AD and (B) late AD OPLS-DA models. The red line indicates the VIP score cut-off at 1.84 for early AD and 1.93 for late AD respectively, before a 'drop-off' in the VIP score.

Table 5.9 List of top discriminatory metabolites in spleen samples. Table below detailed the top discriminatory metabolites and their corresponding chemical shifts (spectral bins), VIP scores and rank for early and late AD group.

Early AD: J20 young vs WT young			
Top discriminatory metabolites	**Bin (ppm)**	**VIP score**	**VIP rank**
glucose	3.42....3.44. 3.38....3.40. 3.76....3.78.	2.13 2.02 1.91	2 3 7
unsaturated lipid	5.36....5.38. 5.20....5.22.	1.95 1.87	4 9
lactate	4.08....4.10.	1.93	6
glutamine	2.44....2.46.	1.89	8
lipoprotein	2.92....2.94.	1.84	12

Late AD: J20 old vs WT old			
Top discriminatory metabolites	**Bin (ppm)**	**VIP score**	**VIP rank**
alanine	1.46....1.48. 1.48....1.50.	2.48 2.15	1 5
glucose	3.50....3.52.	2.33	2
glutamine	2.46....2.48. 2.44....2.46. 2.42....2.44. 2.14....2.16.	2.28 2.25 2.10 1.99	3 4 7 12
threonine	3.58....3.60.	2.05	8
PUFA	2.00....2.02.	2.03	9

5.2.5.2 Concentration of top spleen metabolites during early and late AD phase

Two-way ANOVA was performed to investigate the concentration of spleen top metabolites. The unsaturated lipids reported significant interaction of $p<0.001$ (Figure 5.14A), but genotype ($p=0.386$) and age ($p=0.521$) main effects were not significant. In early AD cohort, marked increase ($p<0.05$) of unsaturated lipids in J20 young (-0.00004 ± 0.0001) was seen when compared against WT young

(-0.0001 ± 0.0001). Ageing effect was notable in J20 animals, as the level of unsaturated lipids in J20 old dropped significantly ($p<0.05$) to -0.001 ± 0.0001 when compared to J20 young.

Interaction was noted in lipoprotein (Figure 5.14B, $p<0.05$), with genotype ($p=0.273$) and age ($p=0.162$) main effects were revealed not significant. Ageing impacted the level of lipoprotein level in WT, as WT old (0.0006 ± 0.0002) showed a reduced concentration ($p<0.05$) when compared to WT young (0.0008 ± 0.0003). This effect of age onto J20 cohort was not observed, with J20 old and J20 young retaining the same value of 0.0006 ± 0.0003.

Besides that, glucose showed notable interaction ($p<0.05$), genotype ($p<0.01$) and age ($p<0.05$) main effects (Figure 5.14C). No difference was seen in glucose level in early AD, when J20 young (0.00080 ± 0.00019) was compared to WT young (0.00082 ± 0.00013). However, in late AD, J20 old (0.00080 ± 0.00018) displayed marked decrease in glucose concentration in contrast to WT old (0.00099 ± 0.00016). Ageing effect was seen to have an impact on the glucose level in WT cohort, with WT old exhibited elevated level in oppose to WT young ($p<0.05$). Furthermore, the two-way ANOVA analysis on glutamine presented genotype main effect of $p<0.001$ (Figure 5.14D). Glutamine level was shown to be lower in J20 old (0.0181 ± 0.0013) when compared against WT old (0.0197 ± 0.0016).

In addition, significant genotype main effect ($p<0.001$) was also observed threonine (Figure 5.14E). In early AD, J20 young (0.0085 ± 0.0008) displayed notably higher ($p<0.05$) threonine level in comparison to WT young (0.0079 ± 0.0009). Similar trend was also seen in late AD with J20 old (0.0085 ± 0.0005) showed elevated ($p<0.05$) threonine concentration in contrast to WT old (0.0080 ± 0.0005). PUFA analysis reported meaningful interaction with significance level of $p<0.05$ (Figure 5.14F). However, the genotype ($p=0.171$) and age ($p=0.0325$) main effects did not reach statistical significance. The difference in PUFA level was seen in late AD cohort when J20 old (0.0020 ± 0.0001) demonstrated increased concentration ($p<0.01$) when compared against WT old (0.0019 ± 0.0001). No prominent change was noted in the early AD cohort when J20 young (0.0019 ± 0.0001) was compared to WT young (0.0020 ± 0.0001).

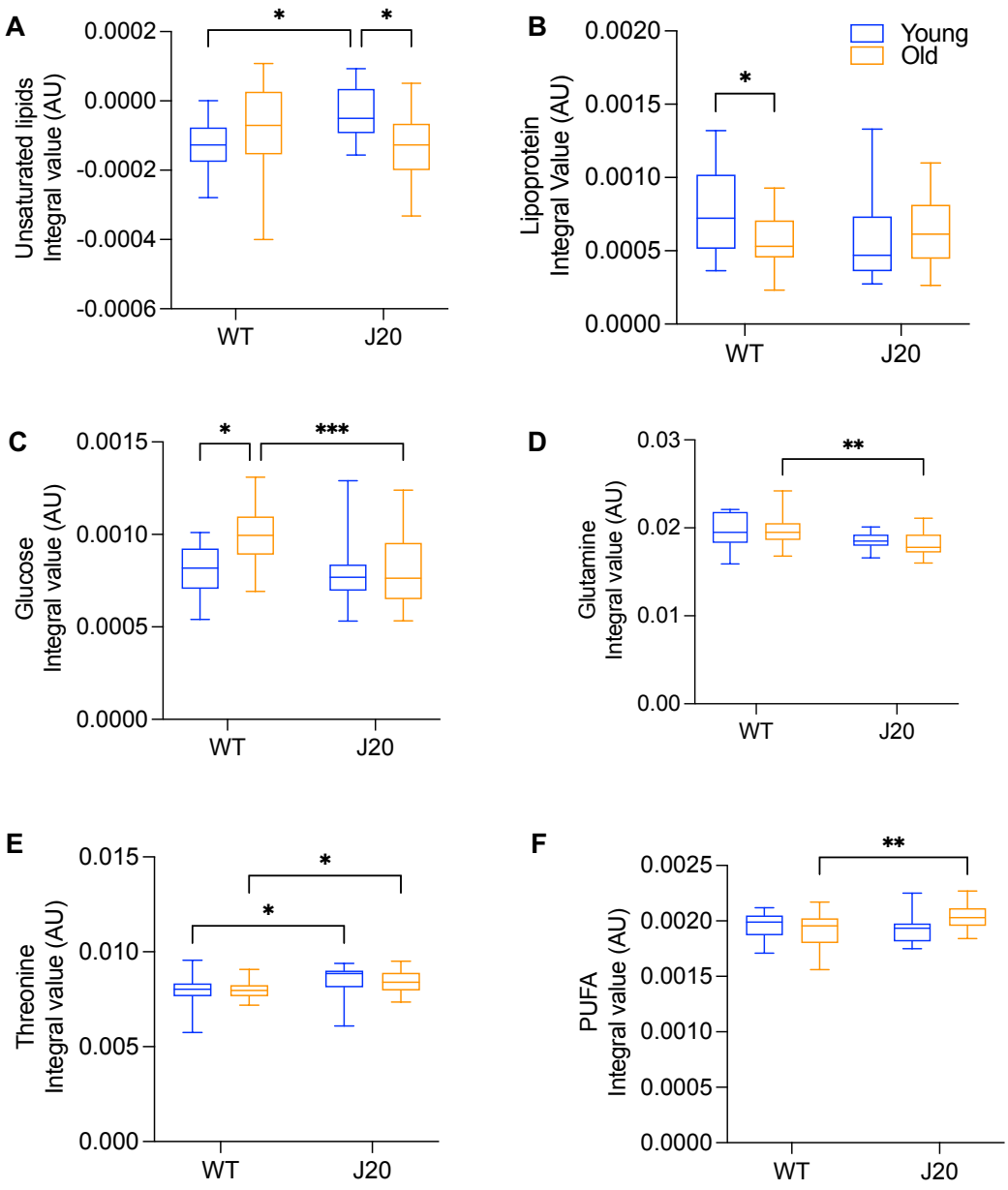


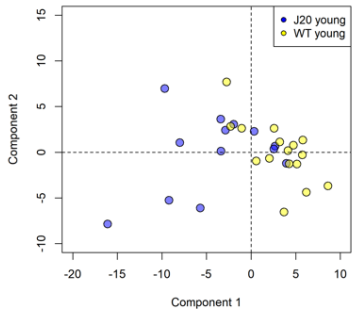
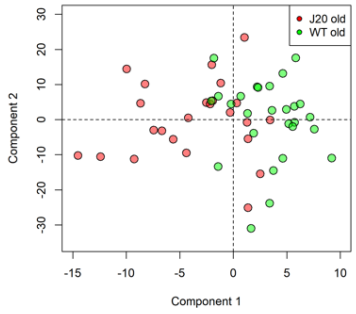
Figure 5.14 Spleen VIP metabolites. Statistical analysis revealed six significant discriminatory metabolites in the spleen, which are (A) unsaturated lipids, (B) lipoprotein, (C) glucose, (D) glutamine, (E) threonine, and (F) PUFA. Analysis was done through two-way ANOVA with Tukey's post-hoc test. Data are expressed as mean ± SD. *p<0.05, **p<0.01, ***p<0.001.

Early AD (total n=28; J20 young n=13; WT young n=15). *Late AD* (total n=53; J20 old n=25; WT old n=28).

5.2.6 Serum

To identify metabolite separation between J20 mutant and WT control, OPLS-DA was used to construct predictive model of J20 young vs WT young (Table 5.10; early AD) and J20 old vs WT old (Table 5.10; late AD). The representative OPLS-DA scores plot revealed no separation in the early AD group. However, a great distinction between J20 and WT in late AD group was noted.

Table 5.10 Serum OPLS-DA plots illustrated a great separation for J20 vs WT samples late AD stage, but not in the early AD stage. The predictive accuracy, specificity, and sensitivity of the models are expressed in mean ± SD. ****p<0.0001 by Kolmogorov-Smirnov test. Purple = J20 young, yellow = WT young, red = J20 old, green = WT old.

Serum samples	OPLS-DA plot	Details	
Early AD (J20 young vs WT young)		Sample number	Total (n = 29) J20 young (n=13) WT young (n=16)
		Accuracy ± SD (%)	53 ± 6 (ns)
		Specificity ± SD (%)	59 ± 11 ***
		Sensitivity ± SD (%)	48 ± 10 (ns)
Late AD (J20 old vs WT old)		Sample number	Total (n=51) J20 old (n=24) WT old (n=27)
		Accuracy ± SD (%)	70 ± 4 ****
		Specificity ± SD (%)	75 ± 7 ****
		Sensitivity ± SD (%)	66 ± 6 ****

The mean predictive accuracy for the J20 young vs WT young OPLS-DA model showed no difference to the random chance model with 53 ± 6% vs 51 ± 11% (Figure 5.15A). The OPLS-DA model generated for J20 old vs WT old reported significantly higher predictive mean of 70 ± 4% as compared to random chance model of 48 ± 9% (Figure 5.15B).

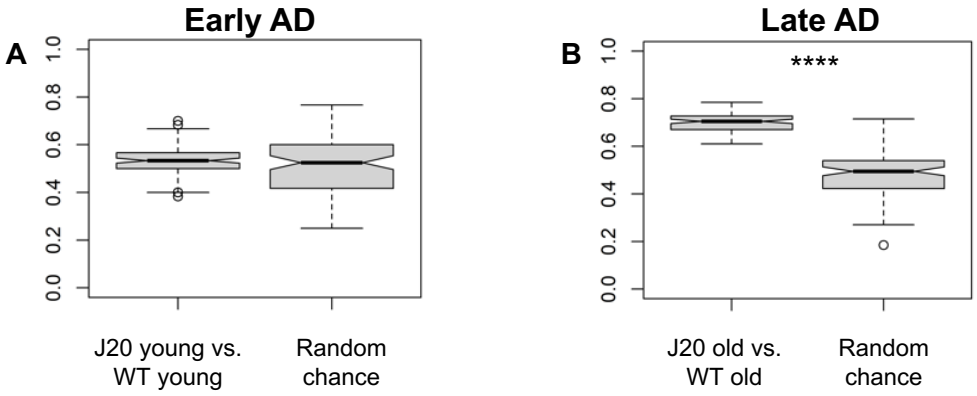


Figure 5.15 Box plots of predictive accuracies from the serum OPLS-DA models of J20 vs WT against random chance. Figures illustrate the box plots for (A) early AD and (B) late AD stage. ****indicates p<0.0001 by Kolmogorov-Smirnov test.

5.2.6.1 Identifying serum top discriminatory metabolites

To identify the discriminatory metabolites from the J20 vs WT OPLS-DA models late AD, VIP ranking plot was generated (Figure 5.16). No VIP ranking plot was produced for early AD as the model was not significant. The VIP score cut-off of 2.06 was determined for late AD and the top metabolites are detailed in Table 5.11. Eight principal metabolites driving the separation between J20 and WT in serum were discovered, which are PUFA, fatty acid βCH2, proline, lipoprotein VLDL, acetoacetate, lipoprotein HDL, myo-inositol, and glucose.

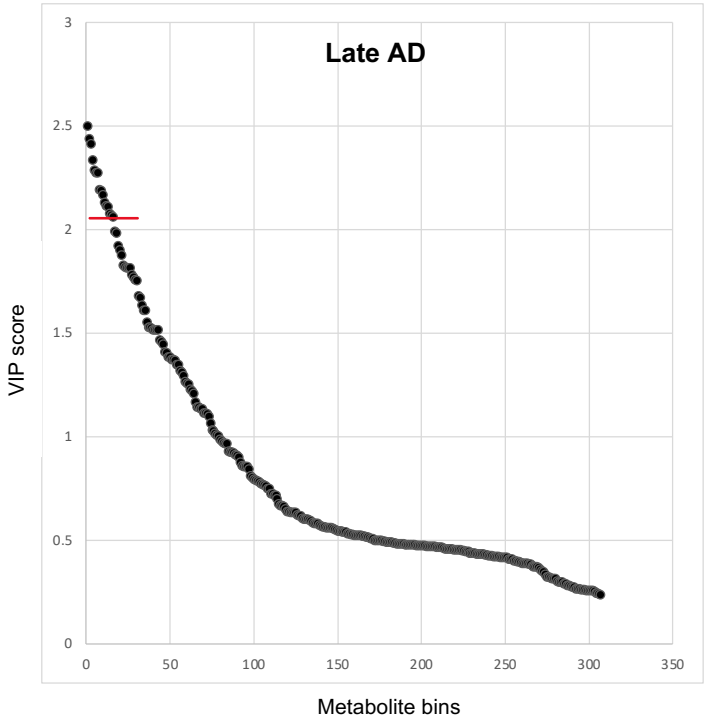


Figure 5.16 VIP ranking plot for serum samples. The VIP ranking plot identifies the top discriminatory metabolites in late AD OPLS-DA models, with the cut-off point at 2.06 as indicated by the red line. Top discriminatory metabolites are recognised as the metabolites with the VIP scores above this cut-off point.

Table 5.11 List of top discriminatory metabolites in serum samples. Table below detailed the op discriminatory metabolites and their corresponding chemical shifts (spectral bins), VIP scores and rank for late AD group.

Late AD: J20 old vs WT old			
Top discriminatory metabolites	**Bin (ppm)**	**VIP score**	**VIP rank**
polyunsaturated fatty acid	2.04....2.06. 2.06....2.08.	2.50 2.27	1 6
fatty acid bCH2	1.56....1.58. 1.58....1.60.	2.44 2.42	2 3
proline	2.24....2.26	2.34	4
lipoprotein VLDL	1.28....1.30. 1.30....1.32. 1.34....1.36	2.29 2.27 2.19	5 7 9
acetoacetate	2.22....2.24.	2.19	8
lipoprotein HDL	0.90....0.92.	2.17	10
myo-inositol	3.52....3.54.	2.11	13
glucose	3.74....3.76.	2.07	15

5.2.6.2 Concentration of top serum metabolites during early and late AD phase

Two-way ANOVA analysis was performed for top serum metabolites. PUFA reported significant interaction ($p<0.001$), although genotype ($p=0.328$) and age ($p=0.414$) main effects did not reach statistical significance (Figure 5.17A). Tukey's post-hoc analysis disclosed $p<0.01$ difference when J20 old (0.0302 ± 0.0063) was compared against WT old (0.0246 ± 0.0033). Ageing was revealed to have an impact onto the WT cohort, with PUFA level showed a massive drop ($p<0.01$) in WT old in contrast to WT young (0.0300 ± 0.0052). This observation was not seen in J20 cohort with J20 old (0.0302 ± 0.0063) showed negligible difference to J20 young (0.0268 ± 0.0061).

Fatty acid βCH2 reported significant interaction ($p<0.001$), genotype ($p<0.05$) and age ($p<0.05$) main effects (Figure 5.17B). In late AD cohort, J20 old (0.0065 ± 0.0023) exhibited elevated ($p<0.0001$) fatty acid βCH2 concentration as opposed to WT old (0.0040 ± 0.0011), with 1.63-fold difference. Moreover, age factor was shown to play a role in WT cohort, with WT old showed a massive reduction ($p<0.001$) of fatty acid βCH2 concentration in comparison to WT young (0.0064 ± 0.0020).

The two-way ANOVA described interaction at $p<0.01$ for proline (Figure 5.17C). Proline level was shown to be significantly higher in J20 old (0.0041 ± 0.0013) when compared to WT old (0.0028 ± 0.0006). Within WT cohort, age was shown to influence proline level, with a marked decrease ($p<0.01$) in concentration was

seen in WT old when compared against WT young (0.0041 ± 0.0012). No marked difference was seen when J20 old was compared to J20 young (0.0037 ± 0.0011).

Furthermore, the lipoprotein VLDL (Figure 5.17D; interaction $p<0.001$) and acetoacetate (Figure 5.17E; interaction $p<0.01$; genotype main effect $p<0.05$) showed similar graph trend to proline. The level of lipoprotein VLDL was shown higher in J20 old (0.0735 ± 0.0275) when compared to WT old (0.0475 ± 0.0122). Within WT cohort, age effect was seen when WT old displayed reduced ($p<0.01$) lipoprotein VLDL level in contrast to WT young (0.0726 ± 0.0228). Besides that, the level of acetoacetate in J20 old (0.0026 ± 0.0007) was notably higher ($p<0.001$) than WT old (0.0018 ± 0.0005) in late AD group. The age effect on WT cohort was revealed with WT old demonstrating lower ($p<0.01$) acetoacetate concentration when compared to its WT young counterpart (0.0025 ± 0.0007).

In addition, lipoprotein HDL revealed significant interaction (Figure 5.17F; $p<0.05$), with Tukey's post-hoc analysis reported significant increase ($p<0.05$) in J20 old (0.0200 ± 0.0060) as opposed to WT old (0.0156 ± 0.0036) in late AD cohort. No difference was seen in the early AD cohort, with J20 young (0.0191 ± 0.0045) against WT young (0.0199 ± 0.0054) at $p=0.969$. However, age effect was seen to lower the lipoprotein HDL level in WT old when compared to WT young with statistical significance of $p<0.05$.

Figure 5.17G portrays the two-way ANOVA analysis of myo-inositol (interaction $p<0.01$, with Tukey's post-hoc analysis revealed notable reduction of myo-inositol concentration in J20 old (0.0070 ± 0.0011) when compared to WT old (0.0080 ± 0.0008). Moreover, significant interaction ($p<0.05$) and age main effect ($p<0.05$) was reported for glucose (Figure 5.16H). In late AD cohort, the J20 old (0.0343 ± 0.0060) was shown to have lower ($p<0.01$) glucose level in opposition to WT old (0.0387 ± 0.0037). No difference was demonstrated in early AD cohort, when J20 young (0.0341 ± 0.0036) was compared to WT young (0.0339 ± 0.0043). However, age factor was shown to influence WT cohort with WT old displaying an elevated glucose level in contrast to WT young ($p<0.01$).

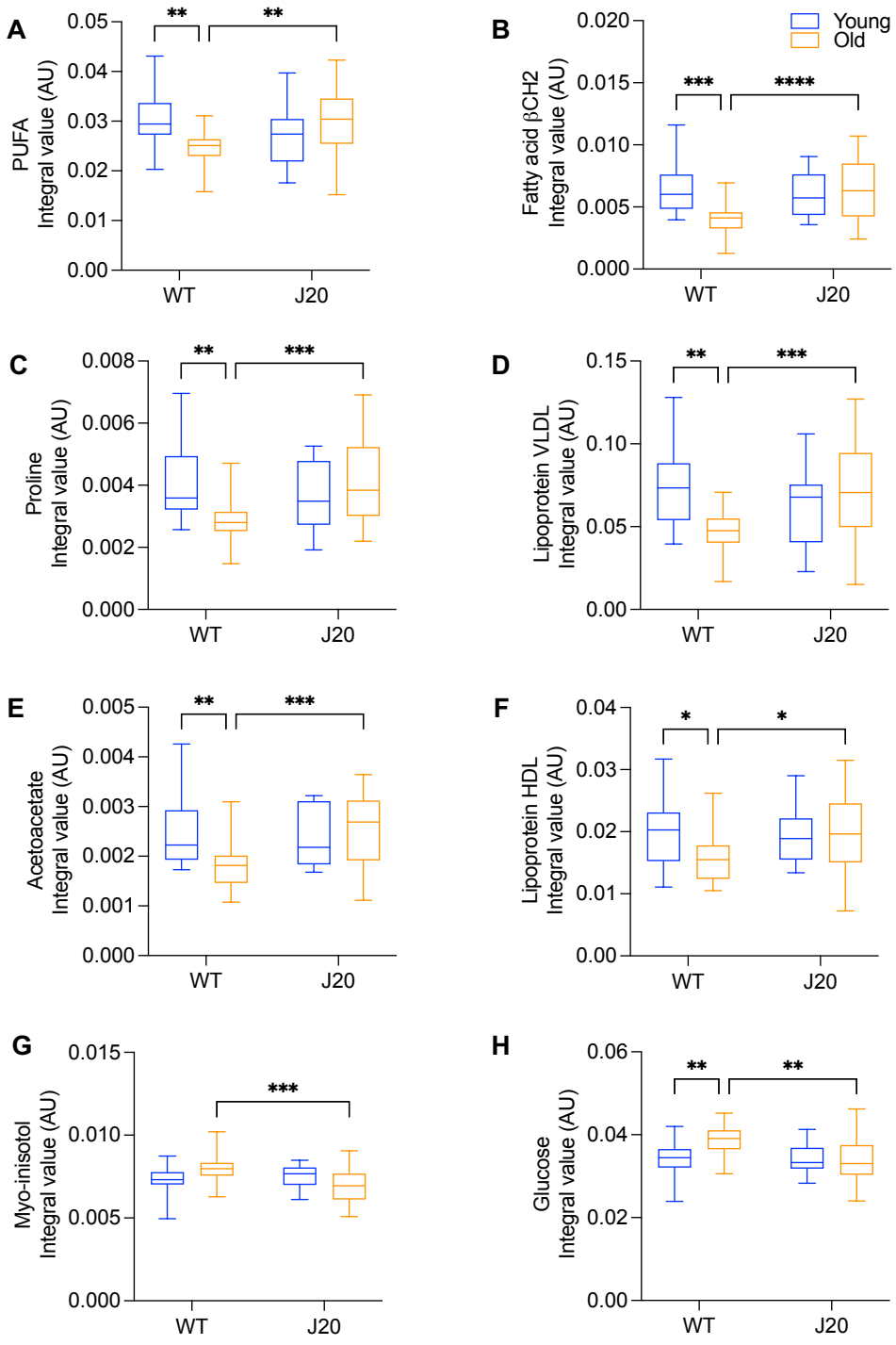


Figure 5.17 Serum VIP metabolites. Statistical analysis revealed eight significant discriminatory metabolites in the serum, which are (A) PUFA, (B) fatty acid βCH2 (C) proline, (D) lipoprotein VLDL, (E) acetoacetate, (F) lipoprotein HDL, (G) myo-inositol, and (H) glucose. Analysis was performed through two-way ANOVA with Tukey's post-hoc test. Data are expressed as mean ± SD. *p<0.05, **p<0.01, ***p<0.001, ****p<0.0001.

Early AD (total n=29; J20 young n=13; WT young n=16). *Late AD* (total n=51; J20 old n=24; WT old n=27).

5.2.7 Overlapping brain-periphery metabolites

To investigate the metabolites that are significant in both brain and periphery, a summary of significant metabolites across tissues was generated (Table 5.12). Citrate, glucose, and glutamine was found to be in the brain and at least one of the periphery organs, with post-hoc significance in J20 vs WT group. Further, a heatmap was produced for these three metabolites outlying their mean concentration in all tissues investigated (Figure 5.18).

Table 5.12 Summary of principal VIP metabolites across tissues. The principal VIP metabolites are the top discriminatory metabolites discovered to be significant through two-way ANOVA analysis.

Metabolite/ Tissue	PFC	HC	Liver	Spleen	Serum
Citrate	■		■		
Fatty acyl chain =CH-CH2-CH=	■				
Lactate	■	■			
Glucose	■			■	■
Glutamine	■		■	■	
Lysine	■		■		
Choline		■			
Histidine			■		
Unsaturated lipid				■	
Lipoprotein				■	■
Threonine				■	
PUFA				■	■
Fatty acid βCH2					■
Proline					■
Acetoacetate					■
Myoinositol					■

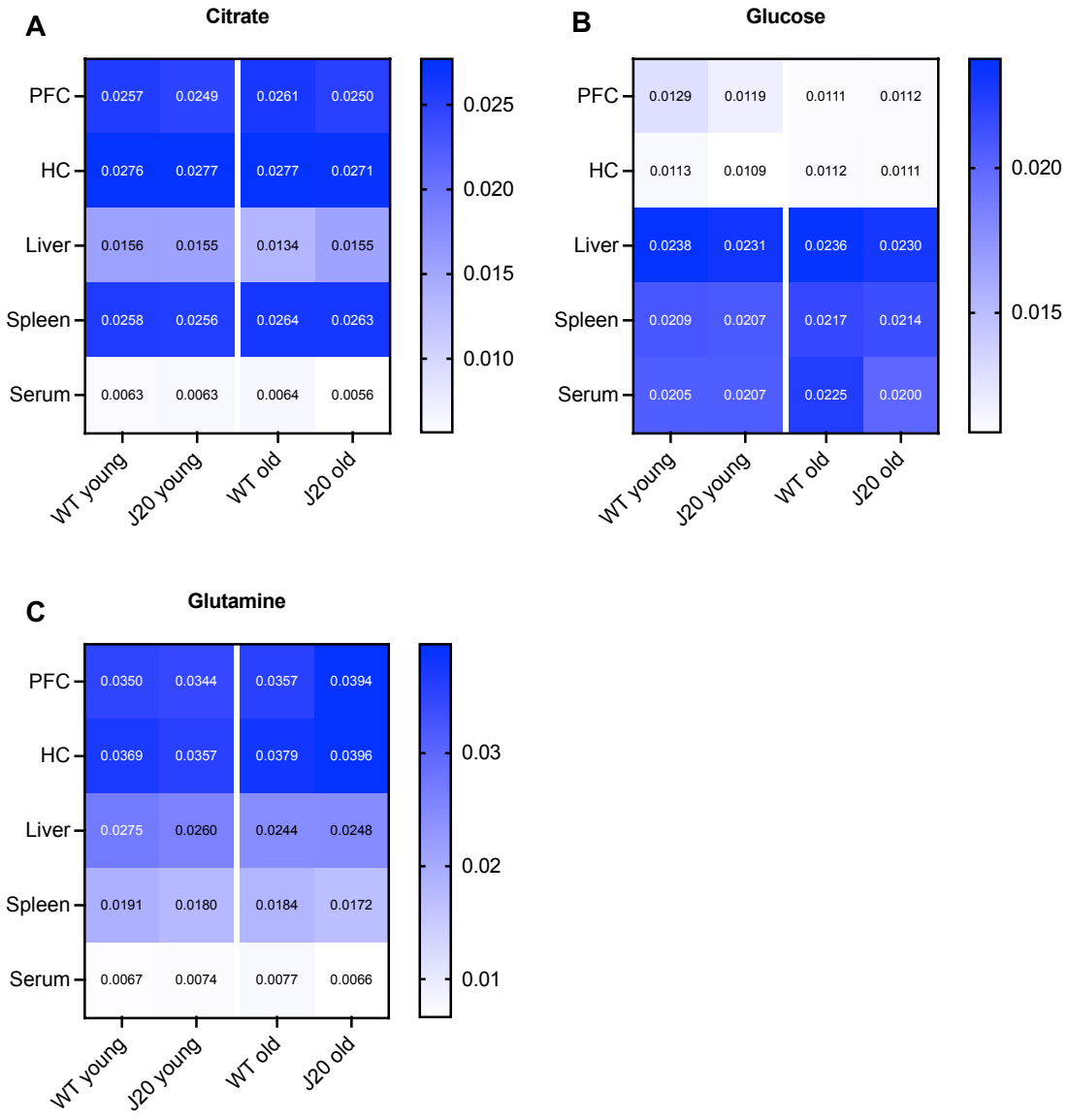


Figure 5.18 Heatmap on principal VIP metabolites that are present in both brain and periphery tissues. The heatmap illustrate the mean concentration of citrate, glucose, and glutamine metabolites across PFC, HC, liver, spleen, and serum.

5.3 Discussion

5.3.1 Principal findings

In this chapter, I verified the existence of distinct metabolomic differences between J20 mutants and WT controls. This distinction is not only confined to the brain where the pathology is abundant, but also extends to the peripheral organs. Five tissues were subjected to analysis in this chapter, namely PFC, HC, liver, spleen, and serum. The mice were grouped into early and late AD at 19 weeks old cut-off, corresponding to pre-clinical and MCI-AD dementia phase respectively, based on the J20 mutant phenotypic timeline. OPLS-DA analysis was adopted to explore the evidence of metabolic separation between J20 mutants and WT controls in both early and late AD stage. The OPLS-DA findings revealed distinct metabolomic profile between J20 and WT in PFC, HC, and spleen of early AD. The liver and serum showed negligible difference between J20 and WT during early AD stage. Importantly, all tissues exhibited significant metabolite separation during the late AD stage.

Top discriminatory metabolites were determined from VIP ranking plot graph, and the metabolite assignment was performed through literature findings and HMDB platform. The top discriminatory metabolite is defined as the metabolites above the drop-off point in the VIP ranking plot, which is a point used to determine the variables that may influence the separation seen in OPLS-DA model construct. Following top discriminatory metabolite identification, principal VIP metabolites (defined as the metabolites with significant p value) were determined through

two-way ANOVA analysis and their changes in concentration across early and late AD phase are subsequently investigated.

Principal VIP metabolites identified in PFC tissue were citrate, fatty acyl chain =CH-CH2-CH=, lactate, glucose, glutamine, and lysine (Figure 5.5), whereas principal metabolites for HC were lactate and choline (Figure 5.8). Besides that, liver principal VIP metabolites were discovered to be citrate, glutamine, lysine, and histidine (Figure 5.11). Spleen showed unsaturated lipids, lipoprotein, glucose, glutamine, threonine and PUFA discovery (Figure 5.14), whereas serum samples reported PUFA, fatty acid βCH2, proline, lipoprotein VLDL, acetoacetate, lipoprotein HDL, myo-inositol, and glucose as its principal VIP metabolites (Figure 5.17). In addition, citrate, glucose, and glutamine was shown to be the overlapping metabolites that are present in both CNS and periphery tissues which may hold the potential as peripheral biomarkers for AD (Figure 5.18).

5.3.2 Potential peripheral biomarkers of AD

5.3.2.1 Glucose

Transgenic AD J20 model excellently mimics the dysfunctional glucose metabolism seen in human AD patients. Glucose level was found to be lower in J20 old when compared to WT old (late AD cohort) in PFC (Figure 5.5D), spleen (Figure 5.14C), and serum (Figure 5.17H). In human, cerebral glucose hypometabolism characterised by impaired glucose uptake, brain insulin resistance as well as progressive mitochondrial dysfunctions has been consistently recognised as one of early anomalies of AD, and a progressive sign of AD into clinical stage (Van Der Velpen et al., 2019; X. Yan, Hu, Wang, Wang, & Zhang, 2020). 18F-fluorodeoxyglucose-positron emission tomography (FDG-PET) is widely adopted to support clinical diagnosis in patient suspected with neurodegenerative disorder (Ou et al., 2019). Injection of FDG-PET enables in vivo visualisation of abnormal metabolic activity in the brain, primarily the information on rate of glucose metabolism, rate of oxygen consumption and cerebral blood flow (Newington, Harris, & Cumming, 2013).

Ou and team (2019) revealed that MCI patients with reduced FDG-PET uptake, which corresponded to significantly impaired brain glucose metabolism had a higher probability to progress to AD dementia (Ou et al., 2019). This view is also supported by Kato and colleagues who reported reduced brain glucose consumption in AD subjects when compared to normal ageing (Kato, Inui, Nakamura, & Ito, 2016). Neuronal function and neurotransmission can be impacted by altered glucose metabolism, leading to diminished memorising and

learning ability (Hammond & Lin, 2022; X. Yan et al., 2020). Furthermore, insulin and insulin growth factor-1 (IGF-1) signalling was shown to play a critical role in cognitive function, and thus insulin resistance pose as a risk factor for AD (X. Yan et al., 2020). Metabolic dysfunction in AD was suggested to not only confined within CNS but extends to the systemic level, and have been implied to contribute to the disease progression (Van Der Velpen et al., 2019). Despite representing only 2% of the body's total mass, human brain requires approximately 20% of the body's total energy. The brain relies predominantly on glucose metabolism through mitochondrial respiration and glycolytic pathway, which yield 2 and 36 adenosine triphosphate (ATP) energy generation respectively. Thus, pyruvate oxidation in the mitochondria has been deemed to be the main source of energy for neurons (Newington et al., 2013; X. Yan et al., 2020).

Peripheral blood such as serum or plasma has been extensively studied for blood-based biomarker of AD. In a study of 71 dementia patients, a significantly lower fasting blood glucose level was observed in AD patients when compared against individuals with unspecified dementia (Landin, Blennow, Wallin, & Gottfries, 1993). This is in accordance with the present finding, as lower serum glucose concentration was noted in the J20 cohort when compared to control. However, a contradicting finding from another study reported decreased memory function in 345 cognitively normal older adults associated with an increased fasting serum glucose. The same study proposed that the elevated fasting serum glucose as an indicator of metabolic dysfunction and a risk factor for AD predisposition (Burns et al., 2013). In addition, there is paucity of information on

reduced glucose metabolism in the spleen, which may suggest an area for future research as AD peripheral biomarker.

5.3.2.2 Citrate

In the present study, the level of citrate was found to be altered in PFC and liver of J20 mutant when compared to WT control. In PFC, reduction in citrate was seen in J20 mutants of early and late AD cohort when compared to their age-matched WT controls (Figure 5.5A). On the contrary, liver demonstrated lower concentration of citrate only in J20 vs WT of late AD cohort (Figure 5.11A). In line with the present citrate findings, post-mortem study conducted by Paglia and colleagues (2016) onto frontal cortex of human AD subjects discovered significant reduction in citrate level as opposed to the non-demented subjects. Altered citrate level was suggested to be a result of dysfunctional transport mechanism between mitochondria and cytosol (Paglia et al., 2016). Citrate is generated intra-mitochondrially through tricarboxylic acid (TCA) cycle (also known as the Krebs cycle or citric acid cycle) by the action of citrate synthase that utilizes acetyl-Coenzyme A (acetyl-CoA) and oxaloacetate as its substrates. Citrate acts as the primary transport for acetyl units to move into the cytoplasm for fatty acid and cholesterol formation in the brain and liver. There is also evidence that citrate helps in the translocation of acetyl unit intended for ACh production in the brain (Endemann & Brunengraber, 1980).

Citrate synthase is the key mitochondrial enzyme and is often considered as the marker for oxidative capacity in the cells and tissues. Low CS activity has been

noted in the brain homogenates of AD patients, which is associated with low citrate formation, reduced cellular energy, decreased acetyl-CoA and ACh synthesis. Low cellular energy induces the production of ROS that in turn promotes Aβ16–22 protein aggregation and enhances neurodegeneration. Furthermore, reduced citrate level in the mitochondria and neuronal cytoplasm leads to impaired memory function due to decreased ACh concentration (Chhimpa, Singh, Puri, & Kayath, 2023). The liver-brain axis has increasingly being pursued in AD, as peripheral inflammation primarily in the liver has long been correlated with the induction of inflammation in the CNS (Do-geun Kim et al., 2016). There is a gap in knowledge on citrate metabolic dysfunction in AD liver, which could be investigated in future studies, perhaps using targeted metabolomics approach for a proof-of-principle and to validate the current finding in post-mortem human liver tissues.

5.3.2.3 Glutamine

The glutamate-glutamine cycle is essential for numerous neural functions, especially in maintaining the neurotransmitter precursor and excitatory synaptic transmission. Glutamate synthesis occurred in the neurons and released into the synaptic cleft during neurotransmission. Efficient glutamate uptake by astrocytes prevents excessive glutamate accumulation in the synapse, and the glutamate is subsequently converted into glutamine through glutamine synthetase (GS) action within astrocyte (D. H. Kim, Gim, Yoon, Kim, & Kim, 2017). Neuronal survival and brain development relies heavily on GS as human and rodent studies reported brain malformation and neonatal death from congenital GS deficiency. Increased

oxidation due to ageing may degrade and reduce GS activity (J. Chen & Herrup, 2015). The frontal lobe was observed to be two times more vulnerable to oxidation-induced reduction of GS activity when compared to occipital lobe, implying brain-region specific susceptibility. Furthermore, GS activity was found to be significantly reduced in AD frontal cortex when compared against age-matched controls (Smith et al., 1991). Butterfield et al (2006) also discovered elevated GS oxidation in both MCI and AD groups in contrast to age-matched controls (Butterfield et al., 2006). Moreover, increased glutamine level in the CSF of 72 probable AD cases (scored positive on amyloid and tau index) as opposed to 71 age-matched controls was observed, which suggest that glutamine concentration may function as a subclinical biomarker for cognitive changes (Madeira, Caroline Vargas-Lopes, Charles Brandao, Reis, Laks, Panuzzutti, & Ferreira, 2018).

In conformation to this finding, the present study indicated that the concentration of glutamine was shown altered in PFC (Figure 5.5E) in late AD cohort, which is the experimental group corresponding to MCI-AD dementia stage of the J20 mutant phenotypic timeline. Both PFC and liver (Figure 5.11B) showed higher glutamine level in J20 old when compared to WT old, whereas spleen (Figure 5.14D) displayed an opposite trend with lower glutamine level in J20 old against WT control. The differences in level of glutamine in the liver and spleen in relation to PFC should be noted, and the relative quantification of glutamine metabolism in these peripheral organs may serve as the surrogate marker for cerebral glutamine metabolism during MCI-AD dementia stage.

CHAPTER 6

FINAL DISCUSSION AND CONCLUSION

Chapter 6 : Final discussion and conclusion

6.1 Key contributions

The broad aim of this thesis was to investigate the existence of two-hit phenomenon in exacerbating AD progression, focusing on the effect of acute TBI on transgenic J20 mouse model. The “first hit” demonstrates the existing AD pathology in the mutant, and the “second hit” is the TBI imposed in acute or chronic manner. The work presented in this thesis centred on amyloid hypothesis as its fundamental reference of AD pathogenesis, henceforth an extensive usage of transgenic J20 mutant that overexpresses human APP was adopted in this thesis. In chapter 3, two age groups of transgenic J20 mutant representing prodromal/MCI and AD dementia group respectively were used to explore if varying burden level of AD pathology would affect the APR outcome following TBI. In the second part of this chapter, a continuation study was carried out to investigate the effect of acute TBI on transgenic P301S mouse model, to examine if acute TBI on tauopathy will yield the same outcome as observed in J20 mouse model. The effect of chronic TBI was also investigated in these two transgenic AD models in chapter 4. In chapter 5, brain-periphery metabolite profiling of J20 mutant was generated using untargeted metabolomics approach, and potential metabolites for future peripheral AD biomarker consideration was reported. The key findings in this thesis are as follows:

1. The two-hit phenomenon is deemed true in TBI + J20 (amyloid pathology), but not in TBI + P301S (tauopathy) acute TBI model.

2. Degree of amyloid pathology plays a role in shaping APR profile outcome, with heightened APR level observed in prodromal/ MCI group as compared to AD dementia group.
3. Chronic TBI onto amyloid or tau pathology did not show altered systemic inflammatory profile when compared to controls.
4. Metabolite profiling of J20 mutant revealed citrate, glucose, and glutamine as potential peripheral AD biomarkers.

6.2 General discussion, future research, and conclusion

The pathophysiology of AD is intricate, involving a multitude of factors that contribute to and exacerbate its progression. These factors range from internal and external insults affecting both central and systemic organs, as highlighted by various researchers (Asby, Boche, Allan, Love, & Miners, 2021; Gilbert et al., 2014; V. E. Johnson et al., 2010; Kamer, Dasanayake, Craig, & Glodzik-sobanska, 2008; Shishido et al., 2019; Walker et al., 2023). Alarmingly, the prevalence of AD is on a continuous rise, with predictions indicating a tripling of cases by 2050 (D. H. Kim et al., 2017). This escalating trend underscores the urgency and significance of ongoing AD research. While extensive studies have been conducted on the molecular and histological aspects of AD in the CNS, research on the interplay between the brain and systemic organs in AD pathogenesis remains limited. This gap is what my thesis has primarily sought to address.

A key focus of my work has investigated the mechanisms behind accelerated AD progression following TBI, especially since AD patients, predominantly the

elderly, are highly susceptible to TBIs, notably falls (Faul & Coronado, 2015). Often, mild-to-moderate TBI cases, such as falls, are overlooked, particularly in the absence of visible external injuries. Chapter 3 of my thesis presented significant findings of the contribution of the systemic immunological response following acute TBI in transgenic AD models. These insights are vital for raising awareness among caregivers and physicians about the need for attentive care for AD patients who suffer TBIs. The findings should be viewed as a preliminary concept, necessitating further clinical studies to explore the AD-TBI interaction in humans from molecular and histological perspectives.

In Chapter 4, I found an accelerated increase in AT8 tau burden after chronic TBI in transgenic P301S mice, both in the ipsilateral and contralateral cortex of the injury area. This histological finding was accompanied by an elevated hepatic *IL-6* expression in P301S TBI by 3.7-fold difference when compared to WT TBI. However, this outcome was not translated to any increase in peripheral leukocyte numbers, as measured through liver neutrophil and Kupffer cells count. Additionally, no significant difference was seen in brain microglia and neutrophil numbers in the brain, both in J20 and P301S mice when compared to WT after chronic TBI. Further investigations can be conducted to assess the severity of brain damage in AD models compared to WT models. The extent of immune cell infiltration alone is insufficient to determine the severity of brain damage. Future studies should include assessments of neuronal dysfunction, levels of oxidative stress and the extent of blood-brain BBB breakdown following TBI. Additionally, the presence of brain atrophy in transgenic AD mice, as compared to WT, should be examined to understand the long-term effects of TBI on overall brain volume.

An interesting area for future research is the evaluation of the glymphatic system's capacity post-brain trauma. This could involve measuring the clearance rate of injected tracers to assess the system's efficiency. Furthermore, monitoring TBI biomarkers in peripheral blood plasma, such as S100 calcium-binding protein B (S100B) and neuron-specific enolase, could confirm the release of endogenous brain substances into the systemic circulation. Immunofluorescence analysis of AQP4 and GFAP (astrocyte marker) expression and localization could provide insights into their activity post-TBI in AD models.

The role of exosomes in mediating the communication between the brain and periphery in the AD-TBI two-hit scenario is still unclear. The elementary EV work in my thesis could be expanded to characterize the parental cells of these exosomes and their contents, enhancing our understanding of their role in TBI effects in the presence of AD-like pathology. Adoptive studies, such as injecting EVs from P301S TBI animals into naive mice, could elucidate their protective or pathogenic nature.

The growing body of literature supports the notion that metabolic dysfunction is a crucial aspect of AD progression. Consequently, forthcoming research could emphasize the analysis of metabolomics in early acute and chronic TBI samples. Moreover, exploring the potential influence of gender on immune responses and outcomes could be beneficial, particularly considering the higher prevalence of AD in females and the observed behavioural differences in female *APOE4* carriers (Wilkins & Trushina, 2018). Female *APOE4* carriers were shown to exhibit higher score of disinhibitions as compared to male *APOE4* carriers in moderate to severe AD. From the perspective of neuropsychiatric disorder,

interaction was noted between gender and *APOE4* status. Accelerated tau phosphorylation was associated to psychosis symptom, whereas increased Aβ protein was related to irritability and agitation symptoms in patients. Corresponding to this observation, female *APOE4* carriers exhibited higher NFT and Aβ burden in their brains (Xing, Tang, & Jia, 2015).

Chapter 5's untargeted metabolomics approach will be useful to guide future targeted metabolite studies. This thesis emphasized potential novel peripheral biomarkers in AD, but the findings could also help refine the selection of molecules for novel pre-clinical AD stage biomarkers. Identifying these biomarkers is crucial for early detection, distinguishing AD from other dementia causes, and understanding novel mechanistic pathways for disease-modifying drug development and personalized medicine.

In conclusion, the interplay between brain-peripheral axis in neuropathology is gaining recognition in the medical field. The findings from this thesis contribute significantly to the knowledge base in the AD/neuroinflammation/brain-peripheral interconnection domain and lay a foundation for future studies in this area.

BIBLIOGRAPHY

Bibliography

Abeysinghe, A. A. D. T., Deshapriya, R. D. U. S., & Udawatte, C. (2020). Alzheimer's disease; a review of the pathophysiological basis and therapeutic interventions. *Life Sciences*, *256*(June), 117996. https://doi.org/10.1016/j.lfs.2020.117996

Aderemi, A. V., Ayeleso, A. O., Oyedapo, O. O., & Mukwevho, E. (2021). Metabolomics: A scoping review of its role as a tool for disease biomarker discovery in selected non-communicable diseases. *Metabolites*, *11*(7). https://doi.org/10.3390/metabo11070418

Aertker, B. M., Bedi, S., & Cox, C. S. (2016). Strategies for CNS repair following TBI. *Experimental Neurology*, *275*, 411–426. https://doi.org/10.1016/j.expneurol.2015.01.008

Akamatsu, Y., & Hanafy, K. A. (2020). Cell Death and Recovery in Traumatic Brain Injury. *Neurotherapeutics*, *17*(2), 446–456. https://doi.org/10.1007/s13311-020-00840-7

Alam, Aftab, Thelin, E. P., Tajsic, T., Khan, D. Z., Khellaf, A., Patani, R., & Helmy, A. (2020). Cellular infiltration in traumatic brain injury. *Journal of Neuroinflammation*, *17*(1), 1–17. https://doi.org/10.1186/s12974-020-02005-x

Alam, Azeem, Hana, Z., Jin, Z., Suen, K. C., & Ma, D. (2018). Surgery, neuroinflammation and cognitive impairment. *EBioMedicine*, *37*, 547–556. https://doi.org/10.1016/j.ebiom.2018.10.021

Allen, B., Ingram, E., Takao, M., Smith, M. J., Jakes, R., Virdee, K., … Goedert, M. (2002). Abundant tau filaments and nonapoptotic neurodegeneration in transgenic mice expressing human P301s tau protein. *Journal of Neuroscience*, *22*(21), 9340–9351. https://doi.org/10.1523/jneurosci.22-21-09340.2002

Alonso, A. D., Cohen, L. S., Corbo, C., Morozova, V., ElIdrissi, A., Phillips, G., & Kleiman, F. E. (2018). Hyperphosphorylation of Tau Associates with changes in its function beyond microtubule stability. *Frontiers in Cellular Neuroscience*, *12*(October), 1–11. https://doi.org/10.3389/fncel.2018.00338

Alzforum. (2019). Research Models J20 (PDGF-APPSw,Ind). Retrieved from https://www.alzforum.org/research-models/j20-pdgf-appswind

Alzforum. (2024). Research Models hTau.P301S. Retrieved from https://www.alzforum.org/research-models/htaup301s

Alzheimer's Association. (2018). 2018 Alzheimer's disease facts and figures. *Alzheimer's and Dementia*, *14*(3), 367–429. https://doi.org/10.1016/j.jalz.2018.02.001

Anglin, R. E., Rosebush, P. I., & Mazurek, M. F. (2010). Neuroleptic malignant syndrome: A neuroimmunologic hypothesis. *CMAJ*, *182*(18), 14–19. https://doi.org/10.1503/cmaj.091442

Annaert, W., & De Strooper, B. (2002). A Cell Biological Perspective on Alzheimer's Disease. *Annual Review of Cell and Developmental Biology*,

18(1), 25–51. https://doi.org/10.1146/annurev.cellbio.18.020402.142302

Anthony, D. C., Couch, Y., Losey, P., & Evans, M. C. (2012). The systemic response to brain injury and disease. *Brain, Behavior, and Immunity*, *26*(4), 534–540. https://doi.org/10.1016/j.bbi.2011.10.011

Anthony, D. C., Walker, K., & Perry, V. H. (2005). The therapeutic potential of CXC chemokine blockade in acute inflammation in the brain. *Expert Opinion on Investigational Drugs*, *8*(4), 363–371. https://doi.org/10.1517/13543784.8.4.363

Apostolakis, S., Chalikias, G. K., Tziakas, D. N., & Konstantinides, S. (2011). Erythrocyte Duffy antigen receptor for chemokines (DARC): Diagnostic and therapeutic implications in atherosclerotic cardiovascular disease. *Acta Pharmacologica Sinica*, *32*(4), 417–424. https://doi.org/10.1038/aps.2011.13

Asby, D., Boche, D., Allan, S., Love, S., & Miners, J. S. (2021). Systemic infection exacerbates cerebrovascular dysfunction in Alzheimer's disease. *Brain*, *144*(6), 1869–1883. https://doi.org/10.1093/brain/awab094

Ashrafian, H., Sounderajah, V., Glen, R., Ebbels, T., Blaise, B. J., Kalra, D., … Cascante, M. (2021). Metabolomics: The Stethoscope for the Twenty-First Century. *Medical Principles and Practice*, *30*(4), 301–310. https://doi.org/10.1159/000513545

Bachiller, S., Jiménez-Ferrer, I., Paulus, A., Yang, Y., Swanberg, M., Deierborg, T., & Boza-Serrano, A. (2018). Microglia in neurological diseases: A road map to brain-disease dependent-inflammatory response. *Frontiers in Cellular Neuroscience*, *12*(December), 1–17. https://doi.org/10.3389/fncel.2018.00488

Bailes, J. E., Petraglia, A. L., Omalu, B. I., Nauman, E., & Talavage, T. (2013). Role of subconcussion in repetitive mild traumatic brain injury. *Journal of Neurosurgery*, *119*(5), 1235–1245. https://doi.org/10.3171/2013.7.JNS121822

Baumgart, M., Snyder, H. M., Carrillo, M. C., Fazio, S., Kim, H., & Johns, H. (2015). Summary of the evidence on modifiable risk factors for cognitive decline and dementia: A population-based perspective. *Alzheimer's and Dementia*, *11*(6), 718–726. https://doi.org/10.1016/j.jalz.2015.05.016

Becker, A., Thakur, B. K., Weiss, J. M., Kim, H. S., Peinado, H., & Lyden, D. (2016). Extracellular Vesicles in Cancer: Cell-to-Cell Mediators of Metastasis. *Cancer Cell*. https://doi.org/10.1016/j.ccell.2016.10.009

Behl, T., Kaur, I., Sehgal, A., Singh, S., Sharma, N., Makeen, H. A., … Bungau, S. (2022). "Aducanumab" making a comeback in Alzheimer's disease: An old wine in a new bottle. *Biomedicine and Pharmacotherapy*, *148*(January), 112746. https://doi.org/10.1016/j.biopha.2022.112746

Bekris, L. M., Yu, C.-E., Bird, T. D., & Tsuang, D. W. (2010). Genetics of Alzheimer's disease. *J Geriatr Psychiatry Neurol*, *23*(4), 213–227. https://doi.org/10.1201/9781315381572

Belanger, H. G., Curtiss, G., Demery, J. A., Lebowitz, B. K., & Vanderploeg, R. D. (2005). Factors moderating neuropsychological outcomes following mild

traumatic brain injury: A meta-analysis. *Journal of the International Neuropsychological Society*, *11*(3), 215–227. https://doi.org/10.1017/S1355617705050277

Ben Khalifa, N., Tyteca, D., Courtoy, P. J., Renauld, J. C., Constantinescu, S. N., Octave, J. N., & Kienlen-Campard, P. (2012). Contribution of Kunitz protease inhibitor and transmembrane domains to amyloid precursor protein homodimerization. *Neurodegenerative Diseases*, *10*(1–4), 92–95. https://doi.org/10.1159/000335225

Bernardini, S., & Zima, T. (2019). Alzheimer's disease: Making the point. *Clinical Biochemistry*. https://doi.org/10.1016/j.clinbiochem.2019.05.007

Bertogliat, M. J., Morris-Blanco, K. C., & Vemuganti, R. (2020). *Epigenetic mechanisms of neurodegenerative diseases and acute brain injury*. *Physiology & behavior* (Vol. 176). https://doi.org/10.1016/j.neuint.2019.104642.Epigenetic

Bertram, L., Lill, C. M., & Tanzi, R. E. (2010). The genetics of alzheimer disease: Back to the future. *Neuron*, *68*(2), 270–281. https://doi.org/10.1016/j.neuron.2010.10.013

Bharti, S. K., & Roy, R. (2012). Quantitative 1H NMR spectroscopy. *TrAC - Trends in Analytical Chemistry*, *35*, 5–26. https://doi.org/10.1016/j.trac.2012.02.007

Bi, C., Bi, S., & Li, B. (2019). Processing of mutant β-amyloid precursor protein and the clinicopathological features of familial alzheimer's disease. *Aging and Disease*, *10*(2), 383–403. https://doi.org/10.14336/AD.2018.0425

Biogen. (2024). Biogen to Realign Resources for Alzheimer's Disease Franchise. *Biogen*. Retrieved from https://investors.biogen.com/news-releases/news-release-details/biogen-realign-resources-alzheimers-disease-franchise#:~:text=CAMBRIDGE%2C Mass.%2C Jan.,near and long-term growth.

Bishara, D., Justin, S., & Taylor, D. (2015). The pharmacological management of Alzheimer ' s disease. *Progress in Neurology and Psychiatry*, (July/August), 9–16.

Bodnar, C. N., Roberts, K. N., Higgins, E. K., & Bachstetter, A. D. (2019). Reviews A Systematic Review of Closed Head Injury Models of Mild Traumatic Brain Injury in Mice and Rats, *1706*, 1683–1706. https://doi.org/10.1089/neu.2018.6127

Bondi, M. W., Edmonds, E. C., & Salmon, D. P. (2017). Alzheimer's disease: Past, present, and future. *Journal of the International Neuropsychological Society*, *23*(9-10 Special Issue), 818–831. https://doi.org/10.1017/S135561771700100X

Bourin, M., & Hascoët, M. (2003). The mouse light/dark box test. *European Journal of Pharmacology*, *463*(1–3), 55–65. https://doi.org/10.1016/S0014-2999(03)01274-3

Braak, H., & Del Tredici, K. (2015). The preclinical phase of the pathological process underlying sporadic Alzheimer's disease. *Brain*, *138*(10), 2814–2833. https://doi.org/10.1093/brain/awv236

Bradburn, S., McPhee, J., Bagley, L., Carroll, M., Slevin, M., Al-Shanti, N., … Murgatroyd, C. (2018). Dysregulation of C-X-C motif ligand 10 during aging and association with cognitive performance. *Neurobiology of Aging*, *63*, 54–64. https://doi.org/10.1016/j.neurobiolaging.2017.11.009

Brandt, R., Trushina, N. I., & Bakota, L. (2020). Much More Than a Cytoskeletal Protein: Physiological and Pathological Functions of the Non-microtubule Binding Region of Tau. *Frontiers in Neurology*. https://doi.org/10.3389/fneur.2020.590059

Briggs, R., Kennelly, S. P., & O'neill, D. (2016). Drug treatments in Alzheimer's disease. *Clinical Medicine*, *16*(3), 247–253.

Brilkova, M., Nigri, M., Kumar, H. S., Moore, J., Mantovani, M., Keller, C., … Böttger, E. C. (2022). Error-prone protein synthesis recapitulates early symptoms of Alzheimer disease in aging mice. *Cell Reports*, *40*(13). https://doi.org/10.1016/j.celrep.2022.111433

Brøchner, A. C., & Toft, P. (2009). Pathophysiology of the systemic inflammatory response after major accidental trauma. *Scandinavian Journal of Trauma, Resuscitation and Emergency Medicine*, *17*(1), 1–10. https://doi.org/10.1186/1757-7241-17-43

Budnik, V., Ruiz-Cañada, C., & Wendler, F. (2016). Extracellular vesicles round off communication in the nervous system. *Nature Reviews Neuroscience*, *17*(3), 160–172. https://doi.org/10.1038/nrn.2015.29

Burns, C. M., Chen, K., Kaszniak, A. W., Lee, W., Alexander, G. E., Bandy, D., … Reiman, E. M. (2013). Higher serum glucose levels are associated with cerebral hypometabolism in Alzheimer regions. *Neurology*, *80*(17), 1557–1564. https://doi.org/10.1212/WNL.0b013e31828f17de

Butterfield, D. A., Poon, H. F., St. Clair, D., Keller, J. N., Pierce, W. M., Klein, J. B., & Markesbery, W. R. (2006). Redox proteomics identification of oxidatively modified hippocampal proteins in mild cognitive impairment: Insights into the development of Alzheimer's disease. *Neurobiology of Disease*, *22*(2), 223–232. https://doi.org/10.1016/j.nbd.2005.11.002

Bye, N., Habgood, M. D., Callaway, J. K., Malakooti, N., Potter, A., Kossmann, T., & Morganti-Kossmann, M. C. (2007). Transient neuroprotection by minocycline following traumatic brain injury is associated with attenuated microglial activation but no changes in cell apoptosis or neutrophil infiltration. *Experimental Neurology*, *204*(1), 220–233. https://doi.org/10.1016/j.expneurol.2006.10.013

Cacace, R., Sleegers, K., & Broeckhoven, C. Van. (2016). Molecular genetics of early-onset Alzheimer ' s disease revisited. *Alzheimer's & Dementia*, *12*(6), 733–748. https://doi.org/10.1016/j.jalz.2016.01.012

Campbell, S. J., Anthony, D. C., Oakley, F., Carlsen, H., Elsharkawy, A. M., Blomhoff, R., & Mann, D. A. (2008). Hepatic nuclear factor κB regulates neutrophil recruitment to the injured brain. *Journal of Neuropathology and Experimental Neurology*, *67*(3), 223–230. https://doi.org/10.1097/NEN.0b013e3181654957

Campbell, S. J., Hughes, P. M., Iredale, J. P., Wilcockson, D. C., Waters, S.,

Docagne, F., … Anthony, D. C. (2003). CINC-1 is an acute-phase protein induced by focal brain injury causing leukocyte mobilization and liver injury. *The FASEB Journal : Official Publication of the Federation of American Societies for Experimental Biology*, *17*(9), 1168–1170. https://doi.org/10.1096/fj.02-0757fje

Campbell, S. J., Meier, U., Mardiguian, S., Jiang, Y., Littleton, E. T., Bristow, A., … Anthony, D. C. (2010). Sickness behaviour is induced by a peripheral CXC-chemokine also expressed in Multiple Sclerosis and EAE. *Brain, Behavior, and Immunity*, *24*(5), 738–746. https://doi.org/10.1016/j.bbi.2010.01.011

Campbell, S. J., Perry, V. H., Pitossi, F. J., Butchart, A. G., Chertoff, M., Waters, S., … Anthony, D. C. (2005). Central nervous system injury triggers Hepatic CC and CXC chemokine expression that is associated with leukocyte mobilization and recruitment to both the central nervous system and the liver. *American Journal of Pathology*, *166*(5), 1487–1497. https://doi.org/10.1016/S0002-9440(10)62365-6

Capizzi, A., Woo, J., & Verduzco-Gutierrez, M. (2020). Traumatic Brain Injury: An Overview of Epidemiology, Pathophysiology, and Medical Management. *Medical Clinics of North America*, *104*(2), 213–238. https://doi.org/10.1016/j.mcna.2019.11.001

Castellani, R. J., & Perry, G. (2017). Dementia Pugilistica Revisited. *Journal of Alzheimer's Disease*, *60*(4), 1209–1221. https://doi.org/10.3233/JAD-170669

Ceciliani, F., Giordano, A., & Spagnolo, V. (2002). The Systemic Reaction During Inflammation: The Acute-Phase Proteins. *Protein and Peptide Letters*, *9*(3), 211–223. Retrieved from http://www.ncbi.nlm.nih.gov/pubmed/12144517

Cernak, I. (2005). Animal models of head trauma. *NeuroRx*, *2*(3), 410–422. https://doi.org/10.1602/neurorx.2.3.410

Chen, C., Hou, J., Lu, J., Zhu, Z., Yang, Y., Peng, W., & Pi, R. (2022). A novel simple traumatic brain injury mouse model. *Chinese Neurosurgical Journal*, *8*(1), 1–9. https://doi.org/10.1186/s41016-022-00273-5

Chen, G., Xu, T., Yan, Y., Zhou, Y., Jiang, Y., Melcher, K., & Xu, H. E. (2017). Amyloid beta : structure , biology and structure-based therapeutic development. *Nature Publishing Group*, *38*(9), 1205–1235. https://doi.org/10.1038/aps.2017.28

Chen, J., & Herrup, K. (2015). *Glutamine as a Potential Neuroprotectant in Alzheimer's Disease*. *Diet and Nutrition in Dementia and Cognitive Decline*. Elsevier Inc. https://doi.org/10.1016/B978-0-12-407824-6.00070-7

Cheng, I. H., Scearce-Levie, K., Legleiter, J., Palop, J. J., Gerstein, H., Bien-Ly, N., … Mucke, L. (2007). Accelerating amyloid-β fibrillization reduces oligomer levels and functional deficits in Alzheimer disease mouse models. *Journal of Biological Chemistry*, *282*(33), 23818–23828. https://doi.org/10.1074/jbc.M701078200

Chételat, G. (2018). Multimodal Neuroimaging in Alzheimer's Disease: Early Diagnosis, Physiopathological Mechanisms, and Impact of Lifestyle. *Journal*

of Alzheimer's Disease, *64*(s1), S199–S211. https://doi.org/10.3233/JAD-179920

Chételat, G., Arbizu, J., Barthel, H., Garibotto, V., Law, I., Morbelli, S., … Drzezga, A. (2020). Amyloid-PET and 18F-FDG-PET in the diagnostic investigation of Alzheimer's disease and other dementias. *The Lancet Neurology*, *19*(11), 951–962. https://doi.org/10.1016/S1474-4422(20)30314-8

Chhimpa, N., Singh, N., Puri, N., & Kayath, H. P. (2023). The Novel Role of Mitochondrial Citrate Synthase and Citrate in the Pathophysiology of Alzheimer's Disease. *Journal of Alzheimer's Disease*, *94*, S453–S472. https://doi.org/10.3233/JAD-220514

Chow, V. W., Mattson, M. P., Wong, P. C., & Gleichmann, M. (2010). An overview of APP processing enzymes and products. *Neuromolecular Medicine*, *12*(1), 1–12. https://doi.org/10.1007/s12017-009-8104-z

Cnossen, M. C., Van Der Naalt, J., Spikman, J. M., Nieboer, D., Yue, J. K., Winkler, E. A., … Lingsma, H. F. (2018). Prediction of Persistent Post-Concussion Symptoms after Mild Traumatic Brain Injury. *Journal of Neurotrauma*, *35*(22), 2691–2698. https://doi.org/10.1089/neu.2017.5486

Corsellis, J. A. N., Bruton, C. J., & Freeman-Browne, D. (1973). The aftermath of boxing. *Physiological Medicine*, *3*, 270–303.

Couch, Y., Akbar, N., Roodselaar, J., Evans, M. C., Gardiner, C., Sargent, I., … Anthony, D. C. (2017). Circulating endothelial cell-derived extracellular vesicles mediate the acute phase response and sickness behaviour associated with CNS inflammation. *Scientific Reports*, *7*(1), 1–12. https://doi.org/10.1038/s41598-017-09710-3

Cray, C., Zaias, J., & Altman, N. H. (2009). Acute phase response in animals: A review. *Comparative Medicine*, *59*(6), 517–526.

Cummings, J. L., Tong, G., & Ballard, C. (2019). Treatment Combinations for Alzheimer's Disease: Current and Future Pharmacotherapy Options. *Journal of Alzheimer's Disease*, *67*(3), 779–794. https://doi.org/10.3233/JAD-180766

Dai, M. H., Zheng, H., Zeng, L. D., & Zhang, Y. (2018). The genes associated with early-onset Alzheimer's disease. *Oncotarget*, *9*(19), 15132–15143. https://doi.org/10.18632/oncotarget.23738

Danysz, W., & Parsons, C. G. (2003). The NMDA receptor antagonist memantine as a symptomatological and neuroprotective treatment for Alzheimer's disease: preclinical evidence. *International Journal of Geriatric Psychiatry*, *18*(September 2003), S23–S32.

De Strooper, B., & Karran, E. (2016). The Cellular Phase of Alzheimer's Disease. *Cell*, *164*(4), 603–615. https://doi.org/10.1016/j.cell.2015.12.056

Decourt, B., Boumelhem, F., Pope, E. D., Shi, J., Mari, Z., & Sabbagh, M. N. (2021). Critical Appraisal of Amyloid Lowering Agents in AD. *Current Neurology and Neuroscience Reports*, *21*(8). https://doi.org/10.1007/s11910-021-01125-y

DeFina, P. A., Moser, R. S., Glenn, M., Lichtenstein, J. D., & Fellus, J. (2013). Alzheimer's disease clinical and research update for health care practitioners. *Journal of Aging Research*, *2013*. Retrieved from http://www.embase.com/search/results?subaction=viewrecord&from=export&id=L369930943%5Cnhttp://dx.doi.org/10.1155/2013/207178

Delic, V., Beck, K. D., Pang, K. C. H., & Citron, B. A. (2020). Biological links between traumatic brain injury and Parkinson's disease. *Acta Neuropathologica Communications*, *8*(1), 1–16. https://doi.org/10.1186/s40478-020-00924-7

Della Sala, S., Spinnler, H., & Venneri, A. (2004). Walking difficulties in patients with Alzheimer's disease might originate from gait apraxia. *Journal of Neurology, Neurosurgery and Psychiatry*, *75*(2), 196–201. https://doi.org/10.1136/jnnp.2002.008805

Dembic, Z. (2015). Cytokines of the Immune System. In *The Cytokines of the Immune System* (pp. 241–262). https://doi.org/10.1016/b978-0-12-419998-9.00007-9

Deture, M. A., & Dickson, D. W. (2019). The neuropathological diagnosis of Alzheimer's disease. *Molecular Neurodegeneration*. Molecular Neurodegeneration. https://doi.org/10.1186/s13024-019-0333-5

Dickens, A. M., Tovar-y-Romo, L. B., Yoo, S.-W., Trout, A. L., Bae, M., Kanmogne, M., … Haughey, N. J. (2017). Astrocyte-shed extracellular vesicles regulate the peripheral leukocyte response to inflammatory brain lesions Alex. *Sci Signal.*, *10*(473), 139–148. https://doi.org/10.1126/scisignal.aai7696.Astrocyte-shed

Dixon, K. J. (2017). Pathophysiology of Traumatic Brain Injury. *Physical Medicine and Rehabilitation Clinics of North America*, *28*(2), 215–225. https://doi.org/10.1016/j.pmr.2016.12.001

Doher, N., Davoudi, V., Magaki, S., Townley, R. A., Haeri, M., & Vinters, H. V. (2023). Illustrated Neuropathologic Diagnosis of Alzheimer's Disease. *Neurology International*, *15*(3), 857–867. https://doi.org/10.3390/neurolint15030054

Dowton, S. B., Peters, C. N., & Jestus, J. J. (1991). Regulation of serum amyloid a gene expression in Syrian hamsters by cytokines. *Inflammation*, *15*(5), 391–397. https://doi.org/10.1007/BF00917355

Duan, R. S., Yang, X., Chen, Z. G., Lu, M. O., Morris, C., Winblad, B., & Zhu, J. (2008). Decreased fractalkine and increased IP-10 expression in aged brain of APPswe transgenic mice. *Neurochemical Research*, *33*(6), 1085–1089. https://doi.org/10.1007/s11064-007-9554-z

Dubois, B., Feldman, H. H., Jacova, C., DeKosky, S. T., Barberger-Gateau, P., Cummings, J., … Scheltens, P. (2007). Research criteria for the diagnosis of Alzheimer's disease: revising the NINCDS-ADRDA criteria. *Lancet Neurology*. https://doi.org/10.1016/S1474-4422(07)70178-3

Dubois, B., Hampel, H., Feldman, H. H., Scheltens, P., Aisen, P., Andrieu, S., … Jack, C. R. (2016). *Preclinical Alzheimer's disease: Definition, natural history, and diagnostic criteria*. *Alzheimer's and Dementia* (Vol. 12).

https://doi.org/10.1016/j.jalz.2016.02.002

Edwards, G., Zhao, J., Dash, P. K., Soto, C., & Moreno-Gonzalez, I. (2020). Traumatic brain injury induces tau aggregation and spreading. *Journal of Neurotrauma*, *37*(1), 80–92. https://doi.org/10.1089/neu.2018.6348

Elder, G., Sosa, M., & Gasper, R. (2010). Transgenic Mouse Models of Alzheimer's Disease. *Mt Sinai J Med*, *77*(1), 69–81. https://doi.org/10.1016/B978-008045046-9.00546-5

Emwas, A. H., Roy, R., McKay, R. T., Tenori, L., Saccenti, E., Nagana Gowda, G. A., … Wishart, D. S. (2019). Nmr spectroscopy for metabolomics research. *Metabolites*. https://doi.org/10.3390/metabo9070123

Endemann, G., & Brunengraber, H. (1980). The source of acetyl coenzyme A for acetylcholine synthesis in the perfused rat phrenic nerve-hemidiaphragm. *Journal of Biological Chemistry*, *255*(23), 11091–11093. https://doi.org/10.1016/s0021-9258(19)70257-9

Endres, K., & Deller, T. (2017). Regulation of alpha-secretase ADAM10 in vitro and in vivo: Genetic, epigenetic, and protein-based mechanisms. *Frontiers in Molecular Neuroscience*, *10*(March), 1–18. https://doi.org/10.3389/fnmol.2017.00056

Fan, L., Young, P. R., Barone, F. C., Feuerstein, G. Z., Smith, D. H., & McIntosh, T. K. (1996). Experimental brain injury induces differential expression of tumor necrosis factor-α mRNA in the CNS. *Molecular Brain Research*, *36*(2), 287–291. https://doi.org/10.1016/0169-328X(95)00274-V

Fani, G., Mannini, B., Vecchi, G., Cascella, R., Cecchi, C., Dobson, C. M., … Chiti, F. (2021). Aβ Oligomers Dysregulate Calcium Homeostasis by Mechanosensitive Activation of AMPA and NMDA Receptors. *ACS Chemical Neuroscience*, *12*(4), 766–781. https://doi.org/10.1021/acschemneuro.0c00811

Faul, M., & Coronado, V. (2015). *Epidemiology of traumatic brain injury OVERVIEW : IMPORTANCE OF INJURY*. *Traumatic Brain Injury* (1st ed., Vol. 127). Elsevier B.V. https://doi.org/10.1016/B978-0-444-52892-6.00001-5

Ferrer, I. (2022). Hypothesis review: Alzheimer's overture guidelines. *Brain Pathology*, *33*(1), 1–12. https://doi.org/10.1111/bpa.13122

Finder, V. H., & Glockshuber, R. (2007). Amyloid-β aggregation. *Neurodegenerative Diseases*, *4*(1), 13–27. https://doi.org/10.1159/000100355

Flavin, W. P., Hosseini, H., Ruberti, J. W., Kavehpour, H. P., Giza, C. C., & Prins, M. L. (2023). Traumatic brain injury and the pathways to cerebral tau accumulation. *Frontiers in Neurology*, *14*(August), 1–17. https://doi.org/10.3389/fneur.2023.1239653

Foers, A. D., Cheng, L., Hill, A. F., Wicks, I. P., & Pang, K. C. (2017). Review: Extracellular Vesicles in Joint Inflammation. *Arthritis and Rheumatology*, *69*(7), 1350–1362. https://doi.org/10.1002/art.40076

Francis, P. T. (2005). The interplay of neurotransmitters in Alzheimer's disease.

CNS Spectrums, *10*(11 SUPPL. 18), 6–9. https://doi.org/10.1017/s1092852900014164

Fricker, M., Tolkovsky, A. M., Borutaite, V., Coleman, M., & Brown, G. C. (2018). Neuronal cell death. *Physiological Reviews*. https://doi.org/10.1152/physrev.00011.2017

Galimberti, D., Schoonenboom, N., Scheltens, P., Fenoglio, C., Bouwman, F., Venturelli, E., … Scarpini, E. (2006). Intrathecal chemokine synthesis in mild cognitive impairment and Alzheimer disease. *Archives of Neurology*, *63*(4), 538–543. https://doi.org/10.1001/archneur.63.4.538

Gao, C., Jiang, J., Tan, Y., & Chen, S. (2023). Microglia in neurodegenerative diseases: mechanism and potential therapeutic targets. *Signal Transduction and Targeted Therapy*, *8*(1). https://doi.org/10.1038/s41392-023-01588-0

Gerothanassis, L. P., Troganis, A., Exarchoou, V., & Barbarossou, K. (2002). NUCLEAR MAGNETIC RESONANCE (NMR) SPECTROSCOPY: BASIC PRINCIPLES AND PHENOMENA, AND THEIR APPLICATIONS TO CHEMISTRY, BIOLOGY AND MEDICINE. *Chem. Educ. Res. Pract.*, *3*(2), 229–252. https://doi.org/10.1039/b2rp90018a

Ghidoni, R., Paterlini, A., & Benussi, L. (2013). Translational proteomics in Alzheimer's disease and related disorders. *Clinical Biochemistry*, *46*(6), 480–486. https://doi.org/10.1016/j.clinbiochem.2012.10.012

Ghosh, A., Mizuno, K., Tiwari, S. S., Proitsi, P., Gomez Perez-Nievas, B., Glennon, E., … Giese, K. P. (2020). Alzheimer's disease-related dysregulation of mRNA translation causes key pathological features with ageing. *Translational Psychiatry*, *10*(1). https://doi.org/10.1038/s41398-020-00882-7

Gilbert, M., Snyder, C., Corcoran, C., Norton, M. C., Lyketsos, C. G., & Tschanz, J. A. T. (2014). The association of traumatic brain injury with rate of progression of cognitive and functional impairment in a population-based cohort of Alzheimer's disease: The Cache County Dementia Progression Study. In *International Psychogeriatrics* (Vol. 26, pp. 1593–1601). https://doi.org/10.1017/S1041610214000842

Gowda, G. A. N., & Raftery, D. (2019). *NMR-Based Metabolomics*. *Humana Press*.

Gowda, G. A. N., Zhang, S., Gu, H., Asiago, V., Shanaiah, N., & Raftery, D. (2008). Metabolomics-based methods for early disease diagnostics. *Expert Review of Molecular Diagnostics*. https://doi.org/10.1586/14737159.8.5.617

Grossberg, G. T., Tong, G., Burke, A. D., & Tariot, P. N. (2019). Present Algorithms and Future Treatments for Alzheimer's Disease. *Journal of Alzheimer's Disease*, *67*(4), 1157–1171. https://doi.org/10.3233/JAD-180903

Grover, S., & Jain, S. (2022). Aducanumab: a review of the first approved amyloid-targeting antibody for Alzheimer's disease. *Drugs and Therapy Perspectives*, *38*(10), 443–454. https://doi.org/10.1007/s40267-022-00944-4

Guo, S., Wang, H., & Yin, Y. (2022). Microglia Polarization From M1 to M2 in

Neurodegenerative Diseases. *Frontiers in Aging Neuroscience*. https://doi.org/10.3389/fnagi.2022.815347

Gyoneva, S., & Ransohoff, R. (2015). Inflammatory reaction after traumatic brain injury: Therapeutic potential of targeting cell-cell communication by chemokines. *Trends Pharmacol Sci*, *36*(7), 471–480. https://doi.org/10.4049/jimmunol.1801473.The

H. Ferreira-Vieira, T., M. Guimaraes, I., R. Silva, F., & M. Ribeiro, F. (2016). Alzheimer's disease: Targeting the Cholinergic System. *Current Neuropharmacology*, *14*(1), 101–115. https://doi.org/10.2174/1570159x13666150716165726

Haarbauer-Krupa, J., Pugh, M. J., Prager, E. M., Harmon, N., Wolfe, J., & Yaffe, K. (2021). Epidemiology of Chronic Effects of Traumatic Brain Injury. *Journal of Neurotrauma*, *38*(23), 3235–3247. https://doi.org/10.1089/neu.2021.0062

Haass, C., Kaether, C., Thinakaran, G., & Sisodia, S. (2012). Trafficking and proteolytic processing of APP. *Cold Spring Harbor Perspectives in Medicine*, *2*(5), 1–25. https://doi.org/10.1101/cshperspect.a006270

Haddad, H. W., Malone, G. W., Comardelle, N. J., Degueure, A. E., Kaye, A. M., & Kaye, A. D. (2022). Aducanumab, a Novel Anti-Amyloid Monoclonal Antibody, for the Treatment of Alzheimer's Disease: A Comprehensive Review. *Health Psychology Research*, *10*(1), 1–12. https://doi.org/10.52965/001c.31925

Halks-Miller, M., Schroeder, M. L., Haroutunian, V., Moenning, U., Rossi, M., Achim, C., … Horuk, R. (2003). CCR1 Is an Early and Specific Marker of Alzheimer's Disease. *Annals of Neurology*, *54*(5), 638–646. https://doi.org/10.1002/ana.10733

Hammond, T. C., & Lin, A. (2022). Glucose Metabolism is a Better Marker for Predicting Clinical Alzheimer's Disease than Amyloid or Tau. *J Cell Immunol*, *4*(1), 15–18.

Hampton, D. W., Webber, D. J., Bilican, B., Goedert, M., Spillantini, M. G., & Chandran, S. (2010). Cell-mediated neuroprotection in a mouse model of human tauopathy. *Journal of Neuroscience*, *30*(30), 9973–9983. https://doi.org/10.1523/JNEUROSCI.0834-10.2010

Harada, K., Kamiya, T., & Tsuboi, T. (2016). Gliotransmitter release from astrocytes: Functional, developmental, and pathological implications in the brain. *Frontiers in Neuroscience*. https://doi.org/10.3389/fnins.2015.00499

Hardy, J. A., & Higgins, G. A. (1992). Alzheimer's disease: The amyloid cascade hypothesis. *Science*, *256*(5054), 184–185. https://doi.org/10.1126/science.1566067

Hazelton, I., Yates, A., Dale, A., Roodselaar, J., Akbar, N., Ruitenberg, M. J., … Couch, Y. (2018). Exacerbation of Acute Traumatic Brain Injury by Circulating Extracellular Vesicles. *Journal of Neurotrauma*, 639–651.

Helmy, A., De Simoni, M. G., Guilfoyle, M. R., Carpenter, K. L. H., & Hutchinson, P. J. (2011). Cytokines and innate inflammation in the pathogenesis of human traumatic brain injury. *Progress in Neurobiology*, *95*(3), 352–372. https://doi.org/10.1016/j.pneurobio.2011.09.003

Herrera, M. L., Deza-Ponzio, R., Ghersi, M. S., de la Villarmois, E. A., Virgolini, M. B., Pérez, M. F., … Hereñú, C. B. (2020). Early Cognitive Impairment Behind Nigrostriatal Circuit Neurotoxicity: Are Astrocytes Involved? *ASN Neuro*, *12*. https://doi.org/10.1177/1759091420925977

Hill, A. F. (2019). Extracellular Vesicles and Neurodegenerative Diseases. *Journal of Neuroscience*, *39*(47), 9269–9273.

Hippius, H., & Neundorfer, G. (2003). The discovery of Alzheimer's disease. *Dialogues in Clinical Neuroscience*, *5*(1), 439–459. https://doi.org/10.4324/9781315079097-30

Hoeijmakers, L., Heinen, Y., Dam, A. Van, & Lucassen, P. J. (2016). Microglial Priming and Alzheimer ' s Disease : A Possible Role for (Early) Immune Challenges and Epigenetics ?, *10*(August), 1–15. https://doi.org/10.3389/fnhum.2016.00398

Huang, X. (2020). *Alzheimer's Disease: Drug Discovery*. *Alzheimer's Disease: Drug Discovery*. https://doi.org/10.36255/exonpublications.alzheimersdisease.2020

Hunsberger, H. C., Greenwood, B. P., Tolstikov, V., Narain, N. R., Kiebish, M. A., & Denny, C. A. (2020). Divergence in the metabolome between natural aging and Alzheimer's disease. *Scientific Reports*, *10*(1), 1–15. https://doi.org/10.1038/s41598-020-68739-z

Husna Ibrahim, N., Yahaya, M. F., Mohamed, W., Teoh, S. L., Hui, C. K., & Kumar, J. (2020). Pharmacotherapy of Alzheimer's Disease: Seeking Clarity in a Time of Uncertainty. *Frontiers in Pharmacology*, *11*(March), 1–16. https://doi.org/10.3389/fphar.2020.00261

Hyman, B., Phelps, C., Beach, T., Bigio, E., Cairns, N., Carillo, M., … Montine, T. J. (2012). National Institute on Aging–Alzheimer's Association guidelines for the neuropathologic assessment of Alzheimer's disease. *Alzheimers Dement.*, *8*(1), 1–13. https://doi.org/10.1016/j.jalz.2011.10.007.National

Iboaya, A., Harris, J. L., Arickx, A. N., & Nudo, R. J. (2019). Models of Traumatic Brain Injury in Aged Animals: A Clinical Perspective. *Neurorehabilitation and Neural Repair*, *33*(12), 975–988. https://doi.org/10.1177/1545968319883879

Ikonomovic, M. D., Uryu, K., Abrahamson, E. E., Ciallella, J. R., Trojanowski, J. Q., Lee, V. M., … Dekosky, S. T. (2004). Alzheimer ' s pathology in human temporal cortex surgically excised after severe brain injury, *190*, 192–203. https://doi.org/10.1016/j.expneurol.2004.06.011

Italiani, P., & Boraschi, D. (2014). From monocytes to M1/M2 macrophages: Phenotypical vs. functional differentiation. *Frontiers in Immunology*, *5*(OCT), 1–22. https://doi.org/10.3389/fimmu.2014.00514

Italiani, P., & Boraschi, D. (2015). New Insights Into Tissue Macrophages: From Their Origin to the Development of Memory. *Immune Network*, *15*(4), 167. https://doi.org/10.4110/in.2015.15.4.167

Jang, S. H., & Kwon, H. G. (2017). Severe disinhibition due to injuries of neural tracts related to emotion circuit in a patient with traumatic brain injury. *Medicine (United States)*, *96*(52), 30–33.

https://doi.org/10.1097/MD.0000000000009493

Jayaraj, R. L., Azimullah, S., Beiram, R., Jalal, F. Y., & Rosenberg, G. A. (2019). Neuroinflammation: Friend and foe for ischemic stroke. *Journal of Neuroinflammation*, *16*(1), 1–24. https://doi.org/10.1186/s12974-019-1516-2

Jha, M. K., Jo, M., Kim, J. H., & Suk, K. (2019). Microglia-Astrocyte Crosstalk: An Intimate Molecular Conversation. *Neuroscientist*, *25*(3), 227–240. https://doi.org/10.1177/1073858418783959

Jian, Z., Liu, R., Zhu, X., Smerin, D., Zhong, Y., Gu, L., … Xiong, X. (2019). The Involvement and Therapy Target of Immune Cells After Ischemic Stroke. *Frontiers in Immunology*, *10*(September), 1–15. https://doi.org/10.3389/fimmu.2019.02167

Joe, E., & Ringman, J. M. (2019). Cognitive symptoms of Alzheimer's disease: Clinical management and prevention. *The BMJ*. https://doi.org/10.1136/bmj.l6217

Johnson, N. H., de Rivero Vaccari, J. P., Bramlett, H. M., Keane, R. W., & Dietrich, W. D. (2023). Inflammasome activation in traumatic brain injury and Alzheimer's disease. *Translational Research*. Elsevier Inc. https://doi.org/10.1016/j.trsl.2022.08.014

Johnson, V. E., Stewart, J. E., Begbie, F. D., Trojanowski, J. Q., Smith, D. H., & Stewart, W. (2013). Inflammation and white matter degeneration persist for years after a single traumatic brain injury. *Brain*, *136*(1), 28–42. https://doi.org/10.1093/brain/aws322

Johnson, V. E., Stewart, W., & Smith, D. H. (2010). Traumatic brain injury and amyloid - β pathology : a link to Alzheimer ' s disease ?, *11*(mAy), 361–370.

Joseph, H. (2021). What is the clinical evidence supporting , and controversy surrounding , the use of aducanumab (Aduhelm TM) for Alzheimer disease ? Retrieved from https://dig.pharmacy.uic.edu/faqs/2021-2/october-2021-faqs/what-is-the-clinical-evidence-supporting-and-controversy-surrounding-the-use-of-aducanumab-aduhelm-tm-for-alzheimer-disease/

Jouanne, M., Rault, S., & Voisin-Chiret, A. S. (2017). Tau protein aggregation in Alzheimer's disease: An attractive target for the development of novel therapeutic agents. *European Journal of Medicinal Chemistry*, *139*, 153–167. https://doi.org/10.1016/j.ejmech.2017.07.070

Juengst, S. B., Kumar, R. G., Arenth, P. M., & Wagner, A. K. (2014). Exploratory associations with Tumor Necrosis Factor-α, disinhibition and suicidal endorsement after traumatic brain injury. *Brain, Behavior, and Immunity*, *41*(1), 134–143. https://doi.org/10.1016/j.bbi.2014.05.020

Julien, J., Joubert, S., Ferland, M. C., Frenette, L. C., Boudreau-Duhaime, M. M., Malo-Véronneau, L., & de Guise, E. (2017). Association of traumatic brain injury and Alzheimer disease onset: A systematic review. *Annals of Physical and Rehabilitation Medicine*, *60*(5), 347–356. https://doi.org/10.1016/j.rehab.2017.03.009

Kadavath, H., Hofele, R. V., Biernat, J., Kumar, S., Tepper, K., Urlaub, H., … Zweckstetter, M. (2015). Tau stabilizes microtubules by binding at the

interface between tubulin heterodimers. *Proceedings of the National Academy of Sciences of the United States of America*, *112*(24), 7501–7506. https://doi.org/10.1073/pnas.1504081112

Kamer, A. R., Dasanayake, A. P., Craig, R. G., & Glodzik-sobanska, L. (2008). Alzheimer's Disease and Peripheral Infections: The Possible Contribution from Periodontal Infections, Model and Hypothesis. *Journal of Alzheimer's Disease*, *13*, 437–449.

Kang, X., Zuo, Z., Hong, W., Tang, H., & Geng, W. (2019). Progress of Research on Exosomes in the Protection Against Ischemic Brain Injury. *Frontiers in Neuroscience*, *13*(October), 1–8. https://doi.org/10.3389/fnins.2019.01149

Kanno, M., Suzuki, S., Fujiwara, T., Yokoyama, A., Sakamoto, A., Takahashi, H., … Tanaka, J. (2005). Functional expression of CCL6 by rat microglia: A possible role of CCL6 in cell-cell communication. *Journal of Neuroimmunology*, *167*(1–2), 72–80. https://doi.org/10.1016/j.jneuroim.2005.06.028

Karve, I. P., Taylor, J. M., & Crack, P. J. (2016). The contribution of astrocytes and microglia to traumatic brain injury. *British Journal of Pharmacology*, *173*(4), 692–702. https://doi.org/10.1111/bph.13125

Kato, T., Inui, Y., Nakamura, A., & Ito, K. (2016). Brain fluorodeoxyglucose (FDG) PET in dementia. *Ageing Research Reviews*, *30*, 73–84. https://doi.org/10.1016/j.arr.2016.02.003

Kent, S. A., Spires-Jones, T. L., & Durrant, C. S. (2020). The physiological roles of tau and Aβ: implications for Alzheimer's disease pathology and therapeutics. *Acta Neuropathologica*. Springer Berlin Heidelberg. https://doi.org/10.1007/s00401-020-02196-w

Khalil, R. H., & Al-Humadi, N. (2020). Types of acute phase reactants and their importance in vaccination (Review). *Biomedical Reports*, *12*(4), 143–152. https://doi.org/10.3892/br.2020.1276

Khellaf, A., Khan, D. Z., & Helmy, A. (2019). Recent advances in traumatic brain injury. *Journal of Neurology*, *266*(11), 2878–2889. https://doi.org/10.1007/s00415-019-09541-4

Kim, D. H., Gim, J. A., Yoon, D., Kim, S., & Kim, H. S. (2017). Metabolomics and mitochondrial dysfunction in Alzheimer's disease. *Genes and Genomics*, *39*(3), 295–300. https://doi.org/10.1007/s13258-016-0494-3

Kim, Do-geun, Krenz, A., Toussaint, L. E., Maurer, K. J., Robinson, S., Yan, A., … Bynoe, M. S. (2016). Non-alcoholic fatty liver disease induces signs of Alzheimer ' s disease (AD) in wild- type mice and accelerates pathological signs of AD in an AD model. *Journal of Neuroinflammation*, 1–18. https://doi.org/10.1186/s12974-015-0467-5

Kim, Dohoon, & Tsai, L. H. (2009). Bridging Physiology and Pathology in AD. *Cell*, *137*(6), 997–1000. https://doi.org/10.1016/j.cell.2009.05.042

Kim, Park, & Choi. (2019). The role of astrocytes in the central nervous system focused on BK channel and heme oxygenase metabolites: A review. *Antioxidants*, *8*(5), 7–13. https://doi.org/10.3390/antiox8050121

Kim, Y. S., & Joh, T. H. (2006). Kim & Joh. *Experimental and Molecular Medicine*, *38*(4), 333–347.

Knoblach, S. M., Fan, L., & Faden, A. I. (1999). Early neuronal expression of tumor necrosis factor-α after experimental brain injury contributes to neurological impairment. *Journal of Neuroimmunology*, *95*(1–2), 115–125. https://doi.org/10.1016/S0165-5728(98)00273-2

Knudson, A. (1971). Detailed 3D LDV measurement of flow field near end wall inside a turbine rotor. *Proceedings of the National Academy of Sciences of the United States of America*, *68*(4), 820–823. https://doi.org/10.2514/6.2001-3975

Kögel, D., Deller, T., & Behl, C. (2012). Roles of amyloid precursor protein family members in neuroprotection, stress signaling and aging. *Experimental Brain Research*, *217*(3–4), 471–479. https://doi.org/10.1007/s00221-011-2932-4

Kolonics, F., Kajdácsi, E., Farkas, V. J., Veres, D. S., Khamari, D., Kittel, Á., … Ligeti, E. (2020). Neutrophils produce proinflammatory or anti-inflammatory extracellular vesicles depending on the environmental conditions. *Journal of Leukocyte Biology*, *109*(4), 793–806. https://doi.org/10.1002/JLB.3A0320-210R

Konishi, H., Koizumi, S., & Kiyama, H. (2022). Phagocytic astrocytes: Emerging from the shadows of microglia. *Glia*, *70*(6), 1009–1026. https://doi.org/10.1002/glia.24145

Kossmann, T., Hans, V., Imhof, H. G., Trentz, O., & Morganti-Kossmann, M. C. (1996). Interleukin-6 released in human cerebrospinal fluid following traumatic brain injury may trigger nerve growth factor production in astrocytes. *Brain Research*, *713*(1–2), 143–152. https://doi.org/10.1016/0006-8993(95)01501-9

Kraeuter, A.-K., Guest, P. C., & Sarnyai, Z. (2019). The Y-Maze for Assessment of Spatial Working and Reference Memory in Mice. In *Pre-Clinical Models* (Vol. 1916, pp. 105–122). https://doi.org/10.1007/978-1-4939-8994-2_12

Krauthausen, M., Kummer, M. P., Zimmermann, J., Reyes-Irisarri, E., Terwel, D., Bulic, B., … Müller, M. (2015). CXCR3 promotes plaque formation and behavioral deficits in an Alzheimer's disease model. *Journal of Clinical Investigation*, *125*(1), 365–378. https://doi.org/10.1172/JCI66771

Kubotera, H., Ikeshima-Kataoka, H., Hatashita, Y., Allegra Mascaro, A. L., Pavone, F. S., & Inoue, T. (2019). Astrocytic endfeet re-cover blood vessels after removal by laser ablation. *Scientific Reports*, *9*(1), 1–10. https://doi.org/10.1038/s41598-018-37419-4

Kumar, A., & Loane, D. J. (2012). Neuroinflammation after traumatic brain injury: Opportunities for therapeutic intervention. *Brain, Behavior, and Immunity*, *26*(8), 1191–1201. https://doi.org/10.1016/j.bbi.2012.06.008

Kwan, A. H., Mobli, M., Gooley, P. R., King, G. F., & MacKay, J. P. (2011). Macromolecular NMR spectroscopy for the non-spectroscopist. *FEBS Journal*, *278*(5), 687–703. https://doi.org/10.1111/j.1742-4658.2011.08004.x

LaFleur, A. M., Lukacs, N. W., Kunkel, S. L., & Matsukawa, A. (2004). Role of

CC chemokine CCL6/C10 as a monocyte chemoattractant in a murine acute peritonitis. *Mediators of Inflammation*, *13*(5–6), 349–355. https://doi.org/10.1080/09629350400014172

Landin, K., Blennow, K., Wallin, A., & Gottfries, C. -G. (1993). Low blood pressure and blood glucose levels in Alzheimer's disease Evidence for a hypometabolic disorder? *Journal of Internal Medicine*, *233*(4), 357–363. https://doi.org/10.1111/j.1365-2796.1993.tb00684.x

Lawrence, T., Helmy, A., Bouamra, O., Woodford, M., Lecky, F., & Hutchinson, P. J. (2016). Traumatic brain injury in England and Wales: Prospective audit of epidemiology, complications and standardised mortality. *BMJ Open*, *6*(11), 1–9. https://doi.org/10.1136/bmjopen-2016-012197

Lee, J. Y., & Kim, H. S. (2017). Extracellular Vesicles in Neurodegenerative Diseases: A Double-Edged Sword. *Tissue Engineering and Regenerative Medicine*, *14*(6), 667–678. https://doi.org/10.1007/s13770-017-0090-x

Letertre, M. P. M., Giraudeau, P., & de Tullio, P. (2021). Nuclear Magnetic Resonance Spectroscopy in Clinical Metabolomics and Personalized Medicine: Current Challenges and Perspectives. *Frontiers in Molecular Biosciences*, *8*(September), 1–25. https://doi.org/10.3389/fmolb.2021.698337

Leuzy, A., Chiotis, K., Lemoine, L., Gillberg, P. G., Almkvist, O., Rodriguez-Vieitez, E., & Nordberg, A. (2019). Tau PET imaging in neurodegenerative tauopathies—still a challenge. *Molecular Psychiatry*, *24*(8), 1112–1134. https://doi.org/10.1038/s41380-018-0342-8

Lewczuk, P., Łukaszewicz-Zając, M., Mroczko, P., & Kornhuber, J. (2020). Clinical significance of fluid biomarkers in Alzheimer's Disease. *Pharmacological Reports*. Springer International Publishing. https://doi.org/10.1007/s43440-020-00107-0

Li, W., Chang, N., & Li, L. (2022). Heterogeneity and Function of Kupffer Cells in Liver Injury. *Frontiers in Immunology*, *13*(June), 1–13. https://doi.org/10.3389/fimmu.2022.940867

Liddelow, S. A., Marsh, S. E., & Stevens, B. (2020). Microglia and Astrocytes in Disease: Dynamic Duo or Partners in Crime? *Trends in Immunology*, *41*(9), 820–835. https://doi.org/10.1016/j.it.2020.07.006

Lindqvist, D., Janelidze, S., Hagell, P., Erhardt, S., Samuelsson, M., Minthon, L., … Brundin, L. (2009). Interleukin-6 Is Elevated in the Cerebrospinal Fluid of Suicide Attempters and Related to Symptom Severity. *Biological Psychiatry*, *66*(3), 287–292. https://doi.org/10.1016/j.biopsych.2009.01.030

Liu, C. C., & Ahearn, J. M. (2004). Acute-Phase Proteins and Inflammation: Immunological and Clinical Implications. In *Measuring Immunity: Basic Science and Clinical Practice* (pp. 131–143). https://doi.org/10.1016/B978-012455900-4/50272-5

Liu, P. P., Xie, Y., Meng, X. Y., & Kang, J. S. (2019). History and progress of hypotheses and clinical trials for alzheimer's disease. *Signal Transduction and Targeted Therapy*, *4*(1). https://doi.org/10.1038/s41392-019-0063-8

Liu, X., Zhang, L., Cao, Y., Jia, H., Li, X., Li, F., … Zhang, J. (2023).

Neuroinflammation of traumatic brain injury: Roles of extracellular vesicles. *Frontiers in Immunology*, *13*(January), 1–14. https://doi.org/10.3389/fimmu.2022.1088827

Liu, Z., Waters, J., & Rui, B. (2022). Metabolomics as a promising tool for improving understanding of multiple sclerosis: A review of recent advances. *Biomedical Journal*. Chang Gung University. https://doi.org/10.1016/j.bj.2022.01.004

Livak, K. J., & Schmittgen, T. D. (2001). Analysis of relative gene expression data using real-time quantitative PCR and the 2-ΔΔCT method. *Methods*, *25*(4), 402–408. https://doi.org/10.1006/meth.2001.1262

Loane, D., Kumar, A., Stoica, B., Cabatbat, R., & Faden, A. (2014). Progressive Neurodegeneration after Experimental Brain Trauma: Association with Chronic Microglial Activation. *J Neuropathol Exp Neurol*, *73*(1), 14–29. https://doi.org/10.4267/2042/56283

Loi, S. M., Eratne, D., Kelso, W., Velakoulis, D., & Looi, J. C. L. (2018). Alzheimer disease: Non-pharmacological and pharmacological management of cognition and neuropsychiatric symptoms. *Australasian Psychiatry*, *26*(4), 358–365. https://doi.org/10.1177/1039856218766123

Lombó, M., Ruiz-díaz, S., Gutiérrez-adán, A., & Sánchez-calabuig, M. J. (2021). Sperm metabolomics through nuclear magnetic resonance spectroscopy. *Animals*, *11*(6), 1–11. https://doi.org/10.3390/ani11061669

Long, H.-Z., Zhou, Z. W., Cheng, Y., Luo, H. Y., Li, F. J., Xu, S. G., & Gao, L. C. (2022). The Role of Microglia in Alzheimer's Disease From the Perspective of Immune Inflammation and Iron Metabolism. *Frontiers in Aging Neuroscience*, *14*(June), 1–18. https://doi.org/10.3389/fnagi.2022.888989

Lopez Sanchez, M. I. G., van Wijngaarden, P., & Trounce, I. A. (2019). Amyloid precursor protein-mediated mitochondrial regulation and Alzheimer's disease. *British Journal of Pharmacology*, *176*(18), 3464–3474. https://doi.org/10.1111/bph.14554

Lordan, R., Tsoupras, A., & Zabetakis, I. (2019). *Inflammation*. *The Impact of Nutrition and Statins on Cardiovascular Diseases*. Elsevier Inc. https://doi.org/10.1016/B978-0-12-813792-5.00002-1

Luan, K., Rosales, J. L., & Lee, K. Y. (2013). Viewpoint: Crosstalks between neurofibrillary tangles and amyloid plaque formation. *Ageing Research Reviews*, *12*(1), 174–181. https://doi.org/10.1016/j.arr.2012.06.002

Lucke-Wold, B. P., Turner, R. C., Logsdon, A. F., Bailes, J. E., Huber, J. D., & Rosen, C. L. (2014). Linking traumatic brain injury to chronic traumatic encephalopathy: Identification of potential mechanisms leading to neurofibrillary tangle development. *Journal of Neurotrauma*, *31*(13), 1129–1138. https://doi.org/10.1089/neu.2013.3303

Lucke-Wold, B., Seidel, K., Udo, R., Omalu, B., Ornstein, M., Nolan, R., … Ross, J. (2017). Role of Tau Acetylation in Alzheimer's Disease and Chronic Traumatic Encephalopathy: The Way Forward for Successful Treatment. *J Neurol Neurosurg*, *4*(2).

Madeira, Caroline Vargas-Lopes, Charles Brandao, C. O., Reis, T., Laks, J.,

Panuzzutti, R., & Ferreira, S. T. (2018). Elevated glutamate and glutamine levels in the cerebrospinal fluid of patients with probable Alzheimer's disease and depression. *Frontiers in Psychiatry*, *9*(561), 1–8. https://doi.org/10.3389/fpsyt.2018.00561

Mandrekar, S., & Landreth, G. E. (2010). Microglia and Inflammation in Alzheimer's Disease. *CNS Neurol Disord Drug Targets*, *9*(2), 156–167.

Márquez, F., & Yassa, M. A. (2019). Neuroimaging Biomarkers for Alzheimer ' s Disease, *5*, 1–14.

Marshall, D. D., & Powers, R. (2017). Beyond the Paradigm: Combining Mass Spectrometry and Nuclear Magnetic Resonance for Metabolomics Darrell. *Prog Nucl Magn Reson Spectrosc.*, *100*, 1–16. https://doi.org/10.1016/j.pnmrs.2017.01.001.Beyond

McDade, E., Cummings, J. L., Dhadda, S., Swanson, C. J., Reyderman, L., Kanekiyo, M., … Bateman, R. J. (2022). Lecanemab in patients with early Alzheimer's disease: detailed results on biomarker, cognitive, and clinical effects from the randomized and open-label extension of the phase 2 proof-of-concept study. *Alzheimer's Research and Therapy*, *14*(1), 1–17. https://doi.org/10.1186/s13195-022-01124-2

McDonald, S. J., Sharkey, J. M., Sun, M., Kaukas, L. M., Shultz, S. R., Turner, R. J., … Corrigan, F. (2020). Beyond the Brain: Peripheral Interactions after Traumatic Brain Injury. *Journal of Neurotrauma*, *37*(5), 770–781. https://doi.org/10.1089/neu.2019.6885

McKhann, G., Knopman, D., Chertkow, H., Hyman, B., Jack Jr, C., Hawas, C., … Phelps, C. (2012). The diagnosis of dementia due to Alzheimer's disease. *Alzheimers Dement*, *7*(3), 263–269. https://doi.org/10.1016/j.jalz.2011.03.005.The

McNaughton, D., Knight, W., Guerreiro, R., Ryan, N., Lowe, J., Poulter, M., … Mead, S. (2012). Duplication of amyloid precursor protein (APP), but not prion protein (PRNP) gene is a significant cause of early onset dementia in a large UK series. *Neurobiology of Aging*, *33*(2), 426.e13-426.e21. https://doi.org/10.1016/j.neurobiolaging.2010.10.010

McQuade, A., & Blurton-Jones, M. (2019). Microglia in Alzheimer's Disease: Exploring How Genetics and Phenotype Influence Risk. *Journal of Molecular Biology*, *431*(9), 1805–1817. https://doi.org/10.1016/j.jmb.2019.01.045

Mendez, M. F. (2019). Early-onset Alzheimer disease and its variants. *CONTINUUM Lifelong Learning in Neurology*, *25*(1), 34–51. https://doi.org/10.1212/CON.0000000000000687

Mendiola-Precoma, J., Berumen, L. C., Padilla, K., & Garcia-Alcocer, G. (2016). Therapies for Prevention and Treatment of Alzheimer's Disease. *BioMed Research International*. Hindawi Publishing Corporation. https://doi.org/10.1155/2016/2589276

Miedel, C. J., Patton, J. M., Miedel, A. N., Miedel, E. S., & Levenson, J. M. (2017). Assessment of spontaneous alternation, novel object recognition and limb clasping in transgenic mouse models of amyloid-β and tau neuropathology. *Journal of Visualized Experiments*, *2017*(123), 1–8.

https://doi.org/10.3791/55523

Minter, M. R., Taylor, J. M., & Crack, P. J. (2016). The contribution of neuroinflammation to amyloid toxicity in Alzheimer's disease. *Journal of Neurochemistry*, *136*(3), 457–474. https://doi.org/10.1111/jnc.13411

Mira, R. G., Lira, M., & Cerpa, W. (2021). Traumatic Brain Injury: Mechanisms of Glial Response. *Frontiers in Physiology*. https://doi.org/10.3389/fphys.2021.740939

Möller, H.-J., & Graeber, M. B. (1998). The case described by Alois Alzheimer in 1911. *European Archives of Psychiatry and Clinical Neuroscience*, *248*(3), 111–122. https://doi.org/10.1007/s004060050027

Mucke, L., Masliah, E., Yu, G., Mallory, M., & Rockenstein, E. (2000). High-Level Neuronal Expression of Aβ1–42 in Wild-Type..Synaptotoxicity without Plaque Formation.pdf. *J Neurosci*, *20*(11), 4050–4058.

Mulaj, M., Foley, J., & Muschol, M. (2014). Amyloid oligomers and protofibrils, but not filaments, self-replicate from native lysozyme. *Journal of the American Chemical Society*, *136*(25), 8947–8956. https://doi.org/10.1021/ja502529m

Muntsant, A., & Giménez-Llort, L. (2022). Crosstalk of Alzheimer's disease-phenotype, HPA axis, splenic oxidative stress and frailty in late-stages of dementia, with special concerns on the effects of social isolation: A translational neuroscience approach. *Frontiers in Aging Neuroscience*, *14*(September), 1–13. https://doi.org/10.3389/fnagi.2022.969381

Myer, D. J., Gurkoff, G. G., Lee, S. M., Hovda, D. A., & Sofroniew, M. V. (2006). Essential protective roles of reactive astrocytes in traumatic brain injury. *Brain*, *129*(10), 2761–2772. https://doi.org/10.1093/brain/awl165

Naj, A. C., & Schellenberg, G. D. (2017). Genomic variants, genes, and pathways of Alzheimer's disease: An overview. *American Journal of Medical Genetics, Part B: Neuropsychiatric Genetics*, *174*(1), 5–26. https://doi.org/10.1002/ajmg.b.32499

Nandoe, R. D. S., Scheltens, P., & Eikelenboom, P. (2002). Head trauma and Alzheimer ' s disease, *4*, 303–308.

Needham, E. J., Helmy, A., Zanier, E. R., Jones, J. L., Coles, A. J., & Menon, D. K. (2019). The immunological response to traumatic brain injury. *Journal of Neuroimmunology*, *332*(April), 112–125. https://doi.org/10.1016/j.jneuroim.2019.04.005

Newington, J. T., Harris, R. A., & Cumming, R. C. (2013). Reevaluating Metabolism in Alzheimer's Disease from the Perspective of the Astrocyte-Neuron Lactate Shuttle Model. *Journal of Neurodegenerative Diseases*, *2013*, 1–13. https://doi.org/10.1155/2013/234572

Ng, S. Y., & Lee, A. Y. W. (2019). Traumatic Brain Injuries: Pathophysiology and Potential Therapeutic Targets. *Frontiers in Cellular Neuroscience*, *13*(November), 1–23. https://doi.org/10.3389/fncel.2019.00528

Nguyen-Lefebvre, A. T., & Horuzsko, A. (2015). Kupffer Cell Metabolism and Function Anh. *J Enzymol Metab*, *1*(1).

Nichols, E., Szoeke, C. E. I., Vollset, S. E., Abbasi, N., Abd-Allah, F., Abdela, J., … Murray, C. J. L. (2019). Global, regional, and national burden of Alzheimer's disease and other dementias, 1990–2016: a systematic analysis for the Global Burden of Disease Study 2016. *The Lancet Neurology*, *18*(1), 88–106. https://doi.org/10.1016/S1474-4422(18)30403-4

Noonin, C., & Thongboonkerd, V. (2021). Exosome-inflammasome crosstalk and their roles in inflammatory responses. *Theranostics*, *11*(9), 4436–4451. https://doi.org/10.7150/THNO.54004

O'Brien, R. J., & Wong, P. C. (2011). Amyloid precursor protein processing and alzheimer's disease. *Annual Review of Neuroscience*, *34*, 185–204. https://doi.org/10.1146/annurev-neuro-061010-113613

Obenaus, A., Ng, M., Orantes, A. M., Kinney-Lang, E., Rashid, F., Hamer, M., … Smit, D. H. (2018). Coagulopathy induced by traumatic brain injury: Systemic manifestation of a localized injury. *Scientific Reports*, *8*(1), 1–14. https://doi.org/10.1039/c8lc00672e

Oberheim, N., Goldman, S., & Nedergaard, M. (2012). Heterogeneity of Astrocytic Form and Function Nancy. *Methods Mol Biol.*, (814), 23–45. https://doi.org/doi:10.1007/978-1-61779-452-0_3

Ohsawa, I., Takamura, C., & Kohsaka, S. (1997). The amino-terminal region of amyloid precursor protein is responsible for neurite outgrowth in rat neocortical explant culture. *Biochemical and Biophysical Research Communications*, *236*(1), 59–65. https://doi.org/10.1006/bbrc.1997.6903

Okamura, N., Harada, R., Furumoto, S., Arai, H., Yanai, K., & Kudo, Y. (2014). Tau PET Imaging in Alzheimer's Disease. *Current Neurology and Neuroscience Reports*, *14*(11). https://doi.org/10.1007/s11910-014-0500-6

Ou, Y. N., Xu, W., Li, J. Q., Guo, Y., Cui, M., Chen, K. L., … Yu, J. T. (2019). FDG-PET as an independent biomarker for Alzheimer's biological diagnosis: A longitudinal study. *Alzheimer's Research and Therapy*, *11*(1), 1–11. https://doi.org/10.1186/s13195-019-0512-1

Paglia, G., Stocchero, M., Cacciatore, S., Lai, S., Angel, P., Alam, M. T., … Astarita, G. (2016). Unbiased Metabolomic Investigation of Alzheimer's Disease Brain Points to Dysregulation of Mitochondrial Aspartate Metabolism. *Journal of Proteome Research*, *15*(2), 608–618. https://doi.org/10.1021/acs.jproteome.5b01020

Pais, M., Martinez, L., Ribeiro, O., Loureiro, J., Fernandez, R., Valiengo, L., … Forlenza, O. V. (2020). Early diagnosis and treatment of Alzheimer's disease: New definitions and challenges. *Brazilian Journal of Psychiatry*, *42*(4), 431–441. https://doi.org/10.1590/1516-4446-2019-0735

Panpalli Ates, M., Karaman, Y., Guntekin, S., & Ergun, M. A. (2016). Analysis of genetics and risk factors of Alzheimer's Disease. *Neuroscience*, *325*, 124–131. https://doi.org/10.1016/j.neuroscience.2016.03.051

Pawluk-Kołc, M., Zieba-Palus, J., & Parczewski, A. (2006). Application of false discovery rate procedure to pairwise comparisons of refractive index of glass fragments. *Forensic Science International*, *160*(1), 53–58. https://doi.org/10.1016/j.forsciint.2005.08.016

Pepys, M. B. (2014). The acute phase response and C-reactive protein. In *Oxford Textbook of Medicine*. https://doi.org/10.1093/med/9780199204854.001.1

Perluigi, M., Barone, E., Di Domenico, F., & Butterfield, D. A. (2016). Aberrant protein phosphorylation in Alzheimer disease brain disturbs pro-survival and cell death pathways. *Biochimica et Biophysica Acta - Molecular Basis of Disease*, *1862*(10), 1871–1882. https://doi.org/10.1016/j.bbadis.2016.07.005

Phares, T. W., Stohlman, S. A., Hinton, D. R., & Bergmann, C. C. (2013). Astrocyte-Derived CXCL10 Drives Accumulation of Antibody-Secreting Cells in the Central Nervous System during Viral Encephalomyelitis. *Journal of Virology*, *87*(6), 3382–3392. https://doi.org/10.1128/jvi.03307-12

Plummer, S., Van Den Heuvel, C., Thornton, E., Corrigan, F., & Cappai, R. (2016). The neuroprotective properties of the amyloid precursor protein following traumatic brain injury. *Aging and Disease*, *7*(2), 163–179. https://doi.org/10.14336/AD.2015.0907

Popiolek-Barczyk, K., & Mika, J. (2016). Targeting the Microglial Signaling Pathways: New Insights in the Modulation of Neuropathic Pain. *Current Medicinal Chemistry*, *23*, 2908–2928. https://doi.org/10.2174/0929867323666161606071

Porsteinsson, A. P., Isaacson, R. S., Knox, S., Sabbagh, M. N., & Rubino, I. (2021). Diagnosis of Early Alzheimer's Disease: Clinical Practice in 2021. *Journal of Prevention of Alzheimer's Disease*, *8*(3), 371–386. https://doi.org/10.14283/jpad.2021.23

Prins, M., Greco, T., Alexander, D., & Giza, C. C. (2013). The pathophysiology of traumatic brain injury at a glance. *Disease Models & Mechanisms*, *6*(6), 1307–1315. https://doi.org/10.1242/dmm.011585

Qiu, W. Q., Ferreira, A., Miller, C., Koo, E. H., & Selkoe, D. J. (1995). Cell-surface β-amyloid precursor protein stimulates neurite outgrowth of hippocampal neurons in an isoform-dependent manner. *Journal of Neuroscience*, *15*(3 II), 2157–2167. https://doi.org/10.1523/jneurosci.15-03-02157.1995

Rahman, A., Hossen, M. A., Chowdhury, M. F. I., Bari, S., Tamanna, N., Sultana, S. S., … Saif-Ur-Rahman, K. M. (2023). Aducanumab for the treatment of Alzheimer's disease: a systematic review. *Psychogeriatrics*, 512–522. https://doi.org/10.1111/psyg.12944

Ramanan, V. K., & Day, G. S. (2023). Anti-amyloid therapies for Alzheimer disease: finally, good news for patients. *Molecular Neurodegeneration*, *18*(1), 1–3. https://doi.org/10.1186/s13024-023-00637-0

Ramos-Cejudo, J., Wisniewski, T., Marmar, C., Zetterberg, H., Blennow, K., de Leon, M. J., & Fossati, S. (2018). Traumatic Brain Injury and Alzheimer's Disease: The Cerebrovascular Link. *EBioMedicine*, *28*, 21–30. https://doi.org/10.1016/j.ebiom.2018.01.021

Raposo, G., Nijman, H. W., Stoorvogel, W., Leijendekker, R., Harding, C. V, Melief, C. J. M., & Geuze, H. J. (1996). B lymphocytes secrete antigen-presenting vesicles. *Journal of Experimental Medicine*, *183*(3), 1161–1172. https://doi.org/10.1084/jem.183.3.1161

Rees, A. J. (2010). Monocyte and macrophage biology: An overview. *Seminars in Nephrology*, *30*(3), 216–233. https://doi.org/10.1016/j.semnephrol.2010.03.002

Reitz, C., Brayne, C., & Mayeux, R. (2011). Epidemiology of Alzheimer disease. *Nature Reviews Neurology*, *7*(3), 137–152. https://doi.org/10.1038/nrneurol.2011.2

Roberts, G. W., Gentleman, S. M., Lynch, A., Murray, L., Landon, M., & Graham, D. I. (1994). β Amyloid protein deposition in the brain after severe head injury: Implications for the pathogenesis of Alzheimer's disease. *Journal of Neurology, Neurosurgery and Psychiatry*, *57*(4), 419–425. https://doi.org/10.1136/jnnp.57.4.419

Roberts, Gareth W, Allsop, D., & Bruton, C. (1990). The occult aftermath of boxing. *Journal of Neurology Neurosurgery and Psychiatry*, *53*, 373–378.

Rosales, C. (2018). Neutrophil: A cell with many roles in inflammation or several cell types? *Frontiers in Physiology*, *9*(FEB), 1–17. https://doi.org/10.3389/fphys.2018.00113

Ruet, A., Bayen, E., Jourdan, C., Ghout, I., Meaude, L., Lalanne, A., … Azouvi, P. (2019). A detailed overview of long-term outcomes in severe traumatic brain injury eight years post-injury. *Frontiers in Neurology*, *10*(FEB), 1–13. https://doi.org/10.3389/fneur.2019.00120

Sá-Pereira, I., Roodselaar, J., Couch, Y., Consentino Kronka Sosthenes, M., Evans, M. C., Anthony, D. C., & Stolp, H. B. (2018). Hepatic acute phase response protects the brain from focal inflammation during postnatal window of susceptibility. *Brain, Behavior, and Immunity*, *69*, 486–498. https://doi.org/10.1016/j.bbi.2018.01.008

Saber, A. T., Lamson, J. S., Jacobsen, N. R., Ravn-Haren, G., Hougaard, K. S., Nyendi, A. N., … Vogel, U. (2013). Particle-Induced Pulmonary Acute Phase Response Correlates with Neutrophil Influx Linking Inhaled Particles and Cardiovascular Risk. *PLoS ONE*, *8*(7), 1–10. https://doi.org/10.1371/journal.pone.0069020

Sahlender, D. A., Savtchouk, I., & Volterra, A. (2014). What do we know about gliotransmitter release from astrocytes? *Philosophical Transactions of the Royal Society B: Biological Sciences*. https://doi.org/10.1098/rstb.2013.0592

Sanabria-Castro, A., Alvarado-Echeverría, I., & Monge-Bonilla, C. (2017). Molecular pathogenesis of alzheimer's disease: An update. *Annals of Neurosciences*, *24*(1), 46–54. https://doi.org/10.1159/000464422

Sawant, K. V., Poluri, K. M., Dutta, A. K., Sepuru, K. M., Troshkina, A., Garofalo, R. P., & Rajarathnam, K. (2016). Chemokine CXCL1 mediated neutrophil recruitment: Role of glycosaminoglycan interactions. *Scientific Reports*, *6*, 4–11. https://doi.org/10.1038/srep33123

Scharre, B. D. W. (2019). Preclinical, Prodromal, and Dementia Stages of Alzheimer's Disease. *Practical Neurology Magazine*, (June), 36–47.

Scheltens, P., De Strooper, B., Kivipelto, M., Holstege, H., Chételat, G., Teunissen, C. E., … van der Flier, W. M. (2021). Alzheimer's disease. *The*

Lancet, *397*(10284), 1577–1590. https://doi.org/10.1016/S0140-6736(20)32205-4

Schetters, S. T. T., Gomez-Nicola, D., Garcia-Vallejo, J. J., & Van Kooyk, Y. (2018). Neuroinflammation: Microglia and T cells get ready to tango. *Frontiers in Immunology*, *8*(JAN). https://doi.org/10.3389/fimmu.2017.01905

Schweber, M. (1986). Etiologic theories of Alzheimer's disease. *The American Journal of Alzheimer's Care and Related Disorders*, 24–31.

Selkoe, D. J. (2019). Early network dysfunction in Alzheimer's disease. *Science*, *365*(6453), 540–541. https://doi.org/10.1126/science.aay5188

Selmaj, K. W., Farooq, M., Norton, W. T., Raine, C. S., & Brosnan, C. F. (1990). Proliferation of astrocytes in vitro in response to cytokines. A primary role for tumor necrosis factor. *Journal of Immunology*, *144*(1), 129–135. Retrieved from https://www.unhcr.org/publications/manuals/4d9352319/unhcr-protection-training-manual-european-border-entry-officials-2-legal.html?query=excom 1989

Sempere, L., Rodríguez-Rodríguez, A., Boyero, L., & Egea-Guerrero, J. J. (2019). Experimental models in traumatic brain injury: from animal models to in vitro assays. *Medicina Intensiva*, *43*(6), 362–372. https://doi.org/10.1016/j.medin.2018.04.012

Semple, B. D., Bye, N., Rancan, M., Ziebell, J. M., & Morganti-Kossmann, M. C. (2010). Role of CCL2 (MCP-1) in traumatic brain injury (TBI): Evidence from severe TBI patients and CCL2-/- mice. *Journal of Cerebral Blood Flow and Metabolism*, *30*(4), 769–782. https://doi.org/10.1038/jcbfm.2009.262

Serafini, G., Pompili, M., Elena Seretti, M., Stefani, H., Palermo, M., Coryell, W., & Girardi, P. (2013). The role of inflammatory cytokines in suicidal behavior: A systematic review. *European Neuropsychopharmacology*, *23*(12), 1672–1686. https://doi.org/10.1016/j.euroneuro.2013.06.002

Serrano, I., Luque, A., & Aran, J. M. (2018). Exploring the immunomodulatory moonlighting activities of acute phase proteins for tolerogenic dendritic cell generation. *Frontiers in Immunology*, *9*. https://doi.org/10.3389/fimmu.2018.00892

Shan, Z., & Ju, C. (2020). Hepatic Macrophages in Liver Injury. *Frontiers in Immunology*, *11*(April), 1–9. https://doi.org/10.3389/fimmu.2020.00322

Shavit-Stein, E., Gerasimov, A., Aharoni, S., Gofrit, S. G., Pikus, E., Pick, C. G., & Maggio, N. (2021). Unexpected role of stress as a possible resilience mechanism upon mild traumatic brain injury (mTBI) in mice. *Molecular and Cellular Neuroscience*, *111*, 103586. https://doi.org/10.1016/j.mcn.2020.103586

Shibly, A. Z., Sheikh, A. M., Michikawa, M., Tabassum, S., Azad, A. K., Zhou, X., … Nagai, A. (2023). Analysis of Cerebral Small Vessel Changes in AD Model Mice. *Biomedicines*, *11*(1), 1–17. https://doi.org/10.3390/biomedicines11010050

Shin, M. K., Vázquez-Rosa, E., Koh, Y., Dhar, M., Chaubey, K., Cintrón-Pérez, C. J., … Pieper, A. A. (2021). Reducing acetylated tau is neuroprotective in brain injury. *Cell*, *184*(10), 2715-2732.e23.

https://doi.org/10.1016/j.cell.2021.03.032

Shippy, D. C., Watters, J. J., & Ulland, T. K. (2022). Transcriptional response of murine microglia in Alzheimer's disease and inflammation. *BMC Genomics*, *23*(1), 1–12. https://doi.org/10.1186/s12864-022-08417-8

Shishido, H., Kishimoto, Y., Kawai, N., & Toyota, Y. (2016). Traumatic brain injury accelerates amyloid-B deposition and impairs spatial learning in the triple-transgenic mouse model of Alzheimer's disease. *Neuroscience Letters*, *629*, 62–67. https://doi.org/10.1016/j.neulet.2016.06.066

Shishido, H., Ueno, M., Sato, K., Matsumura, M., Toyota, Y., Kirino, Y., … Kishimoto, Y. (2019). Traumatic Brain Injury by Weight-Drop Method Causes Transient Amyloid- β Deposition and Acute Cognitive Deficits in Mice, *2019*.

Simats, A., García-Berrocoso, T., Penalba, A., Giralt, D., Llovera, G., Jiang, Y., … Montaner, J. (2018). CCL23: a new CC chemokine involved in human brain damage. *Journal of Internal Medicine*, *283*(5), 461–475. https://doi.org/10.1111/joim.12738

Simon, D. W., McGeachy, M., Bayir, H., Clark, R. S., Loane, D. J., & M, K. P. (2017). Neuroinflammation in the Evolution of Secondary Injury, Repair, and Chronic Neurodegeneration after Traumatic Brain Injury. *Nat Rev Neurol.*, *13*(3), 171–191. https://doi.org/10.1038/nrneurol.2017.13.Neuroinflammation

Simpson, A. J., Simpson, M. J., & Soong, R. (2012). Nuclear magnetic resonance spectroscopy and its key role in environmental research. *Environmental Science and Technology*, *46*(21), 11488–11496. https://doi.org/10.1021/es302154w

Sims, R., Hill, M., & Williams, J. (2020). The multiplex model of the genetics of Alzheimer's disease. *Nature Neuroscience*, *23*(3), 311–322. https://doi.org/10.1038/s41593-020-0599-5

Singh-Manoux, A., Dugravot, A., Brunner, E., Kumari, M., Shipley, M., Elbaz, A., & Kivimaki, M. (2014). Interleukin-6 and C-reactive protein as predictors of cognitive decline in late midlife. *Neurology*, *83*(6), 486–493. https://doi.org/10.1212/WNL.0000000000000665

Sirkis, D. W., Bonham, L. W., Johnson, T. P., La Joie, R., & Yokoyama, J. S. (2022). Dissecting the clinical heterogeneity of early-onset Alzheimer's disease. *Molecular Psychiatry*, *27*(6), 2674–2688. https://doi.org/10.1038/s41380-022-01531-9

Sluimer, J. D., Vrenken, H., Blankenstein, M. A., Fox, N. C., Scheltens, P., Barkhof, F., & Van Der Flier, W. M. (2008). Whole-brain atrophy rate in Alzheimer disease: Identifying fast progressors. *Neurology*, *70*(19 PART 2), 1836–1841. https://doi.org/10.1212/01.wnl.0000311446.61861.e3

Smith, C. D., Carney, J. M., Starke-Reed, P. E., Oliver, C. N., Stadtman, E. R., Floyd, R. A., & Markesbery, W. R. (1991). Excess brain protein oxidation and enzyme dysfunction in normal aging and in Alzheimer disease. *Proceedings of the National Academy of Sciences of the United States of America*, *88*(23), 10540–10543. https://doi.org/10.1073/pnas.88.23.10540

Söderberg, L., Johannesson, M., Nygren, P., Laudon, H., Eriksson, F., Osswald,

G., … Lannfelt, L. (2022). Lecanemab, Aducanumab, and Gantenerumab — Binding Profiles to Different Forms of Amyloid-Beta Might Explain Efficacy and Side Effects in Clinical Trials for Alzheimer's Disease. *Neurotherapeutics*, (0123456789). https://doi.org/10.1007/s13311-022-01308-6

Soria Lopez, J. A., González, H. M., & Léger, G. C. (2019). Alzheimer's disease. *Handbook of Clinical Neurology*, *167*, 231–255. https://doi.org/10.1016/B978-0-12-804766-8.00013-3

Soulet, D., & Rivest, S. (2008). Microglia. *Current Biology*, *18*(12), 506–508. https://doi.org/10.1016/j.cub.2008.04.047

Sreejit, G., Fleetwood, A. J., Murphy, A. J., & Nagareddy, P. R. (2020). Origins and diversity of macrophages in health and disease. *Clinical and Translational Immunology*, *9*(12), 1–19. https://doi.org/10.1002/cti2.1222

Steel, D. M., Rogers, J. T., DeBeer, M. C., DeBeer, F. C., & Whitehead, A. S. (1993). Biosynthesis of human acute-phase serum amyloid A protein (A-SAA) in vitro: The roles of mRNA accumulation, poly(A) tail shortening and translational efficiency. *Biochemical Journal*, *291*(3), 701–707. https://doi.org/10.1042/bj2910701

Steuer, A. E., Brockbals, L., & Kraemer, T. (2019). Metabolomic strategies in biomarker research-new approach for indirect identification of drug consumption and sample manipulation in clinical and forensic toxicology? *Frontiers in Chemistry*. https://doi.org/10.3389/fchem.2019.00319

Stocchetti, N., & Zanier, E. R. (2016). Chronic impact of traumatic brain injury on outcome and quality of life: A narrative review. *Critical Care*, *20*(1), 1–10. https://doi.org/10.1186/s13054-016-1318-1

Stock, A. J., Kasus-Jacobi, A., & Pereira, H. A. (2018). The role of neutrophil granule proteins in neuroinflammation and Alzheimer's disease. *Journal of Neuroinflammation*, *15*(1), 1–15. https://doi.org/10.1186/s12974-018-1284-4

Sun, X., Chen, W. D., & Wang, Y. D. (2015). β-Amyloid: The key peptide in the pathogenesis of Alzheimer's disease. *Frontiers in Pharmacology*, *6*(SEP), 1–9. https://doi.org/10.3389/fphar.2015.00221

Synnott, P. G., Whittington, M. D., Lin, G. A., Rind, D. M., & Pearson, S. D. (2021). The effectiveness and value of aducanumab for Alzheimer's disease. *Journal of Managed Care and Specialty Pharmacy*, *27*(1), 1613–1617. https://doi.org/10.18553/JMCP.2021.27.11.1613

Tahami Monfared, A. A., Byrnes, M. J., White, L. A., & Zhang, Q. (2022). Alzheimer's Disease: Epidemiology and Clinical Progression. *Neurology and Therapy*, *11*(2), 553–569. https://doi.org/10.1007/s40120-022-00338-8

Takao, K., & Miyakawa, T. (2006). Light/dark transition test for mice. *Journal of Visualized Experiments*, (1), 1–3. https://doi.org/10.3791/104

Takeshita, Y., Fujikawa, S., Serizawa, K., Fujisawa, M., Matsuo, K., Nemoto, J., … Kanda, T. (2021). New BBB Model Reveals That IL-6 Blockade Suppressed the BBB Disorder, Preventing Onset of NMOSD. *Neurology(R) Neuroimmunology & Neuroinflammation*, *8*(6), 1–13.

https://doi.org/10.1212/NXI.0000000000001076

Tanzi, R. E. (2012). The Genetics of Alzheimer Disease, 1–10.

Tcw, J., & Goate, A. M. (2017). Genetics of β-Amyloid Precursor Protein in Alzheimer's Disease. *Cold Spring Harbor Perspectives in Medicine*, *7*(6), 1–11. https://doi.org/10.1101/cshperspect.a024539

Thalhauser, C. J., & Komarova, N. L. (2012). Alzheimer ' s disease : rapid and slow progression, (June 2011), 119–126.

Therriault, J., Zimmer, E. R., Benedet, A. L., Pascoal, T. A., Gauthier, S., & Rosa-Neto, P. (2022). Staging of Alzheimer's disease: past, present, and future perspectives. *Trends in Molecular Medicine*, *28*(9), 726–741. https://doi.org/10.1016/j.molmed.2022.05.008

Thorn, C. F., Lu, Z. Y., & Whitehead, A. S. (2003). Tissue-specific regulation of the human acute-phase serum amyloid A genes, SAA1 and SAA2, by glucocorticoids in hepatic and epithelial cells. *European Journal of Immunology*, *33*(9), 2630–2639. https://doi.org/10.1002/eji.200323985

Tosh, J. L., Fisher, E. M. C., Wiseman, F. K., Rickman, M., Rhymes, E., Norona, F. E., … Isaacs, A. M. (2018). The integration site of the APP transgene in the J20 mouse model of Alzheimer's disease. *Wellcome Open Research*, *2*(0), 1–13. https://doi.org/10.12688/wellcomeopenres.12237.2

Trejo-Lopez, J. A., Yachnis, A. T., & Prokop, S. (2022). Neuropathology of Alzheimer's Disease. *Neurotherapeutics*. Springer International Publishing. https://doi.org/10.1007/s13311-021-01146-y

Trinchieri, G. (2007). Interleukin-10 production by effector T cells: Th1 cells show self control. *Journal of Experimental Medicine*, *204*(2), 239–243. https://doi.org/10.1084/jem.20070104

Trzeciakiewicz, H., Tseng, J. H., Wander, C. M., Madden, V., Tripathy, A., Yuan, C. X., & Cohen, T. J. (2017). A dual pathogenic mechanism links tau acetylation to sporadic tauopathy. *Scientific Reports*, *7*(March), 1–13. https://doi.org/10.1038/srep44102

Uhlar, C. M., & Whitehead, A. S. (1999). Serum amyloid A, the major vertebrate acute-phase reactant. *European Journal of Biochemistry*, *265*(2), 501–523. https://doi.org/10.1046/j.1432-1327.1999.00657.x

Urabe, F., Kosaka, N., Ito, K., Kimura, T., Egawa, S., & Ochiya, T. (2020). Extracellular vesicles as biomarkers and therapeutic targets for cancer. *American Journal of Physiology - Cell Physiology*, *318*(1), C29–C39. https://doi.org/10.1152/ajpcell.00280.2019

Vakhshiteh, F., Atyabi, F., & Ostad, S. N. (2019). Mesenchymal stem cell exosomes: A two-edged sword in cancer therapy. *International Journal of Nanomedicine*, *14*, 2847–2859. https://doi.org/10.2147/IJN.S200036

Van Der Velpen, V., Teav, T., Gallart-Ayala, H., Mehl, F., Konz, I., Clark, C., … Popp, J. (2019). Systemic and central nervous system metabolic alterations in Alzheimer's disease. *Alzheimer's Research and Therapy*, *11*(1), 1–12. https://doi.org/10.1186/s13195-019-0551-7

Van Niel, G., D'Angelo, G., & Raposo, G. (2018). Shedding light on the cell

biology of extracellular vesicles. *Nature Reviews Molecular Cell Biology*, *19*(4), 213–228. https://doi.org/10.1038/nrm.2017.125

Van Wagoner, N. J., Oh, J. W., Repovic, P., & Benveniste, E. N. (1999). Interleukin-6 (IL-6) production by astrocytes: Autocrine regulation by IL-6 and the soluble IL-6 receptor. *Journal of Neuroscience*, *19*(13), 5236–5244. https://doi.org/10.1523/jneurosci.19-13-05236.1999

VanItallie, T. B. (2019). Traumatic brain injury (TBI) in collision sports: Possible mechanisms of transformation into chronic traumatic encephalopathy (CTE). *Metabolism: Clinical and Experimental*, *100*, 1–6. https://doi.org/10.1016/j.metabol.2019.07.007

Vilca-Melendez, S., Uthaug, M. V., & Griffin, J. L. (2021). 1H Nuclear Magnetic Resonance: A Future Approach to the Metabolic Profiling of Psychedelics in Human Biofluids? *Frontiers in Psychiatry*, *12*(December). https://doi.org/10.3389/fpsyt.2021.742856

Villapol, S., Kryndushkin, D., Balarezo, M. G., Campbell, A. M., Saavedra, J. M., Shewmaker, F. P., & Symes, A. J. (2015). Hepatic Expression of Serum Amyloid A1 Is Induced by Traumatic Brain Injury and Modulated by Telmisartan. *American Journal of Pathology*, *185*(10), 2641–2652. https://doi.org/10.1016/j.ajpath.2015.06.016

Vinaiphat, A., & Sze, S. K. (2019). Clinical implications of extracellular vesicles in neurodegenerative diseases. *Expert Review of Molecular Diagnostics*, *19*(9), 813–824. https://doi.org/10.1080/14737159.2019.1657407

Vyklicky, V., Korinek, M., Smejkalova, T., Balik, A., Krausova, B., Kaniakova, M., … Vyklicky, L. (2014). Structure, function, and pharmacology of NMDA receptor channels. *Physiological Research*, *63*(SUPPL.). https://doi.org/10.33549/physiolres.932678

Walker, K. A., Le Page, L. M., Terrando, N., Duggan, M. R., Heneka, M. T., & Bettcher, B. M. (2023). The role of peripheral inflammatory insults in Alzheimer's disease: a review and research roadmap. *Molecular Neurodegeneration*, *18*(1), 1–19. https://doi.org/10.1186/s13024-023-00627-2

Webster, K. M., Sun, M., Crack, P., Brien, T. J. O., Shultz, S. R., & Semple, B. D. (2017). Inflammation in epileptogenesis after traumatic brain injury. *Journal of Neuroinflammation*, 1–17. https://doi.org/10.1186/s12974-016-0786-1

Weggen, S., & Beher, D. (2012). Molecular consequences of amyloid precursor protein and presenilin mutations causing autosomal-dominant Alzheimer's disease. *Alzheimer's Research and Therapy*, *4*(2). https://doi.org/10.1186/alzrt107

Wilkins, J. M., & Trushina, E. (2018). Application of metabolomics in Alzheimer's disease. *Frontiers in Neurology*. https://doi.org/10.3389/fneur.2017.00719

Wishart, D. S., Feunang, Y. D., Marcu, A., Guo, A. C., Liang, K., Vázquez-Fresno, R., … Scalbert, A. (2018). HMDB 4.0: The human metabolome database for 2018. *Nucleic Acids Research*, *46*(D1), D608–D617. https://doi.org/10.1093/nar/gkx1089

Wisniewski, H. M., Moretz, R. C., & Lossinsky, A. S. (1981). Evidence for induction of localized amyloid deposits and neuritic plaques by an infectious agent. *Annals of Neurology*, *10*(6), 517–522. https://doi.org/10.1002/ana.410100605

Woodcock, T., & Morganti-Kossmann, M. C. (2013). The role of markers of inflammation in traumatic brain injury. *Frontiers in Neurology*, *4 MAR*(March), 1–18. https://doi.org/10.3389/fneur.2013.00018

Wright, A. L., Zinn, R., Hohensinn, B., Konen, L. M., Beynon, S. B., Tan, R. P., … Vissel, B. (2013). Neuroinflammation and Neuronal Loss Precede Aβ Plaque Deposition in the hAPP-J20 Mouse Model of Alzheimer's Disease. *PLoS ONE*, *8*(4). https://doi.org/10.1371/journal.pone.0059586

Xia, M. Q., Bacskai, B. J., Knowles, R. B., Qin, S. X., & Hyman, B. T. (2000). Expression of the chemokine receptor CXCR3 on neurons and the elevated expression of its ligand IP-10 in reactive astrocytes: In vitro ERK1/2 activation and role in Alzheimer's disease. *Journal of Neuroimmunology*, *108*(1–2), 227–235. https://doi.org/10.1016/S0165-5728(00)00285-X

Xing, Y., Tang, Y., & Jia, J. (2015). Sex Differences in Neuropsychiatric Symptoms of Alzheimer's Disease: The Modifying Effect of Apolipoprotein e ε 4 Status. *Behavioural Neurology*, *2015*. https://doi.org/10.1155/2015/275256

Xiong, Y., Mahmood, A., & Chopp, M. (2013). Animal models of traumatic brain injury. *Nature Reviews Neuroscience*, *14*(2), 128–142. https://doi.org/10.1038/nrn3407

Xiong, Y., Mahmood, A., & Chopp, M. (2018). Current understanding of neuroinflammation after traumatic brain injury and cell-based therapeutic opportunities. *Chinese Journal of Traumatology - English Edition*, *21*(3), 137–151. https://doi.org/10.1016/j.cjtee.2018.02.003

Yan, H., Jiang, J., Pang, Y., Achyut, B., Lizardo, M., Liang, X., … Yang, L. (2015). CCL9 induced by TGF-β signaling in myeloid cells enhances tumor cell survival in the premetastatic organ. *Cancer Res*, *75*(24), 5283–5298. https://doi.org/10.1158/0008-5472.CAN-15-2282-T.CCL9

Yan, X., Hu, Y., Wang, B., Wang, S., & Zhang, X. (2020). Metabolic Dysregulation Contributes to the Progression of Alzheimer's Disease. *Frontiers in Neuroscience*, *14*(November), 1–20. https://doi.org/10.3389/fnins.2020.530219

Yang, C., & Xiao, S. (2015). Are the revised diagnostic criteria for Alzheimer's disease useful in low- and middle-income countries? *Shanghai Archives of Psychiatry*, *27*(2), 119–123. https://doi.org/10.11919/j.issn.1002-0829.215001

Yang, Q., Zhang, A. H., Miao, J. H., Sun, H., Han, Y., Yan, G. L., … Wang, X. J. (2019). Metabolomics biotechnology, applications, and future trends: A systematic review. *RSC Advances*, *9*(64), 37245–37257. https://doi.org/10.1039/c9ra06697g

Yang, Y., Ye, Y., Chen, C., Kong, C., Su, X., Zhang, X., … He, X. (2019). Acute Traumatic Brain Injury Induces CD4 + and CD8 + T Cell Functional

Impairment by Upregulating the Expression of PD-1 via the Activated Sympathetic Nervous System. *NeuroImmunoModulation*, *26*(1), 43–57. https://doi.org/10.1159/000495465

Yao, H. W., & Kuan, C. Y. (2020). Early neutrophil infiltration is critical for inflammation-sensitized hypoxic-ischemic brain injury in newborns. *Journal of Cerebral Blood Flow and Metabolism*, *40*(11), 2188–2200. https://doi.org/10.1177/0271678X19891839

Yau, J. L. W., McNair, K. M., Noble, J., Brownstein, D., Hibberd, C., Morton, N., … Seckl, J. R. (2007). Enhanced hippocampal long-term potentiation and spatial learning in aged 11β-hydroxysteroid dehydrogenase type 1 knock-out mice. *Journal of Neuroscience*, *27*(39), 10487–10496. https://doi.org/10.1523/JNEUROSCI.2190-07.2007

Yeh, F. L., Hansen, D. V., & Sheng, M. (2017). TREM2, Microglia, and Neurodegenerative Diseases. *Trends in Molecular Medicine*, *23*(6), 512–533. https://doi.org/10.1016/j.molmed.2017.03.008

Yin, C., Harms, A. C., Hankemeier, T., Kindt, A., & de Lange, E. C. M. (2023). Status of Metabolomic Measurement for Insights in Alzheimer's Disease Progression—What Is Missing? *International Journal of Molecular Sciences*, *24*(5). https://doi.org/10.3390/ijms24054960

Yurgelun-Todd, D. A., Bueler, C. E., McGlade, E. C., Churchwell, J. C., Brenner, L. A., & Lopez-Larson, M. P. (2011). Neuroimaging correlates of traumatic brain injury and suicidal behavior. *Journal of Head Trauma Rehabilitation*, *26*(4), 276–289. https://doi.org/10.1097/HTR.0b013e31822251dc

Zaheer, S., Thangavel, R., Wu, Y., Khan, M. M., Kempuraj, D., & Zaheer, A. (2013). Enhanced expression of glia maturation factor correlates with glial activation in the brain of triple transgenic Alzheimer's disease mice. *Neurochemical Research*, *38*(1), 218–225. https://doi.org/10.1007/s11064-012-0913-z

Zhang, L., Chen, J., Li, Y., Zhang, Z. G., & Chopp, M. (2000). Quantitative measurement of motor and somatosensory impairments after mild (30 min) and severe (2 h) transient middle cerebral artery occlusion in rats. *Journal of the Neurological Sciences*, *174*(2), 141–146. https://doi.org/10.1016/S0022-510X(00)00268-9

Zhang, X., Zhu, X., Wang, C., Zhang, H., & Cai, Z. (2016). Non-targeted and targeted metabolomics approaches to diagnosing lung cancer and predicting patient prognosis. *Oncotarget*, *7*(39), 63437–63448. https://doi.org/10.18632/oncotarget.11521

Zhang, Y., Liu, Y., Liu, H., & Tang, W. H. (2019). Exosomes: Biogenesis, biologic function and clinical potential. *Cell and Bioscience*, *9*(1), 1–18. https://doi.org/10.1186/s13578-019-0282-2

Zhang, Y. W., Thompson, R., Zhang, H., & Xu, H. (2011). APP processing in Alzheimer's disease. *Molecular Brain*, *4*(1), 1–13. https://doi.org/10.1186/1756-6606-4-3

Zheng, H., & Koo, E. H. (2011). Biology and pathophysiology of the amyloid precursor protein. *Molecular Neurodegeneration*, *6*(1), 1–16.

https://doi.org/10.1186/1750-1326-6-27

Zhou, F., Sun, Y., Xie, X., & Zhao, Y. (2023). Blood and CSF chemokines in Alzheimer's disease and mild cognitive impairment: a systematic review and meta-analysis. *Alzheimer's Research and Therapy*. BioMed Central. https://doi.org/10.1186/s13195-023-01254-1

Zidarič, T., Gradišnik, L., & Velnar, T. (2022). Astrocytes and human artificial blood-brain barrier models. *Bosnian Journal of Basic Medical Sciences*, *22*(5), 651–672. https://doi.org/10.17305/bjbms.2021.6943

Ziebell, J. M., & Morganti-Kossmann, M. C. (2010). Involvement of Pro- and Anti-Inflammatory Cytokines and Chemokines in the Pathophysiology of Traumatic Brain Injury. *Neurotherapeutics*, *7*(1), 22–30. https://doi.org/10.1016/j.nurt.2009.10.016